Promotoren:

Prof. dr. ir. R. Baets	Universiteit Gent, INTEC
Prof. dr. ir. D. Van Thourhout	Universiteit Gent, INTEC

Overige leden van de examencommissie:

Prof. dr. ir. D. Zutter, voorzitter	Universiteit Gent, INTEC
Prof. dr. ir. G. Morthier, secretaris	Universiteit Gent, INTEC
dr. ir. P. Absil	IMEC, Leuven
Prof. dr. A. Driessen	Universiteit Twente
Prof. dr. ir. C. Leys	Universiteit Gent, Toegepaste Fysica
Prof. dr. ir. I. Moerman	Universiteit Gent, INTEC

Universiteit Gent
Faculteit Ingenieurswetenschappen

Vakgroep Informatietechnologie (INTEC)
Sint-Pietersnieuwstraat 41
B-9000 Gent
België

Tel: +32 9 264 33 16
Fax: +32 9 264 35 93
http://www.intec.ugent.be
http://www.photonics.intec.ugent.be

Dit werk kwam tot stand in het kader van een specialisatiebeurs van het IWT - Instituut voor de Aanmoediging van Innovatie door Wetenschap en Technologie in Vlaanderen
This work was carried out in the context of a specialization grant from the Flemish Institute for the Industrial Advancement of Scientific and Technological Research (IWT).

Dankwoord

Maandagavond, 11 april, zes uur 's avonds, Sint-Pietersnieuwstraat 41, blok A, 1ste verdiep. De gang is redelijk uitgestorven, het mooie weer lokt mensen naar een terrasje. Karien zit verder op de gang toch nog als gewoonlijk financiële spitstechnologie te bedrijven.

Eerste bureau aan de linkerkant leg ik de laatste hand aan dit boekje. De gifgroene muren van dit lokaal hebben veel volk zien passeren. Van de 'groeiers' waarmee ik hier gestart ben tot de huidige fotonica-bezetting. Ze hebben allemaal hun steentje bijgedragen tot dit proefwerk. Er zullen er een paar ontbreken maar toch een paar speciale vermeldingen: Ingrid, ze zat wel nooit op mijn bureau maar is toch de eerste die me dit wereldje van de opto-elektronica heeft binnengeloodst. Spijtig dat de groei moest stoppen maar het was toch een leerrijk en aangenaam jaar. Tom, Koen, Bart, Mark, Jan, ... maakten het vele wachten bij groeien plezant. Joff heeft het als bureau-oudste hier nog het langst uitgehouden op onze bureau terwijl die langzaam steeds meer ingepalmd werd door fotonica-mensen. Thierry, een verhaal op zich, een complete time-warp toen hij enkele maanden geleden hier weer op Intec opdook. Dan al mijn jongere collega's, Wouter, Doos, Hans, Stijn, Joost, merci voor de goeie sfeer. Nog een speciale vermelding voor Günther, thesisstudent eerste klas, en die daarna een waardevolle collega werd. Heel aangenaam om eens van gedachten te kunnen wisselen met iemand die met iets verwants bezig is. En dan nog Hendrik, onze redder in bange dagen, die altijd wel weet waar je dat ene ding in de meetkamer kan vinden en nog veel meer.

Eerste bureau rechts, de thuishaven van Kristien en vroeger van Liesbet en Steven. Kristien waar je altijd eens je hart kan gaan luchten met een koffietje in de hand als het te veel tegen zit. Steven en Liesbet die bleven processen en processen hoewel de problemen bleven komen en komen, bedankt, zonder jullie was het niet gelukt.

Een bureautje verder, Dries en Geert. Geert die alle Newton-perikelen in goeie banen bleef leiden en Dries, waar je altijd alles kan aan gaan vragen.

Ik ben vast niet de enige die vindt dat je wel een jaartje vroeger had mogen terugkomen uit de V.S.

Nog ietsje verder Roel, die me de kans gaf om na de groeiproblemen mijn toekomst in de fotonica te beproeven. Bedankt voor het vertrouwen, alle ideeën en steun. Ilse op het einde van de gang, die meestal samen met mij zich afvroeg waar Roel naar toe was.

Op het einde van de gang is er nog bureau waar je eerst op de kast botst alvorens mensen te zien: Jan, Danaë, Kurt, Olivier, Sam, Jonathan, Frederik en nog natuurlijk Mathias, onze rebel with(out) a cause, maar altijd een bemoedigend woord klaar. De 39, ja dat vervallen gebouw hiernaast, dat binnenkort geschiedenis is en ons al die barbecues opleverde, een aparte enclave waar je je maar waagt met een specifieke vraag. Reinhard die met mij samen het Newton-project deelde, Pieter waarmee ik eens over ringen kon leuteren, Peter waar je met iets theoretisch altijd terecht kon, niet-lineaire dingen proberen meten met Gino, Wim, Bert, Bart, Frederik, Joris, . . .

En dan zijn er nog zo veel belangrijke mensen daarbuiten. Al mijn vrienden die zich niet direct lieten afschrikken door het woord opto-elektronica maar zelfs de uitleg over een ringresonator wisten te doorstaan en de enkeling die zelfs wist te onthouden dat ik met één of ander filter bezig was. Ze deden meer dan ze beseften door telkens nog eens te vragen hoe het ging ’met het doctoraat’.

Mijn ouders, van me leren rekenen toen ik klein was, al is dat nog altijd geen succes, tot klagen bij de buren als ze te veel lawaai maakten en ik moest blokken, zonder jullie was dit nooit gelukt. Bedankt.

En traditioneel als laatste: Sebastian, er zijn geen woorden om te beschrijven wat jij allemaal voor mij gedaan hebt, ik ga het dan ook niet proberen. Het dankwoord is het meest gelezen deel van een doctoraat maar dat zal niet zo blijven als het honderden bladzijden lang wordt. Tijd om samen van vakantie te genieten. En tijd om me ook eens op een terrasje te wagen.

Inhoudsopgave

Nederlandstalige Tekst

Nederlandstalige Samenvatting

1. Inleiding

1.1 Achtergrond

Dit onderzoek kadert in het onderzoeksgebied van de fotonica, wat in essentie alles beslaat wat met de studie van licht te maken heeft. Dit gaat van spectroscopie, alle mogelijke sensoren, lasers, verlichting, ... tot alle toepassingen in de telecommunicatie die één van de grootste afzetmarkten vormt voor dit soort onderzoek. In de rest van deze inleiding zullen we ons dan ook voornamelijk toespitsen op de telecommunicatietoepassingen al is het meeste ook van toepassing op de andere gebieden.

Hoewel de telecommarkt een paar jaar geleden een serieuze klap heeft gekregen, is en blijft het een belangrijke en groeiende markt. De vraag naar meer bandbreedte blijft stijgen door het toenemend aantal gebruikers en de stijgende groei van toepassingen die steeds meer bandbreedte vragen. Om dit probleem aan te pakken bestaat een brede consensus dat het nodig zal zijn om over te stappen naar volledig optische netwerken. Optische vezels zijn nu al lang het medium waarlangs de data wordt getransporteerd op de grote lijnen van het netwerk. Toch wordt dit optische signaal nog regelmatig omgezet naar een elektrisch signaal om het signaal te regenereren, te routeren naar een bepaalde bestemming etc. Veel onderzoek wordt verricht naar het volledig optisch maken van al deze functies. Daar komt nog bij dat als het volledig optische netwerk wil doordringen tot dicht bij de gebruiker en niet enkel in de ruggegraat van het netwerk, de kost heel belangrijk is.

1.2 Toekomstperspectieven

Als we proberen voorspellen wat de toekomst is voor de fotonica, kunnen we de vergelijking maken met de ontwikkeling die de elektronica heeft doorgemaakt, die vooral te maken heeft met miniaturisatie en integratie.

Er zijn verscheidene redenen waarom dit in de fotonica nog niet gebeurd is, enkele hiervan worden hier besproken.

Een eerste reden is het feit dat voor fotonische componenten geen consensus bestaat over het gebruik van een bepaald materiaalsysteem. Voor elektronische toepassingen is Si al jaren het materiaal bij uitstek en de fabricagetechnieken op basis van Si zijn dan ook erg volwassen en uitgewerkt. Voor fotonische toepassingen bestaat geen materiaalsysteem dat de uitgesproken voorkeur geniet. Daarom zijn verschillende benaderingen in gebruik gaande van een volledige monolithische integratie waarbij alles in InP wordt gefabriceerd, zowel passieve als actieve functies, tot volledige hybride toepassingen die verschillende elementen in verschillende materiaalsystemen uitwerken en deze daarna samenbrengen. De eerste aanpak heeft het nadeel dat andere materiaalsystemen als eigenlijk beter geschikt zijn voor passieve functies, dat InP vrij duur is, de processingtechnieken hiervoor niet zo volwassen zijn als voor Si, . . . De hybride integratie heeft het nadeel dat grotere componenten ontstaan, en dat vaak gebruik moet gemaakt worden van dure alignatietechnieken voor het samenbrengen van de onderdelen.

Een tweede reden is het feit dat de fotonica niet beschikt over een schaalbare, veelzijdige component zoals de transistor voor de elektronica.

1.3 Ringresonatoren en waferbonding

Een integratie-aanpak die zich situeert tussen de twee uitgelegd in de vorige paragraaf, is de heterogene integratie waarbij ook verschillende materiaalsystemen worden gebruikt maar een veel hogere integratie word nagestreefd dan bij hybride integratie en de processen zoveel mogelijk op waferschaal gebeuren zonder nood aan veeleisende actieve alignatie. Dit proces steunt op het gebruik van 'waferbonding' technieken om de verschillende materiaalsystemen met elkaar te integreren.

De ringresonator is in essentie een vrij eenvoudige component, de werking zal in de volgende paragraaf worden uiteengezet. Het idee van een ringresonator kwam van Marcatili in de jaren '60. In het begin van de jaren '80 werden de eerste ringresonatoren gefabriceerd maar deze hadden een straal van enkel mm. De fabricage van ringresonatoren met een straal in de orde van enkele tientallen micrometer of enkele micrometer, microingresonatoren, dateert van de tweede helft van de jaren '90 toen fabricagetechnieken voldoende op punt stonden om deze kleine componenten te fabriceren. De interesse in microringresonatoren is daarna enorm gestegen en een wijde waaier aan toepassingen werd gedemonstreerd wat duidelijk de veelzijdigheid van de ringresonator illustreert.

Zoals hierboven al aangehaald wordt verregaande integratie op fotonische chips bemoeilijkt door het feit dat, in tegenstelling tot elektronische toepassingen, fotonica niet beschikt over een duidelijke basiscomponent die erg veelzijdig en schaalbaar is, zoals de transistor. Er werd al geopperd dat de microring resonator de transistor van de fotonica zou kunnen zijn. Of hij deze rol zal kunnen waarmaken valt nog te zien maar de voorbeelden in de volgende paragrafen tonen in elk geval de veelzijdigheid en schaalbaarheid van de microringresonator.

2. Werking van een ringresonator

2.1 Wat is een ringresonator?

Een ringresonator is in essentie een vrij eenvoudige opto-elektronische component die bestaat uit twee rechte golfgeleiders en één ringvormige golfgeleider in het midden zoals geïllustreerd in Fig. 1. De werking van de component is als volgt: licht wordt geïnjecteerd via poort A en een beetje van het licht koppelt over van de rechte golfgeleider naar de ring. Er zijn dan twee situaties mogelijk: in de eerste situatie is de golflengte van het geïnjecteerde licht niet juist om een resonantie in de ring op te wekken. Het licht passeert dan vrij ongestoord de ring zoals te zien is op Fig. 2(b). Als het licht echter de juiste golflengte heeft, zal het na één keer volledig rond de ring gegaan te zijn constructief interfereren. De ring is dan in resonantie en het elektrische veldpatroon is zoals te zien op Fig. 2(a).

Als het licht in resonantie is, kan een deel van het licht in de ring zelf weer overkoppelen naar de tweede rechte golfgeleider en naar poort C. Vermits het gedrag van de component golflengte-afhankelijk is, is de meest voor de hand liggende toepassing ervan een golflengte-selectief filter. De transmissie aan poort B en C in functie van de golflengte is te zien op Fig. 3.

De formules voor de transmissies aan poort B en C zijn de volgende

$$\frac{E_C}{E_A} = \frac{-t_1 t_2 \sqrt{A}\, exp(\frac{-j\phi}{2})}{1 - A r_1 r_2 exp(-j\phi)}$$

$$\frac{E_B}{E_A} = \frac{r_1 - r_2 A\, exp(-j\phi)}{1 - r_1 r_2 A\, exp(-j\phi)}$$

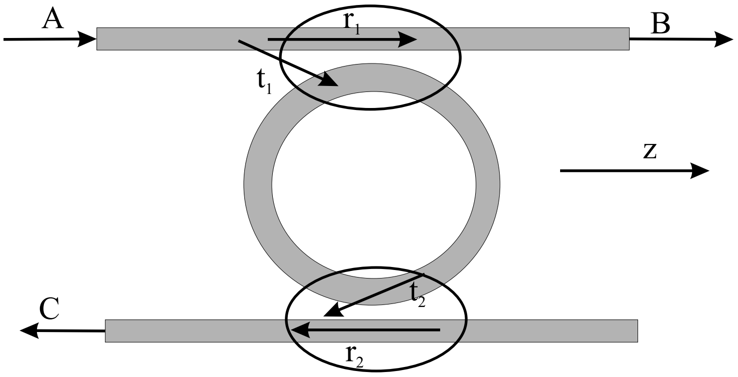

Figuur 1: Een eenvoudige ringresonator

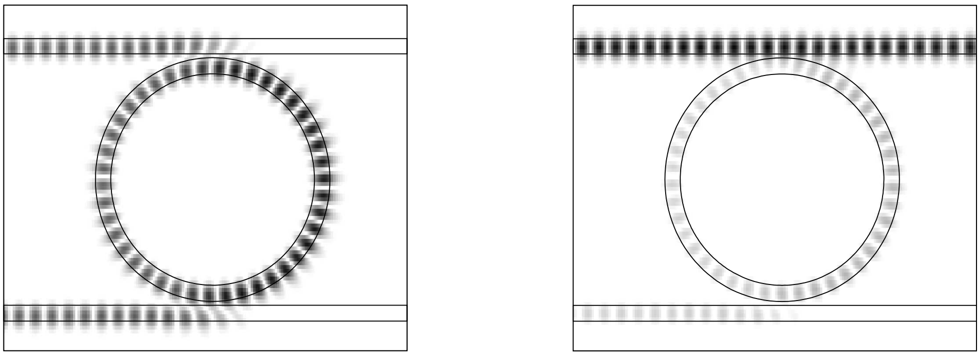

(a) In resonantie

(b) Uit resonantie

Figuur 2: Het veldprofiel van de ringresonator in en uit resonantie

waarbij

$$\begin{aligned} A &= exp(-\alpha L) \\ \phi &= \frac{2\pi}{\lambda} n_{eff} 2L \\ L &= \pi R_r \end{aligned} \tag{1}$$

L is de halve omtrek van de ring, R_r is de buitenstraal van de ring, α is de vermogenverliescoëfficiënt, λ de vacuüm-golflengte van het licht en n$_{eff}$ is de effectieve index van de mode in de ring berekend op straal R$_r$. t_1, t_2, r_1 en r_2 zijn amplitude-transmissie- en reflectiecoëfficiënten en zijn aangeduid op Fig. 1. Deze formules zijn voor asymmetrische ringen: dit wil zeggen dat de ingangs-koppelaar en de uitgangskoppelaar niet identiek hoeven te

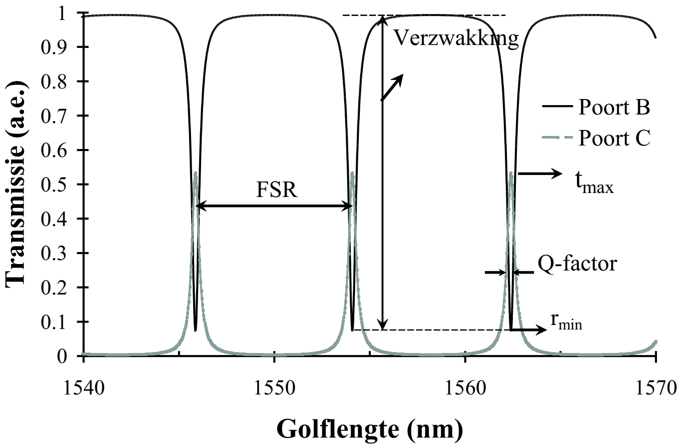

Figuur 3: De transmissie aan poort B en C van een ringresonator

zijn: $r_1 \neq r_2$ en $t_1 \neq t_2$. Deze formules werden ook opgesteld voor verliesloze koppelaars zodat $r_1^2 + t_1^2 = 1$ wat tot gevolg heeft dat de fase van de mode in de ring- en de busgolfgeleiders 90 graden verschilt. Het geval voor verlieshebbende koppelaars wordt later besproken.

Wat normaal gemeten wordt, is het vermogen aan poort B en C. Dit wordt voor symmetrische ringen berekend met de volgende formules:

$$\begin{aligned}
\frac{I_C}{I_A} &= \frac{I_C}{I_0} = \frac{t_{max}}{1 + Fsin^2(\frac{\phi}{2})} \\
t_{max} &= \frac{(1-R)^2 A}{(1-RA)^2} \\
F &= \frac{4RA}{(1-RA)^2} \\
\frac{I_B}{I_A} &= \frac{r_{min} + Fsin^2(\phi/2)}{1 + Fsin^2(\phi/2)} \\
r_{min} &= \frac{(1-A)^2 R}{(1-RA)^2}
\end{aligned} \tag{2}$$

2.2 Parameters voor de performantie van een ring

In deze paragraaf bespreken we de belangrijkste parameters om de performantie van een ring te kwantificeren. Enkele hiervan werden al geïllustreerd op Fig. 3. Behalve de parameters die hier besproken zullen worden zijn nog andere belangrijk zoals het fase-antwoord, de vorm van de resonantiepiek, de dispersie, ...

2.2.1 De spectrale afstand tussen twee resonanties

De afstand op golflengteschaal tussen twee resonanties (FSR: Free Spectral Range) is een eerste belangrijke parameter:

$$FSR = \frac{\lambda^2}{2n_g L}$$

waarbij n_g de groepsindex is:

$$n_g = n - \lambda \frac{dn}{d\lambda}$$

2.2.2 De Q-factor en de Finesse

De Q-factor en de Finesse $\mathcal{F}$ zijn beide gerelateerd aan de breedte van de resonantiepieken en meer bepaald aan de breedte op halve hoogte (FWHM):

$$\begin{aligned} Q &= \frac{\lambda}{\delta\lambda_{FWHM}} \\ &= \frac{\pi n 2L\sqrt{AR}}{\lambda(1-AR)} \end{aligned}$$

$$\mathcal{F} = \frac{FSR}{\delta\lambda_{FWHM}} = \pi\frac{\sqrt{AR}}{1-AR}$$

De Q-factor en de Finesse zijn als volgt gerelateerd:

$$Q = \frac{\mathcal{F} 2nL}{\lambda}$$

2.2.3 De extractie-efficiëntie ER

De extractie-efficiëntie is de verhouding tussen het vermogen dat nog overblijft in poort B als de ring in resonantie is, r_{min}, tot het vermogen in poort B als de ring niet in resonantie is. Voor verscheidene toepassingen kan het erg belangrijk zijn om het signaal bij resonantie volledig te extraheren uit poort B omwille van overspraak. Voor symmetrische koppeling wordt r_{min} gegeven door:

$$r_{min} = \frac{(1-A)^2 R}{(1-RA)^2}$$

2.2.4 De maximum transmissie t$_{max}$

Het vermogen dat bij resonantie overgekoppeld wordt naar poort C is t$_{max}$. Dit wordt gegeven door:

$$t_{max} = \frac{(1 - R_1)(1 - R_2)A}{(1 - \sqrt{R_1 R_2}A)^2}$$

In het symmetrische geval vereenvoudigt dit zich tot:

$$t_{max} = \frac{(1 - R)^2 A}{(1 - RA)^2}$$

2.2.5 De veldversterking in de ring FE

Het licht dat in de ring gekoppeld wordt, blijft daar normaal lange tijd opgesloten zodat een hoge veldsterkte, veel hoger dan de veldsterkte van het signaal aan poort A, kan ontstaan. Dit sterke veld kan gebruikt worden voor bvb. niet-lineaire toepassingen.

$$FE = |\frac{E_r}{E_A}|_{\phi=0} = \frac{t_1}{1 - r_1 r_2 A}$$

2.3 Invloed van de ontwerpsparameters op de performantie

De verschillende ontwerpsparameters die ter beschikking staan zijn de straal, de koppeling en het verlies. Men kan argumenteren dat het verlies niet echt een ontwerpsparameter is vermits die niet vrij te controleren is, maar in het geval van actieve ringen is dit wel het geval. De meest interessante verliesterm die hier kan gebruikt worden is het verlies na één propagatie rond de ring (RTL: roundtrip loss).

$$RTL = 1 - A^2$$

2.3.1 Symmetrische ringresonator

Voor een symmetrisch gekoppelde ringresonator moet een compromis gezocht worden tussen hoge maximum transmissie (wat samengaat met een kleine r$_{min}$) en een hoge Q-factor. De maximum transmissie stijgt immers als de koppelingsfactor stijgt, maar de Q-factor daalt dan. Dit is geïllustreerd op de Figuren 4, 5 en 6. Als men geïnteresseerd is in een grote veldversterking bestaat echter wel een optimum, zoals te zien is op Fig. 7.

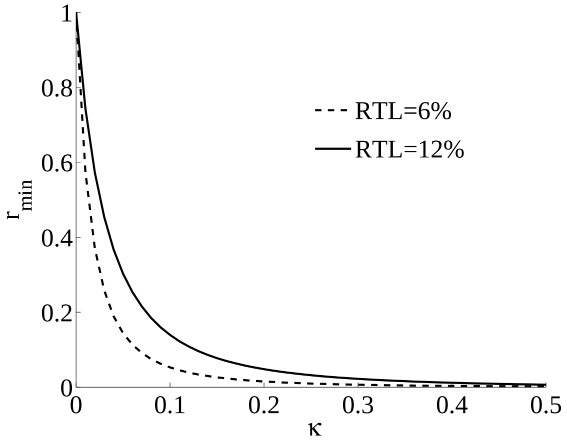

Figuur 4: Vermogen in poort B bij resonantie als functie van de koppelingscoëfficiënt

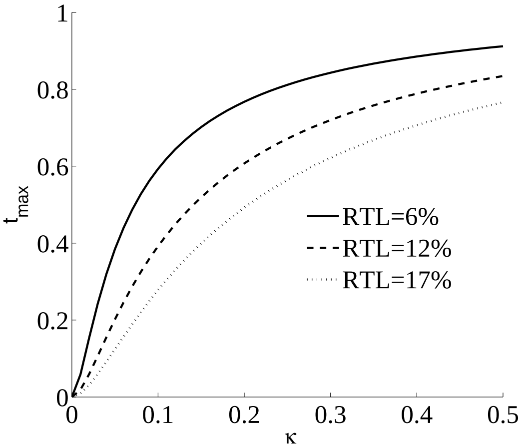

Figuur 5: Vermogen in poort C bij resonantie als functie van de koppelingscoëfficiënt

2.3.2 Asymmetrische ringresonator

De koppelingscoëfficiënten van beide koppelaars niet dezelfde bij een asymmetrisch gekoppelde ringresonator en dus wordt een extra vrijheidsgraad geïntroduceerd. Het belangrijkste gevolg hiervan is dat een ringresonator gemaakt kan worden waarbij, ongeacht de verliesfactor, alle vermogen uit poort B kan geëxtraheerd worden als de koppelingscoëfficiënten voldoen aan

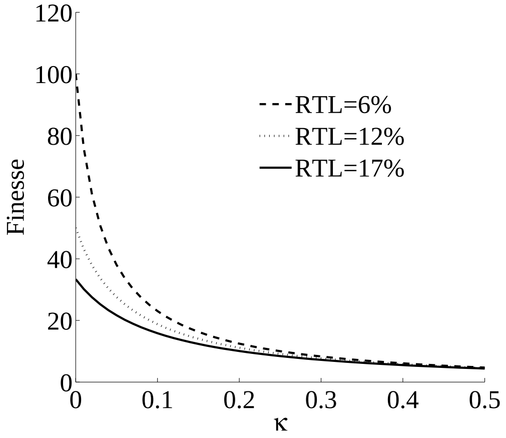

Figuur 6: Finesse als functie van de koppelingscoëfficiënt

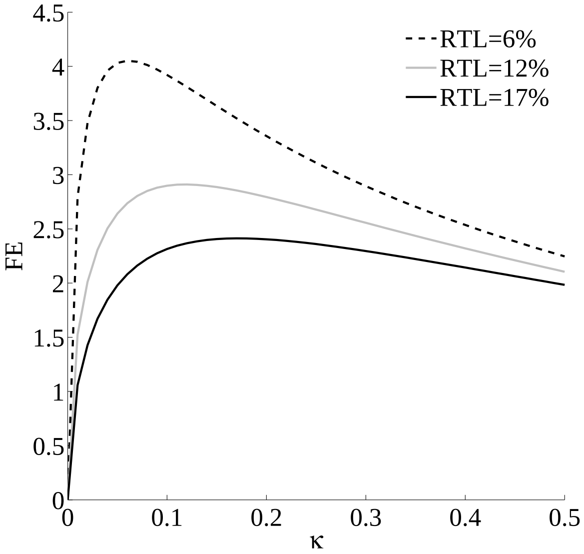

Figuur 7: Veldversterking als functie van de koppelingscoëfficiënt

volgende vergelijking:

$$r_1 = r_2 A$$

3. Fabricagemogelijkheden en literatuuroverzicht

3.1 Inleiding

De verschillende ontwerpen van ringresonatoren zijn in twee categorieën in te delen: verticale en laterale integratie. Bij laterale integratie bevinden de rechte golfgeleiders zich in hetzelfde vlak als de ring, bij verticale integratie bevinden ze zich boven of onder de ring. Beide mogelijkheden zijn geïllustreerd in Fig. 8. Beide aanpakken hebben hun voor- en nadelen.

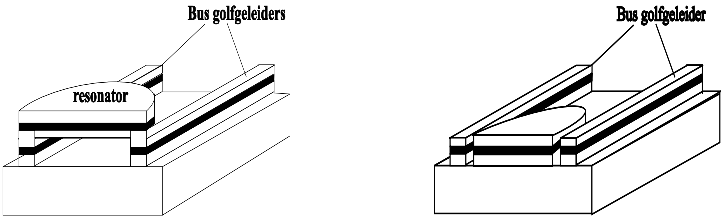

(a) Verticale integratie (b) Laterale integratie

Figuur 8: Verticaal en lateraal geïntegreerde ringresonatoren

De eerste microringresonatoren werden gefabriceerd met behulp van laterale integratie. Het probleem is hier echter dat de koppeling tussen de rechte en de ring vrij moeilijk te controleren valt. Een gebogen golfgeleider verliest een deel van het licht door middel van afstraling. Dit verlies wordt groter naarmate de straal kleiner wordt. Om het verlies te beperken is het nodig om een groot brekingsindexverschil te voorzien langs de rand van de ring. In veel materialen wordt dit gerealiseerd door de gebogen golfgeleider diep te etsen zodat de keerlaag lucht wordt, wat een brekingsindex n=1 heeft. Het nadeel aan deze aanpak is echter dat de mode die het licht geleidt in de gebogen golfgeleider nu erg goed opgesloten is, waardoor koppelen met de mode van de rechte golfgeleider onmogelijk is tenzij beide golfgeleiders erg dicht bij elkaar gebracht worden. In de praktijk wil dit zeggen dat de spleet tussen de rechte golfgeleider en de ring ver beneden een micron is en dat maakt het onmogelijk om de standaard lithografietechnieken nog te gebruiken. Dit is geïllustreerd in Fig. 9(b) waar de velden van de rechte golfgeleider en de gebogen golfgeleider getoond worden. Zelfs met een spleet die maar 200 nm breed is, is het duidelijk dat de overlap tussen deze 2 velden vrij klein is. De koppeling is bovendien exponentieel afhankelijk van de grootte van deze spleet wat controle over de koppeling erg moeilijk maakt.

Om dit probleem op te lossen werd de verticale koppeling bedacht. Hierbij bevindt de rechte golfgeleider zich onder de ring. Dat heeft tot gevolg dat

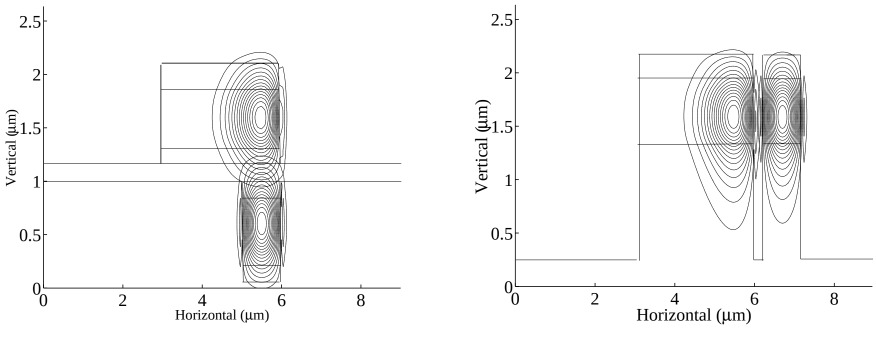

(a) (b)

Figuur 9: Veldprofielen voor een horizontale en verticaal gekoppelde ringresonator

de afstand tussen de twee bepaald wordt door de nauwkeurigheid van de epitaxiaalgroei die gebruikt wordt om de lagen te deponeren. Vermits deze zeer goed is, is de controle over de koppeling veel groter. Het is echter al duidelijk dat de fabricage van dit soort component meer complexe stappen zal inhouden, met name waferbonding.

Een andere oplossing voor het moeilijk koppelen in de laterale configuratie is gebruik maken van een renbaan-ontwerp. Hierbij worden rechte stukken toegevoegd aan de ringresonator zodat het gebied waarover de ring kan koppelen met de rechte golfgeleiders veel groter wordt. Dit heeft echter een negatief effect op de FSR.

3.2 Fabricage van ringresonatoren met verticale integratie

In dit werk werd gekozen om de verticaal gekoppelde route te volgen. De fabricageprocedure die daarbij gevolgd werd is de volgende: om te beginnen wordt een epitaxiaal-lagenstructuur (Fig. 10(a)) gegroeid die bestaat uit twee lagen met hogere brekingsindex die dienst zullen doen als de kernlagen voor de ringgolfgeleider en de rechte golfgeleiders. Deze lagen worden omsloten door keerlagen met een lagere brekingsindex. De lagenstructuur bevat nog een derde laag, net boven het substraat, een etsstoplaag die zal gebruikt worden om het substraat te verwijderen.

Vervolgens worden in deze lagenstructuur twee rechte golfgeleiders gedefinieerd door middel van lithografie en droog etsen (Fig. 10(b)).

Daarna wordt de hele structuur omgekeerd vastgemaakt op een ander substraat, het transfersubstraat. Deze procedure zullen we het 'bonden' noemen bij gebrek aan een equivalent Nederlands woord. Dit kan op verscheide-

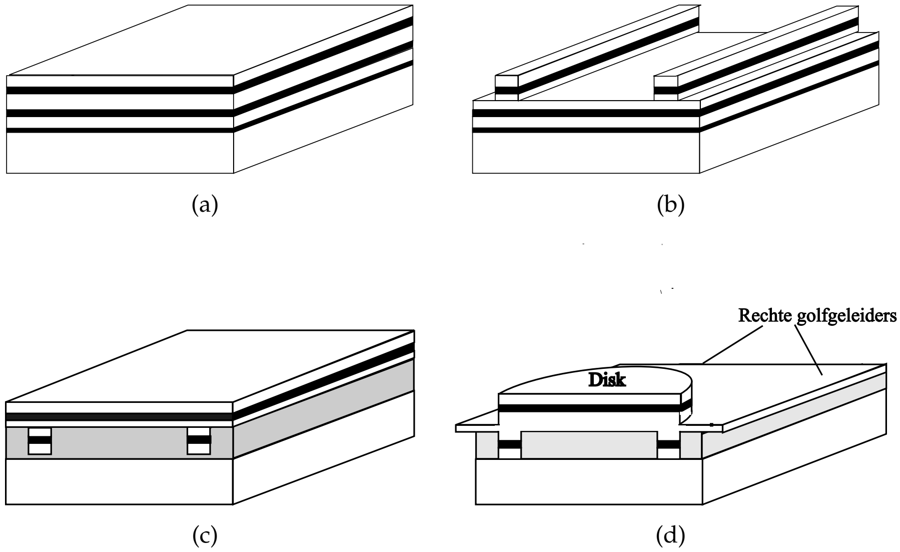

Figuur 10: Fabricage van een verticale gekoppelde ringresonator met behulp van BCB bonding

ne manieren gebeuren maar wij hebben gekozen om dit te doen met behulp van het polymeer benzocyclobuteen (BCB). De procedure hiervoor wordt verder uitgebreid besproken. Daarna wordt door middel van een combinatie van mechanisch polijsten en chemisch etsen het oorspronkelijk substraat verwijderd. Het chemische etsprocédé stopt op de etsstoplaag die inert is voor het gebruikte etsmengsel (Fig. 10(c))

Vervolgens wordt de ring gedefineerd en geëtst. Na klieven van de facetten en eventueel aanbrengen van anti-reflectie lagen is de component af (Fig. 10(d)).

3.3 Materiaalsystemen

Ringresonatoren werden reeds in veel verschillende materiaalsystemen gemaakt. Tabel 1 geeft een overzicht van de verschillende materiaalsystemen waarin tot nu toe al ringen gemaakt werden, met enkele relevante parameters: het verticale en laterale indexcontrast bepalen mee hoeveel stralings- en verstrooiingsverlies de component zal hebben, voor actieve componenten is het belangrijk dat het mogelijk is winst te induceren met het materiaalsysteem. Ook de mogelijke mechanismen voor afstembaarheid werden vermeld (1:thermo-optisch, 2: elektro-optisch, 3: injectie van ladingsdragers). Tabel

Materiaal-systeem	Verticaal index contrast	Lateraal index contrast	Winst?	afstembaarheid
InP	3.4-3.16	3.4-1	ja	1-2-3
GaAs	3.4-3.16	3.4-1	ja	1-2-3
Glass	1.8-1.44	1.8-1	nee	1
Polymers	1.5-1.44	1.5-1	nee	1-2
SOI	3.47-1.44	3.47-1	nee	1-(2-3)
SiON	2.2-1.44	2.2-1	nee	1
hydex	25%	25%	nee	1

Tabel 1: Enkele parameters van de verschillende materialen

2 geeft een overzicht van de performantie van passieve ringen die gerapporteerd werden in de literatuur. De referenties zijn terug te vinden in Hoofdstuk 3 van het Engelstalige gedeelte van dit werk.

3.4 Toepassingen

Ringresonatoren zijn erg veelzijdige, kleine en schaalbare componenten. In deze paragraaf zullen we enkele toepassingen aanhalen om dit te illustreren.

- 'Add-drop' filters

  De eerste toepassing is de meest voor de hand liggende: gebruik van een ringresonator als golflengtefilter. Om zo optimaal mogelijk gebruik te maken van de enorme bandbreedte van de optische vezel worden signalen op meer draagfrequenties tegelijkertijd geïnjecteerd in de ring. Deze kanalen hebben typische een golflengtespatiëring van 0.4 of 0.8 nm. Om in een knooppunt een specifiek signaal (een bepaalde golflengte dus) uit het netwerk te halen of toe te voegen aan het netwerk is een golflengtefilter als de ringresonator erg nuttig. Bovendien kunnen meerdere ringresonatoren vrij makkelijk geïntegreerd worden om een component te maken die alle golflengtes uit het signaal kan extraheren of toelaat meerdere golflengtes toe te voegen.

- Afstembare filters en schakelaars

  Het is uiteraard interessant als de karakteristiek van de ringresonator aangepast kan worden. Hiermee bedoelen we twee dingen: ten eerste kan dezelfde karakteristiek verschoven worden over de golflengte zodat andere golflengtes in resonantie komen, ten tweede kan het verlies

Materiaal-systeem	FSR (nm)	Straal (μm)	Finesse	lateraal/ verticaal	ER (dB)
InP	10	12	50	verticaal	
	21	5	91	lateraal	-10
GaAs	21.6	5.25	120	lateraal	-3
	11.14	10	22.28	verticaal	-12
Polymeren	7.5	32	117	verticaal	
	23.7	10	192	lateraal	erg laag
	17.6	10 (renbaan)	21	lateraal	-1
SOI	14	5 (renbaan)	28	lateraal	-24
	24	3(renbaan)	28	lateraal	-7
	$\approx$ 5	30	$\approx$145	lateraal	-22
	$\approx$ 8	20	$\approx$715	lateraal	-15
Glas	6	40	40	verticaal	
	20.1	10.35	34	verticaal	
SiON	8	25	182	lateraal	-3
	29	5	24	verticaal	-18
hydex	$\approx$4	40		verticaal	

Tabel 2: Enkele typische karakteristieken van ringresonatoren gerapporteerd in de literatuur

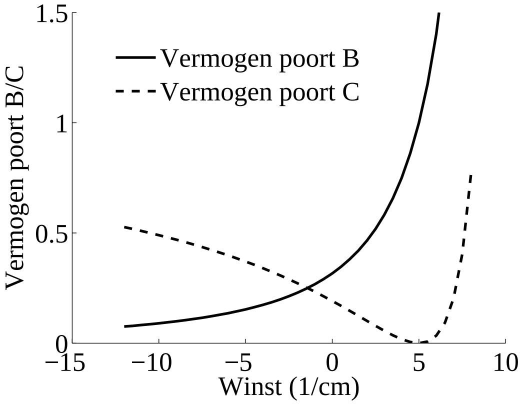

Figuur 11: Het schakelen van een ringresonator door het veranderen van winst/verlies in de ring

in de ring gewijzigd worden om een schakelaar te maken waarbij door middel van een elektrische stroom kan beslist worden om een bepaalde golflengte langs poort B te laten passeren, of om te leiden naar poort C. Dit is geïllustreerd in Fig. 11.

- Ringlasers

  Als de ring wordt gefabriceerd in een materiaal dat winst vertoont dan kan door de inherente terugkoppeling die er in de ringresonator aanwezig is, laser-werking optreden.

- Ringresonatoren als golflengte-selectief element voor breed-afstembare lasers

  Afstembare lasers, lasers waarvan men dus de golflengte kan veranderen, zijn heel bruikbare componenten. Om breed-afstembare lasers te maken, maakt men gebruik van het Vernier-effect tussen twee golflengtefilters in de caviteit van de laser. Dit zouden bijvoorbeeld twee ringresonatoren kunnen zijn. Hierbij werd aangetoond dat door de specifieke eigenschappen van ringresonatoren slechts kleine afstembaarheid van beide ringen nodig is om een grote afstembereik van de laser te realiseren.

- Niet-lineaire effecten

  Door de grote veldsterkte die opgebouwd kan worden in de ring, kan men hier niet-lineaire effecten bestuderen zoals zelfschakeling van de component, golflengte omzetting, . . . Dit heeft al geleid tot de fabricage van volledig-optische logische circuits.

4. Waferbonding

In de vorige paragraaf werd beschreven hoe verticaal gekoppelde ringresonatoren kunnen gemaakt worden met behulp van bonding. Dit is een cruciale stap in de fabricage en zal in deze paragraaf verder in detail besproken worden.

4.1. Soorten waferbonding

Het samenbrengen van twee substraten, wafers, en permanent verbinden van beide wordt in het Engels omschreven met 'wafer bonding'. Bij gebrek aan een equivalent Nederlands woord zullen wij ook spreken over waferbonding. Dit is een heel uitgebreid onderzoeksgebied dat in twee grote delen op te splitsen valt: bonden met een tussenlaag en zonder tussenlaag.

Het bonden zonder tussenlaag, ook wel 'fusion bonding' genoemd, werd vooral populair voor de fabricage van SOI-wafers gebruikt in elektronicatoepassingen. Waferbonding heeft echter ook vele toepassingen in het opto-elektronische gebied. Bij dit soort bonden worden de twee wafers bij elkaar gebracht onder hoge druk en temperatuur om een permanente verbinding te verzekeren. De oppervlakteruwheid en de contaminatie van het oppervlak zijn erg belangrijk en maken dit soort bonden een vrij moeilijk proces. De hoge temperatuur is een probleem voor vele componenten. Er werd al veel werk verricht om deze temperatuur te kunnen verlagen maar deze processen staan nog niet op punt. Het bonden van twee wafers met structuren werd ook al gedemonstreerd maar niet op waferschaal, volgens de literatuur kan het nodig zijn één van de twee wafers heel dun te maken opdat die voldoende flexibel zou zijn om spanningen op te vangen, wat het proces bemoeilijkt.

Bonden met een tussenlaag is veel toleranter, veel verschillende soorten material kunnen verbonden worden, grote oppervlakteruwheid en stofdeeltjes kunnen getolereerd worden en het proces kan op waferschaal toegepast worden. Heel veel verschillende soorten materialen zijn mogelijk voor deze tussenlaag: allerlei metalen, polymeren, . . .

4.2 Waferbonding met BCB

In het kader van dit werk werd de procedure voor waferbonding met benzocyclobuteen (BCB) ontwikkeld.

	Duur	Temperatuur	Snelheid
Stap 1			5 °C/min
Niveau 1	5 min	150 °C	
Stap 2			3 °C/min
Niveau 2	60 min	250 °C	

Tabel 3: Gebruikte thermische behandeling

4.2.1 Benzocyclobuteen

Benzocyclobutenen vormen een familie van stoffen die polymerizeren door thermische behandeling. Ze worden vrij veel gebruikt in de elektronica en de fotonica omwille van tal van interessante eigenschappen zoals:

- Lage polymerisatie-temperatuur (250 °C)
- Goede planarisatie-eigenschappen
- Goede thermische stabiliteit
- Weinig absorptie bij telecom-golflengtes
- Goede chemische weerstand
- Er komt weinig gas vrij bij het polymerizeren
- Weinig vochtopname
- Goed te combineren met allerlei soorten metaalcontacten

BCB wordt verkocht in een fotogevoelige en een niet-fotogevoelige variant. Enkel de laatste werd gebruikt in dit werk. BCB wordt aangebracht op de wafer door middel van 'spinnen'. De dikte van de laag wordt dus bepaald door de rotatiesnelheid van de spinner en de viscositeit van de BCB die gebruikt wordt. BCB wordt dan ook in verschillende viscositeiten verkocht, de samenstelling verschilt enkel in de hoeveelheid mesityleen die toegevoegd werd. De bereikbare diktes variëren van 1 tot 26 μm.

Voor de polymerisatie wordt de laag aan een thermische behandeling onderworpen. Dit gebeurt onder een stikstofomgeving. Afhankelijk van de gebruikte temperatuur kan de polymerisatie versneld of vertraagd worden zoals geïllustreerd in Fig. 12. Wij maakten normaal gebruik van een temperatuur van 250 °C gedurende een uur, wat een bijna volledige polymerisatie oplevert (zie Tabel 3).

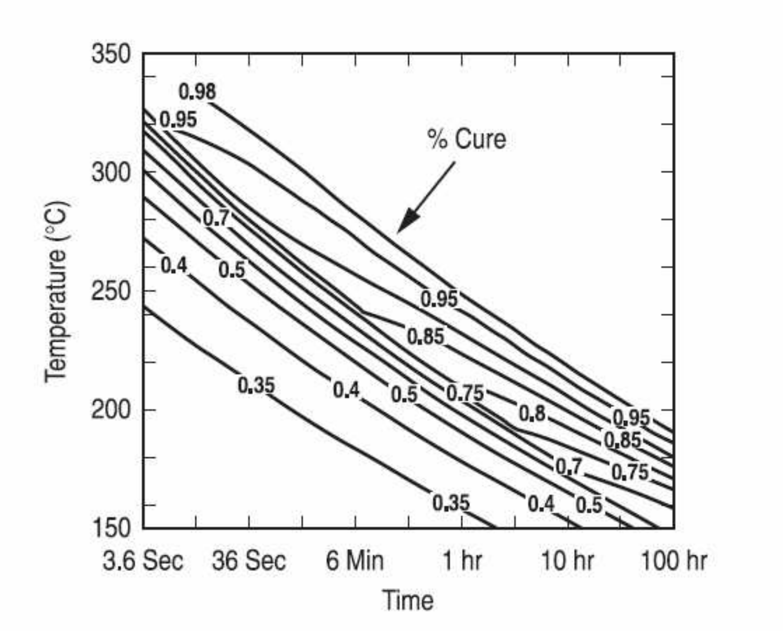

Figuur 12: Graad van polymerisatie in functie van tijd en temperatuur

4.2.2 Waferbonding procedure

De monsters werden eerst allebei grondig gereinigd met behulp van aceton, isopropylalcohol en gedeïoniseerd water. Vervolgens werden ze gedroogd gedurende een half uur. Op beide monsters werd een adhesie-bevorderend middel gesponnen dat ook te koop is bij de leverancier DOW. Dit is echter geen cruciale stap. Daarna werd BCB 3022-46 gesponnen op het monster met de structuren erop. Dit hielp om luchtbellen in de bondinglaag te elimineren. BCB 3022-46 is de tweede minst visceuze variant en levert laagdiktes op van 2.4 tot 5.8 μm. De gebruikte spinsnelheid was 2000 rpm wat een dikte van zo'n 3.8 μm oplevert. Het monster met de BCB werd vervolgens op een hete plaat gelegd. Dit zorgt ervoor dat het oplosmiddel verdampt voóŕ het bonden en dus geen gasbellen kan veroorzaken in de bondinglaag. Bovendien wordt de BCB daardoor wat minder visceus wat het mogelijk maakt na het bonden de samples wat te bewegen ten opzichte van elkaar om ze juist te positioneren. De samples worden dan op elkaar gelegd en samengedrukt. Het geheel wordt dan in een stikstofomgeving uitgebakken volgens de procedure beschreven in Tabel 3.

Daarna wordt het oorspronkelijke substraat verwijderd door een combinatie van mechanisch polijsten en chemisch etsen. Het dunne laagje dat overblijft is doorzichtig en onder een microscoop kan men de rechte golfgeleiders die onderaan de dunne film liggen, zien liggen en men kan de kwaliteit van de bondinglaag inspecteren. Op Fig. 13 zijn stofdeeltjes en luchtbellen gevangen in de bondinglaag te zien. Fig. 14 toont een foto van een goede kwaliteit bondinglaag. Fig. 15 toont een SEM-foto van een monster waarbij bij het monteren de dunne film is losgekomen. De rechte golfgeleiders en de plaats waar ze in de BCB geduwd waren zijn duidelijk te zien.

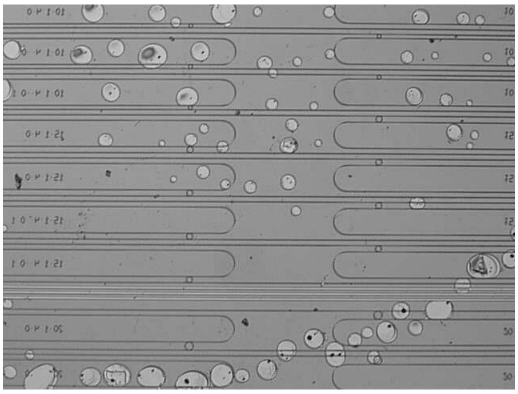

Figuur 13: Voorbeeld van een mindere kwaliteit bondinglaag

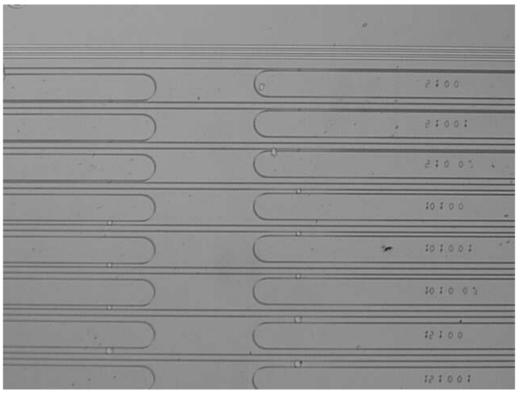

Figuur 14: Voorbeeld van een goede bondinglaag

De positie van de twee monsters ten opzichte van elkaar is erg belangrijk. Vooral de alignatie van de kliefvlakken van beide monsters is belangrijk omdat de component gekliefd moet worden om facetten te creëren langs waar

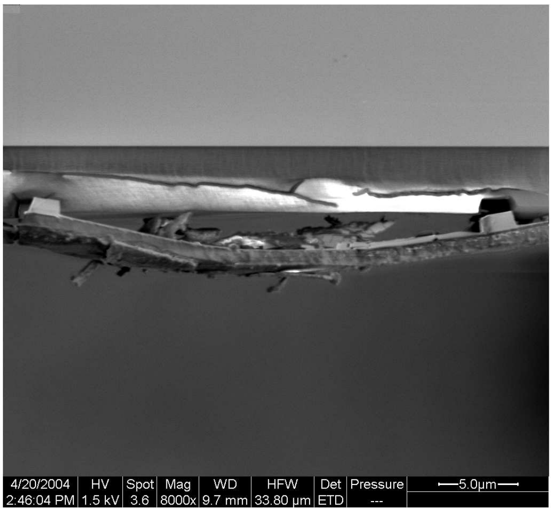

Figuur 15: SEM-foto van een monster met een dunne film die gedeeltelijk losgekomen is

het licht in- en uitgekoppeld wordt. De kwaliteit van deze facetten is erg belangrijk voor de component. Om deze kliefvlakken goed te aligneren worden beide monsters tegen eenzelfde metalen blok geduwd. Figuur 16 toont in bovenaanzicht een voorbeeld van een klief waarbij beide monsters niet goed gealigneerd werden. Het is duidelijk dat beide monsters volgens een andere richting gekliefd werden.

4.3 Gefabriceerde componenten

Met deze techniek werden verscheidene dunne-film-componenten gefabriceerd. Uiteraard werden ringresonatoren gemaakt, de fabricage en metingen hiervan worden verder uitgebreid besproken. Maar ook actieve componenten zoals LED's en lasers werden gemaakt.

4.3.1 LED's

- Fabricage

  De LED's werden gefabriceerd zoals geïllustreerd in Fig.17. Eerst wordt een Ti/Au contact aangebracht. Dit wordt dan 'gebond' op een GaAs substraat (Fig. 17a). Het InP substraat en de etsstoplaag worden dan verwijderd (Fig. 17b). Figuur 17c toont het etsen van de mesa in het InP membraan. Daarna wordt een polyimidelaag aangebracht waarin

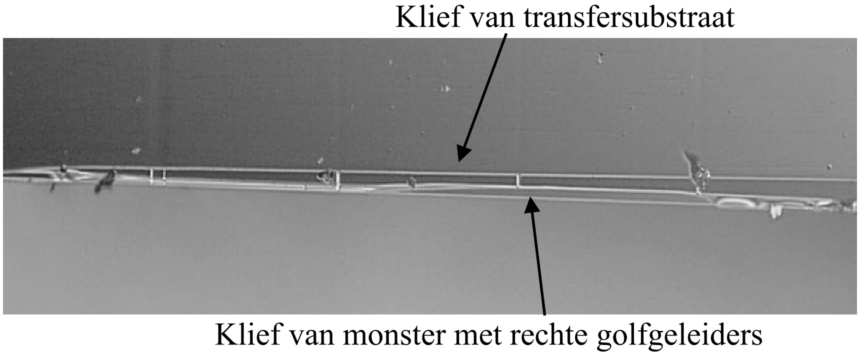

Figuur 16: Bovenaanzicht van een klief van een slecht gealigneerde component

de contactopeningen worden gedefinieerd. Vervolgens worden de contacten gedeponeerd (Fig. 17d).

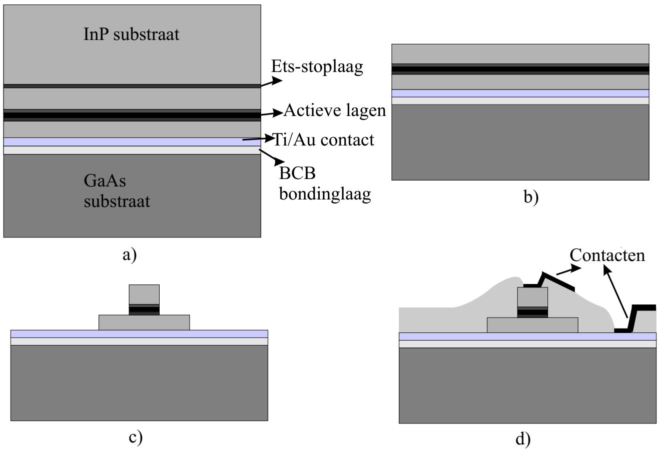

Figuur 17: Fabricage van dunne-film LED's met BCB waferbonding

- Metingen

  De LED's werkten in CW (continuous wave) toestand. Een meting is te zien op Fig. 18, dit toont het gemeten optische vermogen versus de stroom in de component. De metingen van LED's met verschillende grootte toont duidelijk de sterke temperatuursafhankelijkheid van de LED's die het gevolg is van de lage thermische geleidbaarheid van de BCB.

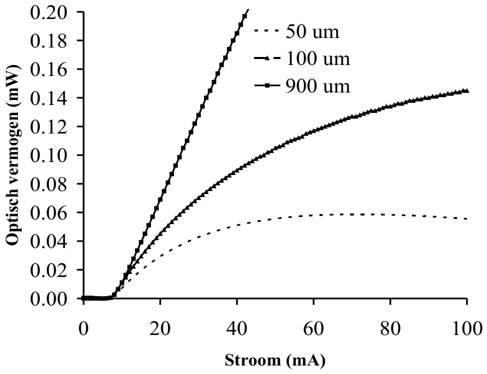

Figuur 18: Optisch vermogen versus stroom voor LED's met verschillende diameters

4.3.2 Lasers

- Fabricage

  Een eerste groep lasers werd gefabriceerd analoog aan de fabricage van de LED's. Een tweede groep werd dan gefabriceerd zoals geïllustreerd in Fig. 19 waarbij het elektrische contact door de BCB-laag wordt geleid tot op het transfersubstraat. Dit kan interessant zijn voor heterogene integratie. Een SEM foto van deze laser is te zien op Fig. 4.15.

- Metingen

  De lasers werkten in een gepulst regime (lengte = 1 mm, breedte = 7.5 μm) met een drempelstroomdichtheid rond 2.65 kA/cm^2. Dit is ongeveer het dubbele van de drempelstroomdichtheid van gewone lasers die tegelijkertijd werden gefabriceerd. Figuur 21 is een meting van het optisch vermogen versus de stroom voor verschillende gepulste regimes. Ook hier is het duidelijk dat er een hoge thermische weerstand is die werking in CW-regime verhinderde. Dit zijn metingen van het eerste laserontwerp. De tweede soort lasers werkten niet wegens een fabricagefout.

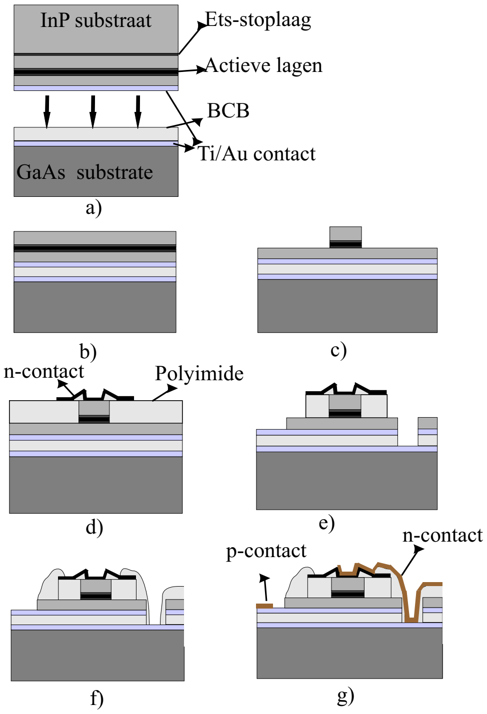

Figuur 19: Fabricage van een dunne-film laser met BCB. Het elektrisch contact werd door de BCB-laag geleid.

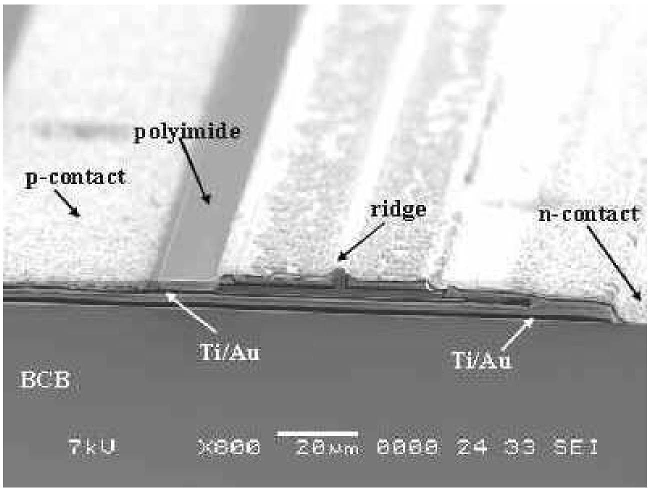

Figuur 20: SEM foto van een dunne-film laser

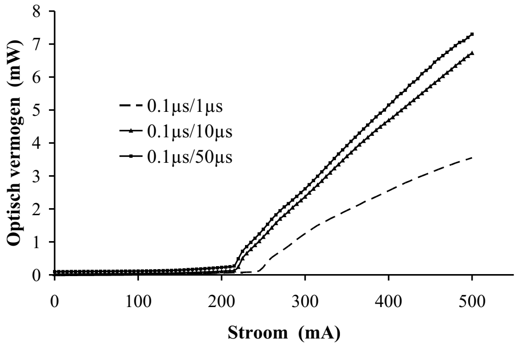

Figuur 21: Optisch vermogen versus stroom voor laser gemeten in verschillende gepulste regimes

4.3.3 Levensduur-testen

Om de kwaliteit van het bonden te bestuderen werden de lasers onderworpen aan levensduur-testen. Ze werden in een oven geplaatst onder een temperatuur van 85 °C en een relatieve vochtigheid van 85 % gedurende 48, 100, 250 en 500 uur. De karakteristieken van de laser bleven hetzelfde ook na de testen (zie Fig. 22) wat een duidelijke indicatie is van de kwaliteit van de bonding-procedure.

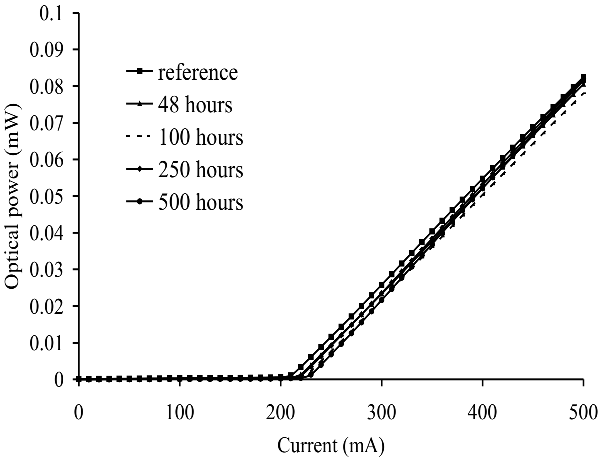

Figuur 22: Invloed van de 85/85 degradatie-testen op de vermogen-stroom karakteristiek van de lasers (gepulst gemeten, 1 μs/50 μs).

5. Simulatie van ringresonatoren

Het simuleren van ringresonatoren is niet gemakkelijk. Men kan proberen om de hele structuur in 1 keer te simuleren met behulp van technieken als eindige differentie, eindige elementen etc. Dit is echter heel tijdrovend, in drie dimensies vaak totaal niet doenbaar en levert bovendien weinig inzicht in de component.

Wij hebben daarom gekozen om de de component op te delen in de aparte golfgeleiders (gebogen en recht) en de koppelsecties zoals geillustreerd in Fig. 23. We zullen deze twee onderdelen apart bespreken.

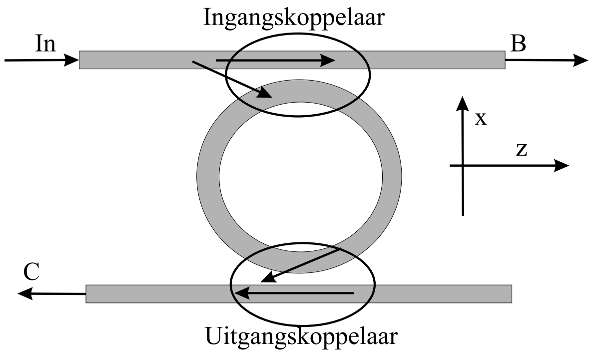

Figuur 23: Opsplitsing van de microringresonator in 2 bochtsecties en 2 koppelingssecties

5.1 Simulatie van de modes van een gebogen golfgeleider

De simulatie van de modes van een rechte golfgeleider is vrij triviaal, er zijn veel commerciële software-pakketten beschikbaar die dit kunnen. De simulatie van gebogen golfgeleiders en dan vooral in drie dimensies is echter andere koek. Eerst zal ingegaan worden op de simulatie in 2D vermits die enkele nuttige fysische inzichten oplevert en dit in sommige gevallen kan volstaan, daarna wordt ingegaan op 3D simulaties.

5.1.1 In 2 dimensies

Om een 2D gebogen golfgeleider te analyseren kan men gebruik maken van de techniek van de conforme transformatie. Deze laat toe de gebogen golfgeleider om te zetten naar een rechte golfgeleider met een gewijzigd index-profiel. Deze kan dan met klassieke technieken geanalyseerd worden. De conforme transformatie is geïllustreerd in Fig. 24.

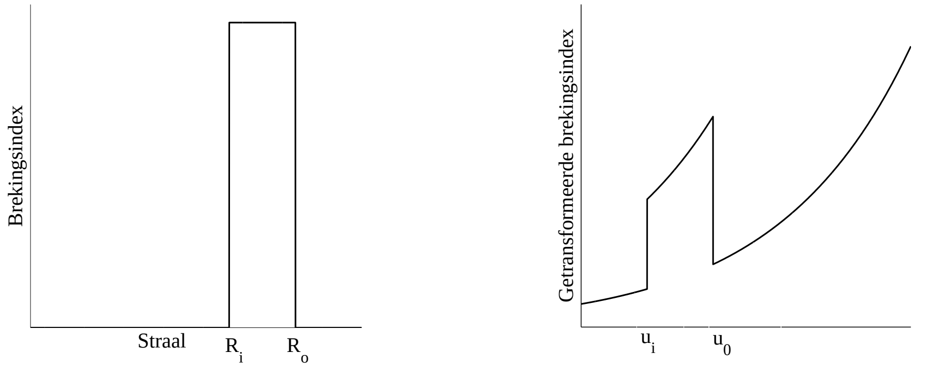

(a) De gebogen golfgeleider

(b) Het brekingsindexprofiel van de golfgeleider na conforme transformatie

Figuur 24: Brekingsindexprofiel van een gebogen golfgeleider voor en na conforme transformatie

De volgende figuren illustreren enkele typische eigenschappen van modes in gebogen golfgeleiders. Figuur 25 toont veldprofielen en fases van de nulde orde mode van een bocht in een systeem met laag brekingsindexcontrast bij verschillende stralen. Het is duidelijk dat de staart van het veld in de keerlaag steeds groter wordt naarmate de straal daalt. Het verlies van deze mode wordt daarmee ook groter. Het verlies wordt bepaald door het brekingsindexcontrast en de straal.

Figuur 26(a) toont de evolutie van de nulde orde mode van een gebogen golfgeleider in een hoog-contrastsysteem als de straal daalt. De staart van het veld in de cladding is hier veel kleiner dan in het vorige geval en het verlies zal ook veel kleiner zijn. Dit is te wijten aan het hogere brekingsindexcontrast. Op de figuur is ook te zien dat het maximum van het veldprofiel verschuift naar de buitenstraal als de straal verkleint. Dit is een typisch verschijnsel voor gebogen golfgeleiders.

Figuur 26(b) toont de hogere orde modes in een gebogen golfgeleider. Hier is te zien dat het veld van de nulde orde mode ter hoogte van de binnenstraal al uitgestorven is. De binnenwand van de gebogen golfgeleider zal dus geen invloed meer hebben op het profiel van de nulde orde mode en ook geen verstrooiingsverliezen voor deze mode meer kunnen veroorzaken. Dit noemen we het 'whispering gallery mode' regime.

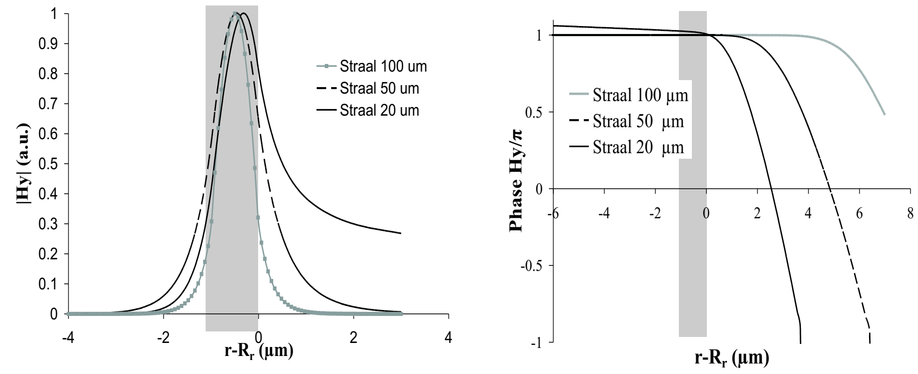

(a) Veldprofiel bij verschillende stralen (b) Faseverloop bij verschillende stralen

Figuur 25: Veldprofiel en fase voor een gebogen golfgeleider in een laag-contrast systeem bij verschillende stralen

Voor de berekening van de modes van een rechte golfgeleider maakt men gebruik van de propagatieconstante β (in $1/\mu$m) en de erbij horende effectieve index n_{eff}. Beide zijn verbonden door volgende vergelijking:

$$\beta = \frac{2\pi n_{eff}}{\lambda}$$

Voor een bocht is de meest voor de hand liggende equivalente parameter een propagatieconstante γ per radiaal. Om hieruit ook een (dimensieloze) effectieve index te extraheren, moet echter een padlengte langs de gebogen golfgeleider, of een straal R gespecifieerd worden.

$$\gamma = \frac{2\pi n_{eff} R}{\lambda}$$

De keuze van deze straal is eigenlijk arbitrair en dus is de waarde van een effectieve index voor een bochtmode ook arbitrair. Omdat het maximum van het modale veld van een bochtmode zich dicht bij de buitenstraal bevindt wordt deze het meest gekozen als waarde.

5.1.2 In 3 dimensies

Een volledig drie-dimensionale simulatie is een stuk complexer. De conforme transformatie zoals die kan toegepast worden voor twee-dimensionale problemen is hier niet meer toepasbaar. De oplossingen zijn ook niet meer ontkoppeld in TE en TM modes maar kunnen heel sterk hybride zijn zodat een

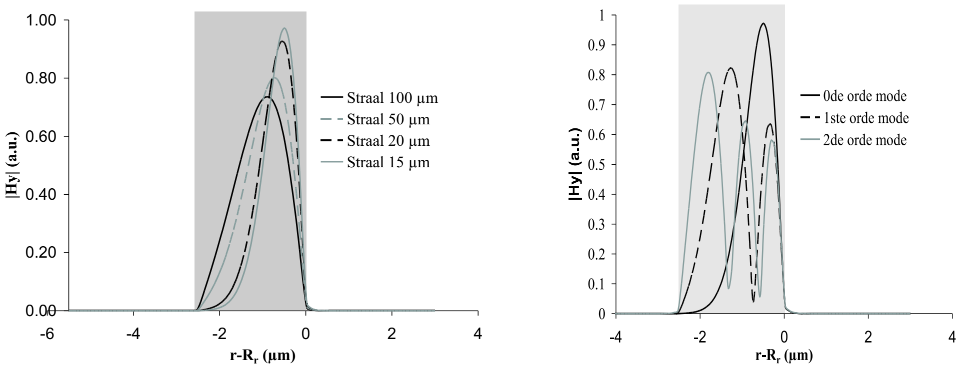

(a) Veldprofiel van de nulde orde mode bij verschillende stralen

(b) Veldprofiel van hogere orde modes

Figuur 26: Veldprofielen in een hoog-contrast systeem

volledige vectoriële oplossing van het probleem noodzakelijk is. Bij rechte golfgeleiders is in veel gevallen de semi-vectoriële aanpak gerechtvaardigd, bij gebogen golfgeleiders is er echter meestal een bereik van stralen waar de modes heel sterk hybride zijn en waar het moeilijk kan zijn om oplossingen te vinden.

Er bestaan een drietal commerciële programma's die toelaten de modes van een gebogen golfgeleider in drie dimensies te berekenen: APSS van Apollo Photonics, Olympios van C2V, Fimmwave van Photondesign. APSS kon slechts oppervlakkig geëvalueerd worden vermits we maar een maand over dit programma konden beschikken. Fimmwave van Photondesign en Olympios van C2V werden echter uitgebreid gebruikt.

Fimmwave is gebaseerd op een techniek van 'film mode matching'. Om reflecties van de wanden het simulatievenster tegen te gaan wordt gebruik gemaakt van PML's (Perfectly Matched Layers). Deze kunnen echter slechts links en rechts van de ribgolfgeleider aangebracht worden en niet langs de substraatkant. Een gebogen golfgeleider met kleine straal zal ook afstralen richting substraat. Dit kan dus moeilijk gemodelleerd worden met dit programma. Het is ook vaak moeilijk om direct een mode bij een bepaalde straal te vinden. Vaak moet men eerst de modes van dezelfde golfgeleider maar met grotere straal zoeken en vervolgens in kleine stapjes afzakken naar de gewenste straal. Als hierbij de modes hybride worden bij een bepaalde straal, loopt de simulatie vaak vast.

Olympios is gebaseerd op eindige differentietechnieken en laat toe om PML's te gebruiken langs alle kanten van het simulatievenster. De modes bij

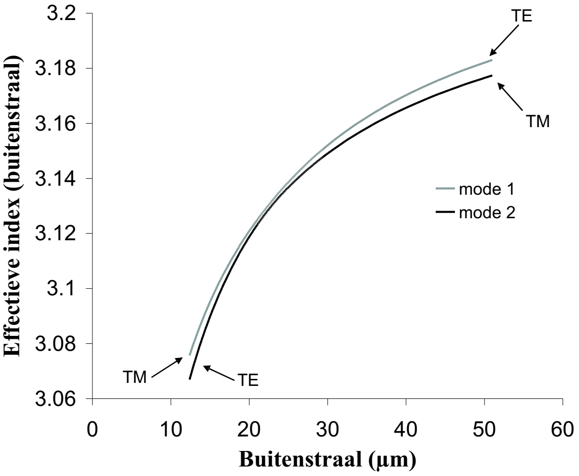

Figuur 27: Evolutie van de mode met de straal van gepolariseerd naar hybride polarisatie

een bepaalde straal kunnen meestal direct gevonden worden maar er worden meestal ook veel niet-fysische modes gevonden en het is aan de gebruiker om de fysische modes te vinden.

Er blijven structuren die niet te simuleren vallen met de huidige simulatieprogramma's zoals SOI-golfgeleiders met heel kleine bochtstralen.

5.2 Berekening van de koppeling tussen de rechte en de gebogen golfgeleider

5.2.1 Eén mode in de rechte golfgeleider, één in de gebogen golfgeleider

Om de koppeling tussen een rechte golfgeleider en een gebogen golfgeleider uit te rekenen moeten de gekoppelde-mode vergelijkingen opgelost worden. De vergelijkingen die hier gebruikt werden zijn de volledige en niet de meer klassieke vergelijkingen waarbij een reeks hogere orde termen wordt verwaarloosd om de gekoppelde differentiaalvergelijkingen te ontkoppelen. Er wordt verondersteld dat het totale veld geschreven kan worden als een combinatie van de velden van de gebogen golfgeleider $\mathbf{E_b}$ en de rechte golfgeleider $\mathbf{E_s}$ apart:

$$\mathbf{E} = a_b(z)\mathbf{E_b} + a_s(z)\mathbf{E_s}$$

$$\begin{pmatrix} \sigma_{bb} & \sigma_{br} \\ \sigma_{rb} & \sigma_{rr} \end{pmatrix} \frac{d}{dz} \begin{pmatrix} a_b \\ a_r \end{pmatrix} = \begin{pmatrix} c_{bb} & c_{br} \\ c_{rb} & c_{rr} \end{pmatrix} \begin{pmatrix} a_b \\ a_r \end{pmatrix} \tag{3}$$

met

$$\sigma_{pq} = \frac{1}{4} \int \mathbf{e}_z.(\mathbf{E}_q \times \mathbf{H}_p^* + \mathbf{E}_p^* \times \mathbf{H}_q) dx$$

$$c_{pq} = -i\frac{\omega\epsilon_0}{4} \int \mathbf{E}_p^*.(\epsilon - \epsilon_q)\mathbf{E}_q dx$$

Een resultaat van dit soort berekening is te zien op Fig. 28.

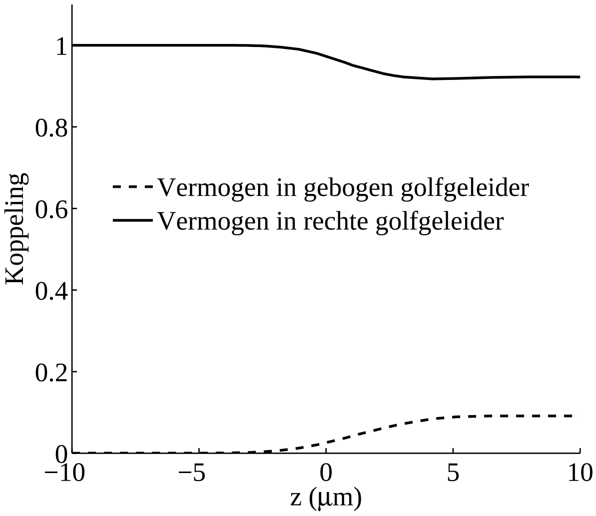

Figuur 28: Berekening van de koppelingscoëfficiënt aan de hand van gekoppelde mode theorie

5.2.2 Met hogere orde modes

Als er hogere orde modes aanwezig zijn moeten de vorige vergelijkingen uitgebreid worden. Een voorbeeld van het resultaat van dit soort berekening is te zien in Fig. 29.

5.4 Enkele niet-ideale effecten

5.4.1 De verlieshebbende koppelaar

Als de koppelaar niet verliesloos is, is de faserelatie tussen de mode in de ring en de busgolfgeleider niet noodzakelijk meer 90^o. Dit leidt tot een asym-

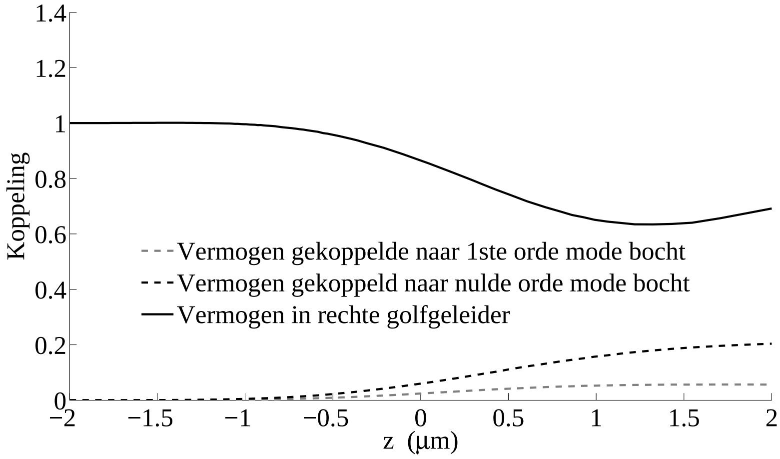

Figuur 29: Voorbeeld van een 2D simulatie waarbij er koppeling naar 2 modes in de gebogen golfgeleider is

metrische karakteristiek aan poort B zoals geïllustreerd in Fig. 30. De resonantiepiek aan poort C valt niet meer perfect samen met de dip in poort B.

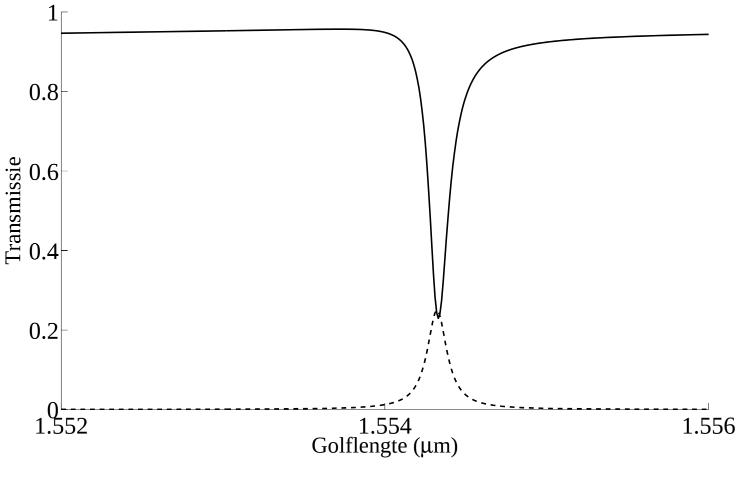

Figuur 30: Het effect van een verlieshebbende koppelaar op de transferfunctie

5.4.2 Excitatie van de mode die propageert in tegen-richting

Als de wand van de microring te ruw is, kan licht gereflecteerd worden in de mode die propageert in de omgekeerde richting. Dit kan leiden tot het splitsen van de resonantiepiek zoals geïllustreerd in Fig. 31. De reflectie hoeft slechts van de orde van de koppelingscoëfficiënt te zijn om de performantie in het gedrang te brengen.

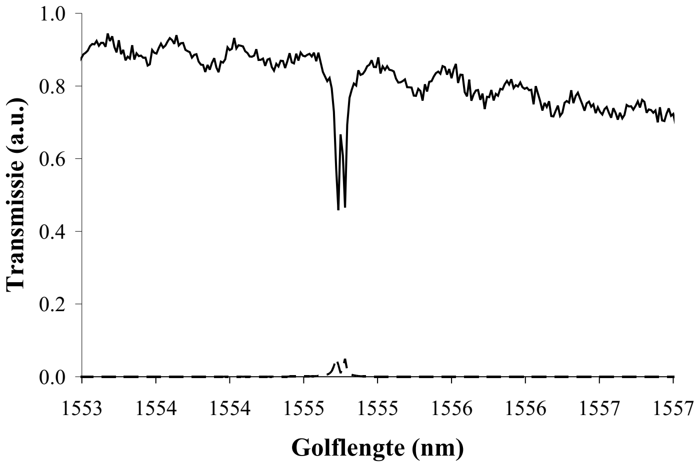

Figuur 31: Meting van een SOI microringresonator met een straal van 5 μm die duidelijk splitsing van de resonantiepiek vertoont

5.4.3 Polarisatie-afhankelijkheid

De resonanties van de ringresonator zijn meestal verschillend voor de TE- en de TM-polarisatie. Het is erg moeilijk, zo niet onmogelijk, om een ringresonator te maken die polarisatie-onafhankelijk is over een breed golflengtebereik. Het is dan ook beter om met polarisatie-diversiteit te werken.

Een andere vorm van polarisatie-afhankelijkheid is polarizatie-rotatie. Als de modes van de microring hybride zijn, kan bijvoorbeeld een zuivere TE-mode in de rechte golfgeleider, beide hybride modes in de ring exciteren. Deze kunnen dan op hun beurt zowel de TE als de TM mode in de uitgangsgolfgeleider exciteren en een deel van het vermogen wordt dus getransfereerd van de TE mode naar de TM mode via de hybride bochtmodes.

	Samenstelling	Laagdikte
Keerlaag	InP	300 nm
Kernlaag busgolfgeleider	Q(1.3μm)	500 nm
Scheidingslaag	InP	500 nm
Kernlaag ringgolfgeleider	Q(1.3μm)	500 nm
Keerlaag	InP	300 nm
Etsstoplaag	Q(1.3μm)	200 nm
Substraat	InP	

Tabel 4: Lagenstructuur

6. Metingen en fabricage

6.1 Fabricage

Een verscheidenheid aan microringresonatoren werden gefabriceerd op de hierboven beschreven manier. De lagenstructuur die hierbij gebruikt werd is te vinden in Tabel 4.

De finale structuur is nog eens geïllustreerd op Fig. 32. De busgolfgeleiders en de ringgolfgeleider werden beide tot 150 nm in de InP scheidingslaag geëtst. Hierdoor blijft in het midden een laag InP met dikte t, de tussenlaag, ongeëtst. Deze dient om de component toleranter te maken aan misalignatie van de rechte golfgeleiders ten opzichte van de ringgolfgeleider.

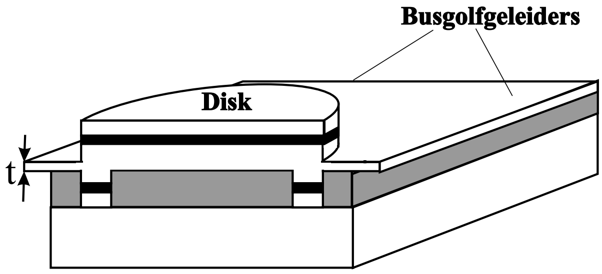

Figuur 32: De microringresonator met tussenlaag t

Deze laag mag echter niet te dik zijn vermits het stralingsverlies dan te groot kan worden. Dit is geïllustreerd op Fig. 33 die het stralingsverlies toont voor een ring met een straal van 20 μm als functie van de dikte t. Om het verlies te beperken wordt de dikte t beperkt tot maximum 300 nm.

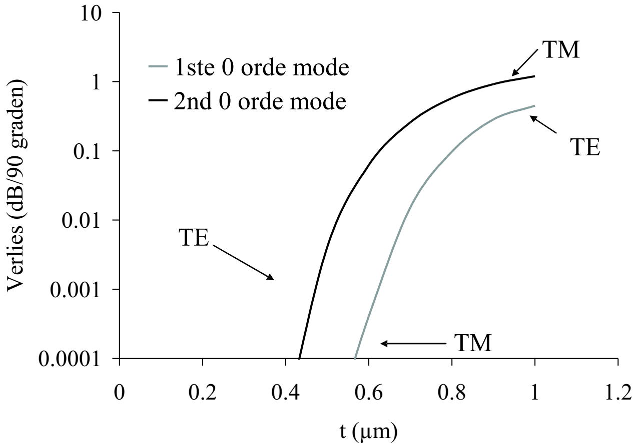

Figuur 33: Het verlies van de nulde orde bochtmodes voor een straal van 20 μm als functie van de dikte van de ongeëtste laag

Figuur 34 toont de invloed van deze ongeëtste laag op de alignatietoleranties. Als de alignatie nul is, wordt hiermee bedoeld dat de buitenzijden van de rechte golfgeleider en de gebogen golfgeleider samenvallen zoals op Fig. 32. Het is duidelijk dat deze ongeëtste laag de alignatietoleranties wel verbetert maar niet voldoende vermits de alignatiefout voor onze fabricagetechnieken rond ± 300 nm ligt. Daarom werden op het masker telkens 3 identieke ringen gezet. Eén ervan was op het masker perfect gealigneerd met de rechte golfgeleiders, de twee andere waren 160 nm naar boven of naar beneden verschoven. Na fabricage was één van de ringen normaliter vrij goed en symmetrisch gealigneerd.

De gefabriceerde golfgeleiders waren 0.8 μm, 1 μm, 1.4 μm breed en werden breder langs de rand van het monster om in- en uitkoppelen te vergemakkelijken.

6.2 Simulatie en metingen

Figuur 35 toont de effectieve index (berekend op de buitenstraal) van de nulde orde diskmodes als functie van de straal en illustreert waar de modes hybride zijn.

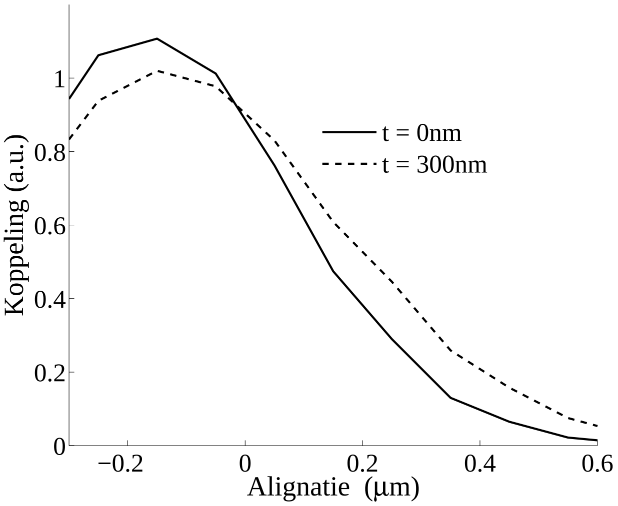

Figuur 34: The influence of the thickness of the middle layer on the alignment tolerance for a 10μm disk coupled to a 0/8 μm wide bus waveguide

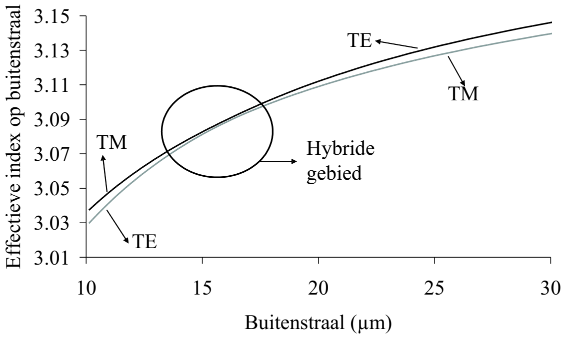

Figuur 35: De effectieve index van de nulde orde bochtmodes als functie van de straal

6.2.1 Stralen buiten het hybride gebied

Figuren 36 en 37 tonen enkele simulaties van koppelingscoëfficiënten voor stralen buiten het hybride gebied - namelijk 10 μm en 20 μm - voor verschillende breedtes van busgolfgeleiders.

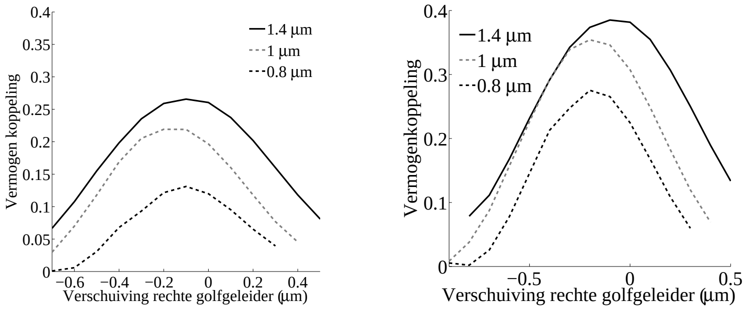

(a) TE (b) TM

Figuur 36: Koppeling naar de nulde orde TE en TM mode voor een resonator met een straal van 20 μm als functie van de alignatie voor verschillende bus golfgeleiders

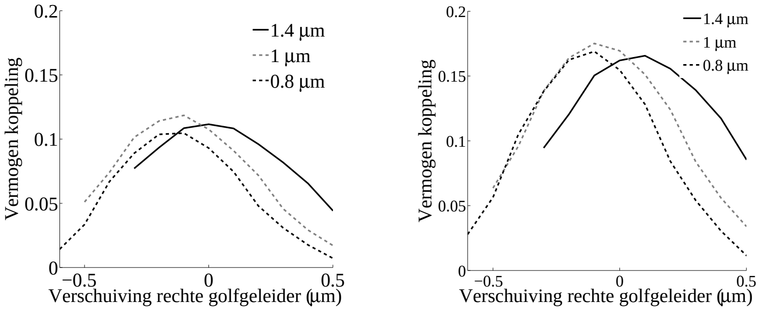

(a) TE (b) TM

Figuur 37: Koppeling naar de nulde orde TE en TM mode voor een resonator met een straal van 10 μm als functie van de alignatie voor verschillende bus golfgeleiders

Figuren 38 en 39 illustreren enkele metingen van microringresonatoren met een straal van 20 μm en 10 μm. Erg smalle busgolfgeleiders zijn dus niet nodig om voldoende koppeling te voorzien.

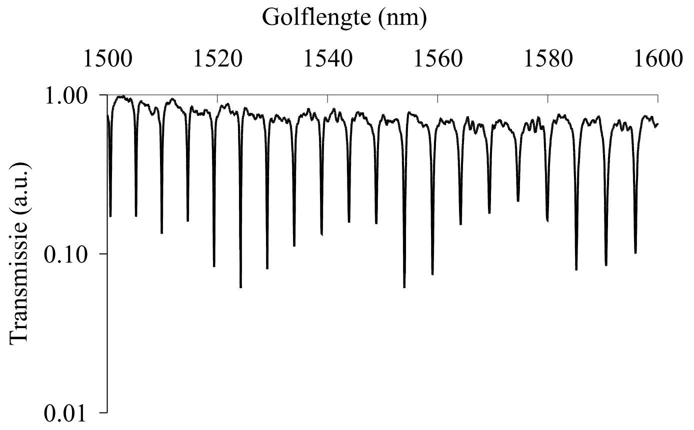

Figuur 38: TE meting van een microring met straal 20 μm gekoppeld naar een 1.4 μm brede busgolfgeleider in TE

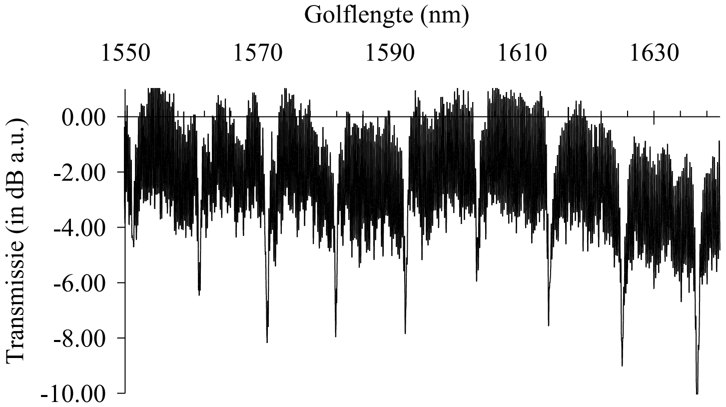

Figuur 39: Meting van een 10 μm straal microring gekoppeld naar een 0.8 μm brede busgolfgeleider in TE

Het is mogelijk dat de nulde orde mode in de rechte golfgeleider niet enkel de nulde orde mode in de gebogen golfgeleider exciteert maar ook hogere orde modes. Een voorbeeld daarvan is te zien op Fig. 40 die een TE meting toont van een 30 μm ring gekoppeld naar een 1 μm brede rechte golfgeleider. De kleine resonantie-pieken naast de grote zijn afkomstig van excitatie van de eerste orde mode van de ring.

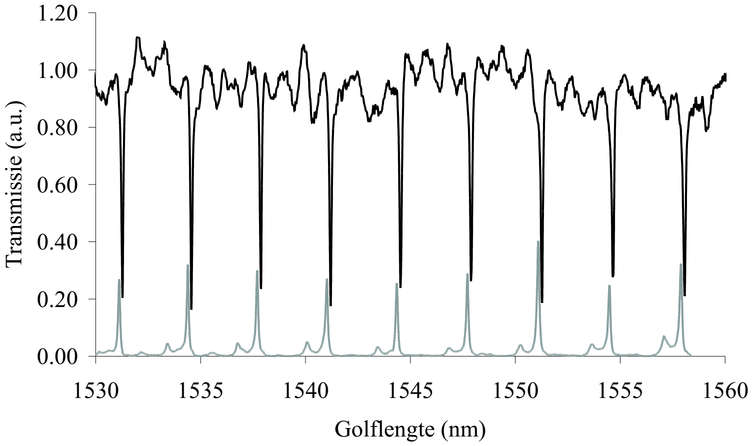

Figuur 40: TE meting van een 30 μm straal ring gekoppeld naar een 1 μm brede busgolfgeleider

6.2.2 Stralen in het hybride gebied

Zoals uitgelegd in de vorige paragraaf kan bij de aanwezigheid van hybride modes, polarizatiedraaiing optreden. Dit is geïllustreerd in Fig. 41 waar een meting van een ring met een straal van 15 μm getoond wordt. Er werd zuiver TE-licht geïnjecteerd en er werd gemeten met een TE polarizator voor de detector, dezelfde meting gebeurde aan de drop poort, en ook nog eens met een TM polarizator. De overlap van bepaalde resonanties duidt duidelijk op polarizatierotatie.

6.3 Thermo-optisch afstembare ringen

Wegens de lage thermische geleidbaarheid van BCB zijn de ringresonatoren efficïent thermisch afstembaar. Na het aanbrengen van een laag polyimide bovenop de ring werd een Cr-contact aangebracht zoals te zien op Fig. 42. Boven de ring wordt de breedte van het Cr-baantje erg smal en volgt het

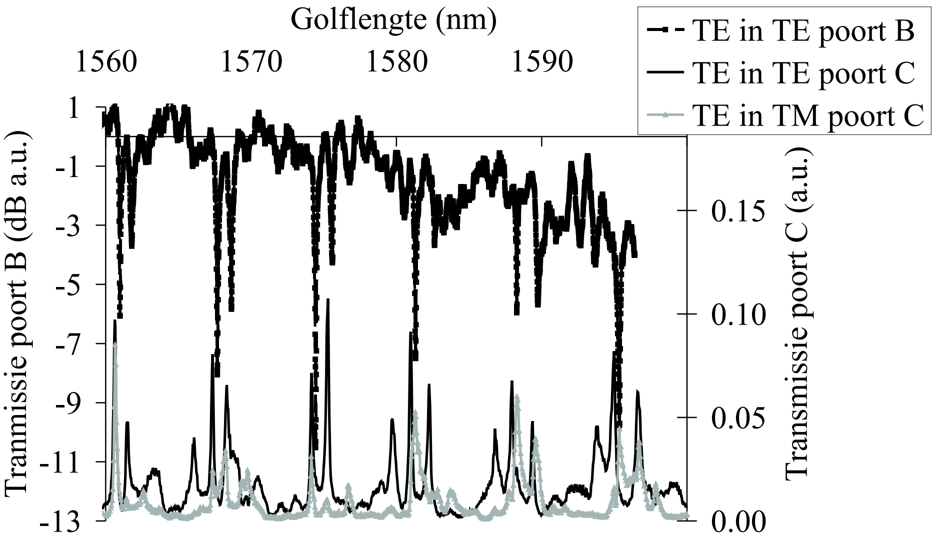

Figuur 41: Polarizatie-draaiing

baantje de omtrek van de ring. De weerstand is daar erg groot en de warmteontwikkeling dus ook.

Figuur 43 toont een voorbeeld van het verschuiven van de karakteristieken bij het thermisch afstemmen en Fig. 44 het afstembereik versus het gebruikte vermogen. Een groot afstembereik is mogelijk met een kleine hoeveelheid vermogen.

6.4 MMI-gekoppelde ringen

Een nieuw masker met gekoppelde ringen werd ontworpen. De opbouw van deze componenten is te zien in Fig. 45. Licht wordt geïnjecteerd aan de linkerkant en wordt door de MMI in twee gelijke delen gesplitst. Deze gaan elk naar een ring en doorlopen enkel beide ringen als de golflengte in resonantie is in beide ringen. Vermits de ringen een lichtjes verschillende straal hebben gebeurt dit niet voor alle resonantiegolflengtes van beide ringen en wordt de FSR van de totale component veel groter. Om de resonantiegolflengtes van beide ringen te laten overlappen zijn contacten aangebracht om de ringen thermisch te kunnen afstemmen.

De componenten werden gefabriceerd maar vertoonden spijtig genoeg geen goede werking. Dit was waarschijnlijk te wijten aan het grote verlies

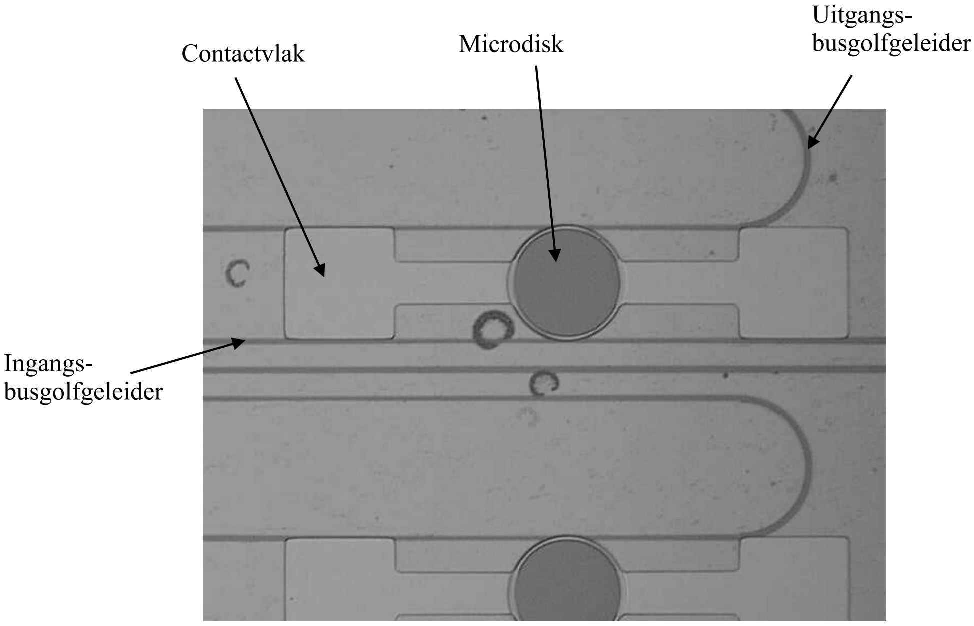

Figuur 42: Foto van een thermo-optisch afstembare microringresonator

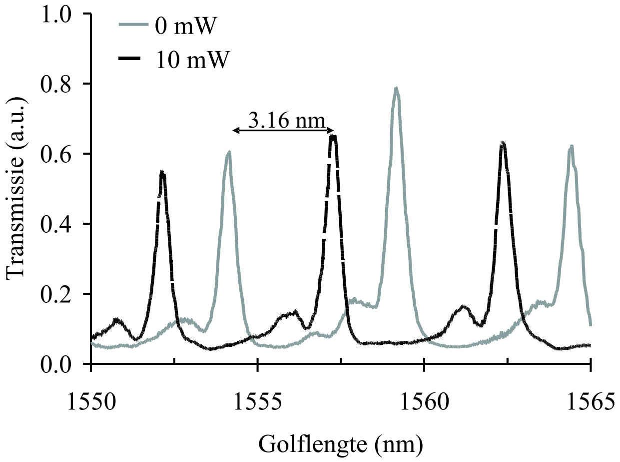

Figuur 43: Voorbeeld van het thermo-optisch afstemmen van een resonator met een straal van 20 μm

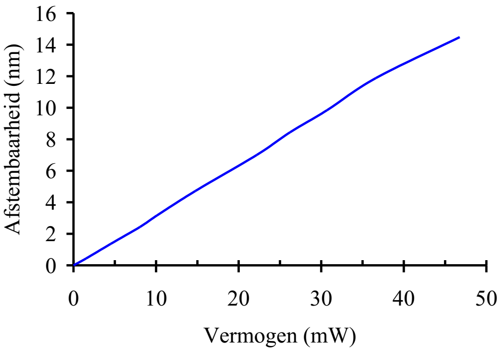

Figuur 44: Afstembereik versus vermogen

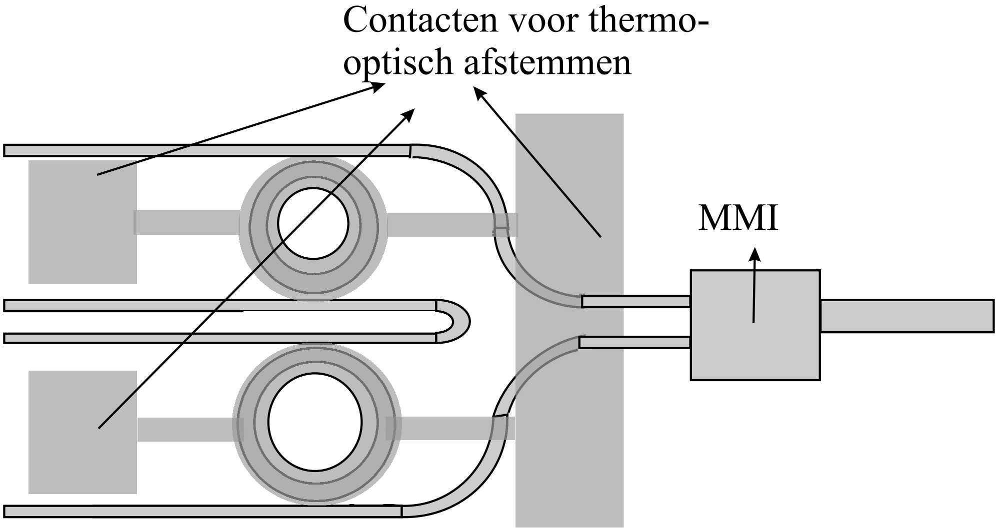

Figuur 45: Opbouw van de component

door verstrooiing omdat het etsproces ondanks grote inspanningen nog niet voldoende geoptimaliseerd was sedert de verhuis naar de nieuwe cleanroom. Dat deze ringen een groot verlies vertonen was ook te concluderen uit metingen van een monster dat gelijktijdig met deze componenten gemaakt werd en waarop met een oud masker enkele ringen gefabriceerd werden. Slechts enkele hiervan vertoonden wat filterwerking en uit deze karakteristieken werd een verlies α tot 30/cm geëxtraheerd.

7 Conclusies

7.1 Resultaten

Dit werk draaide voornamelijk rond waferbonding en microringresonatoren. Het waferbonding proces dat werd ontwikkeld is vrij makkelijk te gebruiken en vereist enkel standaard cleanroom apparatuur. Bovendien laat het toe om erg verschillende materialen te integreren in heterogene integratie. Verschillende membraantype componenten werden gefabriceerd zoals ringresonatoren, lasers en LED's. Levensduurtesten tonen de kwaliteit van het proces aan.

Microringresonatoren werden succesvol gemaakt met dit proces. Het fabriceren van ringresonatoren is echter maar één deel van het verhaal, het andere is het ontwerpen en simuleren ervan. Dit is lange tijd vrij moeilijk geweest door het ontbreken van software voor het berekenen van de modes van een drie dimensionale gebogen golfgeleider en een efficiënte manier om de koppelingscoëfficiënten uit te rekenen. Deze problemen werden in de loop van dit werk opgelost: enkele commerciële software producten werden geëvalueerd. Ondanks het feit dat niet alle structuren te simuleren vallen, zijn deze toch heel nuttig. Met de gekoppelde mode theorie is het nu mogelijk om efficiënt, in 3 dimensies, volledig vectorieel en voor multimodale golfgeleiders de koppelingscoëfficiënten uit te rekenen.

Deze modellering liet toe om verschillende fenomenen als hogere orde mode excitatie en polarizatie-rotatie, die optraden bij de gefabriceerde componenten, te verklaren.

De lage thermische geleidbaarheid van BCB werd gebruikt om de componenten op een efficiënte wijze thermo-optisch afstembaar te maken. De volgende stap was het combineren van twee thermo-optisch afstembare ringen om een wijd-afstembaar filter te maken maar problemen met de processing hebben dit verhinderd.

7.2 Perspectieven

Eerst en vooral zouden enkele laatste problemen metde fabricage van enkele passieve ringen uit de weg geruimd moeten worden. Nu de werktuigen voorhanden zijn om de ringen goed te ontwerpen, zonder excitatie van hogere orde modes, zonder polarizatie-draaiing, kan bijvoorbeeld de lagenstructuur herbekeken worden. Om een ring echter goed te ontwerpen moet het verlies op voorhand gekend zijn. Het etsproces zou dus eerst verder op punt moeten gesteld worden. De lagenstructuren zouden ook nauwkeuriger gegroeid moeten worden, wegens de grote invloed van de laagdiktes op de koppelingscoëfficiënten. Ook zouden op het masker extra structuren kunnen toegevoegd worden aan de rand, deze worden toch afgeklieft om facetten te maken en kunnen gebruikt worden om onder de SEM de alignatie te bekijken zonder de component te vernietigen.

Als het etsen op punt staat kan het laatste masker met de MMI gekoppelde ringen opnieuw gefabriceerd worden. Andere mogelijke routes zijn het fabriceren van een laser met 1 ring of met de MMI gekoppelde ringen voor het maken van een afstembare laser. Andere actieve componenten zijn uiteraard ook mogelijk en de route van het bonden met dunnere lagen kan verder uitgewerkt worden om voor deze componenten de thermische weerstand te verkleinen.

Aan de kant van de waferbonding is heterogene integratie mogelijk en wordt al onderzoek gedaan naar het koppelen van een SOI golfgeleider met een InP actief membraan. Dit biedt veel mogelijkheden voor de toekomst.

English Text

Contents

List of symbols and abbreviations

a.u.		arbitrary units
A		power loss for a certain length
FSR	nm	Free spectral range
$\mathcal{F}$		Finesse
L	μm	half the circumference of the ring
r		amplitude reflection coefficient
R		power reflection coefficient
RTL		Round trip loss
r_{min}	mW	minimum reflection
R_r	μm	radius of the microring
SMSR	dB	Side Mode Supression Ratio
t		amplitude transmission coefficient
t_{max}	mW	maximum transmission
κ		power coupling coefficient
λ	μ m	wavelength
ϕ	rad	phasedelay in the microring

Chapter 1

Introduction

1.1 Context

Photonics or opto-electronics, a strange word to many, is the research field that deals with the manipulation of light. Most people are somewhat familiar with terms such as lasers and optical fibers. This is not surprising since optical fiber technology was an enabling technology for the development of the Internet. The advent of the Internet has revolutionized telecommunications in the same way the invention of the telephone has done before. The Internet has and is fundamentally changing the way the world interacts. The number of subscribers to broadband access continues to rise rapidly with government agencies trying to get everyone on the Internet (e.g. Europe [1], US [2]).

Apart from the growth in the number of subscribers (Fig. 1.1), more and more applications requiring more bandwidth are emerging, putting strain on the available bandwidth. Even though the optical fiber in the backbone of most networks has a huge terahertz size bandwidth, this cannot always be fully exploited due to other bottlenecks. These bottlenecks are mainly due to the electrical components in the optical network. An optical network consists of a lot more than just the optical fibers transporting the data. These other components such as routers, switches, add-drop multiplexers, regenerators, . . . are often not opto-electronic ones. Usually all these tasks are still performed by converting the optical signal into an electrical one and performing the operations in the electrical domain, after which the electrical signal is transformed back to light and transmitted on into the optical fiber. The all-optical network is not yet within our reach but there is a large consensus that this is the way to go, with large telecom companies (Nortel, Cisco, . . .) offering network technologies that are more and more optical and not only

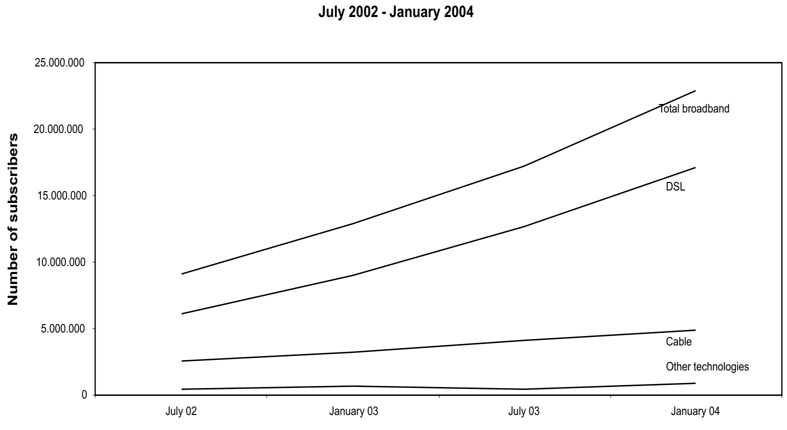

Source: Commission Services

Figure 1.1: Growth of the number of broadband subscribers in the EU

applicable to the backbone of the network but also penetrating more local networks closer to the consumer.

Even though telecommunication applications are among the largest in photonics, other applications are by no means to be neglected: spectroscopy, biophotonics, lighting such as LED's for car lights and traffic lights, sensors, solar cells, . . .

1.2 The future: integration

The route forward for photonics is, just as it was for electronics, integration and miniaturization. This means that the normally quite bulky photonic building blocks have to be reduced in size and different functions have to be integrated onto one chip to increase functionality.

The latter can be difficult because, in photonics, no single material system has emerged as the standard material system for photonic chips such as Si did for electronics. It is difficult to find a single material system that can provide all the functionality needed for a photonic chip without adding too many disadvantages. Different approaches are taken here: from fully sticking to one material system such as InP [3] to provide all the functionality, accepting the downside of smaller wafers, more expensive wafers, expensive epitaxial growth and not so mature processing techniques; to fully hybrid approaches which try to combine the advantages of different material systems whilst avoiding their disadvantages, but at the cost of often more bulky systems, alignment difficulties etc.

A technology located in between is heterogenous integration which typically uses wafer bonding to combine different material systems. A combination of InP/InGaAsP to provide the active components and SOI for the passive waveguiding functions and the electronics for instance, is a very interesting one. The use of SOI allows to fabricate waveguides with standard CMOS technology and the high contrast between the silicon core and the oxide buffer layer makes ultracompact circuits possible. Efficient active optoelectronic devices in SOI are not demonstrated yet and for these functions InP-based components should be used.

The resulting chip can still be quite compact, processing can happen on wafer-scale and difficult alignment procedures can be avoided. This is however still very much in its infancy. Wafer bonding is an enabling technology for heterogenous integration. It also makes 3D photonics possible while we are now still mostly limited to designs in 2D on the surface of the wafer.

1.3 Microring resonators

Another important difference between photonics and electronics is the lack of a very basic component such as the transistor which can be used in numerous ways and combined to achieve a lot of different functions. The microring resonator, discussed in this work, could perhaps be the transistor of photonics. It is a very basic, scalable, small and versatile component.

The microring resonator is a component first suggested by Marcatili [4] in the 1960's. Large ring resonators have been fabricated in the beginning of the 1980's (see for instance ref. [5]) and often these were fiber rings but it has taken till the second half of the 1990's with the advent of better processing technologies for microring resonators to emerge. From there on development has gone fast. Microrings have been fabricated in a multitude of material systems and a huge number of applications has either been suggested or demonstrated, illustrating that indeed the microring is a very versatile, scalable building block [6].

These possible applications for microring resonators will be discussed in detail in Chapter 3 but some of them are already discussed here to illustrate all these qualities of microring resonators.

A basic microring resonator allows to filter out certain wavelengths and by cascading microrings onto a cross-grid a complete add-drop multiplexer for WDM-applications can be constructed (see Figure 3.9). An active microring resonator, in InP/InGaAsP for instance, allows to create a switch or modulator. All-optical memory elements have been demonstrated using microring resonators (see Section 3.3.4) and also all-optical logical functions (see Section 3.3.6). Microring resonators can be fabricated with good performance in a multitude of material systems, as will be shown in Section 3.2.

1.4 Goal

The microring resonator can basically be fabricated in two ways: vertically coupled and laterally coupled, which will be explained in Chapter 3. We chose to develop the vertically coupled approach, the reasons for this will be also be discussed later, but let it suffice to say right now that the vertically coupled approach has certain advantages such as the possibility of fabricating a microring resonator using only basic lithography techniques, it allows for double-sided processing (defining structures on both sides of the epitaxial layers), for easy active-passive integration and it is a step on the route to heterogenous integration. This approach however requires the use of wafer bonding.

The goal of this PhD was therefore to develop a wafer bonding process that would allow to fabricate vertically coupled microring resonators. At the same time, other kinds of wafer-bonded devices would be fabricated to demonstrate the feasibility of heterogenous integration using this technique. The process had to allow the integration of a wide variety of material systems, had to possibly wafer-scale, be low-temperature and require nothing but standard cleanroom equipment.

The rest of the fabrication process for microrings had to be developed but also tools for modelling and designing microring resonators, which were very scarce at the start of this PhD. These tools had to allow for a full-vectorial three-dimensional modelling of the microring resonator in a reasonable time frame. The devices were fabricated in InP/InGaAsP to allow fabrication of active devices in the future.

1.5 Outline

The outline of this thesis is as follows. In Chapter 2 the basic functionality of the microring resonator will be explained together with the most important performance parameters and the influence of the design on these parameters.

In Chapter 3 the different approaches to the fabrication of microrings will be discussed together with an overview of the possible material systems, their advantages and disadvantages, and the performance of microrings fabricated in these different material systems. This chapter ends with a short overview of applications involving microrings reported in literature, demonstrating the versatility of microring resonators.

Chapter 4 gives a short introduction to the vast area of wafer bonding and then elaborates on the BCB wafer bonding process that was developed in this work. This process was chosen to be used in the fabrication of vertically coupled microring resonators but also LED's and lasers were fabricated using wafer bonding.

Chapter 5 focuses on the simulation of microring resonators. This is not a trivial task and can best be tackled by splitting the microring in different segments: the two coupling sections and the bent waveguide. Therefore, this chapter first focuses on the issues involved in calculating the modes of bent waveguides, discussing the 2D case first because this is relatively easy and provides more physical insight, and then moves on to discuss the possibilities and difficulties for the simulation of 3D modes. The next section then focuses on the simulation of the coupling section and mainly on the technique using the complete coupled mode equations. Next, the influence of some non-ideal behaviour such as excitation of higher order modes, polarization conversion, counter-directional coupling, lossy couplers and the influence of the different loss contributions is discussed.

Chapter 6 briefly summarizes the entire processing, elaborating on some details such as alignment tolerances, AR-coatings etc. Next, measurements of passive microrings are discussed followed by measurements on thermo-optically tunable microrings. Thermal bistability and dispersion measurements are also shown.

Chapter 7 ends this thesis with some concluding remarks and recommendations for future work.

This work was done in the frame of the IST-project ”Newton: New Widely Tunable Lasers for Optical Networks”, the ESA project ”Microphotonics”, the GBOU project ”Plastic Photonics”and is continued in the EpSOC project. The author thanks the Flemish Institute for the Industrial Advancement of Scientific and Technological Research (IWT) for a specialization grant.

1.6 Publications

Journals

- Ilse Christiaens, Dries Van Thourhout, Roel Baets, ”Low power thermo-optic tuning of vertically coupled microring resonators”, IEE Electronics Letters, Vol. 40, No. 9, p560-561 (2004).

- I. Christiaens, G. Roelkens, K. De Mesel, D. Van Thourhout, R. Baets, ”Thin film devices fabricated with BCB waferbonding”, Journal of Lightwave Technology, Vol. 23, No.2, p517-523, February (2005).
- Marko Galarza, Jokin Moreno, Manuel Lopez-Amo, Ilse Christiaens, Dries Van Thourhout, Roel Baets, ”Simple low-loss waveguide bends using ARROW effect”, accepted for publication in Applied Physics B, (2005).

Conferences

- K. Ghawana, D. Delbeke, I. Christiaens, S. Verstuyft, R. Baets, ”Grating-assisted resonant-cavity LEDs: towards thin film devices for heterogeneous integration”, SPIE’s International Symposium Photonics Fabrication Europe, 4947, Belgium, (2002).
- I. Christiaens, D. Van Thourhout, R. Baets, ”Microring resonators as building blocks for VLSI photonics”, FTW UGent 4th PhD symposium, Belgium, (2003).
- I. Christiaens, D. Van Thourhout, R. Baets, ”Low power thermo-optic tuning of vertically coupled InP microring resonators”, IPRM 2004, Japan, pp.425-427 (2004).
- G. Morthier, R. Laroy, I. Christiaens, R. Todtd, Th. Jacke, M.-C Amann, J-O. Wesstrom, S. Hammerfeldt, T. Mullane, R. Ryan, M. Todd, ”New widely tunable edge-emitting laser diodes at 1.55 μm developed in the European IST-project Newton”, Asia-Pacific Optical communications, China, (2004).
- R. Baets, W. Bogaerts, P. Dumon, G. Roelkens, I. Christiaens, K. De Mesel, D. Taillaert, B. Luyssaert, J. Van Campenhout, P. Bienstman, D. Van Thourhout, V. Wiaux, J. Wouters, S. Beckx, ”Integration of photonic functions in and with Silicon”, ESSDERC/ESSCIRC (invited), Belgium, (2004).
- G. Roelkens, J. Brouckaert, I. Christiaens, K. De Mesel, P. Dumon, D. Van Thourhout, R. Baets, ”Heterogeneous integration of III-V material and silicon: fabrication and devices”, Proceedings Symposium of the IEEE/LEOS Benelux Chapter, Ghent, Belgium, pp 83-86, (2004)
- Ilse Christiaens, Dries Van Thourhout, Roel Baets, ”Vertically coupled InP microring resonators fabricated with BCB wafer bonding”, Proceedings Symposium of the IEEE/LEOS Benelux Chapter, Ghent, Belgium, pp. 57-60, (2004).

- Pieter Dumon, Ilse Christiaens, Wim Bogaerts, Vincent Wiaux, Johan Wouters, Stephan Beckx, Dries Van Thourhout and Roel Baets, ”Microring resonators in Silicon-on-Insulator”, 12th European Conference on Integrated Optics, ECIO, (2005).

- Marko Galarza, Jokin Moreno, Manuel Lópen-Amo, Ilse Christiaens, Dries Van Thourhout, Roel Baets, ”Simple low-loss waveguide bends using antiresonant reflection optical waveguides”, 12th European Conference on Integrated Optics, ECIO, (2005).

- Günther Roelkens, Dries Van Thourhout, Ilse Christiaens, Roel Baets and Meint Smit, ”Ultra-thin BCB bonding for heterogeneous integration of III-V devices and SOI photonic components”, 12th European Conference on Integrated Optics, ECIO, (2005).

Bibliography

[1] *Connecting Europe at High speed: National Broadband Strategies*, May 2004. http://europa.eu.int/information_society/eeurope/2005/doc/all_about/broadband/com_broadband_en.doc.

[2] G.W. Bush. *Promoting innovation and economic security through broadband technology*, 2004. http://www.whitehouse.gov/infocus/technology/economic_policy200404/chap4.html.

[3] Integration. www.35ph.com. III-V photonics, The Netherlands.

[4] E.A.J. Marcatili. Bends in optical dielectric guides. *Bell Sys. Tech. J.*, 48:2103–2132, 1969.

[5] Kazuo Honda et al. Characteristics of an integrated optics ring resonator fabricated in glass. *IEEE Journal of Lightwave Technology*, LT-2(5):714–719, October 1984.

[6] B. E. Little. A VLSI photonics platform. Optical Fiber Communication Conference (OFC), 2003. Invited talk.

Chapter 2

Basics and theory

2.1 Basic layout and functionality

2.1.1 Introduction

The basic layout of a ring resonator is quite simple. It consists of a circular waveguide and two straight waveguides as depicted in Fig. 2.1.

The two tangential straight waveguides serve as evanescent wave input and output couplers to the ring. If the signal entering port A is on-resonance with the ring or disk, then that signal couples into the circular waveguide cavity, couples out from the cavity into the second waveguide, and exits the device at port C. A signal that is off-resonance with the cavity remains in the input waveguide and exits at port B. Port C will be called the drop port and port B the pass port. Figure 2.2(a) and Fig. 2.2(b) show field profiles of a ring resonator in and out of resonance.

The resonances can be explained by the fact that light that has travelled 360 degrees in the circular waveguide has to be in phase again for constructive interference. This means that the wavelength of the incoming signal 'fits' in the circular waveguide, the circumference of the microring is an integer mutiple of the modal wavelength used. The definition of the circumference is not clear here but this will be explained further on.

Ring resonators come in different shapes and sizes. We will focus on the small ring which is referred to as the microring because of its micron size radius. The term microdisk is also often used but this is just a microring with no inner boundary for the circular waveguide.

The transmission at port B and C as a function of wavelength for an ideal lossless device can be seen in Figure 2.3. One of the most straightforward

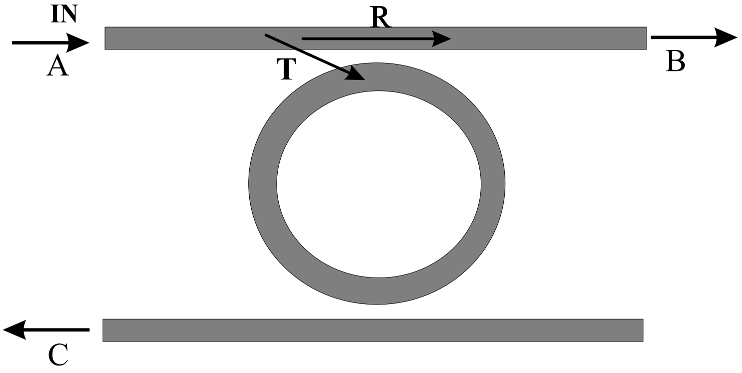

Figure 2.1: Basic microring resonator

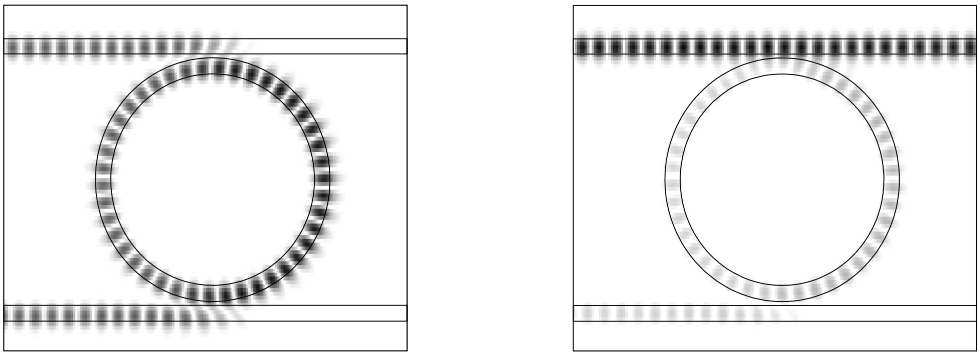

(a) In resonance

(b) Out of resonance

Figure 2.2: Field profiles of a microring in resonance and out of resonance

applications of this kind of comb-like response is an add-drop filter in a WDM system.

2.1.2 Basic equations

The ring resonator is in a way very similar to the commonly known Fabry-Perot resonator (Fig. 2.4). The big difference between the two is that the microring is a travelling wave resonator and the Fabry-Perot a standing wave resonator. Light that enters the Fabry-Perot resonator is partly transmitted and partly reflected. In a ring resonator a small percentage of the power is coupled into the ring. In the Fabry-Perot resonator and in the ring resonator a phase condition has to be fulfilled for the wavelength to be transmitted. Because of this similarity with the Fabry-Perot resonator the signal at the drop

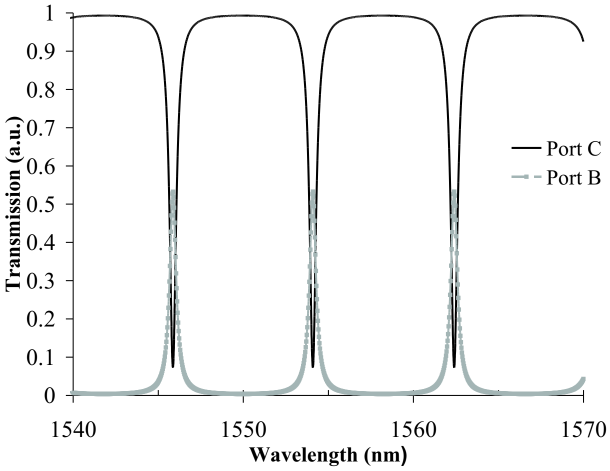

Figure 2.3: Transmission at port B and C

port will often be called the transmission and the signal at the pass port the reflection. Other definitions are also used where the signal at port B is called the transmitted wave, so care has to be taken when consulting literature.

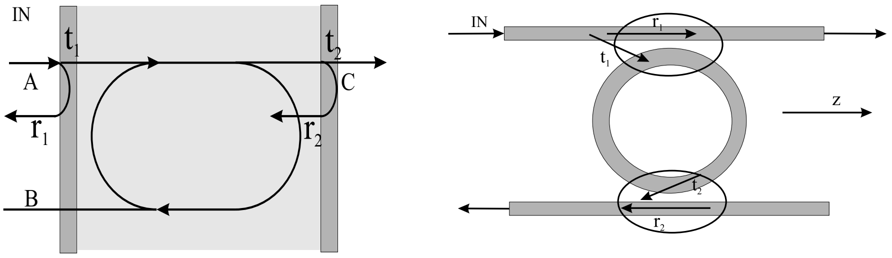

(a) Fabry-Perot resonator

(b) Microring resonator

Figure 2.4: Comparison of the microring resonator with the Fabry-Perot etalon

There are several ways to calculate the transmission characteristics of the ring, the matrix method being one of the most common. We will deduce the equations in a quite intuitive way by adding up all the field amplitudes that contribute to the response. The microring can be split up in the ring itself and 2 coupler sections - one between the input waveguide and the ring, the other between the ring and the output waveguide - which is illustrated in Fig.2.4(b).

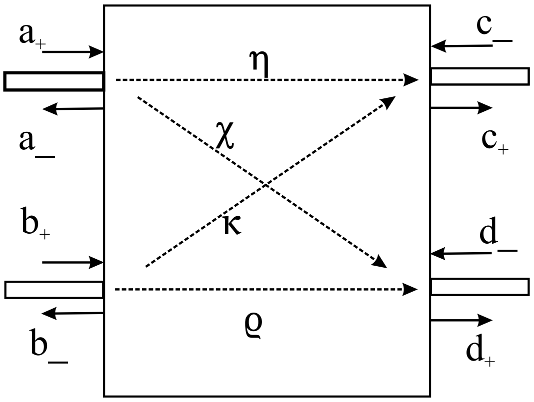

Figure 2.5: The coupler as a four port system

We shall start by calculating the responses at the different ports in the most general way namely with different reflection and transmission coefficients for both coupler sections.

Care has to be taken, also when consulting literature, to assure if one is using power or amplitude coefficients and if L is half or whole of the circumference. We will define L as half of the circumference.

In the following equations t_1 and t_2 are the amplitude transmission coefficients, r_1 and r_2 the amplitude reflection coefficients and α is the power loss coefficient (1/cm).

The coupler can be described as a 4 port system as the one shown in (Fig. 2.5). Let's assume it is lossless. The general transfer matrix for this system is

$$\begin{pmatrix} a_- \\ b_- \\ c_+ \\ d_+ \end{pmatrix} = \begin{pmatrix} 0 & 0 & \eta & \chi \\ 0 & 0 & \kappa & \rho \\ \eta & \kappa & 0 & 0 \\ \chi & \rho & 0 & 0 \end{pmatrix} \begin{pmatrix} a_+ \\ b_+ \\ c_- \\ d_- \end{pmatrix}$$

The zeros appear because the backreflections are assumed to be negligible. The matrix is symmetric because of reciprocity. Because the coupler has a plane of symmetry in the middle, the transmission from b_+ to c_+ is equal to the transmission from d_- to a_-, and therefore κ is equal to χ.

If we assume the coupler is lossless then the matrix has to be unitary [1], which leads to the following conditions:

$$\begin{aligned}&|\rho|^2 + |\kappa|^2 = 1\\&|\chi|^2 + |\eta|^2 = 1\\&\eta\kappa^* + \chi\rho^* = 0\end{aligned}$$

Consequently $|\rho| = |\eta|$. For a proper choice of input- and output planes, ρ and η are real and the matrix becomes

$$\begin{pmatrix} a_- \\ b_- \\ c_+ \\ d_+ \end{pmatrix} = \begin{pmatrix} 0 & 0 & \rho & \kappa \\ 0 & 0 & \kappa & \rho \\ \rho & \kappa & 0 & 0 \\ \kappa & \rho & 0 & 0 \end{pmatrix} \begin{pmatrix} a_+ \\ b_+ \\ c_- \\ d_- \end{pmatrix}$$

If we assume that the system is lossless the following holds

$$\begin{aligned}&\text{if } a_+ = 1, b_+ = c_- = d_- = 0 \text{ then } |\rho|^2 + |\kappa|^2 = 1\\&\text{if } a_+ = 1, b_+ = 1, c_- = d_- = 0 \text{ then } |\rho + \kappa|^2 = 1\end{aligned}$$

From this we can conclude that $\angle(\rho) = \angle(\kappa) + \pi/2$, the signal in the ring and the signal in the bus waveguide have a $\pi/2$ phase shift. Light in the ring has a 90 degree phase shift with light in the bus (at a properly chosen point) therefore jt_1 and jt_2 are used. The relationship between the symbols of Fig. 2.4(b) and Fig. 2.5 are in this case that $\kappa = \chi = r$ and $\eta = \rho = jt$.

This assumes that the coupling system is lossless. If this is not the case the analysis can still be made but is more difficult and provides less physical insight. We refer to ref [2] for the equations in this case. In Section 5.3.5 we will elaborate on the effects of a coupler that is not lossless on the performance of the microring resonator.

The coupling coefficient actually contains a wavelength dependence, a phase factor dependent on the length of the coupling section and the propagation constant should be included. We shall however assume that the coupling occurs in one point, the wavelength dependence is then included in the factor ϕ defined later on. Th propagation constant of the bent waveguide mode is then assumed to be the same everywhere, even close to the bus waveguide.

The ratio of the field at the drop port to the field at the input is

$$\begin{aligned}
\frac{E_C}{E_A} &= -t_1t_2\sqrt{A}\,exp(-j\frac{\phi}{2})\big(1 + Ar_1r_2exp(-2j\frac{\phi}{2}) + A^2r_1^2r_2^2exp(-4j\frac{\phi}{2}) + \dots\big) \\
&= -t_1t_2\sqrt{A}\,exp(-j\frac{\phi}{2})\sum_{k=0}^{\infty} A^k r_1^k r_2^k exp(-jk\phi) \\
&= \frac{-t_1t_2\sqrt{A}\,exp(\frac{-j\phi}{2})}{1 - Ar_1r_2exp(-j\phi)}
\end{aligned}$$

with

$$\begin{aligned}
A &= exp(-\alpha L) \\
\phi &= \frac{2\pi}{\lambda} n_{eff}(R_r)2L \\
L &= \pi R_r
\end{aligned} \tag{2.1}$$

R_r is an arbitray radius, often chosen to be the outer radius of the bend. The value of the effective index n_{eff} is dependent on the radius chosen. The reason for this will become clear in Chapter 5. The different coefficients are indicated on Fig. 2.4.

It is of course more common to look at the power because this is what is actually measured.

$$\begin{aligned}
\frac{I_c}{I_A} &= |\frac{E_C}{E_A}|^2 \\
&= \frac{(1-R_1)(1-R_2)A}{(1-\sqrt{R_1R_2}A)^2 + 4\sqrt{R_1R_2}Asin^2(\frac{\phi}{2})} \\
&= \frac{t_{max}}{1 + Fsin^2(\frac{\phi}{2})}
\end{aligned}$$

with

$$\begin{aligned}
t_{max} &= \frac{(1-R_1)(1-R_2)A}{(1-\sqrt{R_1R_2}A)^2} \\
F &= \frac{4\sqrt{R_1R_2}A}{(1-\sqrt{R_1}R_2A)^2}
\end{aligned}$$

R_1 and R_2 are power reflection coefficients which are related to the amplitude reflection coefficients by

$$R_i = r_i^2$$

and because the coupler is considered lossless,

$$t_i^2 = 1 - r_i^2$$

We will also define the power coupling coefficients κ_1 and κ_2 as

$$\kappa_i = 1 - R_i$$

The ratio of the field at the pass port to the field at the input is

$$\begin{aligned}
\frac{E_B}{E_A} &= r_1 - t_1^2 r_2 A\ exp(-j\phi)\big(1 + r_1 r_2 A exp(-j\phi) + r_1^2 r_2^2 A^2 exp(-2j\phi) + \dots\big) \\
&= r_1 - t_1^2 r_2 A\ exp(-j\phi) \sum_{k=0}^{k=\infty} r_1^k r_2^k A^k exp(-kj\phi) \\
&= r_1 - \frac{t_1^2 r_2 A\ exp(-j\phi)}{1 - r_1 r_2 A exp(-j\phi)} \\
&= \frac{r_1 - r_2 A\ exp(-j\phi)}{1 - r_1 r_2 A\ exp(-j\phi)}
\end{aligned}$$

This is the general equation where the coupling between the input waveguide and the ring t_1 and between the ring and the output waveguide t_2 can differ. For equal input and output coupling which is called symmetrical coupling, the equations simplify.

$$\begin{aligned}
R_1 &= R_2 = R \qquad (2.2) \\
\frac{I_C}{I_A} &= \frac{I_C}{I_0} = \frac{t_{max}}{1 + F sin^2(\frac{\phi}{2})} \qquad (2.3) \\
t_{max} &= \frac{(1-R)^2 A}{(1-RA)^2} \\
F &= \frac{4RA}{(1-RA)^2} \\
\frac{I_B}{I_A} &= \frac{r_{min} + F sin^2(\phi/2)}{1 + F sin^2(\phi/2)} \\
r_{min} &= \frac{(1-A)^2 R}{(1-RA)^2}
\end{aligned}$$

Another configuration that is used from time to time is the all-pass configuration. This is a microring resonator with only one straight waveguide. This will be discussed in depth in Section 2.5. The equations for this case can easily be derived by setting R_2=1 in the equations for the asymmetrically coupled microring resonator.

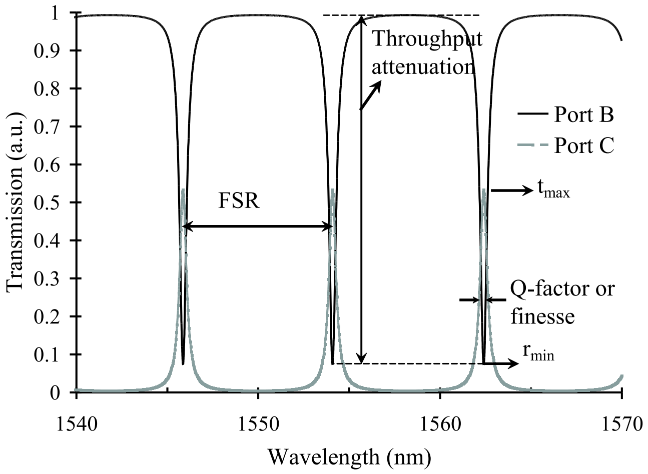

Figure 2.6: Some important parameters

2.2 Important performance parameters

In this Section we will discuss some of the important parameters that are defined to quantify the performance of a microring resonator. Some of them are illustrated on Figure 2.6.

2.2.1 Free spectral range

One of the first and most important parameters is the Free Spectral Range (FSR). This is the distance between two peaks on a wavelength scale. By differentiating eq. 2.1 we get:

$$FSR = \frac{\lambda^2}{2n_g L}$$

where n_g is the group index:

$$n_g = n - \lambda \frac{dn}{d\lambda}$$

2.2.2 Maximum transmission t_{max}

The maximum transmission is the magnitude of the dropped signal on resonance. In the asymmetric case this is given by

$$t_{max} = \frac{(1-R_1)(1-R_2)A}{(1-\sqrt{R_1 R_2}A)^2}$$

In the symmetric case this simplifies to

$$t_{max} = \frac{(1-R)^2 A}{(1-RA)^2}$$

2.2.3 Minimum reflection, throughput attenuation, extinction ratio (ER)

Another important parameter is the minimum reflection, which is directly related to the throughput attenuation or the extinction ratio. The minimum reflection is the signal power left in the input waveguide on resonance. The extinction ratio is the ratio of the power in the pass port on resonance and off resonance. For instance if the ring is used as an add-drop filter it is important that the signal on resonance is extracted completely from the input waveguide to minimize cross-talk. In the asymmetric case this is:

$$r_{min} = \frac{R_1 + R_2 A^2 - 2\sqrt{R_1 R_2} A}{(1 - \sqrt{R_1 R_2} A)^2}$$

In the symmetric case this is

$$r_{min} = \frac{(1-A)^2 R}{(1-RA)^2}$$

2.2.4 Finesse, Q-factor

Finesse, Q-factor, resonance width, bandwidth, these are all terms that are mainly related to the full width at half of the maximum (FWHM) of the transmission. The resonance width, or the bandwidth as it is also often called, is defined as the FWHM of the microring resonance. The Q-factor is the ratio of the bandwidth to the wavelength of the peak and is dimensionless. The Finesse is the ratio of the FSR to the bandwidth and is also dimensionless.

The formula for the FWHM on an angular scale can easily be derived from equation 2.3.

$$\begin{aligned} 2 * \delta\phi_{1/2} &= 4asin\sqrt{\frac{1}{F}} \\ &\approx 4\frac{1-RA}{\sqrt{4RA}} \\ &= 2\frac{1-RA}{\sqrt{RA}} \\ &= \frac{4}{\sqrt{F}} \end{aligned} \tag{2.4}$$

The formula derived is of course for a symmetrically coupled microring resonator. The approximation holds for most 'good' ringresonators because they have large F-values.

We can convert this to the more commonly used wavelength dimension.

$$\begin{aligned}
\phi &= \frac{2\pi n 2L}{\lambda} \\
\delta\phi &= \frac{-2\pi n 2L}{\lambda^2}\delta\lambda \\
\delta\lambda_{FWHM} &= 2\delta\lambda_{1/2} \\
&= \frac{2\delta\phi_{1/2}\lambda^2}{2\pi n 2L} \\
&= \frac{(1-RA)\lambda^2}{\pi n 2L\sqrt{AR}}
\end{aligned}$$

The Finesse $\mathcal{F}$ is closely related to this bandwidth and is defined as the ratio of the FSR and the bandwidth.

$$\mathcal{F} = \frac{FSR}{\delta\lambda_{FWHM}} = \pi\frac{\sqrt{AR}}{1-AR}$$

In this case the group velocity in the equation for the FSR was approximated by the phase velocity.

Another closely related parameter is the Q-factor. The Q-factor is defined as the ratio of the wavelength of the peak to the FWHM of the peak.

$$Q = \frac{\lambda}{\delta\lambda_{FWHM}} = \frac{\pi n 2L\sqrt{AR}}{\lambda(1-AR)}$$

The Q-factor and the Finesse are related by

$$Q = \frac{\mathcal{F}2nL}{\lambda}$$

From a practical point of view the Q-factor is interesting because it provides an immediate absolute idea of the width of the peak. The disadvantage is however that it is related to the physical size of the resonator and therefore less interesting when it comes to comparing different resonators. There the Finesse is more interesting.

There is also another method to define the Q-factor which stems from a more time-domain related approach but this will be discussed in the section on coupling of modes in time (Section 2.6).

It is clear that the Q-factor is very much determined by the coupling coefficients and the loss. Often the terms loaded and unloaded Q-factor are used. The unloaded Q-factor is higher and is only determined by the radiation and scatter losses, the loaded Q-factor is for the entire resonator and is determined by radiation and scatter losses but also by the coupling which can also be viewed as a loss from the resonator's point of view.

2.2.5 Field enhancement

One of the interesting features of a ring resonator is the high field intensity that is built up in the ring resonator on resonance. The field enhancement FE is the ratio of the field amplitude in the ring E$_r$ versus the amplitude in the input bus waveguide.

$$|\frac{E_r}{E_A}|_{\phi=0} = \frac{t_1}{1 - r_1 r_2 A} \tag{2.5}$$

Of course the field is not the same everywhere in the ring and the field enhancement is generally chosen as the field just after the input coupler. For a good ring however the loss is very low and the coupling coefficients are usually not so high so the field in the ring can be assumed to be almost constant.

The square of the field enhancement is the intensity enhancement.

2.2.6 Off resonance insertion loss

The off resonance insertion loss is the loss that a signal in the pass port experiences by passing the ring. Of course this is desired to be as small as possible so the off resonance signal can pass the ring undisturbed.

2.2.7 Line shape, shape factor

The pulse shape of a single microring resonator is often referred to as being a Lorentzian function although this is not exact. The equation of a Lorenztian function is as follows:

$$L(x) = \frac{1}{\pi} \frac{\frac{\Gamma}{2}}{(x - x_0)^2 + (\frac{\Gamma}{2})^2} \tag{2.6}$$

To say that the pulse shape is Lorentzian is thus a first order approximation (some constants have to be changed too but that is not essential) which is a fairly good approximation for resonators with low loss. The FWHM of this kind of function is Γ. By equating eq.2.3 and eq.2.6 (after a first order approximation of the sine function) it is found that $\Gamma = \frac{4}{\sqrt{F}}$ which agrees with eq.2.4.

The roll-off of this kind of function is not very box-like, not very steep. Often for filter functions a transfer characteristic with flat top and steep roll-off is desirable. A steeper roll-off and flatter top can be achieved by for instance serially cascading several microrings as is illustrated in Fig. 2.7. Figure 2.8 shows the response for 1, 2 and 3 identical rings. The coupling factors between these rings have to be chosen properly to achieve a flat top and can be found in ref. [3]. In this context a shape factor is defined as

$$shapefactor = \frac{-1dB\ bandwidth}{-10dB\ bandwidth} \tag{2.7}$$

For a single microring this shape factor is only 0.17. Other definitions such as the ratio between the 3 dB and the 10 dB bandwidth are also used.

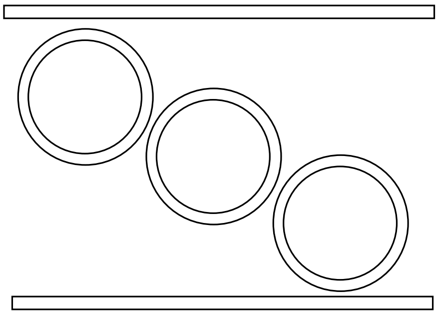

Figure 2.7: Serially coupled microring resonators

2.2.8 Phase response

An element that is often neglected in literature is the phase response of the microring resonator.

The signal of the drop port can be in phase with the signal in the input bus or out of phase. This will alter one peak after the other and is illustrated in Fig. 2.9.

The phase of the pass port however is greatly dependent upon the coupling coefficient. There are three different regimes

- Overcoupled: this means that the power coupled in the ring more than compensates for the loss by scattering and the loss by outcoupling
- Critically coupled: the power coupled in the ring exactly compensates for the loss

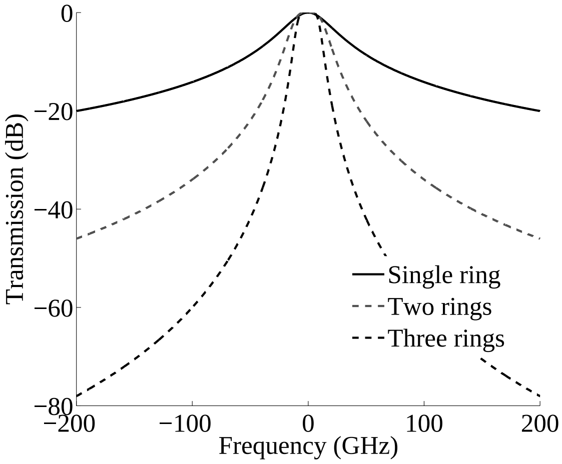

Figure 2.8: The transfer characteristic of a single, double and triple ring filter illustrating the steeper roll-off

- Undercoupled: the power coupled in the ring does not compensate for the loss

The effect this has on the phase reponse can be understood in the following manner. The signal in the pass port has two contributions: one is the signal that is not coupled into the ring (r_1), the other is the signal that is coupled from the ring back into the input waveguide with a phase change of π. In the undercoupled region not enough power is coupled into the ring and the direct signal with phase 0 is the most important one. In the overcoupled regime, the signal coming from the ring on resonance is the dominant one and the phase change is π. In between these two is the critically coupled condition where the phase cannot really be defined on resonance because there is no power left in the input waveguide.

In a symmetric configuration the resonator will always be undercoupled unless a gain section is introduced in the ring to compensate for the inevitable scatter loss (a lossles symmetrical resonator would critically coupled however). It is only in asymmetric configurations (and mainly the all pass configuration which is further explained in Section 2.5) that the phase change of π appears which can be used for instance in a Mach-Zehnder interferometer. In Fig. 2.10 the phase response for a symmetrical and thus always undercoupled microring is shown and in Fig. 2.11 for an all-pass microring. In Fig. 2.12 the different regimes for an all-pass ring are shown.

First there is the undercoupled regime where the phase on resonance is zero as explained before. This curve has peaks on the left and right of the resonance condition. When the coupling power increases and finally reaches the round trip loss value, the resonator is critically coupled. As discussed before, all power is then extracted from the input waveguide and this is the transition between no phase change and π phase change. When the coupling coefficients rises even further the phase change reaches π.

As said before, the main interest in this phase behaviour is for all-pass overcoupled microrings. In that case the microring should ideally act as a pure phase-filter and should influence the amplitude as little as possible but this will be discussed later on.

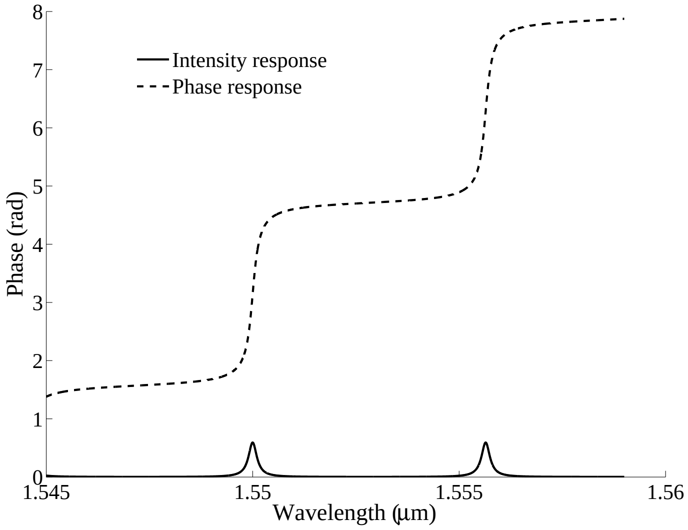

Figure 2.9: The phase at the drop port, the transmission at the drop port is also added to show where the resonances are

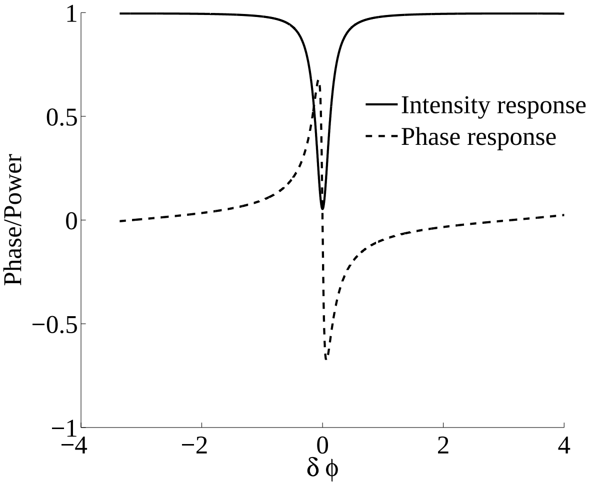

Figure 2.10: The phase at the pass port for a symmetrically coupled microring resonator (undercoupled)

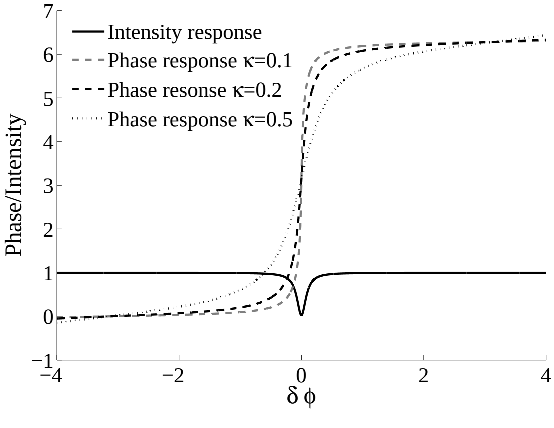

Figure 2.11: The phase at the pass port for a lossless all-pass microring resonator for different coupling factors (overcoupled)

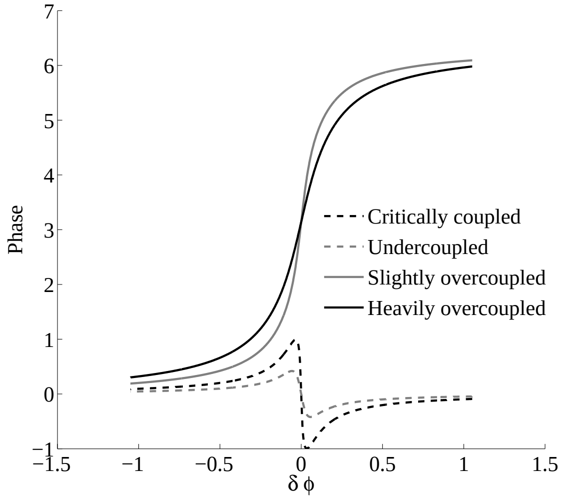

Figure 2.12: The phase at the pass port for an all-pass microring in the different regimes

2.2.9 Dispersion

As will be explained in Section 2.6 the Q-value is a sort of measure of the amount of time the light circles around in the resonator. The higher the Q, the longer it takes for the light to completely leave the resonator. The group delay of a microring resonator can be quite large therefore. Even though this high Q provides us with very narrow peaks, the downside is that the dispersion becomes more important and can compromise use of the microring at high bitrates. Figure 2.13 shows the square wave input signal and the signal after the ring resonator for a resonator with a Q value of 3500. The signal is modulated at 10 Gbit/s. The deformation of the signal is clear but the signal is still usable. When going to higher bitrates or higher Q's the situation deteriorates of course.

Not only the dispersion characteristics of the transmitted signal are important but also dispersion of the reflected signal. Because microring resonators are cascaded to create a multiplexer/demultiplexer for several channels, the phase response of the reflected signal can induce dispersion in a neighbouring channel. The phase response of all-pass filters can however also be used for dispersion compensation. By cascading microring resonators and varying their dispersion charcateristic by changing the coupling coefficient,

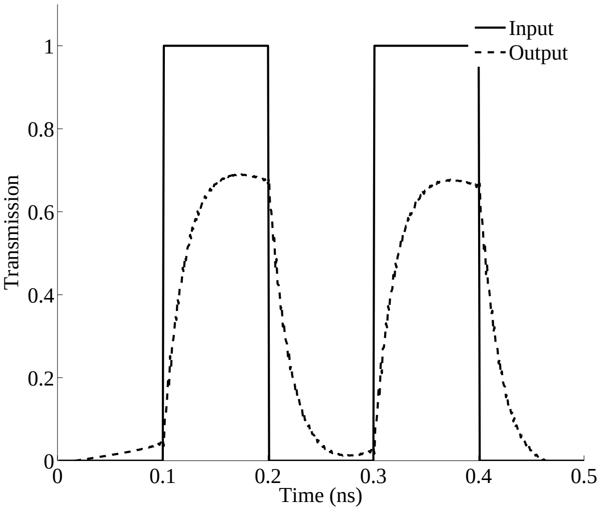

Figure 2.13: Transmission of a 10 Gbit/s signal through a microring with a Q of 3500

the group delay of the filter can be tailored [4]. A more extensive treatment of dispersion can be found in refs. [5, 6].

2.3 Design parameters

When designing a microring resonator there are a few parameters that can be controlled and designed. We will discuss these briefly in the next section, they will be elaborated upon in the following chapters.

2.3.1 Loss

The first and most important one is loss. It can be argued whether or not this is a design parameter because certainly achieving as low a loss as possible is difficult. However rings can be designed that contain gain-sections so there loss is a design parameter. There are several components related to the loss of a ring resonator: the intrinsic radiation loss of a bend, scatterloss, transition losses in the case of a racetrack resonator.

In the previous graphs that have been shown we normally use the Round Trip Loss (RTL). This is the only meaningfull loss number for comparison because the loss is not only influenced by the loss per cm but also by the

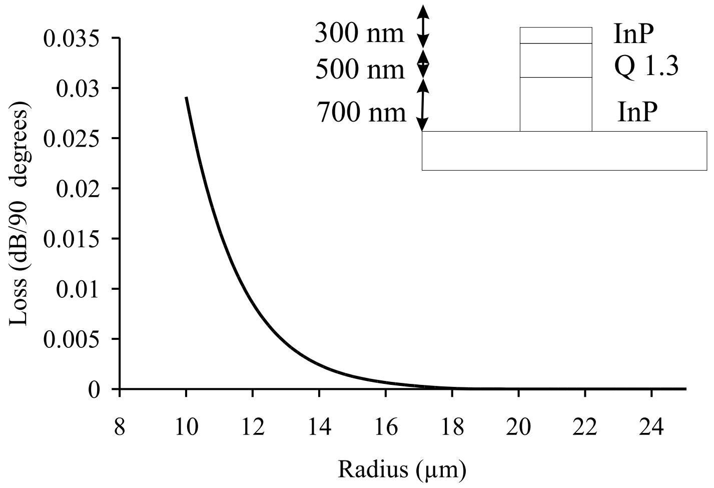

Figure 2.14: Radiation loss versus radius for a high contrast bend

distance the light has to travel, the circumference of the ring. Thus,

$$\text{RTL} = 1 - A^2$$
$$A = exp(-\alpha\pi R_r)$$

where A comprises all loss mechanisms.

Radiation loss

The first loss mechanism to consider in a microring resonator is the intrinsic radiation loss that occurs in bend waveguides. This radiation loss can be modeled with simulation software but we will discuss this in Chapter 5. The loss is highly dependent on the index contrast and the radius of curvature. In practice to make small rings (in the order of micron for the radius) high index contrast materials have to be used. In III-V materials this is commonly achieved by deep etching of the ring or disk. In Fig. 2.14 the simulated radiation loss for a typical InP-based layer structure that is deeply etched is shown. It can be seen that the loss increases exponentially when going to very small radii.

Another factor in the radiation loss that is harder to model analytically is the substrate leakage loss. As the radius of the ring decreases the mode spreads down more and if the vertical index contrast is not high enough, substrate leakage loss will occur.

Scatter loss

In practice one will design the ring resonator to have a high index contrast and up to very small radii the radiation loss will be negligible. The dominant loss mechanism is scatter loss due to surface roughness. This loss is also very dependent on the index contrast. The higher the index contrast, the higher the scatter loss. This implies that a compromise has to be made between radiation loss and scatter loss. Where the bent waveguide couples to the straight waveguide some scatter loss is also induced.

2.3.2 Coupling coefficient κ

The next design parameter is the coupling coefficient on the input and the output side. This is determined by the field overlap between the field of the ring and the bus and the ’phase matching’ between the two. Calculation of this is discussed in Chapter 5.

2.3.3 Radius

One of the clearest consequences of the choice of the radius is the size of the FSR. However the radius also has quite a large effect on the loss, the coupling coefficient and the difficulties in fabrication of the microrings.

2.4 Design considerations

In the next section we will discuss the influence of these three design parameters, loss, coupling and radius, on the different performance parameters.

2.4.1 FSR

The FSR is usually a very basic application-driven parameter in designing a microring resonator. This is most directly related to the radius of the microring. Increasing the FSR thus seems an easy task but several practical issues limit the decrease of the radius. When the radius becomes too small radiation loss has to be taken into account again and loss can become too high to achieve good functionality. Coupling sufficient power to this small ring becomes increasingly difficult but these are issues that will be elaborated upon in Chapters 3 and 5. To achieve very high FSR’s one has to resort to higher order filters using the Vernier effect (as explained in [7]).

2.4.2 Symmetric coupling

As can be seen in Fig. 2.15 and 2.16 to achieve a low minimum reflection and a high maximum transmission, the coupling has to be increased. This however has a negative effect on the Finesse which drops with increasing coupling as illustrated in Fig. 2.17. In the case of symmetric coupling one thus has to compromise between high maximum transmission, low minimum reflection and high Q values. These three parameters are summarized in Fig. 2.18 which shows a parametric plot of the Finesse, maximum transmission and minimum reflection versus the roundtrip loss and the coupling coefficient.

Figure 2.19 illustrates that an optimum does exist if one is mostly interested in high field enhancement.

The previous graphs also clearly show how sensitive all these parameters are to the loss, especially the field enhancement.

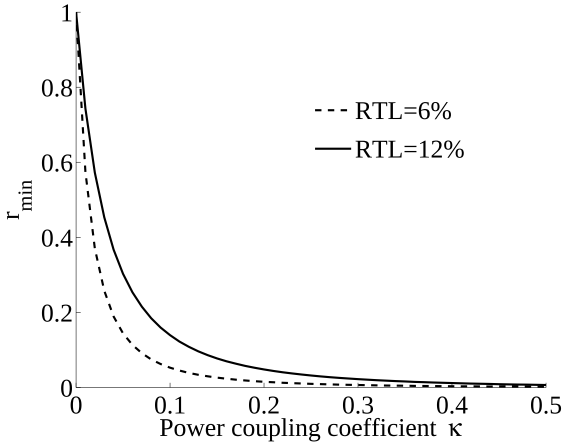

Figure 2.15: Minimum reflection versus coupling coefficient for two loss figures

2.4.3 Asymmetric coupling

In the case of asymmetric coupling the story changes of course due to the addition of another degree of freedom. We will discuss the effect of this extra degree of freedom on the different performance parameters.

Minimum reflection

By carefully adjusting the coupling coefficients the minimum reflection can be brought down to zero for any loss value, which is not possible in the sym-

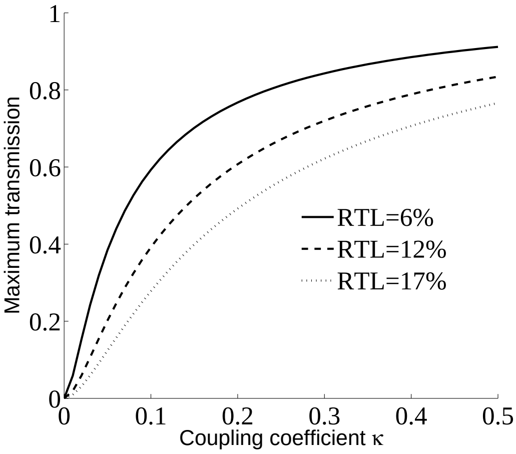

Figure 2.16: Maximum transmission versus coupling coefficient for several loss figures

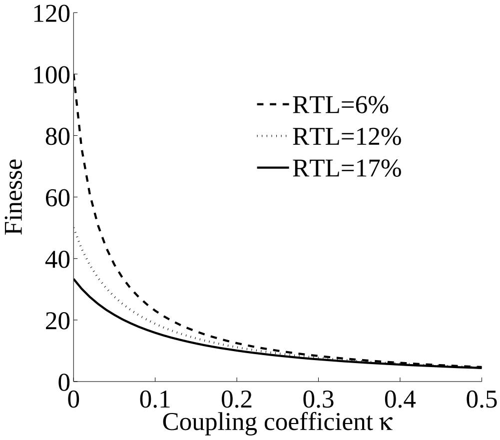

Figure 2.17: Finesse versus coupling coefficient for several loss figures

metric case. Full extraction can be achieved if $r_1 = r_2 A$. This is called critical coupling.

In Fig. 2.20 shows the minimum reflection for an asymmetrically coupled microring with a round trip loss of 8.5 % and an outcouple coefficient of 10 %. One can clearly see that the minimal reflection can be found in a region where the two coupling coefficients are different, more specifically where the incouple coefficient is higher than the outcouple coefficient, and that for very

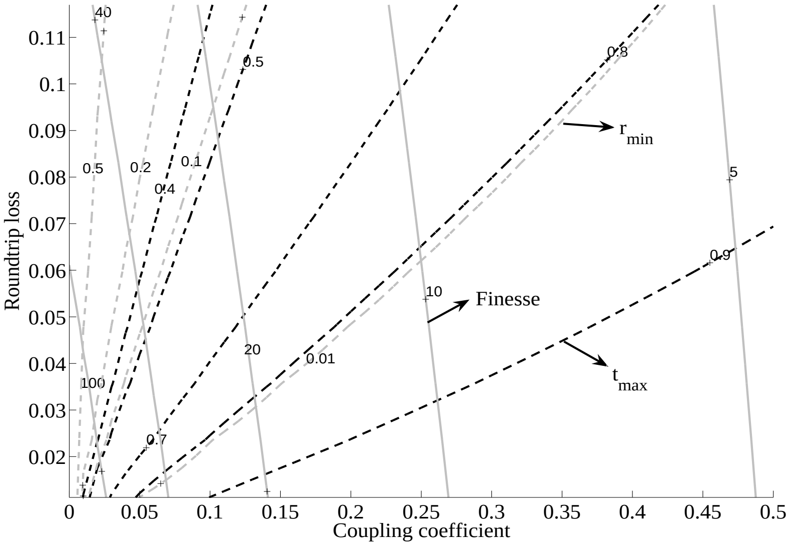

Figure 2.18: Parametric plot of minimum reflection, maximum transmission and finesse versus coupling coefficient and roundtrip loss

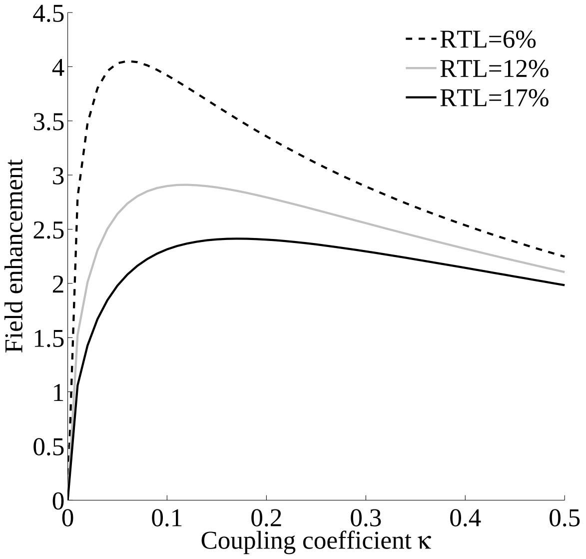

Figure 2.19: Field enhancement versus coupling for several loss figures

high extinction ratio the control over the coupling coefficients has to be very good. The drawback of using asymmetric coupling is that if a signal is going to be added via port C (Fig. 2.1) its extraction from that waveguide will be far from perfect because the asymmetrically coupled microring is used in the wrong direction and the incouple coefficient is smaller than the outcouple coefficient. This is illustrated in Fig. 2.21 where the response of the pass port of an asymmetrically coupled microresonator when excited via port A or via port C is shown.

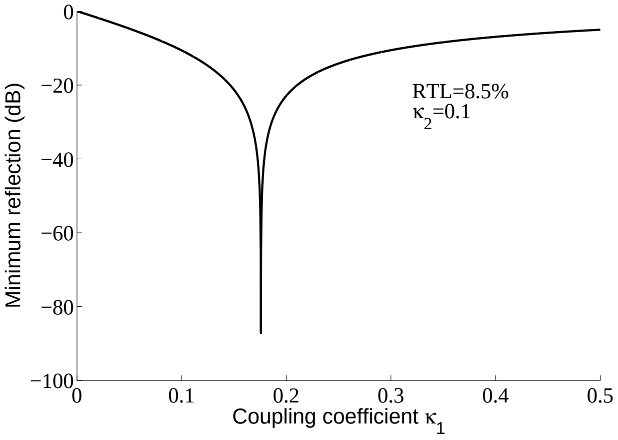

Figure 2.20: The minimum reflectivity versus the input coupling coefficient for an RTL = 8.5% and κ_2=0.1

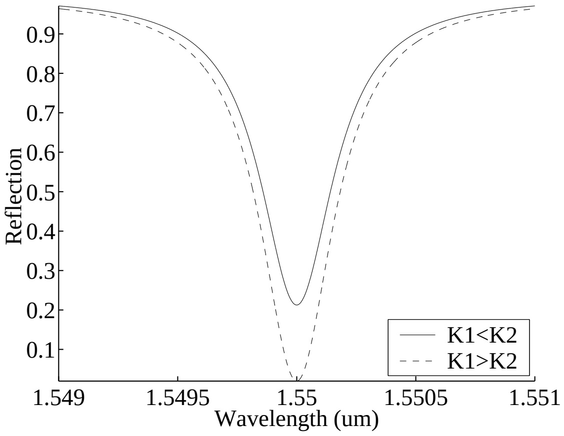

Figure 2.21: Transmission at the pass port for an asymmetrical ring

A critically coupled resonator extracts all the power from the input waveguide. However if the resonator is used in the other direction it is far from critically coupled and a lot of power remains in the input waveguide. The drop response however is the same in both cases because of reciprocity. Where has the rest of the power gone? We shall refer to the case were the ring is excited via the bus waveguide with the highest coupling coefficient as the forward direction, the other one as the backward direction. In Fig. 2.22 an asymmetrically coupled microring is simulated that has been used forward and backward. The drop response is the same in both cases but the pass is very different. The graph also shows the field enhancement which is a lot bigger in the forwardly coupled microring. This causes a lot more power to be lost in the microring which explains where the rest of the power went. The total power is unity in both cases as can be seen in the Figures.

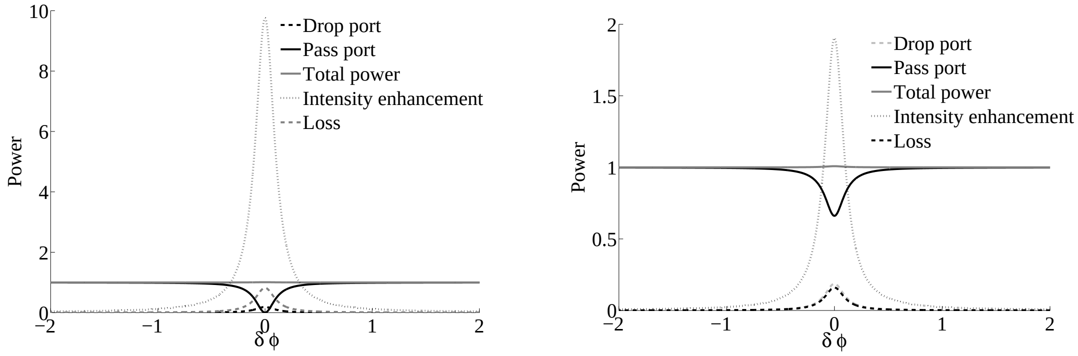

(a) Critically coupled forward

(b) Critically coupled backward

Figure 2.22: A critically coupled microring resonator excited in the forward and in the backward direction

Maximum transmission

Because of reciprocity reasons it is obvious that for the transmission it makes no difference if $\kappa_1 > \kappa_2$ or the other way around so the component can be used in both directions. The optimum in t_{max} for the drop can always be found in symmetric coupling.

Finesse

The equation for the Finesse is symmetrical in the two coupling coefficients and increases with decreasing coupling coefficients.

Field enhancement

From equation 2.5 it is clear that the field enhancement is continously increasing with r_2 and thus all-pass are devices the most interesting when it comes to optimizing the field enhancement. For an all-pass filter the maximum field enhancement can be found by differentiating eq. 2.5. The maximum is achieved when r_1=A. This is the same condition as we found for complete extraction of the input signal (critical coupling). Then the FE equals $1/t_1$ so coupling as little as possible is very important to achieve high field enhancement. All of this is illustrated in Fig. 2.23.

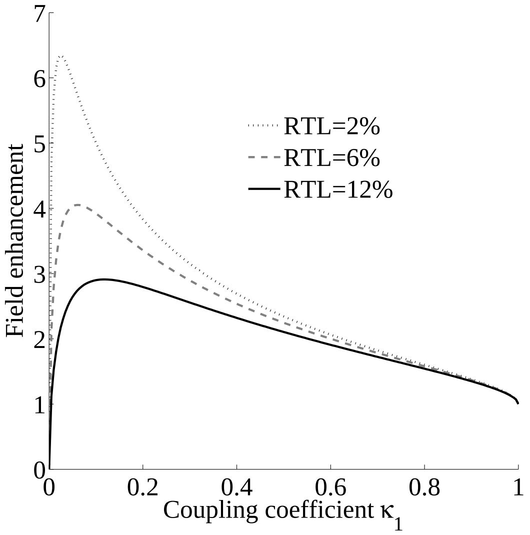

Figure 2.23: The field enhancement versus input coupling coefficient for several loss figures

2.5 All-pass microrings

So far we have mainly focused on the ring with two waveguides. The microring with only one waveguide is however also a very interesting component. This is called the all-pass configuration. Most of the equations listed above can easily be used for this design by changing r_2 to 1. This means that this component has the same functionality as a Fabry-Perot étalon with a perfectly reflection backmirror which is more commonly known as a Gires-Tournois interferometer. In this configuration the ring can be used as a phase filter or as a notch filter.

Phase filter The functionality of the phase filter has already been demonstrated in Fig. 2.11. The idea is to have a filter with a unitary amplitude response and a phase change 2π around resonance. This means that the minimum reflection has to be high so one has to stay out of the region of critical coupling. To achieve the phase change the resonator has to be overcoupled. The loss should be kept as low as possible. This kind of filter can mainly be used in for instance interferometers. The amplitude and phase response can be seen in Fig. 2.24(a).

Notch filter The notch filter is actually a critically coupled all-pass ring resonator. By adjusting the coupling coefficient to the round trip loss complete extinction of the input signal can be achieved. And at the same time as discussed before this is the situation where the highest field enhancement is achieved (Fig. 2.23). The amplitude and phase response can be seen in Fig-notch.

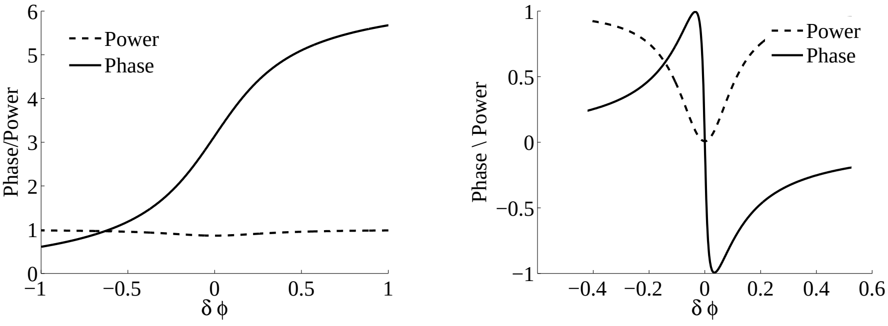

(a) Phase filter

(b) Notch filter

Figure 2.24: The amplitude and phase response of a phase filter and a notch filter

Both filters can have the same loss figure and radius etc. but only differ in the incoupling coefficient. The reason all the power is extracted from the notch filter and not from the phase filter is because the light travels a lot more cycles around the microring in the case of the notch filter. During each cycle some loss is introduced resulting in a zero transmission at the pass port. In the case of the phase filter the light does not travel enough cycles in the microring to suffer much loss.

2.6 Analysis by 'Coupling of modes in time'

Theory

The previous analyses are all referred to as coupling of modes in space. Another way to analyse microring resonators is by means of coupling of modes in time which can provide us with more physical insight and, especially for higher order mode filters, with more intuitive results. The analysis follows closely the paper of Manolatou [8] and of Little [3].

In this analysis the ring resonator is considered as a lumped element, an energy reservoir. The loss, the input and output coupling control the changes of energy in this reservoir. In the analysis one shifts often between an 'energy picture' which refers to the entire amount of energy in the ring, and a 'power picture' which refers to the power flowing through each cross section of the microring at a time t. Similar to the case of the field enhancement, all variations of the power in the microring are neglected.

For the power picture, normal wave amplitudes are used, which will be denoted with small letters. For the energy picture capital letters will be used. The amplitude of the travelling wave in the microring will be denoted as $a(t)$, this is normalized such that $|a(t)|^2$ represents the total power flowing through any section of the microring waveguide at time t. The ring is an oscillator with energy amplitude $A(t)$ normalized so that $|A(t)|^2$ represents the total energy stored in the ring. Power and energy picture are related by the following equation

$$|A(t)|^2 = |a(t)|^2 \frac{2\pi R_r}{v_g}$$

where v_g is the group velocity.

The input bus waveguide is excited by a wave with amplitude s_A. The wave at the pass port has an amplitude s_B, the dropped wave has an amplitude s_C. All these are normalized in the same way as $a(t)$. Three loss mechanisms are considered, each with their characteristic decay time.

- τ_e is the amplitude decay time constant related to the power leaving the ring via the input bus waveguide
- τ_d is the amplitude decay time constant related to the power leaving the ring via the drop waveguide
- τ_l is the amplitude decay time constant related to the power leaving the ring through absorption, surface scattering and radiation losses

The total loss decay time τ is defined by

$$\frac{1}{\tau} = \frac{1}{\tau_e} + \frac{1}{\tau_d} + \frac{1}{\tau_l}$$

Now we can construct the equation that relates these losses with the time rate of change of the energy in the ring.

$$\frac{d}{dt}A = (j\omega_0 - \frac{1}{\tau})A - j\mu s_A \tag{2.8}$$

The factor $-j$ stems from the phase difference between the mode in the microring and the mode in the input waveguide. μ is the factor that controls the coupling between the input bus waveguide and the ring. ω_0 is the resonance frequency of the microring.

The incident and the wave at the pass port are related by

$$s_B = s_A - j\mu A \tag{2.9}$$

The transient behaviour of the microring is now easily described. Consider a microring in which the ring is excited to an energy of $|A_0|^2$ and the incident signal is switched off. The energy in the ring will then decay as

$$|A(t)|^2 = |A_0|^2 exp(\frac{-2t}{\tau})$$

To relate μ with the power coupling coefficient κ (defined in the previous approach) and the loss decay time τ_e we look at the energy decay for a microring with no internal loss and no output bus waveguide. The energy in the ring then decays as

$$|A(t)|^2 = |A_0|^2 exp(\frac{-2t}{\tau_e}) \tag{2.10}$$

The power that is lost, is coupled to port B, contributing to s_B. From the classical approach used before we know that

$$\begin{aligned} |s_B|^2 &= \kappa |a|^2 \\ &= \kappa v_g |A|^2 \frac{1}{2\pi R_r} \end{aligned}$$

The power leaving the ring is the time rate of change of the energy in the ring. The latter is the derivative of equation (2.10). By equating the previous equation with the derivative of equation (2.10) we get:

$$\frac{2}{\tau_e} = \kappa v_g \frac{1}{2\pi R_r}$$

and by using equation (2.9) we get

$$\mu^2 = \frac{2}{\tau_e}$$

From the differential equation (2.8) and equation (2.9) the transfer characteristics in case of a steady state incident signal can be derived.

$$A = \frac{-j\sqrt{\frac{2}{\tau_e}}}{j(\omega - \omega_0) + \frac{1}{\tau}} s_A \tag{2.11}$$

$$s_B = \frac{j(\omega - \omega_0) + \frac{1}{\tau} - \frac{2}{\tau_e}}{j(\omega - \omega_0) + \frac{1}{\tau}} s_A \tag{2.12}$$

$$s_C = \frac{\sqrt{\frac{2}{\tau_e}\frac{2}{\tau_d}}}{j(\omega - \omega_0) + \frac{1}{\tau}} s_A \tag{2.13}$$

The physical understanding on the functionality of microrings is made more difficult by the fact that the incoupling from the bus waveguide is not a pure incoupling, but is at the same time a loss figure. This can clearly be seen in the previous equations.

Q-factor

In this context we can also define the Q-factor. Q-factors are used in different domains of engineering and are usually defined from a time-domain point of view and not a steady-state point of view as done previously. There they are related to the decay time of the energy in the ring.

The Q-factor is ω_0 times the energy stored in the cavity divided by the energy dissipated per cycle. A cycle is the amount of time to travel around the ring once, $T = 2\pi R_r/v_g$ as was explained before.

$$\begin{aligned} Q &= \omega_0 \frac{|A_0|^2}{\frac{1}{T}(|A_0|^2 - |A_0|^2 exp(\frac{-2T}{\tau}))} \\ &= \omega_0 T \frac{1}{1 - exp(\frac{-2T}{\tau})} \\ &\approx \omega_0 T \frac{1}{\frac{2T}{\tau}} \\ &= \omega_0 \frac{\tau}{2} \end{aligned}$$

This is the loaded Q which contains all the different loss contributions. The unloaded Q is defined as

$$Q_{unloaded} = \omega_0 \frac{\tau_l}{2}$$

Q-factors can be defined related to each of the loss factors.

Significance of Q and Finesse

Another to way to look at the Q-factor is the following: say

$$\tau = 2NT \tag{2.14}$$

where N is the amount of cycles needed for the power to decay to $1/e$ and

$$\begin{aligned}\mathcal{F} &= \frac{Q\lambda}{2nL}\\ Q &= \omega_0 \frac{\tau}{2}\end{aligned}$$

then

$$\mathcal{F} = 2\pi N \tag{2.15}$$

The Finesse is a measure of the amount of cycles needed to reduce the power to $1/e$ and the Q-factor is a measure of the number of oscillations the signal makes till it has decayed this much.

Then it is clear that the Q-factor (and the Finesse) are measures for the amount of cycles the light has to travel in the microring before it dies out or alternatively of the photon lifetime in the cavity.

Q, Finesse and field enhancement

One can wonder why the field enhancement and the Q-factor, which are so obviously related, do not show the same behaviour with respect to the coupling coefficient. The field enhancement has a maximum for a particular coupling coefficient and the Q-factor is continuously decreasing. One would assume that the field enhancement would increase with the Q-factor, because the Q-factor is a measure for the photon lifetime in the cavity and the more photons the stronger the field. This is thus not the case. The reason for this is that FE is actually a steady state parameter and the Q-factor a transient one. To define the Q-factor the microring is excited to a certain level and the rate of power decay is considered. In this case, scatter loss, radiation loss and the two coupling coefficients are all loss figures. In the case of the FE the incoupling coefficient is both a loss and a gain factor where an optimum has to be found between the two. In the case of a lossless symmetrical microring, the FE is proportional to Q, they are both continously decreasing with the coupling factor. This is the same for an overcoupled microring resonator. When the coupling is high enough to have compensated for the internal losses in the microring, any further increase in the coupling coefficient is a pure loss figure, causing both the field enhancement and the Q-factor to decrease.

Bibliography

[1] C. Vassallo. *Optical waveguide concepts*. Elsevier, 1991.

[2] M. Hammer et al. *Microresonators as building blocks for VLSI photonics*, chapter Microresonator devices, pages 48–72. International school of Quantum electronics, 39th course. American Institute of Physics, 2004.

[3] B.E. Little et al. Micoring resonator channel dropping filters. *Journal of Lightwave Technology*, 15(6):998–1005, June 1997.

[4] C.K. Madsen and G. Lenz. Optical all-pass filters for phase response design with applications for dispersion compensation. *IEEE Photonics Technology Letters*, 10(7):994–996, July 1998.

[5] Otto Schwelb et al. Transmission, group delay, and dispersion in single-ring optical resonators and add/drop filters - a tutorial overview. *Journal of Lightwave Technology*, 22(5):1380–1394, May 2004.

[6] G. Lenz et al. Dispersive properties of optical filters for WDM systems. *IEEE Journal of Quantum Electronics*, 34(8):1390–1402, August 1998.

[7] M.-A. Amann and J. Buus. *Tunable laser diodes*. Artech House Optoelectronics library, 1998.

[8] Manoulatou et al. Coupling of modes analysis of resonant channel add-drop filters. *IEEE Journal of Quantum Electronics*, 35:1322–1331, 1999.

Chapter 3

Microring resonators: fabrication and applications

In the previous chapter the basic functionality of microring resonators has been explained. This chapter will focus on the different possibilities and difficulties for fabrication, the choice of material system and a review of applications reported in literature.

3.1 Fabrication

3.1.1 Introduction

There are two different fabrication possibilities: laterally coupled and vertically coupled microring resonators. In the laterally coupled approach the microring and the bus waveguides are in the same plane, in the vertically coupled approach the bus waveguides are underneath or above the microring (Fig. 3.1).

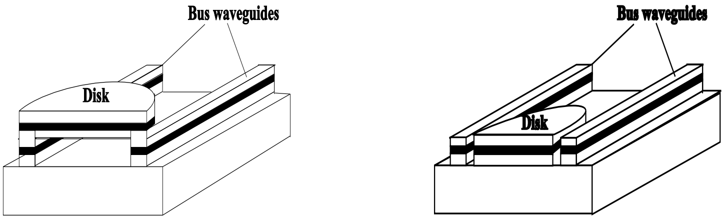

(a) Vertical coupling

(b) Lateral coupling

Figure 3.1: Vertically and laterally coupled microring resonators

The main reason for choosing a vertically coupled approach is the increased control over the power coupling coefficient compared to the laterally coupled approach. The explanation for this is the following: when fabricating small microrings, bends are sharp and care has to be taken to avoid high radiation losses from the bend (see Chapter 5). The most common approach to this problem is to etch the bend very deeply which creates a high index contrast and minimizes radiation losses. The downside to this approach is the high confinement of the mode in the ring and thus difficult coupling to the straight waveguide in the lateral direction.

In the laterally coupled approach the gap between the microring and the bus waveguides usually has to be made quite small (submicron) in order to ensure sufficient coupling. This gap is lithographically defined and usually has to be etched quite deep. The coupling coefficient depends exponentially on the size of the gap and is very difficult to control. Depending on the lithography tool used, for very small gaps processing can fail and fused coupling sections are inadvertently created. To avoid this problem the vertically coupled approach was developed. In this case the layer structure contains two waveguide core layers: one for the bus waveguides and one for the ring. The power coupling is mainly determined by the distance between these two. Because the thickness of this layer is determined by the highly accurate epitaxial growth or depostion, coupling can be controlled more easily than in the laterally coupled approach.

To illustrate this the field profiles of the straight and bend waveguide in a vertically coupled and a laterally coupled configuration have been plotted in Fig. 3.2. This was for a typical InP layer structure and a 20 μm radius bend. It is clear that the field overlap in the laterally coupled configuration is very low even in the case shown here where the gap is only 200 nm wide. The field overlap can be greatly increased in the vertically coupled layout, the main reason for this is that the index contrast in the vertical direction is much lower compared to the index contrast in the horizontal direction.

A first downside to the vertically coupled approach is the increased complexity in processing because wafer bonding, regrowth or re-deposition is required to fabricate these devices. In this work we have focused on the vertically coupled approach with wafer bonding. The details of this wafer bonding process will be described in Chapter 4. Another downside is the fact that two lithography steps are required: one to define the straight waveguides and one to define the ring. These two have to be aligned with each other and this alignment influences the coupling coefficient. This is an issue that does not arise in lateral coupling where the whole microring resonator is defined in one lithography step.

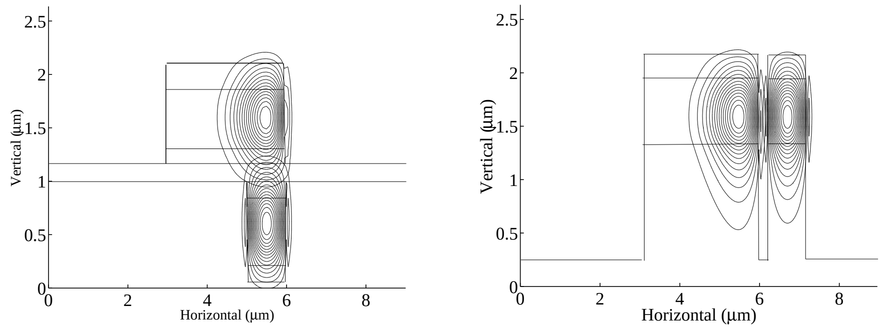

(a) The field profiles in vertical coupling

(b) The field profiles in horizontal coupling

Figure 3.2: The field profiles in a vertically and horizontally coupled layout

	Horizontally coupled	Vertically coupled
Control of coupling coefficient	low	high
wafer bonding or regrowth	no	yes
Lithography	e-beam or deep UV	normal I-line
Design constrictions	some	less
Alignment issues	None	Some

Table 3.1: The advantages and disadvantages of horizontally and vertically coupled microring resonators

However, the vertically coupled approach also opens up possibilities for more complex designs. Because the waveguide core layer and the ring core layer do not have to be identical an extra degree of freedom in design is added allowing, for instance, active-passive integration. The advantages and disadvantages of both techniques have been summarized in Table 3.1.

The vertically coupled approach was first introduced for microrings fabricated in glass where 'regrowth' or rather redeposition of SiO_2 layers is not as cumbersome as regrowth for III-V devices. The idea was then transferred to III-V's by Absil [1] for GaAs and by Grover [2] for InP using polymer wafer bonding. Tishinin [3] was the first to fabricate vertically coupled microring resonators in InP by direct wafer bonding.

3.1.2 Lateral coupling

Microring resonators were first fabricated in the lateral configuration. This only requires one lithography and etch step but as explained before accurate

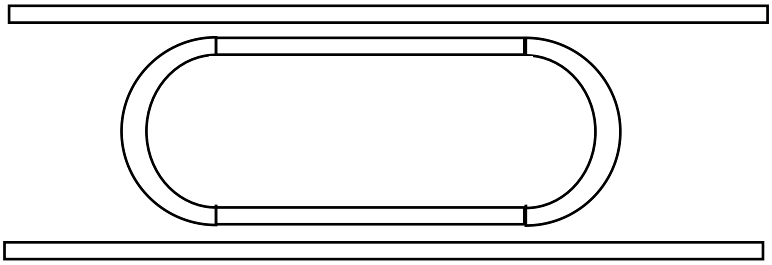

Figure 3.3: The layout of a racetrack resonator

lithography and etching is required to fabricate small rings. To increase the coupling coefficient a racetrack configuration is often used (Fig. 3.3). This of course also increases the circumference of the resonators and decreases the FSR. Also extra loss is induced at the transition between straight waveguide and bent waveguide.

Another way of increasing the coupling coefficient whilst avoiding increasing the FSR was proposed by Chin [4]. For this purpose the bus waveguides are bent around the microring. This is illustrated on Fig. 3.4 where an SEM picture of a 'bend-coupled' SOI ring resonator fabricated at our lab can be seen [5]. This was to our knowledge the first demonstration of this principle. The clear improvement in coupling efficiency is proven by the fact that similar microring resonators (with radii of 5 and 8 μm) coupled to straight waveguides did not function due to insufficient coupling and the bend-coupled microrings showed clear filtering with extinction ratios up to 15 dB.

3.1.3 Vertical coupling

In Fig. 3.5 the different steps in the fabrication of vertically coupled microrings with wafer bonding have been illustrated. The epitaxial layerstructure contains two waveguide core layers and an etchstop layer for the substrate removal, Fig. 3.5(a). In this epi-wafer the straight bus waveguides are lithographically defined and etched, Fig.3.5(b). The whole structure is flipped upside down and bonded onto a transfer substrate. The original substrate is removed by a combination of mechanical thinning and chemical etching which stops on the etch stop layer, Fig. 3.5(c). The etch stop layer is then removed and the ring resonator is lithographically defined and etched resulting in the finished component, Fig. 3.5(d).

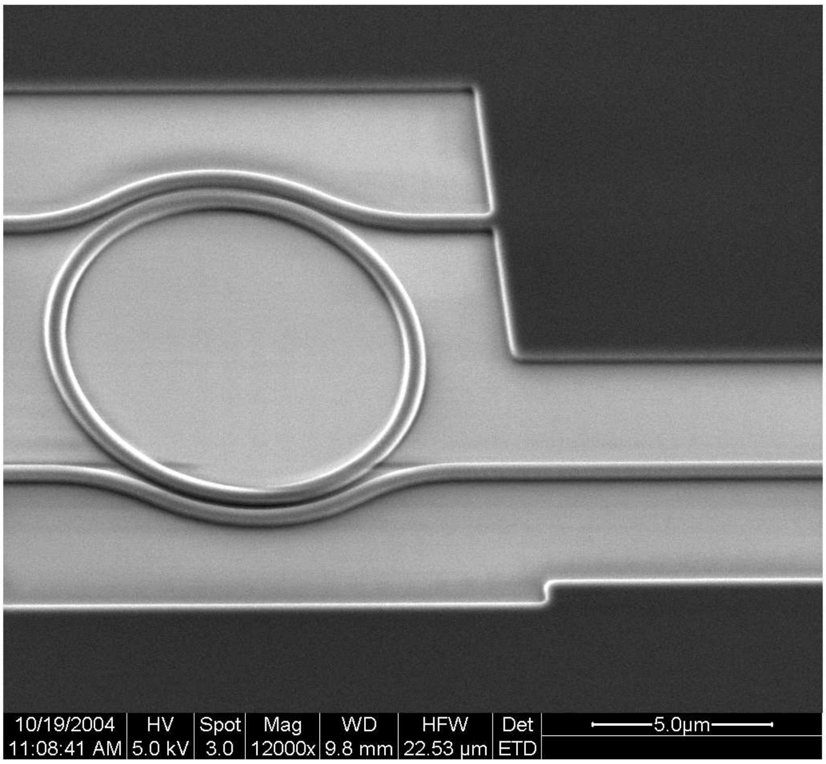

Figure 3.4: A 'bend-coupled' microring resonator in SOI

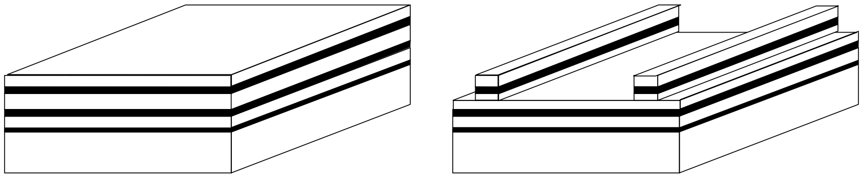

(a) The epitaxial layerstructure

(b) The etching of the bus waveguides

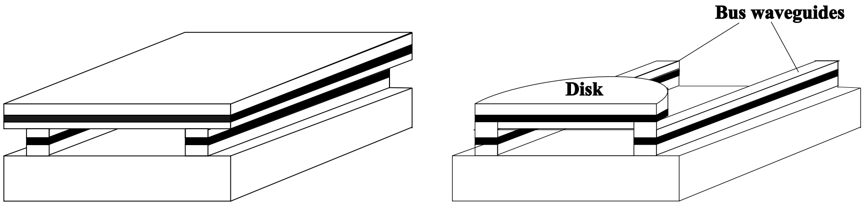

(c) The wafer bonding and substrate removal

(d) The vertically coupled microring resonator

Figure 3.5: The processing sequence for vertically coupled microring resonators fabricated with wafer bonding

Vertically coupled microring resonators can also be fabricated by epitaxial regrowth (e.g. in InP [6]) or etching and deposition by sputtering (e.g. SiO_2 [7]) in which case the processing is as in Fig. 3.6.

3.2 Material systems

Many different material systems are available for the fabrication of microrings. We will summarize the most important ones, comment on some of the advantages and disadvantages of the material and review what has already been fabricated and with what performance.

3.2.1 Overview

In Table 3.2 the properties of different material systems are summarized. Additional comments on each of the material systems can be found in the following paragraphs.

The numbers for the refractive index profiles indicate the core and the cladding index. For the lateral index difference air clad devices are usually considered so this is the highest achievable index contrast. All refractive indices are for wavelengths around 1.55 μm.

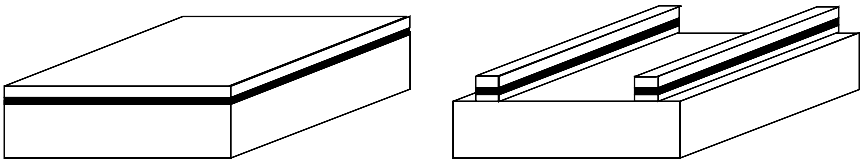

(a) The layerstructure (b) The etching of the bus waveguides

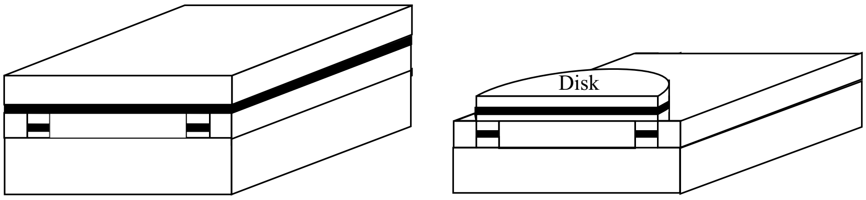

(c) The regrowth (d) The vertically coupled microring resonator

Figure 3.6: The processing sequence for vertically coupled microring resonators fabricated with regrowth

The vertical index contrast for polymers can depend on the substrate on which it is spun, usually this is SiO_2 deposited on a Si substrate, the refractive index of the oxide is 1.44.

The achievable index contrasts in both the lateral and the vertical direction relate directly to the minimum radius that can be attained with negligible bending loss but also to the scatter loss (see Chapter 5). Refractive index differences should not be too low so that fabriction of rings with small radii and neglible radiation loss is possible. At the same time the refractive index difference should not be too big so as not to create too much scatter loss.

The next parameter describes whether light generation is possible in the material system (this is what we refer to as active material) and whether and how the material can be tuned. We consider the three classical tuning mechanisms: 1): thermo-optic 2): electro-optic 3): carrier injection

Another important thing to consider is of course also the maturity of the processing in the different material systems.

3.2.2 GaAs and InP

The classic III-V material systems InGaAsP on InP and AlGaAs on GaAs have been used frequently to fabricate microrings, both in the vertically and the laterally coupled configuration. The main reason why these materials are

Material system	Vertical index contrast	Lateral index contrast	gain?	tuning
InP	3.4-3.16	3.4-1	yes	1-2-3
GaAs	3.4-3.16	3.4-1	yes	1-2-3
Glass	1.8-1.44	1.8-1	no	1
Polymers	1.5-1.44	1.5-1	no	1-2
SOI	3.47-1.44	3.47-1	no	1-(2-3)
SiON	2.2-1.44	2.2-1	no	1
hydex	25%	25%	no	1

Table 3.2: Some material parameters

interesting is because active components, such as lasers can be fabricated in them.

The downside to these materials is the fact that for 'normal' ring radii (10 to 30 μm) the lateral index contrast is too high because they are air-clad. It could be a lot lower and still achieve negligible radiation loss, and the scatter loss would then drop significantly.

Buried rings are not really an option either because they would exhibit too low an index contrast for small microrings. Choi [8] fabricated buried microrings in InP with good performance but with a radius of 200 μm.

3.2.3 Glass

A lot of the first microrings were made on glass and high integration density e.g. arrays of rings was first demonstrated in this material [9, 10, 11]. Usually these components are vertically integrated and fabricated by etching and deposition by sputtering of SiO_2 and SiO_2/Ta_2O_5 and are relatively cheap to make. More details on the fabrication can be found in ref. [7].

The resonators usually have buried bus waveguides with cores of, for instance, SiO_2/ Ta_2O_5 and claddings of SiO_2. The refractive index of the core can be tuned by changing the ratio of the two compounds. The ring has an air cladding which leads to a higher refractive index contrast (for instance 1.8 to 1). This is not so high but rings with radii down to 10 μm can still be fabricated with good performance. Components which are vertically integrated but contain 3 instead of 2 core layers have also been demonstrated in this material system allowing for further freedom in design [12].

The downside to this material system is the difficulty to fabricate active components. Glass can be made active by adding Er doping but optical pumping is needed then. Emission of light is not possible and only limited tuning capabilities, for instance thermo-optically, exist.

3.2.4 Polymers

Polymers have received increasing attention lately. They allow for relatively easy and cheap processing because they can be deposited by spin coating and do not require expensive epitaxial growth techniques. Several microring resonators have already been fabricated with polymers both with classical lithographical techniques [13, 14] and with nano-imprint [15] or soft lithography replica molding [16]. Due to the larger cross section of the waveguide coupling to optical fibers is easier.

There is a huge variety in polymer materials and microring resonators have been fabricated in quite some different materials such as benzocyclobutene, SU-8, polystyrene, . . . already. Their refractive index is usually quite low, around 1.5. The maximum lateral index difference is thus quite limited but small devices have been fabricated nevertheless. The vertical index contrast depends on the substrate used, often this is SiO_2 or another polymer. To increase the vertical index contrast sometimes the SiO_2 on which everything is spun, is underetched to created pedestal underetched polymer waveguides that have a lower cladding that is partially air.

Both vertically coupled and laterally coupled devices exist. No light-generating devices can be fabricated but both electro-optical [17] and thermo-optical tuning is possible. Electro-optic polymers exist and results on microrings in these devices have been reported, but they were quite large due to the low index contrast used (radius of 300μm or more). Polymers which exhibit non-linear optical behaviour also exist and this has great potential but non-linear effects in microring polymers have to the author's knowledge not yet been demonstrated in microring resonators. Apart from the fact that no gain can be introduced using polymers, they are also not very reliable yet and tend to show hysteresis when subjected to a thermal cycle.

3.2.5 SOI, SiON, . . .

Silicon based technology is very mature for electronic purposes. A lot of this technology can be transferred to the fabrication of devices for photonics. This makes it very interesting for very small and highly integrated devices such as microrings. Silicon-on-insulator (SOI) has a layer structure consisting of a Si substrate, an oxide layer and a thin Si layer. When used for optical purposes, light is guided in the top Si layer and confined by air on the top and the oxide layer on the bottom. The thickness of the oxide layer can be varied to increase vertical confinement. SOI can provide a high index contrast in the vertical and in the lateral direction which allows for the fabrication of very sharp bends. A few groups have made ring resonators in SOI [18, 19]. Vertically coupled microrings in Si have recently been reported [20] also.

Another material system that has been used for microrings, is SiON [21], [22]. Here the light is guided in a thin SiON layer instead of a thin Si layer as is the case in SOI. The refractive index contrast depends on the composition of the SiON. The highest refractive index is the one for SiN, n=2.2. Stresses have to be taken into account when combining several materials in this system and the material system tends to suffer from significant intrinsic absorption loss.

The downside to these material systems is the fact that emission of light is not possible. Tuning possibilities are limited to thermo-optic tuning but tuning by carrier injection and by electro-optic effects has been suggested.

3.2.6 Hydex

Hydex is a patented glass-like material system used by the company Little Optics. It has low propagation loss and produces low stress films. Higher order filters with up to 11 ring resonators and with good performance have been demonstrated [23, 24], but apart from thermo-optic tuning no tunable or active devices can be fabricated. Exact numbers for the refractive indices were not found, the refractive index difference can be tuned from 1% to 25%.

3.2.7 Devices

To have some idea of the current state of the art in passive microrings we have summarized some results for the different material systems in Table 3.3. These are not necessarily the best results ever reported. If a certain parameter is not mentioned it was not in the paper and could not be deduced from other values. This is mostly the case for the extinction ratio ER.

3.3 Applications

In this section we will briefly address some of the applications for microring resonators. This is by no means a complete summary but it will demonstrate the extreme versatility of microring resonators.

3.3.1 Basic applications

Most of these basic applications have been discussed in the previous chapter.

Material system	FSR (nm)	radius (μm)	Finesse	lateral/ vertical	ER (dB)	ref
InP	10	12	50	vertical		[25]
	21	5	91	lateral	-10	[26]
GaAs	21.6	5.25	120	lateral	-3	[27]
	11.14	10	22.28	vertical	-12	[1]
Polymers	7.5	32	117	vertical		[13]
	23.7	10	192	lateral	very low	[14]
	17.6	10 (racetrack)	21	lateral	-1	[14]
SOI	14	5 (racetrack)	28	lateral	-24	[18]
	24	3(racetrack)	28	lateral	-7	[19]
	≈ 5	30	$\approx$145	lateral	-22	[28]
	≈ 8	20	$\approx$715	lateral	-15	[29]
Glass	6	40	40	vertical		[30]
	20.1	10.35	34	vertical		[10]
SiON	8	25	182	lateral	-3	[21]
	29	5	24	vertical	-18	[31]
hydex	$\approx$4	40		vertical		[23]

Table 3.3: Some device characteristics

All-pass filter

The all-pass configuration is actually a regular microring resonator but with only one bus waveguide. As stated before the formulas for this kind of device are the same as for an asymmetrically coupled resonator where κ_2=0. In this configuration the ring can be used as a phase filter or as a notch filter depending on the loss.

- Phase filter

  In a phase filter the loss has to be kept as low as possible. The goal is to have an amplitude response that is unity over the entire wavelength range so that the filter only affects the phase of the signal. As we have shown before, at resonance the signal has a phase change of π. This can for instance be used in dispersion compensation [32]. This has been incorporated in one arm of a Mach-Zehnder interferometer creating a notch filter [33, 34].

- Notch filter

  In a notch filter one tries to achieve critical coupling which means that the extraction from the input waveguide at resonance is perfect. For this the coupling coefficient has to be precisely matched to the loss as was explained before. This was demonstrated by Grover in InP [35] where a 25 dB extinction ratio was achieved and in GaAs by Absil where a 20 dB extinction ratio was achieved [33]. As shown before this critically coupled situation also presents a very high field enhancement so this configuration is also used in non-linear experiments.

Add-drop filter

The add-drop functionality is the most basic of all. Multiple rings can be cascaded to achieve a multi-wavelength add-drop filter [10].

3.3.2 Higher order filters

As we discussed previously the Lorentzian line shape of the response of the microring resonator does not allow to satisfy all needs. By cascading ring resonators higher order filters can be achieved. In all these compositions the FSR can be expanded by using the Vernier-effect.

Serially coupled microring resonators

An example of serially coupled microrings can be seen in Fig. 3.7. The response of this kind of cascading of rings can be calculated by means of coupling of modes in time as demonstrated by Little [36]. By cascading the microrings in this way flat top and a steeper roll-off can be achieved. The coupling coefficient between the different rings has a great influence on the resulting response and is not easy to control. Sometimes racetrack resonators are used instead of normal microring resonators to alleviate this problem.

Another critical issue is that the resonances of different rings have to be well aligned. Examples of this can be found in ref. [37] for GaAs and in ref. [23] for Hydex, where filters up to the 11th order have been demonstrated.

Yanagase has shown box-like filter response and higher FSR by a triple coupled ring resonator filter in a Si/SiO2 material system. The rings were vertically coupled to the bus and to each other thus allowing increased control over the coupling [30]. MMI-coupled ring resonators in InP have been demonstrated by Rabus [38].

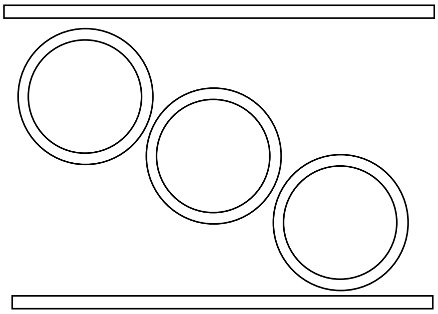

Figure 3.7: Serially cascaded microrings

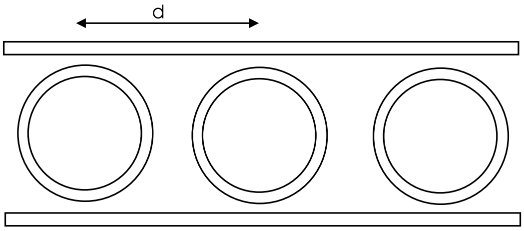

Figure 3.8: Parallel cascaded microrings

All kinds of filters can be synthesized by proper choices of the coupling coefficients. Several papers and books are dedicated to this subject ([39],[11], [40]).

Parallel

Parallel cascaded microrings are arranged as in Fig. 3.8. In this arrangement the roll-off can become steeper and the top flatter than is the case for the single ring. The distance d has to be controlled well to have the waves from the drop port of each microring interfere constructively. This is the major drawback of this design because the proper choice for this distance is wavelength and temperature dependent. The requirement that the resonances of each ring be strictly identical is more relaxed here compared to the serially coupled rings. Nonaligned resonant frequencies now lead to multiple peaks or ripple in the line shape. The FSR can be increased by the Vernier effect if the distance d between the different rings is chosen properly. This has been demonstrated in III-V materials by Grover [41] and in glass by Chu [9].

A theoretical discussion on the synthesis of filters by parallel ring resonator can be found in refs. [42] and [43].

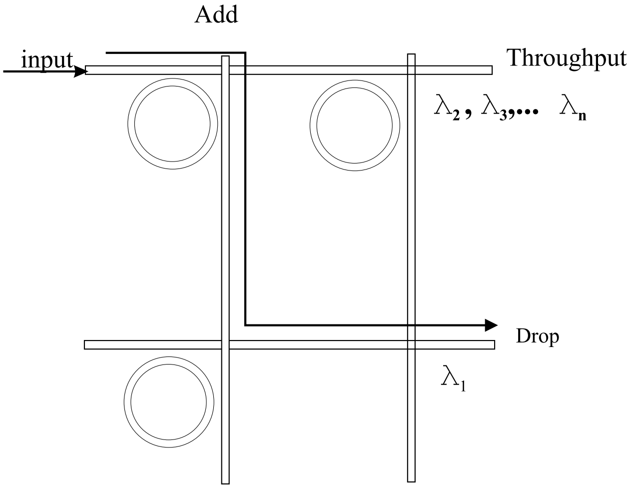

Figure 3.9: Multiple rings coupled via the bus waveguide

Coupling via the bus

This is a kind of serial coupling of the microrings but via the bus waveguides. An example is shown in Fig. 3.9. This is also an example of what this kind of configuration is mostly used for, namely crosstalk reduction and spectrum clean-up in add-drop filters that can drop multiple wavelengths. This has been fabricated in glass [10, 44].

3.3.3 Tunable filters and switching

One of the most interesting things to do with microrings is make them tunable: by this we mean either altering their refractive index thereby shifting the resonance on a wavelength scale or altering their absorption, thereby changing their response. Both of these tuning mechanisms will be discussed followed by an overview of the different physical effects used to realize them and an overview of the reported work, which is predominantly on InP-based devices. A theoretical discussion on these forms of tunings can be found in ref. [45].

Tuning, shifting the refractive index

Tuning the refractive index is commonly known. It is clear from Chapter 2 that altering the refractive index causes the resonances to shift wavelength and causes the FSR to change.

Loss- and gain-trimming

Another way of tuning, less commonly used for other components than ring resonators, is by means of the absorption or gain. By inducing more loss or adding gain the resonator response can be influenced greatly. This can be understood quite intuitively from the coupling of modes in time analysis (section 2.6) where the resonator is treated as a lumped element, a reservoir of energy, and the response is determined by the flow of energy into and out of this reservoir. This is interesting for post-production trimming. Designs of certain higher order filters are very sensitive to the coupling coefficients between the filters and this accuracy can often not be achieved in production. By altering the loss of the different microrings the desidered overall response can still be achieved. In general, as described by Little [46], both gain and loss should be manipulated to achieve any wanted filter function. Often only loss mechanisms are available. It is however possible to include gain sections in the microring to overcome the intrinsic loss. This has been demonstrated by Menon [47], Rabus [48] and Djordjev [49]. By adding gain the resonator can be brought from an undercoupled state to a critically coupled state and the Q-factor can be increased considerably. This is illustrated in Fig. 3.10 where the drop and the pass port of a symmetrically coupled microring resonator are shown. The internal loss in the resonator was 5/cm. When a gain of 5/cm is applied, making the resonator lossless, the dropped power is unity. When the gain is increased further (but not too much or the ring will start lasing) both the dropped and the passed power increase further. By increasing the loss in the ring, the dropped power can be brought down to zero, the passed power is still 60%. In this way the loss/gain can be used to create a switch.

Physical mechanisms

- Thermo-optic tuning

  Thermo-optic tuning is performed by heating the component and in this way changing the refractive index of the material and thus shifting the resonances. This is a fairly slow phenomenon but can be used to trim resonances because it is very difficult to fabricate devices with exactly predefined resonant wavelengths. This was demonstrated in InP [50] and polymers [13] among others. The influence on the absorption is negligible.

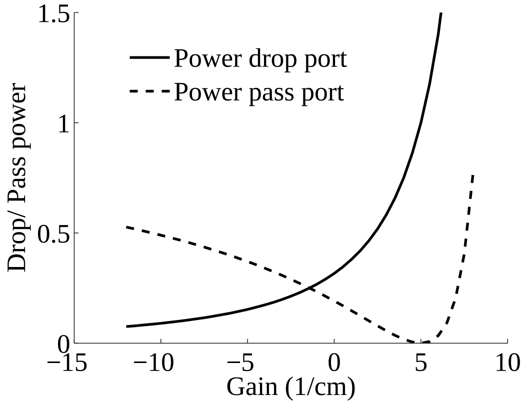

Figure 3.10: An example of loss/gain-trimming

- Electro-optic tuning

Electro-optic tuning changes the properties of the material by applying an electric field. Depending on the design of the device this can predominately alter the refractive index or the absorption.

To mainly achieve changes in the refractive index the bandgap wavelength of the core material should be chosen far enough away from the signal wavelength. In III-V materials this is quite a weak effect but very fast. This has been demonstrated by Grover [2] to tune a laterally coupled notch filter in InP. A tuning of 0.8 nm could be achieved by applying 8V over the device. Higher voltages induced significant losses. This effect is thus quite small and high quality rings have to be used with narrow peaks to achieve usefull functionality.

When the bandgap of the quantum wells is chosen closer to the signal wavelength, absorption becomes important. By applying a small electric field a high change in loss can be induced. The downside is that care has to be taken not to have too high an absorption at zero bias. The extra loss can be used to suppress the resonant power transfer and by switching the field on and off a switch can be created, the dropped power can be controlled. This was first demonstrated in InP by Djordjev [51].

Electro-optic tuning of microrings has also been demonstrated for polymers [13] with a tuning efficiency of 0.82 GHz/V.

- Carrier injection

  A more common approach (at least for InP) is using free carrier injection to alter the refractive index and the absorption/gain. The advantage of using carrier injection is that gain can be introduced. Several approaches have been demonstrated to introduce gain in the cavity.

  First of all a gain section can be incorporated by etching and regrowing part of the cavity [48]. Another approach is to use a vertically stacked asymmetric twin waveguide structure. This structure comprises passive waveguiding layers and active layers on top. The active layers are removed for most of the ring cavity. In a small section they are still present and the light is guided to the active section by means of lateral tapers [47]. It is of course also possible to make the entire cavity active [49] which is quite an evident approach in a vertically coupled layout.

  The previous three references all show the possibility of changing the response of the microring: the extinction ratio, the Q-factor and the maximum transmission. The microring can be switched between dropping and transmitting a signal by changing the loss. Choi [52] reports on the fabrication of an eight-channel switch array with microrings of different radii that extract different wavelengths and can be switched on and off individually. This is behaviour observed close to the bandgap of the core material.

  For wavelengths further away from this bandgap the main effect is just a change of the refractive index and a shift of the resonant wavelengths. Choi used this effect to tune a microring with QW active region over 2.7 nm [53] for 5 mA of input power. The same was done for a bulk active region by Djordjev [54] who reached a tuning range of 2 nm for 5 mA injected current. In both cases the maximum achievable wavelength shift was limited by the counter-acting thermo-optic effect illustrating the importance of proper heatsinking. The effect was also used to tune a filter comprised of 2 rings coupled via the bus waveguide [55]. The tuning was used to accurately align the resonances of the different rings.

  By introducing enough gain microdisk lasers can be fabricated as discussed in the next section.

3.3.4 Microdisk lasers

Ring lasers is a term frequently encountered in literature. However this usually has nothing to do with the microrings discussed here but with fiber lasers, or laser setups in a ring configuration, or very high Q resonators that are not coupled to bus waveguides and are optically pumped. Single InP vertically coupled microdisk lasers were first reported by Choi [56]. They have high Q-factors and show CW- operation. The output power was however very low (order of tens of μW) and unless cooled to below 5 °C, mode hops appeared when the driving current was increased. These lasers have also been fabricated in an array of 8 microdisk lasers with slightly different radii coupled to a common bus waveguide [57].

Hill [58] demonstrated the use of two coupled microring lasers to fabricate an all-optical memory element.

3.3.5 Lasers with passive microrings

Another interesting application of microring resonators is as wavelength-selective elements in lasers.

For a start, we shall review the influence of adding one passive ring to a laser cavity [59, 60]. The design of a laser with a microring as wavelength selective element can have several advantages over more classical approaches such as the DBR laser. First of all the high Q of the microring can provide for high side mode suppression. This high Q also increases the effective cavity length enormously, thereby reducing linewidth and chirp. However as in all designs compromises have to be made and careful consideration has to be given to several factors. The first one is the compromise to be made between high Q and high maximum transmission by choosing an appropiate coupling coefficient. A higher maximum transmission decreases the threshold gain.

The size of the microring also has to be small enough so that the FSR is large enough to span the material gain bandwidth.

Park [61] reported on the fabrication of a laser laterally integrated with one microring in an all-active layout where the ring was pumped separately to transparency.

This can be expanded to the case where two microrings are integrated with the laser (or one ring and one other wavelength filter). Widely tunable lasers use the Vernier effect between two tunable wavelength filters to span a wide wavelength range. The principle is that two wavelength filters are used with a slightly different FSR. Only when the two comb filters have a peak at the same wavelength a significant transmission is achieved. By tuning one of the filters over a limited wavelength range a large jump in total tuning range can be achieved. The tuning enhancement is defined as the ratio of the wavelength change of the tunable laser to the wavelength change one of the filters was tuned by. An extensive review on tunable laser diodes can be found in ref. [62]. Up till now the wavelength filters in tunable lasers are mostly sampled gratings (SG), super structure gratings (SSG) and grating assisted codirectional couplers (GACC).

Several designs using microrings as wavelengths selective elements in tunable lasers can be considered, the first choice being either to use two ring resonators in the laser or one ring and one other filter. If one choses to use two microrings, multiple layouts can still be thought off. The advantages of using microrings are numerous [63].

First of all the ring is a transmissive element which allows to put all the wavelength selective elements on one side of the cavity. The other facet can then be used for outcoupling. This has the advantage that the laser light does not have to pass through a section that is being tuned before exiting which improves the stability of the output power.

Due to the high Q-values possible in rings and the fact that they have a comb-like transmission spectrum with uniform transmission over a very large wavelength range the tuning enhancement is very high. The FWHM of the transmission of the microring can easily be subnanometer, while it is normally in the range of a few nm for SG and SSG's. Therefore only small tuning of the rings is necessary to achieve a large tuning range of the laser.

The achieveable tuning enhancement is mostly limited by the loss in the microring which should be as low as possible. When loss is introduced, the threshold gain rises. This can be compensated again by higher coupling but this in turn broadens the peaks of the filter which could compromise the side mode suppression ratio (SMSR) of the laser. This is the ratio of the power in the dominant mode of the laser to the power in the strongest side-mode. If the peaks of the microring filters are too wide, the combined filter characteristic of the two rings can contain transmission peaks other than the dominant one that carry significant power. To prevent this the difference between the FSR of the two rings should be increased, reducing the achievable tuning enhancement.

The analysis by Liu [63] clearly shows that a tuning enhancement factor of 40 is possible for this design which is far larger than for conventional tunable laser designs where the value is around 6 to 8 [64]. However, the total tuning range achievable now is still hampered by the limited tuning of the individual microrings that has been demonstrated so far. This should be improved first. If the tuning range of the individual ring is quite small, the tuning enhancement has to be large to achieve a large tuning range, which means the difference in peak spacing has to be larger, and the difference in peak spacing should be comparable to the width of the reflection peaks. If the difference in peak spacing is too large, there is a region where the laser frequency is unpredictable during tuning. If it is too small, the overlap of

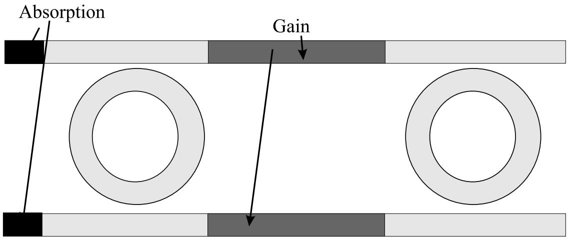

Figure 3.11: A possible layout for a tunable laser with 2 microrings

adjacent reflector peaks is too large and side mode suppression is not large enough.

However with the tuning range currently available, quite widely tunable lasers should already be possible, not record breaking but with very good linewidth. A possible layout for this kind of laser can be seen in Fig. 3.11.

3.3.6 Non-linear effects

As shown in the previous chapter microring resonators can have a very high field enhancement. Due to the very high field in the ring nonlinear effects can be studied. This usually starts off with the study of optical bistability: the large field in the ring induces changes in the refractive index causing optical bistability. The effect can be purely thermal but other effects such as electro-optic effects can also take part. Optical bistability in microrings has been demonstrated in different material systems such as SOI [65], GaAs [66], polymers, . . .

As a consequence of this bistability, self-switching of the microring can be observed, which only requires limited switching power due to the high field enhancement. This means that when the power in the microring is increased for a resonant wavelength, the refractive index (that has an intensity dependent component) changes and the rings moves out of resonance.

More useful is a similar effect but in a pump and probe configuration. Here a pump beam is tuned to one resonant wavelength and by switching it on and off it pulls a signal beam (the probe beam) in and out of resonance. This allows the fabrication of an all-optical switch. Even the fabrication of all-optical logic gates is possible in this way. The theoretical side of this is discussed by Van [67]. Experimental work is presented by Van [67], [68] and Ibrahim [69], [70]. Microrings have also been used for all-optical wavelength conversion in GaAs [71], [72] An more extensive review of non-linear effects in microrings can be found in the PhD of Ibrahim [66].

3.4 Conclusions

In this chapter the different fabrication possibilities and choices of material systems for microring resonators were reviewed together with there advantages and disadvantages. A comparison of the specifications of passive microrings in different material systems provides an overview of the state of the art. Finally an overview was given of some of the different applications for microrings demonstrating their versatile nature.

Bibliography

[1] P. P. Absil et al. Vertically coupled microring resonators using polymer wafer bonding. *IEEE Photonics Technology Letters*, 13(1):49–51, January 2001.

[2] R. Grover et al. A tunable GaInAsP-InP optical microring notch filter. *IEEE Photonics Technology Letters*, 16(2):467–469, February 2004.

[3] D. V. Tishinin et al. Vertical resonant couplers with precise coupling efficiency control fabricated by wafer bonding. *IEEE Photonics Technology Letters*, 11(8):1003–1005, August 1999.

[4] M. K. Chin and S.T. Ho. Design and modelling of waveguide-coupled single-mode microring resonators. *Journal of Lightwave Technology*, 16(8):1433–1446, August 1998.

[5] Pieter Dumon, Ilse Christiaens, et al. Microring resonators in Silicon-on-Insulator. In *European Conference on Integrated Optics*, 2005.

[6] Seung June Choi et al. Microring resonators vertically coupled to buried heterostructure bus waveguides. *IEEE Photonics Technology Letters*, 16(3):828–830, March 2004.

[7] B.E. Little et al. Vertically coupled glass microring resonator channel dropping filters. *IEEE Photonics Technology Letters*, 11(2):215–217, February 1999.

[8] Seung June Choi et al. Laterally coupled buried heterostructure high-Q ring resonators. *IEEE Photonics Technology Letters*, 16(10):2266–2268, October 2004.

[9] Sai T. Chu et al. Second-order filter response from parallel coupled glass microring resonators. *IEEE Photonics Technology Letters*, 11(11):1426–1428, November 1999.

[10] Sai T. Chu et al. An eight-channel add-drop filter using vertically coupled microring resonators over a cross grid. *IEEE Photonics Technology Letters*, 11(6):691–693, June 1999.

[11] Brent E. Little. Advances in microring resonators. In *Integrated Photonics Research, Washington, USA*, 2003. www.littleoptics.com.

[12] Yutaka Hatakeyama et al. Loss-less multilevel crossing of busline waveguide in vertically coupled microring resonator filter. *IEEE Photonics Technology Letters*, 16(2):473–375, February 2004.

[13] Payam Rabiei et al. Polymer micro-ring filters and modulators. *Journal of Lightwave Technology*, 20(11):1968–1975, November 2002.

[14] W.-Y. Chen et al. High-finesse laterally coupled single-mode benzocyclobutene microring resonators. *IEEE Photonics Technology Letters*, 16(2):470–472, February 2004.

[15] Chung-yen Chao and L. Jay Guo. Polymer microring resonators fabricated by nanoimprint technique. *J. Vac. Sci. Technology B*, 20(6):2862–2866, November/December 2002.

[16] Joyce K. S. Poon et al. Soft lithography replica molding of critically coupled polymer microring resonators. *IEEE Photonics Technology Letters*, 16(11):2496–2498, November 2004.

[17] Payam Rabiei et al. Tunable polymer double micro-ring filters. *IEEE Photonics Technology Letters*, 15(9):1255–1277, September 2003.

[18] P. Dumon et al. Low loss SOI photonic wires and ring resonators fabricated with deep UV lithography. *IEEE Photonics Technology Letters*, 16(5):1328–1330, May 2004.

[19] Andreas Vörckel et al. Asymmetrically coupled silicon on insulator microring resonators for compact add-drop multiplexers. *IEEE Photonics Technology Letters*, 15(7):921–923, July 2003.

[20] Prakash Koonath et al. Add-drop filters utilizing vertically coupled microdisk resonators in silicon. In *Leos Annual, Puerto Rico*, page ThA4, 2004.

[21] D.J.W. Klunder et al. Experimental and numerical study of SiON microresonators with air and polymer cladding. *Journal of Lightwave Technology*, 21(4):1099–1110, April 2003.

[22] Andrea Melloni. Ring-resonator filters in silicon oxynitride technology for dense wavelength division multiplexing systems. *Optics Letters*, 28(17):1567–1569, September 2003.

[23] B.E. Little et al. Very high-order microring resonator filters for WDM applications. *IEEE Photonics Technology Letters*, 16(10):2263–2265, October 2004.

[24] B.E. Little. A VLSI photonics platform. In *Optical Fiber Communication Conference 2003*, volume 2, pages 444–445, 2003.

[25] Kostadin Djordjev et al. Study of the effects of the geometry on the performance of vertically coupled InP microdisk resonators. *Journal of Lightwave Technology*, 20(8):1485–1491, August 2002.

[26] Yong Ma et al. InGaAsP thin-film microdisk resonators fabricated by polymer wafer bonding for wavelength add-drop filters. *IEEE Photonics Technology Letters*, 12(11):1495–1497, November 2000.

[27] D. Rafizadeh et al. Waveguide-coupled AlGaAs/GaAs microcavity ring and disk resonators with high finesse and 21.6 nm free spectral range. *Optics letters*, 22(16):1244–1246, August 1997.

[28] Tom Baehr-Jones et al. High-Q ring resonators in thin silicon-on-insulator. *Applied Physics Letters*, 85(16):3346–3347, October 2004.

[29] Jan Niehusmann et al. Ultrahigh-quality-factor silicon-on-insulator microring resonator. *Optics Letters*, 29(24):2861–2863, December 2004.

[30] Yuji Yanagase et al. Box-like filter response and expansion of FSR by a vertically triple coupled microring resonator filter. *Journal of Lightwave Technology*, 20(8):1525–1527, August 2002.

[31] Masashi Ogata et al. Ultracompact vertically coupled microring resonator with buried vacuum cladding structure. *IEEE Photonics Technology Letters*, 17(1):103–105, January 2005.

[32] C.K. Madsen and G. Lenz. Optical all-pass filters for phase response design with applications for dispersion compensation. *IEEE Photonics Technology Letters*, 10(7):994–996, 1998.

[33] P.P. Absil et al. Compact microring notch filters. *IEEE Photonics Technology Letters*, 12(4):398–400, April 2000.

[34] M. Kohtoku et al. 200 GHz FSR periodic multi/demultiplexer with flattened transmission and rejection band by using a mach-zehnder interferometer with a ring resonator. *IEEE Photonics Technology Letters*, 12(9):1174–1176, September 2000.

[35] R. Grover et al. Laterally coupled InP-based single-mode microracetrack notch filter. *IEEE Photonics Technology letters*, 15(8):1082–1084, August 2003.

[36] B.E. Little et al. Microring resonator channel dropping filters. *Journal of Lightwave Technology*, 15(6):998–1005, June 1997.

[37] J.V. Hryniewicz et al. Higher order filter response in coupled microring resonators. *IEEE Photonics Technology Letters*, 12(3):320–322, March 2000.

[38] Dominik G. Rabus et al. MMI-coupled ring resonators in GaInAsP-InP. *IEEE Photonics Technology Letters*, 13(8):812–814, August 2001.

[39] Andrea Melloni et al. Synthesis of direct-coupled-resonators bandpass filters for WDM systems. *Journal of Lightwave Technology*, 20(2):296–303, 2002.

[40] Christi K. Madsen and Jian H. Zhao. *Optical filter design and analysis*. John Wiley & Sons, 1999.

[41] R. Grover et al. Parallel-cascaded semiconductor microring resonators for high-order and wide-FSR filters. *Journal of Lightwave Technology*, 20(5):872–877, May 2002.

[42] Giora Griffel. Synthesis of optical filters using ring resonator arrays. *IEEE Photonics Technology Letters*, 12(7):810–812, July 2000.

[43] Andrea Melloni. Synthesis of a parallel-coupled ring-resonator filter. *Optics Letters*, 26(12):917–919, June 2001.

[44] B.E. Little et al. Microring resonator arrays for VLSI photonics. *IEEE Photonics Technology Letters*, 12(3):323–325, March 2000.

[45] Kostadin Djordjev et al. Active semiconductor microdisk devices. *IEEE Journal of Lightwave Technology*, 20(1):105–113, January 2002.

[46] B.E. Little and Sai T. Chu. Theory of loss and gain trimming of resonator-type filters. *IEEE Photonics Technology Letters*, 12(6):636–638, June 2000.

[47] V.M. Menon et al. Control of quality factor and critical coupling in microring resonators through integration of a semiconductor optical amplifier. *IEEE Photonics Technology Letters*, 16(5):1343–1345, May 2004.

[48] Dominik G. Rabus et al. Optical filters based on ring resonators with integrated semiconductor optical amplifiers in GaInAsP-InP. *IEEE Journal of Selected Topics in Quantum Electronics*, 8(6):1405–1411, November/December 2002.

[49] Kostadin Djordjev et al. Gain trimming of the resonant characteristics in vertically coupled InP microdisk switches. *Applied Physics Letters*, 80(19):3467–3469, May 2002.

[50] Ilse Christiaens et al. Low-power thermo-optic tuning of vertically coupled microring resonators. *IEE Electronics Letters*, 40(9):560–561, April 2004.

[51] Kostadin Djordjev et al. Vertically coupled InP microdisk switching devices with electroabsorptive active regions. *IEEE Photonics Technology Letters*, 14(8):1115–1117, August 2002.

[52] Seung June Choi et al. An eight-channel demultiplexing switch array using vertically coupled active semiconductor microdisk resonators. *IEEE Photonics Technology Letters*, 16(11):2517–2519, November 2004.

[53] Seung June Choi et al. Tunable microdisk resonators vertically coupled to bus waveguides using epitaxial regrowth and wafer bonding techniques. *Applied Physics Letters*, 84(5):651–653, February 2004.

[54] Kostadin Djordjev et al. Microdisk tunable resonant filters and switches. *IEEE Photonics Technology Letters*, 14(6):828–830, June 2002.

[55] Seung June Choi et al. Tunable narrow linewidth all-buried heterostructure ring resonator filters using Vernier effects. *IEEE Photonics Technology Letters*, 17(1):106–108, January 2005.

[56] Seung June Choi et al. Microdisk lasers vertically coupled to output waveguides. *IEEE Photonics Technology Letters*, 15:1330–1333, October 2003.

[57] Seung June Choi et al. Eight-channel microdisk CW laser arrays vertically coupled to common output bus waveguides. *IEEE Photonics Technology Letters*, 16(2):356–358, February 2004.

[58] Martin T. Hill et al. A fast low-power optical memory based on coupled micro-ring lasers. *Nature*, 432:206–207, November 2004.

[59] Bin Liu et al. Passive microring-resonator-coupled-lasers. *Applied Physics Letters*, 79(22):3561–3563, November 2001.

[60] Zhixi Bian et al. InP-based passive ring-resonator-coupled lasers. *IEEE Journal of Quantum Electronics*, 38(7):859–865, July 2003.

[61] Seoijin Park et al. Single-mode lasing operation using a microring resonator as a wavelength selector. *IEEE Journal of Quantum Electronics*, 38(3):270–273, March 2002.

[62] M.-A. Amann and J. Buus. *Tunable laser diodes*. Artech House Optoelectronics library, 1998.

[63] Bin Liu et al. Wide tunable double ring resonator coupled lasers. *IEEE Photonics Technology Letters*, 14(5):600–602, May 2002.

[64] Larry A. Coldren. Monolithic tunable diode lasers. *IEEE Journal on selected topics in Quantum Electronics*, 6(6):988–999, November/December 2000.

[65] Vilson R. Almeida and Michal Lipson. Optical bistability on a silicon chip. *Optics Letters*, 29(20):2387–2389, October 2004.

[66] Tarek A. Ibrahim. *Nonlinear optical semiconductor micro-ring resonators*. PhD thesis, University of Maryland, 2003.

[67] V. Van et al. Optical signal processing using nonlinear semiconductor microring resonators. *IEEE Journal of Selected Topics in Quantum Electronics*, 8(3):605–713, May/June 2002.

[68] V. Van et al. All-optical nonlinear switching in GaAs-AlGaAs microring resonators. *IEEE Photonics Technology Letters*, 14(1):74–76, January 2002.

[69] Tarek A. Ibrahim et al. All-optical AND/NAND logic gates using semiconductor microresonators. *IEEE Photonics Technology Letters*, 10(15):1422–1424, October 2003.

[70] Tarek A. Ibrahim et al. All-optical switching in a laterally coupled microring resonator by carrier injection. *IEEE Photonics Technology Letters*, 15(1):36–38, January 2003.

[71] S. Mikroulis et al. Investigation of an all-optical wavelength converter with reshaping properties based on four-wave mixing in passive micro-ring resonators. *Journal of Lightwave Technology*, 22(12):2473–2478, December 2004.

[72] P.P. Absil et al. Wavelength conversion in GaAs micro-ring resonators. *Optics Letters*, 25(8):554–556, April 2000.

Chapter 4

Wafer bonding

4.1 Introduction

Wafer bonding is a vast area of research. This is understandable because of the enormous amount of applications feasible with this process. The joining of dissimilar materials allows to exploit the advantages of the different materials whilst avoiding their disadvantages, allowing combinations of materials otherwise unattainable with other techniques. One of the best known examples can be found in electronics where wafer bonding allowed the cheap fabrication of SOI wafers.

In essence wafer bonding is the joining of two wafers or two pieces of wafers to each other in a permanent way. The ways to do this is are numerous. In this chapter we will try to give an overview of the different kinds of wafer bonding and then focus on the process developed during this Ph.D.

4.2 Different kinds of wafer bonding

Wafer bonding procedures can roughly be divided into two major groups: bonding with an intermediate layer and without intermediate layer. The latter is called direct bonding or fusion bonding (but a lot of people often do not include anodic bonding in this). When bonding with an intermediate layer, a variety of materials can be used for this ’glue layer’: metals, polymers, spin-on-glass, . . . and names such as adhesion bonding, eutectic bonding, . . . are used depending on the intermediate layer. In the following paragraphs we will review some of the possibilities.

4.2.1 Bonding without intermediate layer

Interaction forces between surfaces

Two surfaces that come into sufficient proximity of each other can interact via the van der Waals attraction forces. These comprise the electromagnetic interaction between two polar molecules, between a polar and a non-polar molecule and between two non-polar molecules. These forces are however quite small and a very flat surface is required to bring the two materials into sufficient contact to achieve good bonding. When the wafers come into very close contact covalent bonds come into play.

To avoid this problem, one of the surface can be made electrically charged by adsorbing or desorbing electrons or ions. The direct Coulombic force between the two surfaces are stronger and do not require the same intimate contact.

A special kind of van der Waals bond which is stronger than most other van der Waals bonds, is the hydrogen bond which deserves some more attention because of its importance in wafer bonding. When a hydrogen atom is bonded to an element which has a large electronegativity (oxygen for instance), the electron cloud of the molecule will shift mostly to the other element, causing a positive charge around the hydrogen atom. An electromagnetic bond can then be formed with a negatively charged part of another molecule. The strength of this bond is larger than that of the other van der Waals forces. This is the origin of the strong attention that is given to hydrophilic and hydrophobic surface preparations. These are surface preparations that make the surface either very attractive or very repellent to water. In the case of hydrophilic surface preparation, usually the surface is covered in some oxide and water spreads easily over the surface. The water helps to start the bonding procedure during room temperature bonding and makes it less sensitive to microroughness. During the subsequent heat treatment the water can react with the surrounding oxide or diffuse away from the surface so that covalent bonds are formed between the surfaces.

Hydrophobic bonding is more sensitive to microroughness because no use can be made of the stronger hydrogen bonds. However in this case no surface oxide is present on the substrate (it was removed by the surface preparation technique, for instance a dip in HF) and after bonding no intermediate oxide is present and true crystal-to-crystal bonding is achieved.

Direct bonding

Direct bonding is a process where two mirror-polished wafers are brought into contact, after which a bond is established by applying pressure and elevated temperature. This process has started off mainly for bonding of silicon wafers for the fabrication of SOI-wafers for electronic purposes. As of the beginning of the 1990's, direct wafer bonding became increasingly popular in the opto-electronics community as an alternative to hetero-epitaxy. This started out with the bonding of InP on InP and GaAs on GaAs [1] and was quickly followed by bonding of InP on GaAs [2]. These first trials required fairly high temperatures (around 650 °C) and were all done on essentially flat surfaces, pressures were in the range of 1 to 20 MPa. Continuing effort allowed to bond InP, GaAs and Si to each other at somewhat lower temperatures, although not much. An extensive treatment of direct bonding for Si and SiO_2 can be found in ref. [3]. Patterned substrates were sometimes used but they consisted of large mesas, or trenches used as escape channels for the chemicals adsorbed at the surface to be able to escape before bonding. They were not small structures such as waveguides [4].

Most of the work performed on direct bonding of III/V materials used hydrophobic surfaces, to assure a true crystal-to-crystal bond and good electrical contacting through the bond. The main downside is still the elevated temperature which causes a lot of stress due to mismatch in thermal expansion coefficient between the two substrates. In recent years a lot of effort has been put into the reduction of the bonding temperature by means of for instance surface activation by an oxygen plasma. The idea is to make the surface more reactive prior to bonding (by inducing defects for instance) so bonding will be easier. Pasquariello [5] reports on InP to Si low temperature wafer bonding with temperatures below 200 °C. However the procedure is not very mature yet and using these low temperatures raised the resistance across the boundary due to a thin oxide layer that is formed.

Devices reported in literature are mostly still fabricated using high temperature annealing steps. Some of them are described in the review paper by Black [6]. They employed temperatures between 550 °C and 650 °C. Sample size ranged from dies less than 1 cm^2 to full 2 inch wafers.

The process was expanded to incorporate patterned samples especially for InP to InP allowing 3D photonics [7]. It turned out that the yield of these patterned samples was strongly dependent on the pressure applied and the sample thickness. The texture and material of the fixtures turned out to be very important. The thickness of the transfer substrate also influenced yield and had to be decreased to 200 μm. The more flexible thinner host substrates were thought to conform better to the patterned wafer and reduce pressure non-uniformities. This involved bonding of dies of 3 cm^2, bonding of larger samples would require reducing the thickness of the host substrate even further which would compromise the mechanical stability. Full details of the process used can be found in the Ph.D. of Maura Raburn [8].

A similar process was used by Djordjev [9] for the fabrication of microring resonators. This also involved the bonding of a patterned, non-flat, InP die to an InP substrate and bonding in a H_2 atmosphere at a temperature of 550 °C.

The downsides to this technology are the need for very clean surfaces (contaminants will prevent local bondings). The surfaces should be very flat, this was especially emphasized for the bonding of full non-patterned wafers, which possibly involves CMP processing steps. Chemical-mechanical polishing (CMP) is a mature process for Si wafers, resulting in wafer roughness below the nm range. This process has not yet reached the same level of maturity with III-V materials. For the procedure using the high temperature, bonding materials with too large a difference in thermal expansion is a big problem. This also makes that the process is not wafer-scale. The high temperature can also be a problem for dopant diffusion and metallizations.

The advantages are clearly the possibility for an electrically conducting bond, which is not the case in adhesive bonding and the possibility to truly integrate dissimilar materials. In other bonding technologies the intermediate layer can get in the way, because it can be non-conducting, absorbing, too thick, have the wrong refractive index, ...

Anodic bonding

This is a bonding procedure used for the bonding of sodium-containing glass wafers to Si wafers under the influence of an external electric field. The thermal expansion coefficient of the glass and the Si should be similar due to the elevated temperatures used (around 500 °C) and the glass should be electrically conductive. The elevated temperature causes the positive sodium-ions in the glass to become mobile and under influence of the electric field they migrate from the surface resulting in a depletion layer with a large potential difference at the surface. The resulting electric field brings the silicon and glass into intimate contact where a permanent chemical bond is formed.

4.2.2 Bonding with intermediate layer

Metal

Metals have often been used to create a bond between two wafers. In a way, the classical flip-chip bonding could be classified here although this will not be discussed further because it is quite a different approach from the ones described here. In the case discussed here the metal is usually deposited on both wafers to be bonded and after mating of the wafers the temperature is increased until bonding is obtained. Popular materials are Pb-Sn, Au-Sn, Sn-Cu. A special kind of metal bonding is eutectic bonding where the low melting temperature of the eutectic alloy is exploited to achieve low temperature bonding. One example is Au-Si [10].

Palladium can be used to form an ohmic contact in-between InP and Si or GaAs at an anneal temperature of 350 °C. Tan [11] reported bonding with layer thicknesses of 200nm.

The downside to this approach is that the metal layer causes absorption. For thin bonding, the roughness should be in the several nanometer region, which is still much less restrictive than for direct wafer bonding.

Silica to silica bonding

In this kind of bonding both the substrates are covered with a thin layer of SiO_2. The wafers are then polished to achieve a smooth surface and the wafers are bonded. A limited annealing temperature of only 200 °C is necessary to increase the bonding energy. This process has been used to bond for instance InP to Si [12] but it is actually the same process as is used to fabricate the SOI wafers mentioned in the previous section. From the point of view of our division of wafer bonding procedures into two categories, silica-to-silica bonding belongs in both. It can be used as a glue layer with no real further function, or adding the silica into the layer structure can be a goal as is the case for SOI-wafers.

Polymer

Polymers permit the joining of very rough or structured wafers to each other and usually require only modest temperatures for bonding. Because of this lower temperature, bonding of dissimilar materials is not a big issue and bonding of small dies or complete wafers does not pose any extra problems either. Several kinds of polymers can be used here such as photoresist, PMMA [13], BCB, . . . The latter will be discussed extensively in the following paragraphs. A review on adhesive wafer bonding can be found in refs. [14] and [15].

Niklaus compared bonding with different adhesives [16] such as BCB, polyimide and photoresist. Bonding with BCB gave the best results.

Spin-on-glass

Spin-on-glass (SOG) are Si-O network polymers suspended in an organic solvent. There is a wide range of SOG materials that can be divided into silicate based compounds, organosilicon compounds and dopant-organic compounds. It is applied by spin-coating and bonding with very thin layers (down to 200nm) should be possible. The use of SOG's stems again from Si-based processing where it is used for planarization and diffusion-doping. Most of the SOG's need to be stored in a refrigerator and they must be at room temperature before applying it to the substrate. Successful wafer bonding has been reported using SOG with layer thicknesses down to 125nm [17] bonding Si to Si and Si to GaAs. The SOG used was silicate based. These are always non-patterned structures. Trials in our lab on bonding with SOG were unsuccessfull though.

4.3 Inspecting the bond

4.3.1 Bonding energy

We shall define the bonding energy as the energy needed to separate the two bonded wafers again (per unit area) (J/m^2). This bonding energy is a measure of the bonding strength. Measuring this bonding energy is a tricky task and usually requires a destructive measurement. The bond can be opened again by all sorts of different techniques, pulling the two wafers apart either by shear force or by tensile force and measuring when the bond breaks. It is not easy to equate the measured quantities with the actual bond energy. Another technique used is the crack opening technique whereby a razor blade is introduced between the two wafers. The two wafers both bend and an equilibrium is achieved between the bonding energy and the energy for elastic deformation of the bended wafers. The length of the resulting crack is a measure of the bonding energy. However, if the bond is too strong and the blade cannot be introduced without cracking one of the bonded wafers, the technique cannot be used.

The bottom line is that accurate direct measurement of the bond strength is very difficult. There are usually some unknown parameters at play so that it is not possible to extract a correct number. The best idea is to stick to one technique and compare results with each other.

In most cases in literature no number is mentioned of the bond strength. At most a crack opening experiment is performed where it is concluded that the substrate breaks more easily than the bond, signifying that the bond energy is higher than the bulk fracture energy of the substrate. To give some idea of the order of magnitude of the bonding energy: for high temperature bonded Si/Si pairs this can be a few J/m^2. For other bonds this can go down to around 0.2 J/m^2.

4.3.2 Inspection

It is interesting to be able to visualize the quality of the bonding layer and see if there are unbonded areas, trapped dust particles or air bubbles. One of the most commonly used methods to detect interface bubbles is based on optical transmission. The light of course has to have a wavelength long enough not to be absorbed by the bonded materials. For our case this means an infrared source and an appropriate camera are necessary. It also requires double-sided polished wafers. This technique has not been used here. Some bonding trials have been performed with glass so that any voids could be observed by the naked eye. It is not straightforward to relate the view of the bonding layer with the bonding energy and more importantly if the sample will hold out during the rest of the processing steps. The most demanding of these processing steps is probably the mechanical thinning described further on. Still samples sometimes failed, or partly debonded during the final step of substrate removal, the chemical etching. Since the proof of the pudding is in the eating, the real test for our bonding was the substrate removal. The downside is this required a lot of work and material. After substrate removal the bonded sample is so thin one can easily look through it with a microscope and inspect the bonding layer.

4.4 BCB wafer bonding

As explained before there are numerous possibilities for wafer bonding. It is clear from the previous discussion that all the technologies have their merit and choice depends mainly on the device to fabricated.

We have opted for the development of the wafer bonding process with Benzocyclobutene or BCB because it is a very versatile process that allows to integrate a large variety of materials, is quite tolerant and does not require expensive cleanroom equipment. Contrary to direct wafer bonding it can be a wafer-scale process. This process was first introduced by Sakamoto [18] in 1999 for the fabrication of electro-optic modulators on GaAs. Absil [19] applied the same process for the fabrication of microring resonators in GaAs and Grover [20] expanded this to InP, also for the fabrication of microring resonators.

4.4.1 BCB

Benzocyclobutenes are a family of thermally polymerizable monomers. The BCB used here is derived from B-staged bisbenzocyclobutene monomers. B-stage means that the polymers are already partially polymerized by heating. Depending on the kind of benzocyclobutene polymer used the properties can change drastically. Discussions on the chemistry of BCB's can be found in ref. [21]. The first documented synthesis of a BCB derivative dates back to 1909. In the late 1970's a research program at The Dow Chemical company focused on BCB's and this resulted in the first patent in 1985. To this day the only supplier of BCB, to our knowledge, is The Dow Chemical company.

Typical properties of BCB are the following

- Low cure temperature (250 °C)
- High degree of planarization
- Good thermal stability
- Transparent at telecom wavelengths
- Low dielectric constant
- Good chemical resistance
- Good compatibility with various metallization systems
- Very low outgassing

Spin speed (rpm)	Cyclotene 3022-35	Cyclotene 3022-46	Cyclotene 3022-57	Cyclotene 30222-63
1000	2.4	5.8	15.6	26
2000	1.7	3.8	9.3	16
3000	1.3	3.0	7.3	13
4000	1.1	2.6	6.3	11
5000	1.0	2.4	5.7	9.5

Table 4.1: Dry-etch grade BCB layer thicknesses (μm)

- Low moisture uptake

Several of these properties will be of importance in the processings described in this chapter. The list of interesting properties is quite long and is confirmed by the huge increase in number of devices fabricated with BCB where it is used for isolation, planarization, as waveguide material, ... One of the downsides to the product is its price however. In low volume a 800 gram bottle costs about 2800 euro. Another disadvantage is the low thermal conductivity, typical for all polymers of course.

The BCB-resins provided by Dow come in two varieties: a photosensitive one (sensitive to G-line and I-line radiation) and a non-photosensitive one (called dry-etch grade). They are sold under the commercial name of Cyclotene. Since the photosensitive property was not of importance to us and considering the price difference between the two (the photosensitive grade is about 30 % more expensive than the dry-etch grade one), we mostly used the dry-etch grade. Each of these grades can be bought in several viscosity levels. These solutions mainly differ in the amount of solvent (mesitylene) added. This varies from 70 % for the least viscous kind (Cyclotene 3022-35) to 30% for the most viscous kind (Cyclotene 3022-63). The recommended shelf life is about 1 year but the only parameter that seems to change is the viscosity due the evaporation of the mesitylene.

The processing of dry-etch grade BCB is a fairly simple one. The BCB is dry-spun onto the substrate. The substrate can first be treated with some kind of adhesion promotor but often this is not so important. The spin speed and the viscosity of the BCB determine the layer thickness as is summarized in Table 4.1. It is evident that with a higher spin speed the layer becomes thinner, but we can also see that the effect of spin speeds higher than 5000 rpm is minimal, especially for the Cyclotene 3022-35. The photosensitive kind is available for a smaller range of layer thickness but the range of mesitylene added is also smaller.

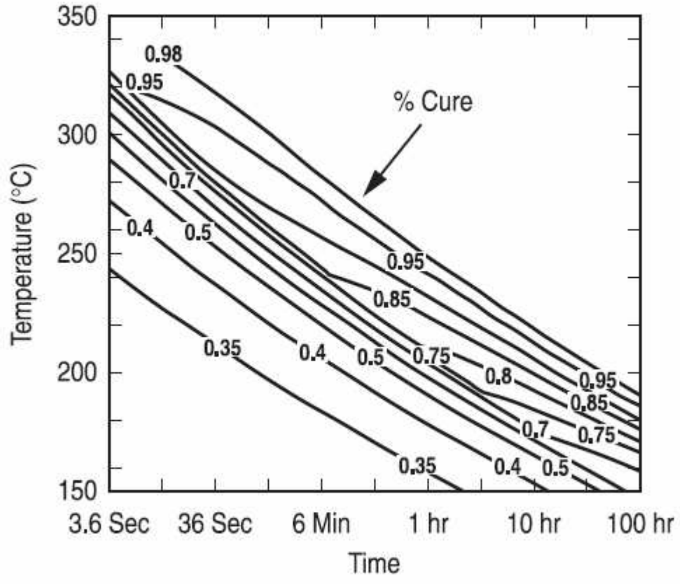

Figure 4.1: Curing percentage as a function of temperature and time (by Dow Chemical)

The BCB is then hardened by a thermal cure in a nitrogen environment. It takes about 1 hour at 250 °C to achieve total polymerization but lower temperatures with longer curing times are possible. A rapid thermal cure of 1 min at 300 °C is also possible. This is illustrated in Fig. 4.1.

Curing to about 100 % of polymerization is referred to as a hard cure, to 75% polymerization as a soft cure. The latter can be advantageous to the adhesion of subsequent layers applied on top of the BCB. This is the case for instance in processes where BCB is used as an isolation layer and other layers are applied on top of the BCB after curing. After the processing is complete, the BCB can be cured completely in a last step. We mostly used a hard cure at 250 °C with the times and temperatures indicated in Table 4.2. The ramp time to, and dwell time at 150 °C could probably still be decreased, this time is only needed for flushing the oven with nitrogen to a level of less than 100 ppm of oxygen and since the oven is quite small this is probably reached quite fast. The cooldown afterwards happens naturally and takes about half an hour. This makes the total curing time about 3 hours.

The glass transition temperature $T_g$is dependent on the percentage of cure. For a 90% cured film, T_g is around 350°C.

Step	Time	Temperature	rate of change
Ramp 1			5 °C/min
Level 1	5 min	150 °C	
Ramp 2			3 °C/min
Level 2	60 min	250 °C	

Table 4.2: Curing times used for the BCB wafer bonding

4.4.2 Bonding

We will now discuss the different steps in the bonding procedure, the subsequent substrate removal and the devices made with this technique. This can also be found in ref. [22].

Substrate preparation

The substrate preparation required for indirect bonding is much less crucial than the preparation required for direct bonding. The wafers are cleaned with IPA, acetone and rinsed with DI water. Afterwards they are dried in an oven at 100 °C. Submicron sized particles at the surface can easily be tolerated and compensated for by the BCB-layer. Even structured wafers with for instance waveguides on them can be bonded. An adhesion promotor provided by DOW Chemical was then spun onto the sample but this is also not critical.

Procedure

The bonding itself is performed by spinning the BCB on the sample. Bonding experiments have been performed with BCB 3022-35 en BCB 3022-46. Initial experiments were performed with BCB 3022-46 and were quite successful. Because of the low thermal conductivity of BCB we then switched to BCB 3022-35 to try and optimise the process with this kind BCB, using layers of around 1 μm in thickness, which would alleviate the thermal issues. The yield of the bonding, even for bonding of two flat wafers, proved to be very low. Using BCB 3022-46, thicker layers (around 3 μm) were spun and after optimisation processing yield was very high. This difference was mainly attributed to the the ability of the thicker BCB to compensate for structures on the wafer. However, experiments performed after moving to a new cleanroom proved that bonding with the thin BCB layers is possible with a high yield leading to the conclusion that particle contamination in the old cleanroom environment was the culprit. This will be further discussed in Section 4.4.6.

We will now discuss the bonding procedure with BCB 3022-46. The BCB is spun onto the sample to be bonded at 2000 rpm which leads to a layer thickness of 3.8 μm. The BCB is then placed onto a hot plate at 140°C for a few minutes to allow some outgassing. An added advantage is the fact that the BCB becomes less viscous at this temperature which allows to move the sample around on the transfer substrate to position it accurately and remove trapped air bubbles. When the sample is in place it is left to cure in an oven under a nitrogen environment at 210 °C for an hour.

When particles get trapped in the bonding layer, either dust or air, they can cause areas where the two wafers are not bonded. This is illustrated in Fig. 4.2 which is a picture through a microscope of an InP film with waveguides etched in it, that was bonded onto a GaAs transfer substrate. The InP wafer was thinned down to a micron or so making it possible to look through the film and observe the bonding layer. Figure 4.3 shows a SEM picture of the cross-section of a bonded waveguide where an air bubble is formed over the waveguide. A good bonding layer quality can be observed in Fig. 4.4.

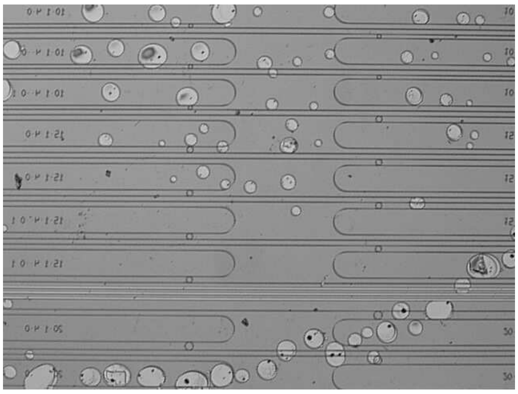

Figure 4.2: Picture of a bonded wafer with waveguides, with many voids in the bonding layer

To achieve the good bonding layer quality, several steps were included in the processing:

- Appropriate cleaning of the wafers and subsequent drying for at least half an hour to eliminate water
- Precuring of the BCB to remove the solvents, this only requires a few minutes on hot plate of around 130°C
- Gradually increasing the bonding contact layer by letting the die fall gradually onto the wafer can help remove air bubbles

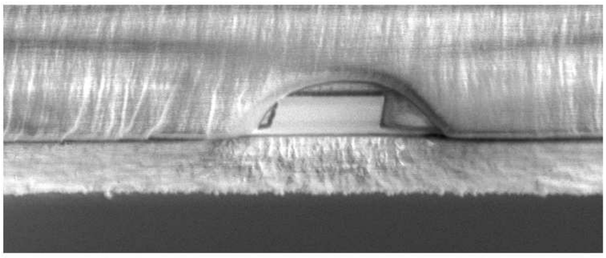

Figure 4.3: An SEM picture of an air bubble trapped around a waveguide

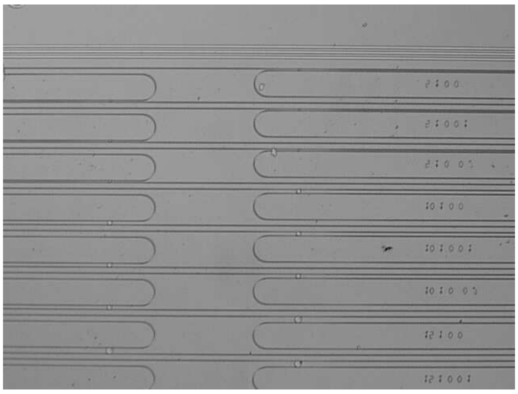

Figure 4.4: Picture of a good bonding layer

- Applying some pressure afterwards
- Moving the die around somewhat, eliminating air bubbles

Some manual pressure was applied after the bonding, but not exactly controlled. Applying pressure can make for a more intimate contact between the two wafers and applying some pressure is important but the control over it is not very crucial. Applying pressure does not have a big influence on the thickness of the layer. Applying pressure during the curing is difficult in our case. Most experiments were performed using small dies. Some BCB always sticks to the backside of the die and when placing a weight on the die during curing, they stick together. This is not an issue when using full wafers and when backside cleaning can be used.

Bonding under a vacuum environment [16] might raise the yield further and especially for more advanced devices could be very useful. This was however not an option for us since commercial wafer bonding equipment is quite expensive. The equipment requires the possibility to heat the sample, establish a vacuum, accurately position the two wafers (especially angular alignment is critical in our case) and perform the bond. Recent experiments using an old mask aligner [1] have been quite succesful.

When bonding patterned wafers, the highest yield was obtained from spinning the BCB on the patterned sample. Bonding of two patterned samples has not yet been performed. Spinning BCB on both the patterned sample and the flat substrate lowered the yield.

The bonding is usually done onto a GaAs substrate, mainly because this substrate is chemically inert during the chemical etching for the InP substrate removal. Silicon could also be used however. We have fabricated structures bonded to silicon, but for waveguide based devices the cleaving of waveguide facets is particularly hard. The larger difference in thermal expansion does not seem to pose problems.

It is clear that this bonding procedure can be performed with nothing but basic standard cleanroom equipment.

Figure 4.5 shows an SEM-picture of a thin InP-film (at the bottom) with two waveguides that was bonded with BCB onto a transfer substrate (at the top). During the mounting of the SEM-sample, which was done without much care, the film came loose, allowing for this instructive picture. The gaps in the BCB where the waveguides fitted can clearly be seen, as well as the thin InP film.

It is worth mentioning here that using SEM to characterise these layers is not trivial. BCB is not electrically conductive and therefore the sample easily suffers from charge-up. This can be avoided by lowering the accelerating voltage used but then image quality can become too low. Applying a thin gold layer to improve conductivity is also an option but this can also mask certain features. The best results were obtained using a low-vacuum SEM where the introduction of a small amount of water vapour in the chamber allows the elimination of most of the charge-up. This is a feature not readily available on most SEM's. Accurate measurements of for instance the thickness of the BCB layer were only possible using a low-vacuum FEG-SEM. This is illustrated in Fig. 4.6 where clearly can be seen that in Fig. 4.6(a) the BCB layer charges up for high vacuum and that in a low vacuum environment, Fig. 4.6(b), the layer can clearly be distinguished and it's thickness measured. Due to the charge-up in the first picture it is difficult to delimit the edges of

---

[1] This came available after a new one was acquired

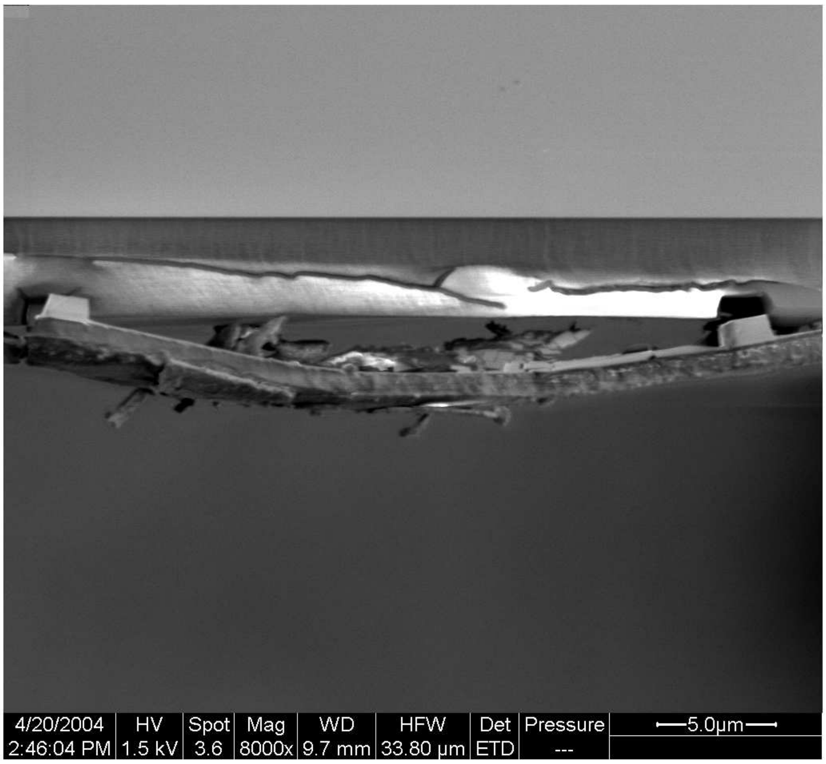

Figure 4.5: An SEM picture of a thin InP-film with waveguide ridges debonded from the transfer substrate

the BCB layer and determine its thickness. These are samples of InP bonded onto Si using a thin bonding layer.

4.4.3 Materials used

Bonding has been done with InP thin films on GaAs, GaAs thin films on InP and InP on Si. Experiments have also been performed bonding metallized wafers since this will be important for the fabrication of active devices. This proved to be no problem either. For plated contacts, debonding occurred during substrate removal but the failure did not occur at the interface between metal and BCB but in the plated layer.

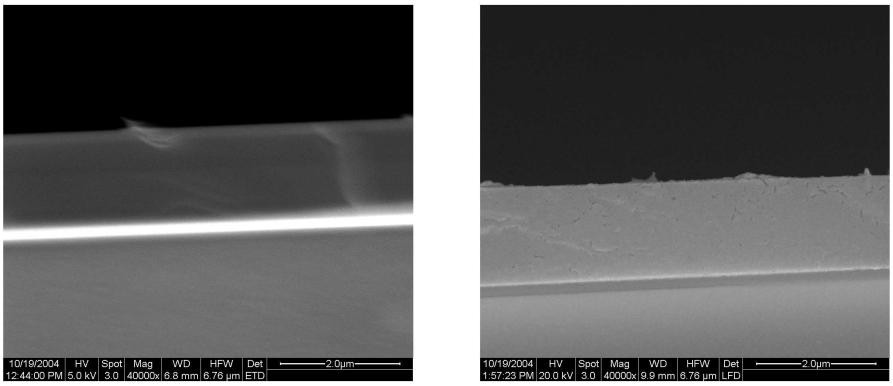

(a) High vacuum (b) Low vacuum

Figure 4.6: SEM pictures of a BCB bonded layer with high and low vacuum

4.4.4 Substrate removal

To remove the original substrate a combination of mechanical polishing and wet chemical etching is used. The substrate is mechanically thinned down to a thickness of about 50 μm or less. For a good bond, one can easily go down to 30 μm. The remaining InP is removed in pure HCl. The etch rate is about 5 μm per minute. To have more control over the process a mixture of HCl with H_3PO_4 can be used to slow down the etch rate but this was not necessary. This etching stops very selectively on the etch-stop layer, which is either a quaternary or ternary layer. The etch stop layer is subsequently removed by a mixture of $H_2O/H_2SO_4/H_2O_2$ in a ratio of 1/1/3.

Complete chemical removal of the substrate would also be possible but this gives rise to slanted ridges at the edge of the sample as can be seen in Fig. 4.7. These ridges have the height of the original substrate (about 350 μm) and make subsequent lithography (especially with contact alignment) very difficult. Removing the ridges by cleaving is a possible solution. These ridges seem to be an issue that only arises when dealing with die to wafer bonding and is assumed to be due to the anisotropic etching along certain crystal planes of InP by HCl. Tests to remove these edges by stirring the sample during etching or adding some kind of 'surface-active material' or 'detergent', as was recommended by third parties, were unsuccessful.

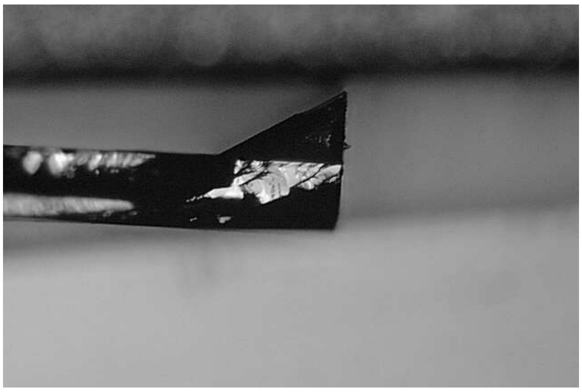

Figure 4.7: Ridges are formed at the edge of the die when using chemical etching to remove the substrate

4.4.5 Alignment

One very important aspect in the bonding procedure is the alignment. In our case no features were present on the transfer substrate before bonding, eliminating the need for any kind of backside alignment marks, a commonly used commercial technique for alignment between two wafers. However, angular alignment of the cleavage planes is very important because this determines the quality of the facets of the waveguides of the device, when it is completely finished and has been cleaved for measurement. Figure 4.8 shows an example of a facet of a poorly aligned bond. The condition of the cleaved facet can heavily deteriorate the functionality of the device.

An initial attempt to achieve this angular alignment was to use a flip chip device available at the lab. This proved to be unsuccessful since the flip-chip equipment was not located in a cleanroom, introducing a lot of dust contamination and additionaly, heating the sample during bonding was not possible. On top of that, alignment was quite time consuming.

We therefore fabricated a simple metal block as drawn in Fig.4.9 where the two samples were simply pressed to the edges. The BCB layers fabricated with BCB 3022-46 were around 3 μm thick and always allowed for some movement of the sample after bonding. A small ridge was fabricated at the edge of the block to position the die not directly on the edge of the transfer substrate, because there is always some damage to the edges of the sample during processing and the BCB is not spun evenly there.

Other alignment issues are between patterns defined on the die before bonding and features on the backside of the die after substrate removal, for instance the alignment of the microring with the bus waveguides. This is

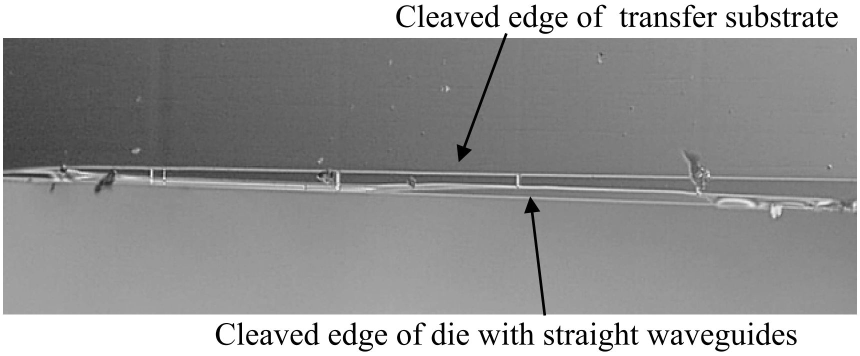

Figure 4.8: A top view of the facet of a poorly aligned bond

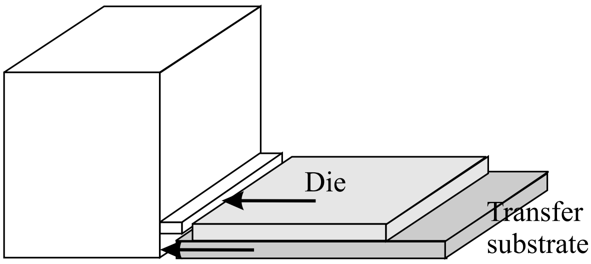

Figure 4.9: Metal block used for aligning the cleavage planes of the transfer substrate and the die

quite similar to normal alignment between different lithography steps. However, depending on the device the structures defined on the die before bonding might not be visible from the backside after substrate removal. Therefore extra alignment markers are etched quite deeply so they will surely be visible from the backside. These are used for alignment. Still, misalignment can occur, about 300 nm in each direction is quite typical for this kind of processing.

4.4.6 Thin bonding

In the last year of this Ph.D. a new cleanroom was opened. Bonding experiments with the thinner BCB 3022-35 were repeated in this new cleanroom environment achieving high bonding yield [2]. The BCB was made even less viscous by adding more solvent to achieve even thinner layers, down to 200 nm. The layer thickness was about 700 nm for a ratio BCB/mesitylene of 2/1 and 200 nm for a ratio of 2/3. Details can be found in ref.[23]. Even Si patterned with shallow trenches could be bonded.

The experiments of bonding with thin layers were then repeated by the author for InP on GaAs, similar to the experiments performed earlier in the previous cleanroom. Bonding with BCB 3022-35 (layer thickness around 1μm) seemed to pose very few problems leading to the conclusion that particle contamination was a very big problem in the previous cleanroom. The class of the new cleanroom is 100, for the old cleanroom no exact number is available for the location where the bonding was performed but it was certainly significantly higher. The same holds for bonding with SOG which from preliminary tests seems to show much higher yield in the new cleanroom.

Since a new mask aligner has been bought, conversion of the old mask aligner to some kind of waferbonder adding, for instance, heating possibilities has been started. For thin layers it is more important to have the position of the die immediately accurate since shifting the die afterwards is not so trivial. Nevertheless experiments without the mask aligner just using the old technique were also successful.

In light of active devices to be fabricated and hoping to alleviate the thermal problems, some experiments were conducted with patterned InP-samples bonded onto GaAs samples. InP wafers with trenched waveguides were used. These were far more deeply trenched than the Si used before, around 1 μm. The width of the trenches varied from 1 to 9 μm. These proved to be successful with layer thicknesses down to around 250 nm. Inspection with a normal microscope does not allow to assess the filling of the trenches and the SEM avalaible in the lab did not allow this either. This remains to be evaluated using a better SEM.

---

[2] These experiments were performed by Günther Roelkens and focussed on bonding InP on Si

4.5 Fabricated devices

We have fabricated several devices using the BCB wafer bonding process. The first are the microring resonators of which the measurements will be discussed elaborately in Chapter 6. Two kinds of active devices were also fabricated, LED's and lasers, allowing to test bonding with metal contact layers, applying contacts through the bonding layer, reliability tests based on for instance the threshold current of the laser, . . . [22] [3] These are the first active devices fabricated with BCB wafer bonding that have been reported to our knowledge. Katsnelson [24] has reported on the fabrication of VCSEL's with BCB but no lasing operation was achieved.

4.5.1 Microrings

The first devices we fabricated with BCB wafer bonding were vertically coupled microring resonators. The fabrication process is illustrated in Fig. 4.10. We start off (Fig. 4.10a) with an epitaxial layer-structure containing two waveguide core layers and an etchstop layer. Next the straight bus waveguides are defined (Fig. 4.10b). This whole structure is flipped upside down and bonded onto a transfer substrate (usually GaAs) with the polymer benzocyclobutene (BCB). The original InP substrate is removed by a combination of mechanical polishing and chemical selective wet etching to the etch stop layer (Fig.4.10c) as described previously. This etch stop layer is also removed. The disk or ring resonator is then etched, the component is cleaved and AR-coated (Fig. 4.10d).

Fig. 4.11 shows a typical measurement of the drop and pass port of one of our fabricated microring resonators. This particular microring resonator was a disk with a radius of 30 μm. The achieved Q-value was around 10000. Measurement of microrings will be discussed extensively in Chapter 6.

4.5.2 LED's

The process used for the fabrication of the LED's is illustrated in Fig. 4.12. On the InP layer structure a Ti/Au contact was applied first. This was then bonded upside down onto the GaAs transfer substrate (Fig. 4.12a). Bonding with a Ti/Au contact deposited on one of the samples proved to be no problem either. Next the original InP substrate and the etch stop layer are removed (Fig. 4.12b). In Fig. 4.12c we can see how the active device is etched in the InP membrane. Then a polyimide layer is deposited through which

---

[3] This work was done in cooperation with Kurt De Mesel and Günther Roelkens

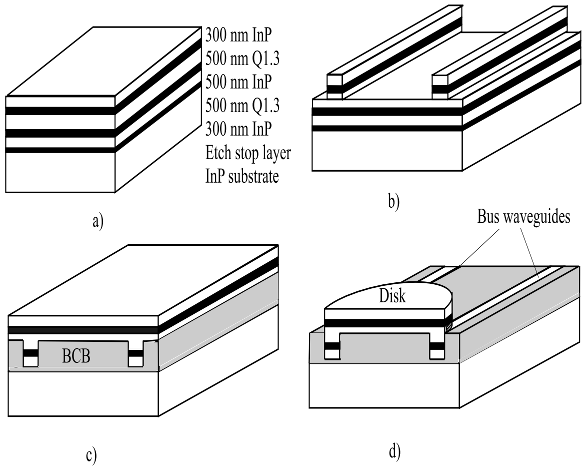

Figure 4.10: Processing of vertically coupled microring resonators fabricated with polymer wafer bonding

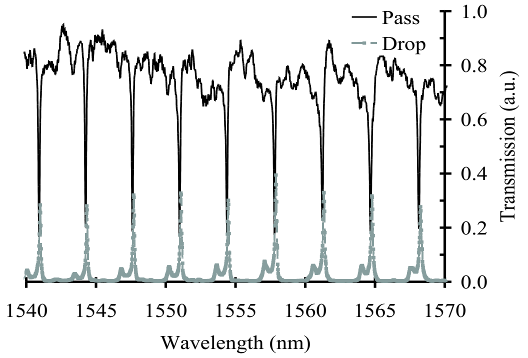

Figure 4.11: The transmission (TE polarisation) at the drop and pass port of a 30 μm radius microdisk resonator

contact openings are defined and contacts are deposited (Fig. 4.12d). The contacts in Fig. 4.12 are ring contacts to allow the LED to emit to the top.

Continuous wave operation was achieved for the bonded LED's. This is illustrated in Fig. 4.13 which plots the measured optical power versus device current. LED's with different sizes were measured showing the strong temperature dependence of the LED's. Small area devices showed higher temperature sensitivity than large area devices due to the lower current density of the latter.

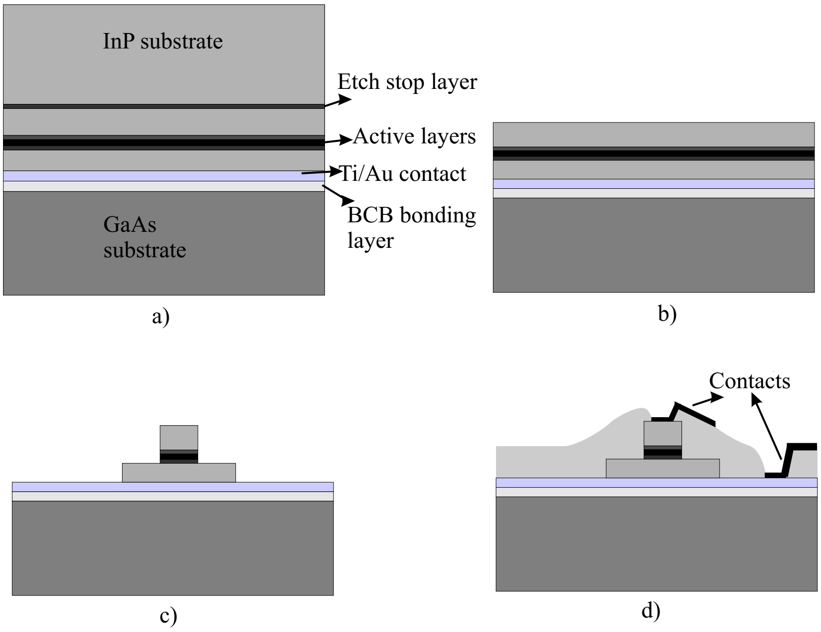

Figure 4.12: Processing of thin film LED's fabricated with BCB wafer bonding

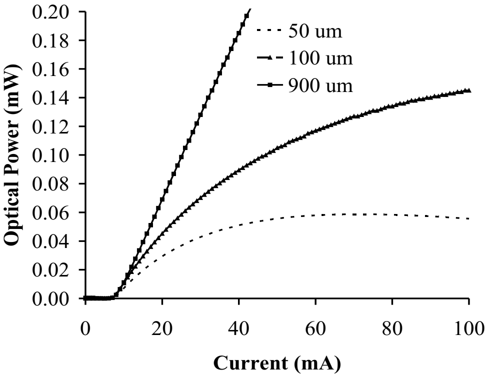

Figure 4.13: Optical power versus current characteristic for III-V membrane LEDs (CW) with different diameters

4.5.3 Lasers

Two sets of lasers were fabricated. The processing sequence of the first batch of lasers was similar to the one of the LED's. The second batch of lasers had electrical contacts through the BCB-layer to metal pads on the underlying substrate. This is interesting from an integration point of view because the III-V component could be connected to underlying Si-circuitry. The added contacts could also serve as a heat sink allowing the laser to function in CW-operation. This will be discussed further in section 4.6.

The processing sequence is illustrated in Fig. 4.14. First both the InP-sample and the GaAs substrate are metallised. Then they are bonded with BCB (Fig. 4.14a). Next the InP substrate is removed (Fig. 4.14b). Then stripes are etched by a combination of dry etching and selective wet etching (Fig. 4.14c). Polyimide is spun on the sample, openings are defined on top of the ridges and n-contacts are deposited and plated (Fig. 4.14d). The metal patterns are then used as a mask in the next etching step that removes the polyimide and the remaining III-V semiconductor on both sides of the metal pattern. An opening is also defined next to the structure (Fig. 4.14e). This structure is then buried in a second polyimide layer and an opening is defined above the ridge, above the opening in the BCB and in the region where the p-contact is to be defined (Fig. 4.14f). Finally a metal bridging structure is defined that contacts the ridge metal with the Ti/Au layer on the GaAs substrate and also the p-contact is defined. These contacts are then deposited and further plated (Fig. 4.14g). The fabricated structure can be seen on Fig. 4.15 which shows an SEM picture with indication of the different regions and contacts.

Edge emitting lasers (length = 1 mm, width = 7.5 μm) were demonstrated in pulsed regime with threshold current densities around 2.65 kA/cm^2 which is about double the threshold current density of standard lasers that were processed on the same wafer. Figure 4.16 plots the measured optical power versus current for different pulse duty cycles. High thermal resistance prohibited reaching continuous wave operation. These are measurements from the first laser design. Due to misprocessing the second laser set had inferior characteristics.

4.6 Thermal issues

We will briefly focus on two thermal issues in this paragraph. The first is the thermally induced stresses when bonding two materials with different coefficients of thermal expansion (CTE), the second is the low thermal conductivity of the BCB. The CTE and thermal conductivity of some materials have been summarized in Table 4.3.

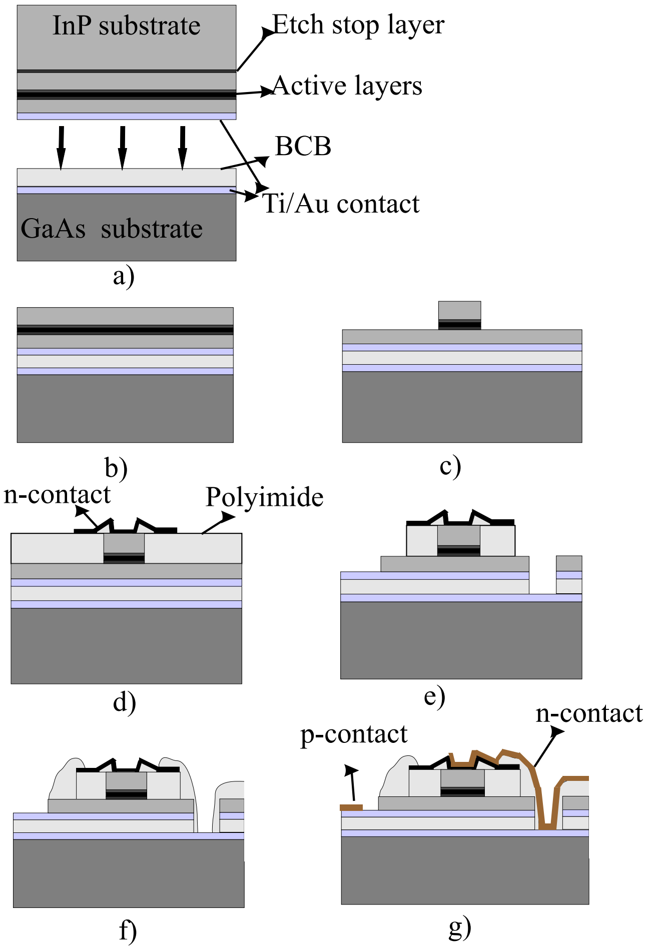

Figure 4.14: Processing of a thin film laser fabricated with BCB wafer bonding. The electrical contact is led through the bonding layer

4.6.1 Thermal stress

Table 4.3 shows that InP and Si have a CTE that differs 50%. Nevertheless bonding these two materials has been performed without problems, even for bigger pieces. The main reason for this is of course the low temperature nature of the BCB bonding process but apart from that BCB acts as good stress buffer.

BCB thin films spun onto a substrate like for instance Si, have tensile residual stresses of around 28 MPa at room temperature due to the difference in thermal expansion coefficient between the BCB and the substrate [25]. The

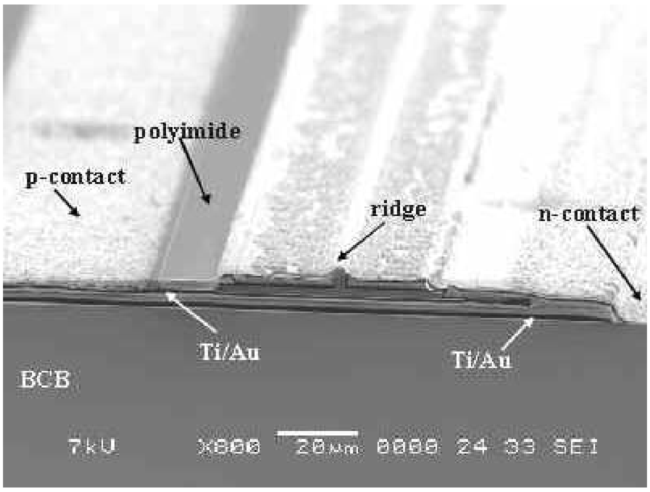

Figure 4.15: SEM picture of a BCB bonded thin film laser with contacting through the bonding layer

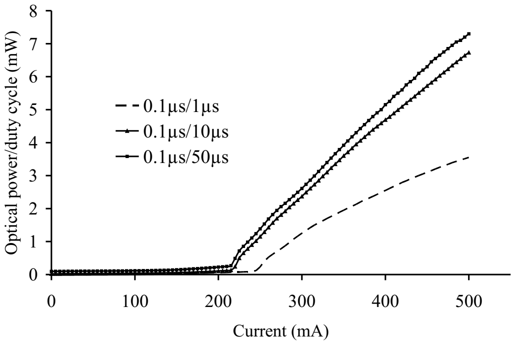

Figure 4.16: Optical power versus current characteristic for III-V membrane lasers for different duty cycles

tensile strength of BCB is up to 85MPa so even more stress can be absorbed. BCB has a CTE that is an order of magnitude larger than that of GaAs, InP and Si. So the BCB layer in between the two bonded wafers is always under tensile stress after the bonded pair has cooled down and the BCB absorbs the stress induced by the difference of thermal expansion between the two materials bonded. Without any further calculations this already shows the possibility of BCB to accommodate materials with a significant difference in thermal expansion coefficient when bonding two different wafers and act as stress buffer. This is also demonstrated by Garrou [26] who used BCB as a

Material	Thermal conductivity	Coefficient of thermal expansion
BCB	0.004 W/cmK	52 10^{-6} /K
GaAs	0.55 W/cmK	5.73 10^{-6} /K
InP	0.68 W/cmK	4.6 10^{-6} /K
Si	1.3 W/cmK	2.6 10^{-6} /K

Table 4.3: Thermal conductivity and CTE of some materials

passivation layer and as a stress buffer to relief the stress between the chip and the package. The same is of course proved by the good performance of the devices fabricated with this technique and will be further justified by the reliability tests performed by damp-heat testing described in section 4.7.

4.6.2 Thermal conductivity

We have already mentioned the low thermal conductivity of BCB in the previous paragraphs. This has been used to our advantage in the fabrication of thermo-optically tunable devices that will be discussed in Chapter 6. However, for active devices this can be a serious issue. Table 4.3 clearly shows the very low thermal conductivity of BCB compared to the semiconductors. The effect of this was clear in the performance of the lasers and the LED's. To resolve this problem first of all one can start to use thinner layers as just recently has been demonstrated. Another possibility is to increase the thickness of the Au contact that is used to contact through the BCB bonding layer and which can act as a heat sink. Simulation shows that by proper design, it should be possible to bring down the thermal resistance of the laser enough to achieve CW operation. This simulation was done for a 3 μm thick BCB layer; with thinner layers the problem should be even easier to solve.

4.7 Reliability issues

For a lot of wafer bonding procedures discussed in this chapter no data are available on the reliability and durability of the bond. To assess the quality and reliability of the BCB-wafer bonding we have performed damp-heat tests on the first batch of lasers described in section 4.5.3. The devices were subjected to tests at 85 °C and 85 % relative humidity (RH). The PI-curves and electrical characteristics of the devices were measured before the tests and after 48, 100, 250 and 500 hours of degradation. Figure 4.17 show the results for a laser. The characteristics stay nearly constant and form a clear indication of the BCB-bonding quality.

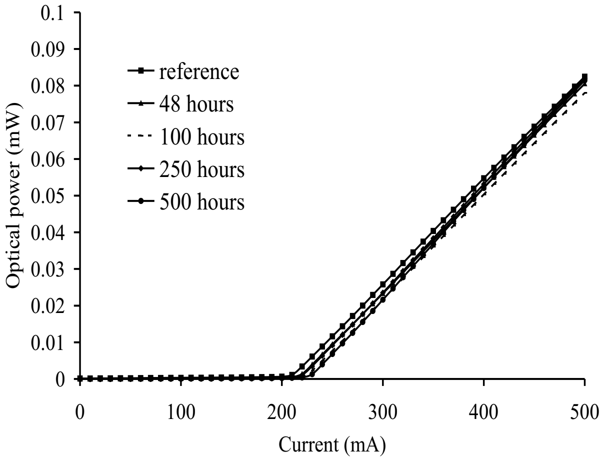

Figure 4.17: Influence of the 85/85 degradation tests on the PI-characteristics of a laser (pulsed, 1 μs/50 μs).

4.8 Conclusion

This chapter gives an overview of the different wafer bonding techniques that exist and then elaborates on the technique developed in this work, namely wafer bonding by means of the polymer BCB. The procedure is described in detail and the quality of the procedure is demonstrated by the quality of the different devices fabricated and the excellent results of reliability tests.

Bibliography

[1] Z. L. Liau and D. E. Mull. Wafer fusion: a novel technique for optoelectronic device fabrication and monolithic integration. *Applied Physics Letters*, 56(8):737–739, February 1990.

[2] Y. H. Lo et al. Bonding by atomic rearrangement of InP/InGaAsP 1.5 μm wavelength lasers on GaAs substrates. *Applied Physics Letters*, 58(18):1961–1963, May 1991.

[3] Q.-Y. Tong et al. *Semiconductor Wafer Bonding*. John Wiley & Sons, 1999.

[4] Z.-H. Zhu et al. Wafer bonding technology and its applications in optoelectronic devices and materials. *IEEE Journal of selected Topics in Quantum Electronics*, 3(3):927–936, June 1997.

[5] Donato Pasquariello and Klas Hjort. Plasma-assisted InP-to-Si low temperature wafer bonding. *IEEE Journal of Selected Topics in Quantum Electronics*, 8(1):118–131, January/February 2002.

[6] A. Black et al. Wafer fusion: materials issues and device results. *IEEE Journal of Selected Topics in Quantum Electronics*, 3(3):943–951, June 1997.

[7] Maura Raburn et al. 3-D photonic circuit technology. *IEEE Journal of Selected Topics in Quantum Electronics*, 8(4):935–942, July/August 2002.

[8] Maura Raburn. *Three-dimensional wafer bonded Indium Phospide photonics waveguide devices*. PhD thesis, University of California, Santa Barbara, 2003.

[9] Kostadin Djordjev et al. High-Q vertically coupled InP microdisk resonators. *IEEE Photonics Technology Letters*, 14(3):331–333, March 2002.

[10] R. F. Wolffenbuttel. Low-temperature intermediate Au-Si wafer bonding; eutectic or silicide bond. *Sensors and actuators*, A62:680–686, 1997.

[11] I.H. Tan et al. Low-temperature Pd bonding of III-V semiconductors. *IEEE Photonics Technology Letters*, 31(7):588–589, March 1995.

[12] C. Seassal et al. InP microdisk lasers on silicon wafer: CW room temperature operation at 1.6 μm. *IEE Electronics Letters*, 37(4):222–223, February 2001.

[13] William P. Eaton and Subhash H. Risbud. Silicon wafer-to-wafer bonding at T lower than 200 ^{o}C with polymethylmethacrylate. *Applied Physics Letters*, 65(4):439–441, 1994.

[14] Frank Niklaus. *Adhesive wafer bonding for microelectronic and microelectromechanical systems*. PhD thesis, Royal Institute of Technology, Stockholm, 2002.

[15] B. G. Yacobi. Adhesive bonding in microelectronics and photonics. *Journal of Applied Physics: Applied Physics Review*, 91(10):6227–6262, May 2002.

[16] Frank Niklaus et al. Low-temperature full wafer adhesive bonding. *Journal of Micromechanics and Microengineering*, 11(2):100–107, 2001.

[17] V. Dragoi et al. Adhesive wafer bonding for MEMS applications. In *SPIE conference proceedings*, volume 5116 of *First International Symposium Microtechnologies for the new millennium*, pages 160–167. SPIE, May 2003.

[18] S.R. Sakamoto et al. Substrate removed GaAs-AlGaAs electro-optic modulators. *IEEE Photonics Technology Letters*, 10(10):1244–1246, October 1999.

[19] P. P. Absil et al. Vertically coupled microring resonators using polymer wafer bonding. *IEEE Photonics Technology Letters*, 13(1):49–51, January 2001.

[20] R. Grover et al. Vertically coupled GaInAsP-InP microring resonators. *Optics Letters*, 26(8):506–508, April 2001.

[21] R.A. Kirchhoff et al. Benzocyclobutenes: a new class of high performance polymers. *Journal of Macromolecular Science: Chemistry*, A28:1079–1113, 1991.

[22] I. Christiaens et al. Thin-film devices fabricated with benzocyclobutene waferbonding. *Journal of Lightwave Technology*, 23(2):517–523, February 2005.

[23] Gunther Roelkens, Ilse Christiaens, et al. Ultra-thin BCB bonding for heterogeneous integration of III-V devices and SOI photonic components. In *European Conference on Integrated Optics*, 2005.

[24] Alex Katsnelson et al. Hybrid integration of III-V optoelectronic devices on Si platform using BCB. In *Photonics Packaging and Integration III*. SPIE, 2003.

[25] Sue Ann Bidstrup Allen et al. Thermo-mechanical stresses in spin-cast polymer films on silicon substrates. *The international Journal of Microcircuits and Electronic Packaging*, 20(1), 1997.

[26] P. E. Garrou et al. Stress-buffer and passivation processes for Si and GaAs IC's and passive components using photosensitive BCB: process technology and reliability data. *IEEE Transactions on advanced packaging*, 22(3):487–498, August 1999.

Chapter 5

Simulation

5.1 Introduction

Simulating a microring resonator is no trivial task. There are several ways to tackle the problem which can roughly be divided into trying to simulate the entire structure at once or dividing the problem into pieces.

Simulating the entire structure at once is quite difficult, very time consuming and provides little physical insight. Some options are the use of FDTD, mode matching techniques or Finite Element techniques:

- FDTD

  Hagness et al. [1] have demonstrated simulations in 2D of the entire microring resonator at once. These were however quite small rings limiting the computational window and the calculation times. When the entire structure is simulated, the wavelength response at the drop and the pass port can be simulated. Here, possible resonances resulting from higher order modes can be seen.

- Mode matching and Finite Element

  The entire structure can be simulated by mode matching techniques or Finite Element techniques and the drop and pass characteristics can be obtained by sweeping the wavelength. This is however quite time-consuming because a small enough grid has to be used and the number of modes has to be very high to achieve an accurate simulation. 3D simulations are therefore definitely not an option.

It is easier to divide the problem into pieces. The first piece is the calculation of the modes in the straight waveguide and the bent waveguide separately. Next the coupling between the straight waveguide and the bent waveguide can be calculated based on these modes. Then the knowledge of the modes in the bent waveguide can be combined with the knowledge of the coupling coefficients to calculate the entire response of the microring resonator. The microring is then split up as can be seen in Fig. 5.1.

In the following sections we will therefore first discuss the calculation of bend modes and subsequently the calculation of the coupling coefficient and how these two should be combined.

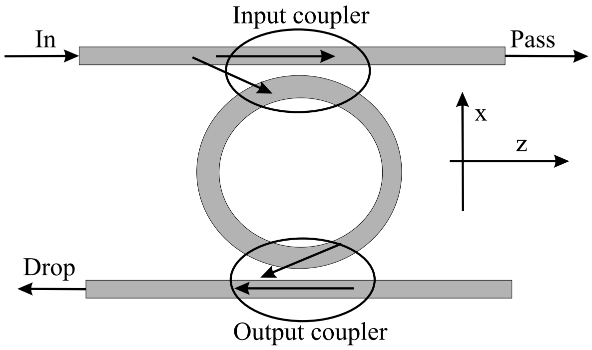

Figure 5.1: Dividing the microring in two bend sections and two coupler sections

5.2 Calculating bend modes

In order to obtain physical insight into the ring resonator it is useful to study the modes of the bus waveguides and especially those of the ring or disk. Whereas calculating the modes of a straight waveguide (2D or 3D) is a fairly trivial task, especially with today's modesolver tools, calculating the modes of a bend waveguide is somewhat more challenging.

To start off with, the mode problem has to be expressed in cylindrical coordinates (r, ϕ, y) as is illustrated in Fig.5.2.

The 3D problem is quite difficult, as is the case for straight waveguides, and provides no analytical solutions. The 2D problem, though an approximation, is relatively easy to solve and provides a lot of physical insight. It will therefore be discussed first.

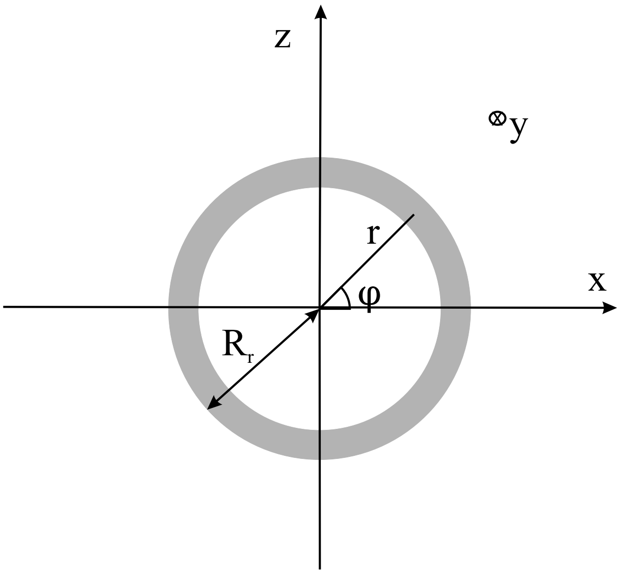

Figure 5.2: The bend in cylindrical coordinates

5.2.1 2D simulations

We start with Maxwell's equations

$$\begin{aligned} \underline{\nabla} \times \underline{E} &= -j\omega\mu_0\underline{H} \\ \underline{\nabla} \times \underline{H} &= j\omega\epsilon\underline{E} \end{aligned}$$

We are looking for a 2D solution which means that the solutions to the equations are independent of the transverse coordinate y:

$$\underline{E}(r,\phi) = \underline{E}_0(r)exp(-j\gamma\phi)$$
$$\underline{H}(r,\phi) = \underline{H}_0(r)exp(-j\gamma\phi)$$

γ is the angular propagation constant. Substituting this into Maxwell's equations yields two groups of equations, independent of each other which are the well-known TE and TM solutions. TE has non-zero field components E_y, H_r, H_ϕ; TM has H_y, E_r, E_ϕ components. By eliminating the r and ϕ components we obtain the familiar Helmholtz equations for TE and TM:

$$r^2\frac{d^2E_{0y}}{dr^2} + r\frac{dE_{0y}}{dr} + (k_0^2n^2r^2 - \gamma^2)E_{0y} = 0 \tag{5.1}$$
$$r^2\frac{d^2H_{0y}}{dr^2} + r\frac{dH_{0y}}{dr} + (k_0^2n^2r^2 - \gamma^2)H_{0y} = 0 \tag{5.2}$$

This form of equation can be solved by means of Bessel functions or other approaches such as described in ref. [2]. The problem can however also be tackled differently.

The equation holds a lot of similarity with the traditional Helmholtz equation for piecewise constant refractive index profiles:

$$\nabla^2\Psi(\mathbf{r}) + k_0 n^2(\mathbf{r})\Psi(\mathbf{r}) = 0 \tag{5.3}$$

where Ψ is one of the field components of the magnetic or electrical field.

We can transform eqs. (5.1) and (5.2) into eq. (5.3) by means of a conformal transformation [3]. Hereby the bent waveguide is transformed into a straight waveguide with a different refractive index profile. The refractive index n that is piecewise constant with respect to the radial coordinate r, is replaced by another refractive index profile, n_t, that is function of a scalar coordinate u.

$$\begin{aligned} u &= R_t\, ln(r/R_t) \\ n_t &= n\, e^{u/R_t} \end{aligned}$$

Here R_t is an arbitrary value which is often chosen to be the outer radius of the bend for reasons that will become clear later. Application of this tranformation to the eqs. (5.1) and (5.2) gives the following:

$$\begin{aligned} \frac{d^2E_{0y}}{du^2} + (k_0^2 n_t(u)^2 - \gamma^2)E_{0y} &= 0 \\ \frac{d^2H_{0y}}{du^2} + (k_0^2 n_t(u)^2 - \gamma^2)H_{0y} &= 0 \end{aligned}$$

This is the same equation as for a straight waveguide but the refractive index profile has to be changed as illustrated in Fig. 5.3.

This problem can then be solved by regular straight waveguide mode solvers or by any of the techniques described in refs. [2, 4, 3]. This transformation has some non- physical effects though: the transformed refractive index ranges from zero to infinity.

In the next paragraphs results of 2D simulations in Fimmwave will be shown to illustrate some typical properties of bend waveguide modes. Figure 5.4 shows some examples of the amplitude and phase of bend modes for a slab waveguide with core index 1.6 and cladding index 1.45. This is quite a low contrast system and it is clear that as the radius decreases the modal field

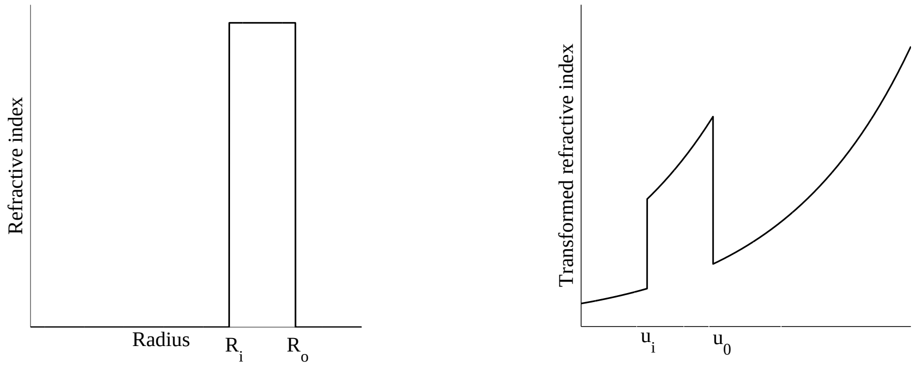

(a) The bend waveguide

(b) The conformal transformation

Figure 5.3: Refractive index profile of a bend before and after conformal transformation

extends further and further into the cladding. These modes will have a lot of radiation loss. The gray area indicates the postion of the core.

Another example can be seen in Figure 5.5 where the modal field is shown for a wider (2.5 μm) waveguide in a high contrast system (refractive index of the core 3 and cladding 1). This clearly illustrates two other effects of bend waveguides. First of all, the peak of the mode shifts outwards as the radius decreases. This can be understood from the transformed refractive index profile. The refractive index is the highest at the outer edge of the bend. When a straight waveguide is connected to a bent waveguide, losses will occur at this transition because of the difference in mode profile. To limit these losses, the straight waveguide can be slightly offset with respect to the bent waveguide, so that the peak of the mode profile of the bent waveguide matches better with the peak of the mode profile of the straight waveguide.

Second, when the radius is small enough the field is zero at the inner boundary of the ridge, and this inner boundary has no more influence on the field profile. This is called the whispering gallery mode regime. This can be interesting because no scattering losses can be observed at this inner boundary anymore as the field amplitude is zero. An approximate 2D formula for the width necessary to reach this whispering gallery mode regime can be found in ref. [2].

Figure 5.6 illustrates some higher order modes in a bend waveguide.

When calculating the modes of a bend waveguide we can calculate an angular propagation constant. This constant contains a real and an imaginary

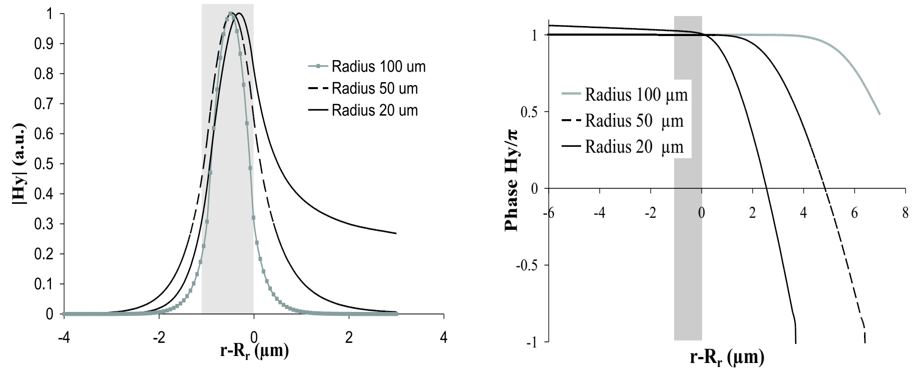

(a) The amplitude of the modal field for different radii

(b) The phase of the modal field for different radii

Figure 5.4: Fundamental TM modes of bent slab waveguides

part.

$$\gamma = \beta_\phi - j\alpha$$

The real part is related to the effective index of the bend mode. It is very important to point out that defining an effective index for a bend waveguide is quite arbitrary. The only really physical parameter to use is the angular propagation constant β_ϕ. To translate this to a propagation constant per unit length and extract an effective index, means defining a pathlength along the bend and defining an arbitrary radius R$_t$ for this path. The effective index and the angular propagation constant are then related in the following way:

$$\beta_\phi = \frac{2\pi}{\lambda} n_{eff} R_t$$

Depending on the choice of this radius R_t the effective index can increase or decrease with radius. Some definitions of the radius however make slightly more sense than others; for instance defining the radius at the point of maximum field intensity has some physical merit. Since, for small radii, this point is close to the outer edge of the bend, the outer radius of the bend is often used as a definition.

The imaginary part of the propagation constant γ relates to the power radiation loss of the bend mode.

$$\begin{aligned} \text{Bend loss (dB/90}^o) &= -10log_{10}(exp(-2\alpha\frac{\pi}{2})) \\ &= \frac{10\pi\alpha}{ln(10)} \end{aligned}$$

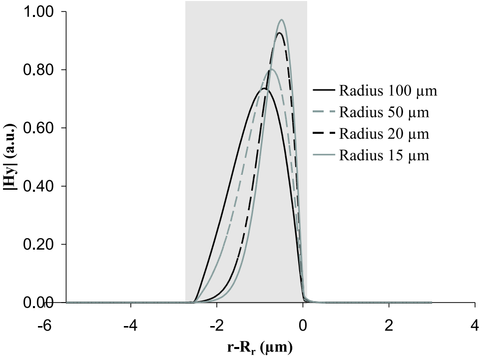

Figure 5.5: Fundamental TM modes of bent slab waveguides in a high contrast system

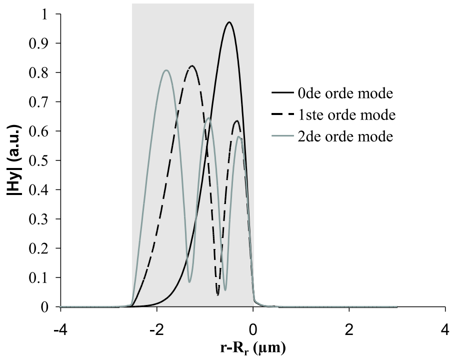

Figure 5.6: Higher order TM modes of bent slab waveguides in a high contrast system

Bend waveguides have inherently lossy modes. The loss increases with decreasing refractive index contrast and decreasing radius. This can be understood intuitively from the transformed refractive index profile of Fig. 5.3(b). The mode of the bend waveguide is mainly located at the region of highest refractive index located at the outer edge of the core. However a region with high refractive index contrast can again be located at higher u-values. When the radius decreases and/or the refractive index contrast decreases, the distance to this region decreases and part of the mode 'tunnels' to this region, introducing loss.

Another explanation for this inherent loss is the following. The field of the bend waveguide has a shape as can be seen in Fig. 5.7. It is clear that the phase fronts at the outside of the bent waveguide start to bend. The phase velocity there would have to exceed the plane wave velocity in the medium outside the waveguide to keep a flat phase front. Since this is not possible the field bends and starts radiating into space.

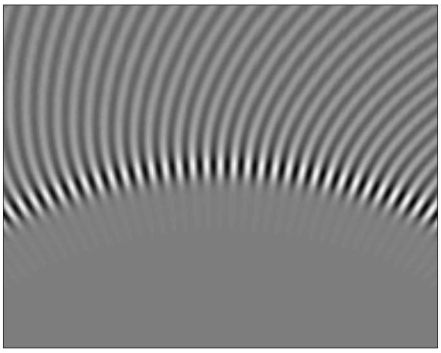

Figure 5.7: Field plot of 20 μm radius bend in a low contrast medium, the mode is propagating counterclockwise

5.2.2 3D simulations

In the general 3D case the solutions to the Maxwell equations take the form of

$$\underline{E}(r, \phi, y) = \underline{E}_0(r, y) exp(-j\gamma\phi)$$

The added dependency on y makes the problem far more difficult and it needs to be tackled by advanced numerical techniques. The conformal transformation technique can not be applied rigorously on the 3D problem.

Several numerical techniques such as Finite element (FE), Finite difference (FD) and mode matching can be used. There are currently, to our knowledge, 3 commercial modesolvers on the market that can calculate 3D bend modes: Fimmwave [5], APSS [6] and Olympios [7], all of which we have used for some time. APSS by Apollo Photonics was only used very briefly by means of trial license and not evaluated very thoroughly. This program is based on Finite Difference techniques.

These all have their down- and upsides. One of the most difficult things is to accurately model the radiation loss. Contrary to the 2D description of the loss we not only have to take into account the radiation loss in the lateral direction but also the substrate leakage loss. Most simulation programs use some kind of special boundary condition to absorb this radiation loss and prevent it from reflecting and influencing the mode. These are often Perfectly Matched Layers (PML) boundary conditions [8]. None of these simulation programs are plug and play. They require some insight to achieve the desired result. Achieving reliable loss figures usually requires several sweeps of parameters to establish if one is working in a stable regime. There are still structures that we have not been able to simulate ourselves with this software such as very small bend waveguides ($<5\ \mu$m) in SOI. Sometimes with a lot of feedback from the software supplier these problems can be solved but they require a profound insight in the algorithm to find the right settings.

Fimmwave

Fimmwave by Photondesign uses a method called Film Mode Matching to calculate the modes of the bend waveguide. This software is available in the lab and has been used most extensively. The Film Mode Matching technique and its application on bend waveguides is discussed in [9].

The biggest downside to this program is the fact that PML boundaries can only be used efficiently on the left and right boundary, not on the top and bottom, making substrate leakage loss difficult to model.

Also it is often not possible to immediately find a mode of a bend waveguide with small radius. The mode of a bend with large radius can be found automatically. This mode has to be used as the starting point for a sweep of the radius down to the radius of interest. This can take quite a long time. When the mode becomes hybrid (which means the mode does not have a clear TE or TM polarization any more but this will be discussed further on) the sweep often fails or takes a very long time. Finding the lower order modes of bend waveguides with large width can be very cumbersome also and for instance calculating the influence of a post (for extraction of higher order modes, which will be discussed later) underneath the microring is next to impossible.

The software also provides the possibility to use transparent boundary conditions to polish the result of a simulation with PML boundary conditions. This is a kind of infinite PML and should provide a reflectionless solution. However, it is the author's experience that care still has to be taken when using this.

Olympios

Olympios is a simulation tool by C2V. It contains a bend mode solver based on a Finite Difference technique. Semi-vectorial and vectorial solutions can be found. PML boundary conditions can be applied on all boundaries. The obtained modes are not labeled, it is up to the user to identify the physical modes (a lot of 'non-physical' modes are found also) and determine the nature (TE, TM or hybrid) of the modes. No conformal transformation is used. In a lot of the cases the mode, even for sharp bends, can be found immediately.

Hybrid modes

In the 3D case the solutions to the Maxwell equations are no longer split into two different groups (TE and TM). For straight waveguides, in most cases the solution is however still predominantly TE or TM, but in bends there is usually a region of radii where the mode is very hybrid. This complicates the solution of the problem since normally a full-vectorial solution is required.

TE and TM for bend waveguides are defined as described in Table 5.1.

Quasi-TE	Quasi-TM
$E_r > E_\phi > E_y$ $H_y > H_\phi > H_r$	$H_r > H_\phi > H_y$ $E_y > E_\phi > E_r$

Table 5.1: Definition of the polarisations

In Fig. 5.8 and Fig. 5.9 the evolution of a mode from completely TM or TE to very hybrid for decreasing radius can be observed. The layer structure was a standard InP waveguide structure consisting of an InP substrate, a 600 nm quaternary layer with bandgap wavelength 1.3 μm and a 300 nm InP cap layer. The ridge was 2 μm wide and the etch depth 900 nm.

Calculating the modes in the very hybrid region can be tricky. Figure 5.10 show the evolution of the effective index (defined at the outer edge of the bend) of the two zero-order modes of the structure. At large radii, the modes are quasi-TE and quasi-TM but around a radius of 20 μm the mode becomes hybrid which is indicated by the fact that the effective indices of the two modes become very similar. At even smaller radii the modes become less hybrid again and the TE and TM mode have switched places. Calculation of the modes in the hybrid region can be very difficult and time-consuming. For bend mode solvers, such as Fimmwave, determining the bend modes at a radius lower than the radius where the modes are hybrid is very difficult.

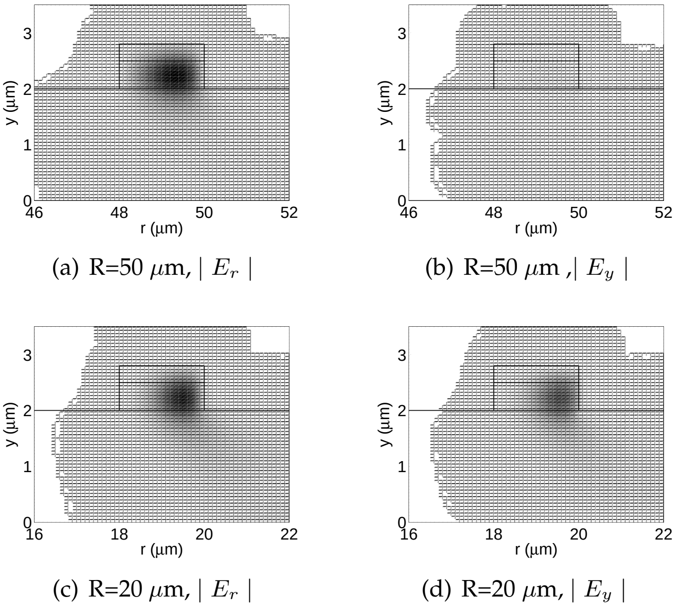

(a) R=50 μm, $\mid E_r \mid$ (b) R=50 μm ,$\mid E_y \mid$

(c) R=20 μm, $\mid E_r \mid$ (d) R=20 μm, $\mid E_y \mid$

Figure 5.8: Evolution of the field profile for a TE mode with decreasing radius

Usually tracking the mode while decreasing the radius is necessary and in the hybrid region the algorithm tends to fail.

In a practical configuration the walls of the bend waveguide are often sloped which can also influence the formation of hybrid modes.

5.3 The coupling section

The second element necessary to simulate the entire structure is the coupler. The most important thing to calculate here is the coupling coefficient between the bend and the straight waveguide. This is again not an easy task. In this section we shall focus on the calculation of the coupling coefficient between a straight waveguide and a bent waveguide. In the case of a racetrack microring resonator, the coupling coefficient can be calculated by the theory of the codirectional coupler. Because this is a much more familiar kind of coupling and easier to simulate, several papers can be found focussing on the effects of non-ideal behaviour in racetrack resonators, such as loss in the coupler and polarization conversion. We will also briefly pay attention to the bend-coupling technique which was introduced in Chapter 3.

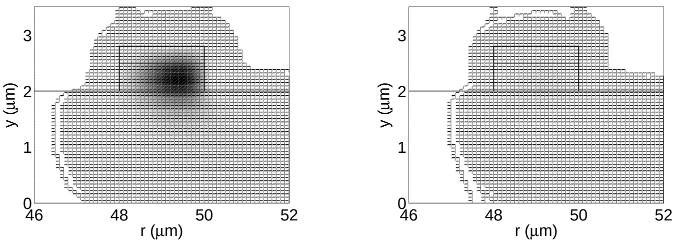

(a) R=50 μm, $\mid H_r \mid$ (b) R=50μm, $\mid H_y \mid$

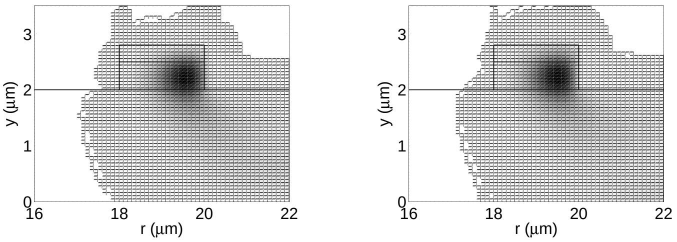

(c) R=20μm, $\mid H_r \mid$ (d) R=20μm, $\mid H_y \mid$

Figure 5.9: Evolution of the field profile for a TM mode with decreasing radius

5.3.1 Finite Difference Time Domain (FDTD)

The coupling coefficient can be calculated by FDTD as was demonstrated by Hagness [1]. A few difficulties arise however when using this technique. To calculate the amplitude of a waveguide mode, the overlap integral of the local field with the mode profile has to be calculated. This is best calculated along a horizontal or vertical cross-section. If the straight waveguide is excited in the simulation and we want to look at the amount of power in the bend, the signal has to propagate to position B in Fig. 5.11. The fields have already become decoupled a lot sooner, so a lot of superfluous calculations are being performed. Also the bend waveguide mode can extend over a very large distance making it difficult to define the overlap integral and making it necessary to increase the computational window. One can however calculate how much power is left in the straight waveguide by placing a sensor at position A after the coupling section, assume that the coupling was lossless and therefore deduce the power in the bend waveguide. Absorbing boundary conditions such as PML's are again a prerequisite for success.

If the bend waveguide is multimodal, calculation of the different bend modes is necessary to assess excitation of these different modes. This requires

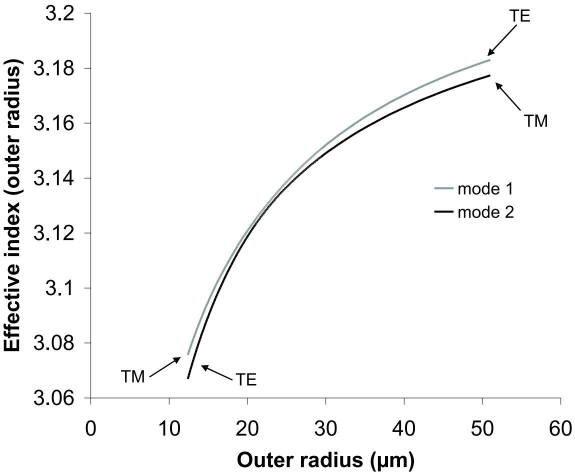

Figure 5.10: The evolution of the effective index of the two zero order bend modes with decreasing radius

a bend mode solver to be integrated into the FDTD simulation as it is no longer possible to assume that the power in the bent waveguide mode is 1 minus the power in the power reminaing in the straight waveguide mode. To look at effects of higher order modes one could also simulate the whole structure at once and look at the different resonances that appear in the drop and the pass port but this is very time consuming.

The results described in ref. [1] have been reproduced by the author with the software Omnisim (developed by Photondesign). For the small rings (up to 5 μm radius) described, FDTD in 2D is a viable option, calculation times were up to a few minutes.

FDTD simulations have only been demonstrated for microrings in 2D and for very small rings, 3D simulations would be even more computationally demanding. An advantage of this technique is the fact that a pulse containing a range of wavelengths can be injected into the structure providing information on the coupling coefficient over a wide wavelength range in one simulation.

5.3.2 Mode matching

The microring can also be simulated by film mode matching techniques. This is quite similar to FDTD in the sense that the entire structure is entered into the software and then cut into slices. This was implemented in 2D in Fimmwave by the author but proved not to be a very straightforward technique.

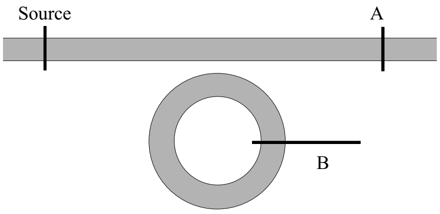

Figure 5.11: Position of the sensors for FDTD simulations

The coupling from the straight waveguide to the ring could be extracted by assuming lossless coupling and looking at the power in the mode in the straight waveguide. Insight into the power coupled into several modes of the microring was difficult or impossible to obtain. PML boundaries conditions, sufficiently small discretization and enough 1D modes have to be included, making an accurate simulation very time-consuming and only an option in 2D.

5.3.3 Coupled mode theory

One of the most interesting techniques of calculating the coupling coefficient is by means of coupled mode theory [10]. The coupled mode equations (see below eqs. 5.4) have to be solved by means of a Runge Kutta integration scheme. The equations used here are more exact than the ones derived by Marcuse ([10]) who neglects higher order terms to simplify things. This approach is however not good enough to achieve accurate results.

In the following paragraphs, the most basic coupling problem will be discussed: between one straight waveguide mode and one bend mode, and this will then be expanded to the case where higher order modes come into play.

One bend mode, one straight waveguide mode The coupled mode equations used here can be derived from the Lorentz reciprocity theorem [11].

$$\begin{pmatrix} \sigma_{bb} & \sigma_{bs} \\ \sigma_{sb} & \sigma_{ss} \end{pmatrix} \frac{d}{dz} \begin{pmatrix} a_b \\ a_s \end{pmatrix} = \begin{pmatrix} c_{bb} & c_{bs} \\ c_{sb} & c_{ss} \end{pmatrix} \begin{pmatrix} a_b \\ a_s \end{pmatrix} \tag{5.4}$$

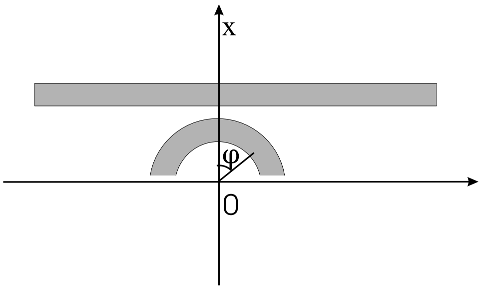

Figure 5.12: The layout of the coupling section for CMT calculations

with

$$\sigma_{pq} = \frac{1}{4} \int \mathbf{e}_z . (\mathbf{E}_q \times \mathbf{H}_p^* + \mathbf{E}_p^* \times \mathbf{H}_q) dx$$
$$c_{pq} = -i \frac{\omega \epsilon_0}{4} \int \mathbf{E}_p^* . (\epsilon - \epsilon_q) \mathbf{E}_q dx$$

Here the subscripts s and b denote the straight and bend waveguide. ϵ_b and ϵ_s are related to the refractive index profiles of the bend only and straight waveguide only. ϵ is related to the total refractive index profile comprising of the bend and the straight waveguide.

The calculation of the coupling coefficients by means of these coupled mode equations was implemented and checked with FDTD simulations by Stoffer [12]. We have implemented the same algorithm based on modal fields provided by Fimmwave.

An example of this kind of simulation with no higher order modes can be seen in Fig. 5.13. This is a 2D simulation of the coupling from a straight waveguide to a 20 μm radius bend. The width of both waveguides was 1 μm, the core refractive index is 1.45, the cladding 1. The gap between the two was 300 nm. This is the kind of situation one could encounter for instance in polymer microrings.

3D simulations Expansion of the technique to 3D is evident [13] and was also implemented. However it also becomes more time-consuming especially for full-vectorial calculations taking into account higher order modes. Examples of these calculations will be shown in Chapter 6. The biggest problem is the calculation of the 3D bend modes that serve as input for the coupled mode theory.

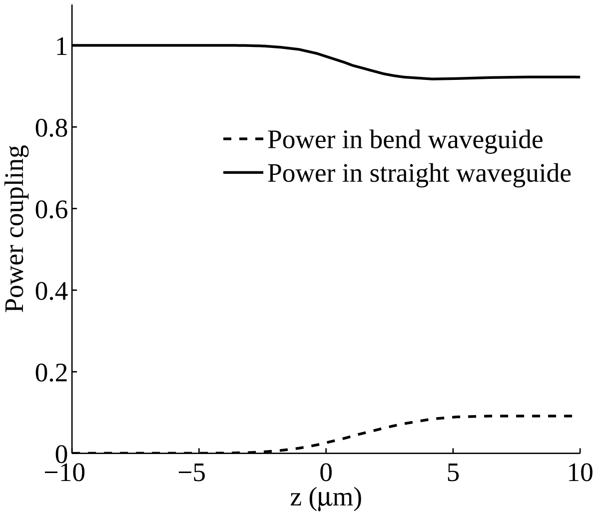

Figure 5.13: Calculation of the coupling coefficient by coupled mode theory

There exists an approximate coupled mode theory developed by Rowland and Love [14], based on theory by Matsuhara and Watanabe [15] and used for instance by Djordjev [16].

Both of these techniques have been implemented and compared in 2D. The technique by Rowland and Love provides results with acceptable physical behaviour with respect to changes in gaps etc. but they are quite different to the results obtained with the full coupled mode theory and are therefore doubtful. This theory has never been validated with FDTD simulations whereas the coupled mode theory has.

Higher order modes This CMT technique is fast (certainly in 2D) and allows to calculate coupling to higher order modes also [17]. For this, equations (5.4) have to be expanded to include the higher order modes in the disk and the straight waveguide, as shown in eq. (5.5). This assumes there are N_s modes in the straight waveguide and N_b in the bent waveguide. The superscript indicates the mode number.

The inclusion of higher order modes can be very important. If higher order modes exist that couple efficiently to the straight waveguide, these have to be included into the simulation as they can change the amount of coupling to the zero order mode also, because the differential equations are all coupled. Examples will be shown in Chapter 6.

$$\begin{pmatrix} \sigma_{bb}^{11} & \sigma_{bb}^{12} & \dots & \sigma_{bb}^{1N_b} & \sigma_{bs}^{11} & \sigma_{bs}^{12} & \dots & \sigma_{bs}^{1N_s} \\ \sigma_{bb}^{21} & \sigma_{bb}^{22} & \dots & \sigma_{bb}^{2N_b} & \sigma_{bs}^{21} & \sigma_{bs}^{22} & \dots & \sigma_{bs}^{2N_s} \\ \vdots \\ \sigma_{bb}^{N_b1} & \sigma_{bb}^{N_b2} & \dots & \sigma_{bb}^{N_bN_b} & \sigma_{bs}^{N_b1} & \sigma_{bs}^{N_b2} & \dots & \sigma_{bs}^{N_bN_s} \\ \sigma_{sb}^{11} & \sigma_{sb}^{12} & \dots & \sigma_{sb}^{1N_s} & \sigma_{ss}^{11} & \sigma_{ss}^{12} & \dots & \sigma_{ss}^{1N_b} \\ \vdots \\ \sigma_{sb}^{N_s1} & \sigma_{sb}^{N_s2} & \dots & \sigma_{sb}^{N_sN_b} & \sigma_{ss}^{N_s1} & \sigma_{ss}^{N_s2} & \dots & \sigma_{ss}^{N_sN_s} \end{pmatrix} \frac{d}{dz} \begin{pmatrix} a_b^1 \\ a_b^2 \\ \dots \\ a_b^{N_b} \\ a_s^1 \\ a_s^2 \\ \dots \\ a_s^{N_s} \end{pmatrix} =$$

$$\begin{pmatrix} c_{bb}^{11} & c_{bb}^{12} & \dots & c_{bb}^{1N_b} & c_{bs}^{11} & c_{bs}^{12} & \dots & c_{bs}^{1N_s} \\ c_{bb}^{21} & c_{bb}^{22} & \dots & c_{bb}^{2N_b} & c_{bs}^{21} & c_{bs}^{22} & \dots & c_{bs}^{2N_s} \\ \vdots \\ c_{bb}^{N_b1} & c_{bb}^{N_b2} & \dots & c_{bb}^{N_bN_b} & c_{bs}^{N_b1} & c_{bs}^{N_b2} & \dots & c_{bs}^{N_bN_s} \\ c_{sb}^{11} & c_{sb}^{12} & \dots & c_{sb}^{1N_s} & c_{ss}^{11} & c_{ss}^{12} & \dots & c_{ss}^{1N_b} \\ \vdots \\ c_{sb}^{N_s1} & c_{sb}^{N_s2} & \dots & c_{sb}^{N_sN_b} & c_{ss}^{N_s1} & c_{ss}^{N_s2} & \dots & c_{ss}^{N_sN_s} \end{pmatrix} \begin{pmatrix} a_b^1 \\ a_b^2 \\ \dots \\ a_b^{N_b} \\ a_s^1 \\ a_s^2 \\ \dots \\ a_s^{N_s} \end{pmatrix} \qquad (5.5)$$

The inclusion of higher order modes does not only influence the magnitude of the coupling coefficients but also the phase relationship as will be discussed in section 5.3.5.

Furthermore including higher order modes into the ring is not just a matter of superposition of these modes.

The coupling to higher order modes can be expected to be quite low in the lateral configuration of the higher contrast systems but can be expected to be more of a problem in the vertically coupled configuration where the field overlap is inherently larger. But also coupling to the other polarization when the modes have become hybrid is possible. This can be analyzed by a full-vectorial 3D CMT calculation.

To eliminate these higher order modes, the use of a post underneath the microring (as illustrated in Fig. 5.14) has been suggested and fabricated by Djordjev [18]. This should enable excited higher order modes to leak out. After inclusion of a post in the structure the reported fabricated devices did not show the clear effects of higher order modes as the previous ones did (though they still seem to be present), but the entire design was quite different making it difficult to judge whether the absence of higher order modes was due to the post or not. We performed a simulation of the mode profile and propagation constant of a structure as the one in the paper by using Olympios by C2V since the bend mode solver from Photondesign was incapable of calculating the modes of this kind of structure. It showed no influence of the post on the first order mode which is surely the most important one to consider. The effective indices of the zeroth and first order mode (at the outer radius) for a 12 μm radius bend with and without post are summarized in Table 5.3.3 and show no significant differences.

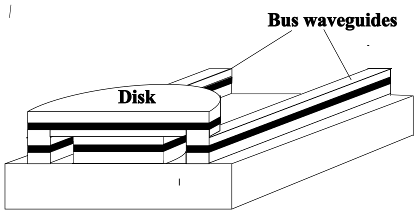

Figure 5.14: Use of a post underneath the microdisk

Without post	Quasi-TE	Quasi-TM
mode 0	3.01772	3.00104
mode 1	2.86646	2.85052
With post		
mode 0	3.01367	3.0008
mode 1	2.86223	2.8508

Table 5.2:

The mode profiles for the TE first order mode are shown in Fig.5.15. There is no real difference with and without post, and leakage of the mode with post to the transfer substrate is surely not clearly noticeable.

This leads us to believe that the post does not really influence the loss of the higher order modes but an improved design reduced coupling to these modes. Examples in Chapter 6 will show the influence of the position of the bus waveguides, the radius, the layer structure ... on the excitation of different modes in the ring. The post was however useful in this design for providing mechanical stability and improves current uniformity for active devices with current injection.

5.3.4 Good coupling

One can now wonder what the design rules are for creating a good coupler. As described in the second chapter, coupling should not be too high. But in general, especially in laterally coupled structures, when a large FSR has to be

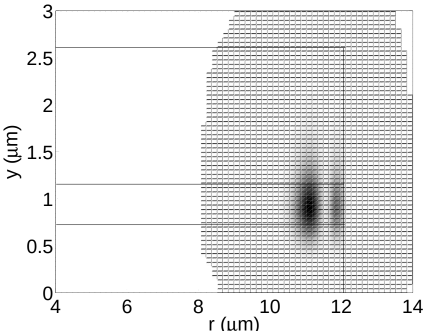

(a) Mode profile without a post

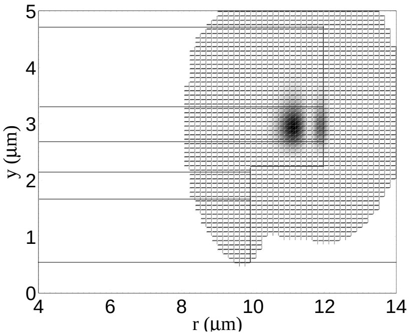

(b) Mode profile with a post

Figure 5.15: The mode profiles of a microdisk with and without post

combined with low radiation loss, everything has to be put into play to make the coupling coefficient as large as possible.

To achieve good coupling, often one refers to achieving good phase matching. This term, which stems from the classical directional coupler, is however very dubious when it comes to coupling between a straight and a bent waveguide. Matching an angular propagation constant and a classical propagation constant per unit length is not possible.

Apart from this problem, simulations indicate that for a structure where only the width of the straight waveguide is varied, thus changing the propagation constant of the straight waveguide, the coupling coefficient is quite tolerant to this change in width [19]. This clearly indicates the limited importance of ’phase matching’. Of course in all these simulations, the effect of the change in field overlap and the change in 'phase matching' could not be distinguished.

The relative weakness of the phase-matching requirement is understandable from the following point of view: if the microring is very small, the region where sufficient field overlap exists to provide possible coupling is quite small. However, due to the sharp bend, the propagation constant of the bend mode, as seen from the straight waveguide, varies considerably, allowing for a large range of propagation constants to couple and relaxing the phase-matching requirement.

Another way to increase the coupling is decreasing the gap between the straight and the bent waveguide which always results in an increase in the coupling coefficient for small microrings. For larger rings, since the coupling region is larger, situations where the power in the ring couples back to the bus are possible, thus decreasing the coupling again.

The coupled mode theory starts to lose its validity when the gap becomes too small and thus the coupling too strong.

5.3.5 Lossy coupler

So far we have assumed that the coupler section was lossless. This is however not necessarily true. When the coupler is not lossless this can lead to detrimental effects for the microring. It is not so much the power loss that compromises the performance but the fact that this alters the phase response in the coupler section. In Chapter 2 it was shown that that the coupler had to be lossless to prove their is a 90 degree phase shift between the wave in the ring and the wave in the bus waveguide. In a lossy coupler this is not necessarily the case, resulting in an undesired distortion of the transfer function. An example is shown in Fig. 5.16 where only a phase distortion of 5 degrees was introduced. As far as the power transmission response is concerned, the effect is only clear in the pass port. In the drop port, the resonance condition is still that the optical path length in the ring is an integer times the wavelength in the ring. However, in the pass port destructive interference has to take place between the power not coupled into the ring and the power coupled into the ring, and coupled back. The phase distortion causes the minimum to shift to other wavelengths.

Little attention has been given to this distortion and only for racetrack ring resonators [20]. They are of course easier to simulate and more intuitive to study. The directional couplers are usually symmetric ones, allowing for lossless coupling. However, from a supermode point of view it is easy to imagine how a phase distortion can be induced. The input coming from the

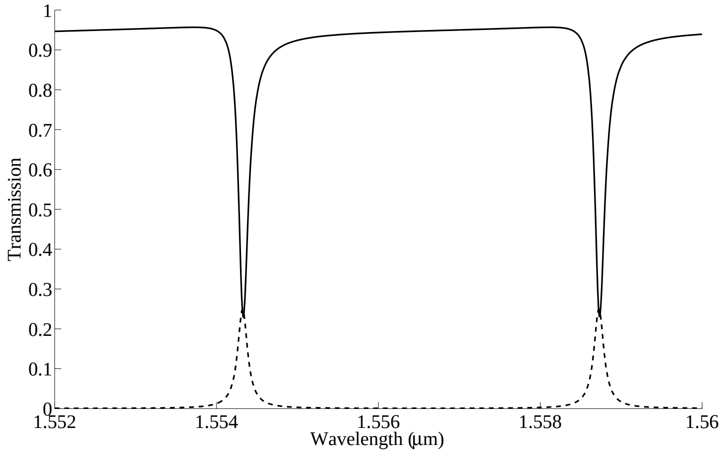

Figure 5.16: The effect of a lossy coupling section on the transfer function

straight bus waveguides couples equally to the even and the uneven supermode of the system. Due to the field profile of the supermodes it is easy to imagine that the even and the uneven supermode do not exhibit the same amount of loss. For instance, if some dust particles or roughness are located in the gap, the even supermode will mainly suffer, since the field of the uneven supermode is zero in the center of the gap. This unbalance in loss causes the phase shift to be different from $\pi/2$ at the end of the coupling section. These racetrack resonators are usually designed to be single mode, both the bent waveguide and the bus waveguide are very small. So coupling to higher order modes does not come into play here. A description of a racetrack resonator with a lossy directional coupler in the coupling section can be found in ref. [21].

Examples of rings where this asymmetrical distortion in the amplitude response of the pass port can be seen are primarily racetrack resonators. Losses in the coupler can be due to two things: first of all, part of the power can be coupled to higher order guided modes, or second, to radiative modes (loss). The first case is not exactly loss but can cause strange effects as will be described further. In microrings or microdisks the phenomenon hasn't been reported yet. Of course if it is small it can be difficult to see, because the one-level of the pass port tends to be noisy due to fabry-perot resonances and often AR-coatings are not good enough to completely remove these fringes.

In ref. [19] general equations can be found for the transfer function of a microring resonator with a lossy coupler.

5.3.6 Bend coupling

As was introduced in Chapter 3 one technique to increase the coupling efficiency is by using bent bus waveguides to increase the coupling region without decreasing the FSR. The layout is illustrated in Fig. 5.17.

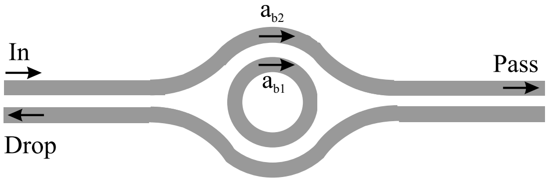

Figure 5.17: Layout of microring resonator coupled to bent waveguides

The complete coupled mode equations as derived in [12] from the Lorentz reciprocity theorem [11] can equally be derived in cylindrical coordinates leading to very similar equations. By neglecting higher order terms as is the case for the derivation of the classical coupled mode equations [10], one easily obtains the classical equations:

$$\frac{da_{b1}}{d\phi} = ic_1 a_{b2} e^{-j(\gamma_1-\gamma_2)}$$
$$\frac{da_{b2}}{d\phi} = ic_2 a_{b1} e^{-j(\gamma_1-\gamma_2)}$$

where a_{b1} and a_{b2} are the amplitudes of the modes in inner and outer bent waveguide and γ_1 and γ_2 are their angular propagation constants. c_1 and c_2 can be calculated analagously to the classical coupled mode equations but in cylindrical coordinates. The same conclusions hold therefore as for the directional coupler: to have considerable change of power between the two bent waveguides, their angular propagation constants have to be phase matched. Since the outer bend has a larger radius this usually means that it has a larger angular propagation constant, this can be compensated for by adjusting the width of the bend, for instance making the outer bend wider. This is illustrated in Fig. 5.18 which shows the angular propagation constant γ for a 10 μm outer radius and a 10.2 μm inner radius bend in a typical InP layerstack as a function of the waveguide width. By designing the inner waveguide with a width of 0.55 μm and the outer with a width of 0.85 μm, phase matching is achieved. Both waveguides should also not be placed too far away from each other. The interaction length is limited due to the radius of the microring.

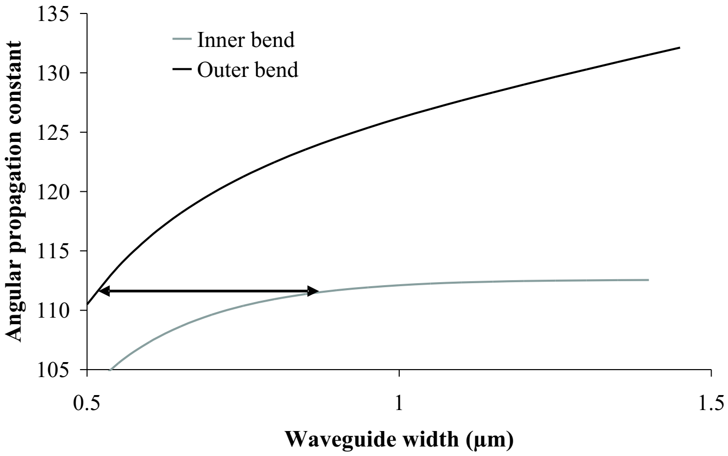

Figure 5.18: The angular propagation constant of a 10 μm outer radius and a 10.2 μm inner radius bend as a function of the waveguide width

5.4 Tying it together

Now that we have calculated the bend modes and the coupling coefficients between the different modes, these can be brought together to calculate the wavelength response of the microring. Fig. 5.19 illustrates the combination of the different pieces.

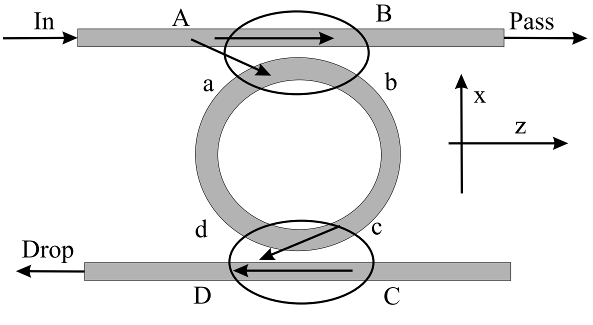

Figure 5.19: Calculating the wavelength response of the microring

The top coupling section is described by the following equations:

$$\begin{pmatrix} B_1 \\ B_2 \\ \vdots \\ B_{N_s} \\ b_1 \\ b_2 \\ \vdots \\ b_{N_b} \end{pmatrix} = \begin{pmatrix} \rho_{11} & \rho_{21} & \dots & \rho_{N_s1} & \kappa_{11} & \kappa_{21} & \dots & \kappa_{N_b1} \\ \rho_{12} & \rho_{22} & \dots & \rho_{N_s2} & \kappa_{12} & \kappa_{22} & \dots & \kappa_{N_b2} \\ \vdots & & & & & & & \\ \rho_{1N_s} & \rho_{2N_s} & \dots & \rho_{N_sN_s} & \kappa_{1N_s} & \kappa_{2N_s} & \dots & \kappa_{N_bN_s} \\ \kappa_{11} & \kappa_{21} & \dots & \kappa_{N_s1} & \tau_{11} & \tau_{21} & \dots & \tau_{N_b1} \\ \kappa_{12} & \kappa_{22} & \dots & \kappa_{N_s2} & \tau_{12} & \tau_{22} & \dots & \tau_{N_b2} \\ \vdots & & & & & & & \\ \kappa_{1N_b} & \kappa_{2N_b} & \dots & \kappa_{N_sN_b} & \tau_{1N_b} & \tau_{2N_b} & \dots & \tau_{N_bN_b} \end{pmatrix} \begin{pmatrix} A_1 \\ A_2 \\ \vdots \\ A_{N_s} \\ a_1 \\ a_2 \\ \vdots \\ a_{N_b} \end{pmatrix}$$

Similar equations hold for the other coupling section.

The subscripts indicate the mode numbers: the first one, the mode where the signal came from, the second, the mode to which it couples. Because of reciprocity the matrix is symmetrical and can be simplified:

$$\begin{aligned} \kappa_{ij} &= \kappa_{ji} \\ \rho_{ij} &= \rho_{ji} \\ \tau_{ij} &= \tau_{ji} \end{aligned}$$

The amplitudes at different places in the bent waveguide can easily be related by the following equations:

$$\begin{aligned} c_i &= b_i exp(-j\phi_i/2) exp(-\alpha_i L) \\ a_i &= d_i exp(-j\phi_i/2) exp(-\alpha_i L) \end{aligned}$$

α_i is the amplitude loss coefficient related to mode i of the bend and ϕ_i is related to the phase change of mode i of the bend by propagation over half the circumference of the ring:

$$\phi_i = \frac{2\pi n_i 2L}{\lambda} \tag{5.6}$$

L is half of the circumference of the ring, and to be more exact should not include the regions covered by the coupling model. n_i should be defined at the same radius that is used for the calculation of the length L, alternatively the angular propagation constant can be used.

The modes and therefore the coupling coefficients are calculated for one particular wavelength. To accurately simulate a microring over a large wavelength range the modes would have to be calculated at different wavelengths as the coupling is known to change quite significantly with the wavelength [1]. We have however only considered the wavelength dependence as it appears in eq. 5.6.

If we calculate this for a structure with one straight waveguide mode, two bend modes and for simplicity assume there is only one bus waveguide, we get the following equations:

$$\frac{B_1}{A_1} = \rho_{11} + \frac{\kappa_{11}^2 P_1 + \kappa_{21} P_2 - (\kappa_{11}^2 \tau_{22} - 2\kappa_{11}\kappa_{21}\tau_{21} + \kappa_{21}^2 \tau_{11}) P_1 P_2}{(1 - \tau_{11} P_1)(1 - \tau_{22} P_2) - \tau_{21}^2 P_1 P_2}$$

with

$$\begin{aligned} P_1 &= exp(-\alpha_1 2\pi R_r) exp(-j\phi_1) \\ P_2 &= exp(-\alpha_2 2\pi R_r) exp(-j\phi_2) \end{aligned}$$

If we compare this with the equation for an all-pass microring with one mode in the bus waveguide and one in the ring, we see some similarities. ρ_{11} is the part of the input power that travels past the microring unhindered. The second and third term are also familiar even though the denominator has become more complex. It is clear that when higher order modes come into play, the response it not just the sum of the different responses associated with the different modes.

5.5 Polarisation dependence and rotation

5.5.1 Polarization dependence

Microring resonators tend to have an inherently strong polarization dependent behaviour. The two polarizations have different propagation constants in the microring and thus different resonance wavelengths. Making devices polarization-independent is very difficult then and requires tight fabrication control. To obtain polarization-independent behaviour, the height and width of the waveguides has to be chosen carefully, thereby severly limiting the design freedom. Several suggestions have been made to make polarization-insensitive devices but none are really satisfactory to the author's opinion. Headly et al. fabricated polarization-independent racetrack resonators in SOI

[22]. They are however only polarization-independent over a wavelength range of less ten 1 nm and have large radii of 400 μm. Little reports on more extensive polarization control in smaller microrings [23, 24]. Kokubun reported on a glass microring resonator that was polarization-independent through the use of birefringent polymer overlay [25]. The approach of using polarization diversity seems the most promising. Here the incoming signal is split into two orthognonal polarizations and one of the states is rotated. Identical operations are then performed in parallel and after this polarization is converted back to its original state and both the polarizations are combined again. An example of using microrings in this scheme is discusses by Klunder [26].

5.5.2 Polarization rotation

As explained before, bent waveguides can contain hybrid modes. These hybrid modes can cause polarization rotation in the microring. First, it is interesting to clearly state the origin of this polarization rotation. In literature one can find misleading statements which lead to believe that the modes in the bent waveguide of the microring are no longer orthogonal due to their hybrid nature and therefore couple. This is a faulty assumption: the modes of a bent waveguide, be it hybrid or not, are still orthogonal in the most strict sense as described by the following equation (where B is a constant)

$$\int \underline{E}(\rho) \times \underline{H}^*(\rho')dA = B\delta(\rho - \rho')$$

This orthogonality relation holds for all structures where the refractive indices are real quantities [27]. The polarization rotation that occurs in a microring resonator happens in the following way. If, for simplicity, we assume that the zero order modes in the straight waveguide are purely TE and TM polarized, then both of these can couple to the hybrid mode in the microring. A TE mode injected in the straight waveguide can couple to the hybrid mode and the hybrid mode can then couple to the TE and the TM mode in the output waveguide [28]. On top of that, part of the hybrid mode can couple back to the TM mode in the input waveguide. Usually coupling to the other zero order hybrid mode in the microring is also possible because of its similar field profile and propagation constant. The hybrid mode in the microring acts as an intermediate level, allowing power to transfer from one polarization to another.

Melloni [29] discussed the effect of polarization rotation in microrings for all-pass racetrack microring resonators. The modes of the straight waveguide section of the microring were used as local modes in a coupled mode theory. The assumption was also made that both modes in the straight waveguide section had the same propagation constant and coupling coefficient. By injecting for instance pure TE in the bus waveguide, this will then couple to pure TE in the straight section of the racetrack. At the transition from straight to bend, both the hybrid modes of the bent waveguide will be excited. By proper design and choice of the length of the bend section, part of the field of the bent waveguide will couple into the TM of the straight waveguide section, where it will couple back to the TM of the pass port. Melloni shows that by proper design a nearly 100 % polarization conversion can take place at resonances.

It is clear that this technique is not an option for real circular microring resonators. There, the full-vectorial 3D calculation of the coupling between the two zero order hybrid modes in the ring and both the polarisations in the bus waveguide by means of the coupled mode equations discussed earlier, inserted into the model for the microring, is a better alternative.

If we were to consider the case of an all-pass microring with two polarisations TE and TM in the bus waveguide and two hybrid modes in the ring, the whole equation for the transfer function at the pass port could be derived as was done in the previous section. Some example of this will be shown in Chapter 6.

Also, when the bus mode can couple to two hybrid modes in the ring, the reasoning followed in Chapter 2 concerning the phase jump at the coupling section is no longer valid and again, the phase relation can be compromised.

5.6 Counter-directional coupling

Another detrimental effect for microring resonators is counterdirectional coupling due to surface roughness. As discussed in Chapter 2, surface roughness causes scatter losses and loss is of great influence on the performance of the microring, for instance the Q-factor will drop with the increase of this scatter loss. Another effect of surface roughness however, is that it can lead to backreflection into the counter-propagating mode. Even a small reflection can cause large effects. This causes the microring resonator to become more of a standing wave resonator instead of a travelling wave resonator. A travelling wave resonator can completely extract the input power from the input waveguide, a standing wave resonator needs two resonators to achieve this goal [30]. A second effect is that the resonant peak splits. This was theoretically explained by Little and Laine [31]. In this model, the backreflections of the surface roughness were grouped in a lumped reflectivity coefficient. This only needs to be of the order of the power coupling coefficient in the ring to degrade the performance.

An experimental example of this can be seen in the following graphs. These are measurements of the drop and pass port of a 5 μm radius microring resonator fabricated in SOI by a colleague. The coupling coefficient was very low, estimated around 3%. Apparently this was too low to overcome the backreflections from the surface roughness, the split peak can clearly be seen in Fig. 5.20. By spinning BCB onto this structure, thus filling the gap between the straight and the bent waveguide with a higher index contrast material, the coupling coefficient could be increased. Fig. 5.21 is a measurement of the same microring resonator but with a BCB cladding, the peak splitting has disappeared. Fig. 5.22 is a 2D simulation of the coupling coefficient by means of the coupled mode theory explained before, which clearly shows the increase in the coupling coefficient by applying the BCB cladding.

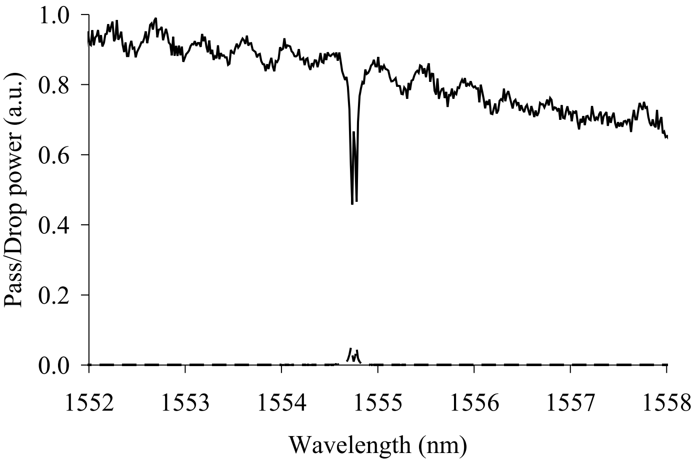

Figure 5.20: Measurement of a 5 μm radius SOI microring with clear splitting of the resonant peak

5.7 Losses

As was elaborated upon in the previous section, 3D simulations tools can be used to calculate the inherent radiation losses of bent waveguides. This is useful to design the bend to limit these losses to a low enough level, usually by increasing the refractive index difference between core and cladding. The radiation loss is however only one part of the total loss of a microring, in real

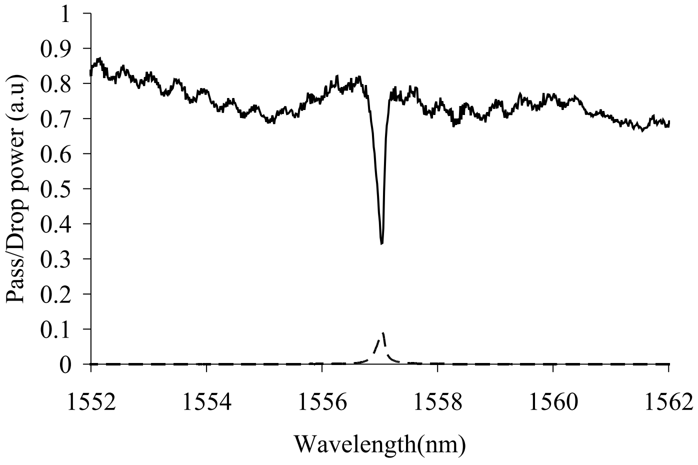

Figure 5.21: Measurement of the same microring but with BCB cladding

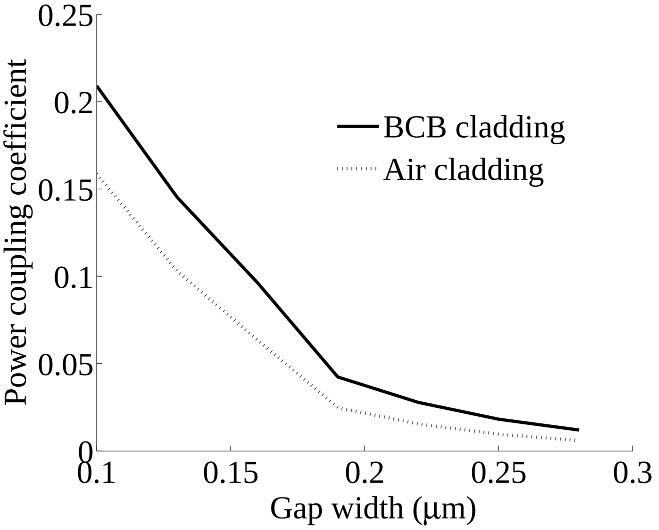

Figure 5.22: Simulation of the coupling coefficient of this microring versus the gap width with air cladding and with BCB cladding

life the scatter loss is far more important. This scatter loss (per unit length) is commonly known to be proportional to the refractive index contrast between core and cladding (in a 2D model) [32, 33]:

$$\alpha_{scatter} \sim (n_{core}^2 - n_{clad}^2)\frac{E_s^2}{\beta}$$

where β is the modal propagation constant, E$_s$ is the field at the core-cladding interface and σ is the root mean square of the surface roughness.

Two things are the consequence of this behaviour: First of all the index contrasts used to fabricate passive microrings are usually too high to achieve optimum behaviour. The refractive index contrast can often be a lot lower to still achieve negligible radiation loss and at the same time, scatter losses are greatly reduced.

A second remark is the fact that the losses do not rise monotonously with decreasing radius if we look at the losses per 90 degrees, which is what is relevant for a microring. In a 2D approach one can show that the radiation loss increases exponentially with decreasing radius as follows [2]:

$$loss_{radiation} = AR^{-3/2}exp(-BR)[dB/90^0]$$

The scatter loss however can decrease with decreasing radius. Even though the field strength on the outer edge of the bent waveguide increases when the radius drops and causes the scatter loss to rise, this can be compensated by the decrease of the circumference. The total loss per 90 degrees then has as slight minimum at a certain radius, goes up exponentially for very small radii in the region where radiation loss is dominant and is slightly higher than the minimum for large radii in the region where scatter loss dominates.(Fig. 5.23) The location of this minimum is of course very dependent upon the refractive index contrast and the processing technology. For very high index contrast, the radiation loss can still be neglible for radii down to 1 μm.

For other configurations such as the racetrack resonator, loss contributions such as transition losses at the junction between straight and bent waveguide are important too of course but these will not be discussed here [32].

5.8 Summary

In this Chapter the simulation of microring resonators has been discussed. Different possibilities have been evaluated: simulating the entire structure in one piece and splitting up the component in bent waveguides and coupling sections. The latter approach proved to be the most interesting. Several simulation programmes for the calculation of bent waveguide modes were evaluated. For the calculation of the coupling section the full coupled mode theory was found to be the most accurate and usefull combining physical insight

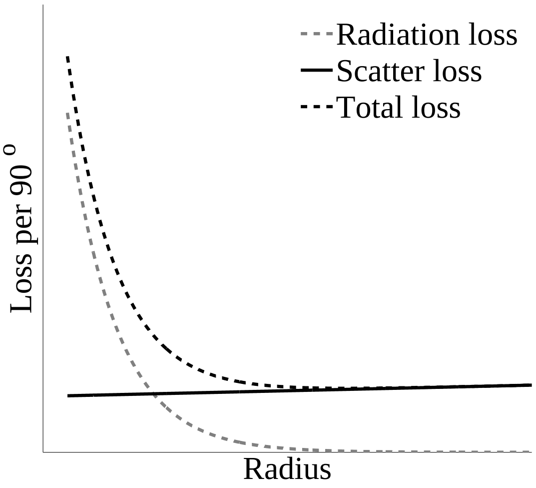

Figure 5.23: The different loss contributions in a microring resonator

with limited calculation times both in 2D and 3D. Finally some non-ideal behaviour such as the excitation of higher order modes, counter-directional coupling, polarization conversion, . . . is discussed.

Bibliography

[1] S.C. Hagness et al. FDTD microcavity simulations: design and experimental realization of waveguide-coupled single-mode ring and whispering-gallery-mode disk resonators. *Journal of Lightwave technology*, 15(11):2154–2165, November 1997.

[2] E. C. M. Pennings. *Bends in optical ridge waveguides*. PhD thesis, Technical University Delft, 1990.

[3] Mordehai Heiblum. Analysis of curved optical waveguides by conformal transformation. *IEEE Journal of Quantum Electronics*, 11(2):75–83, February 1975.

[4] I.C. Goyal et al. Bent planar waveguides and whispering gallery modes: a new method of analysis. *Journal of Lightwave Technology*, 8(5):768–773, May 1990.

[5] *Fimmwave*. www.photond.com.

[6] *APSS*. www.apollophoton.com.

[7] *Olympios*. www.C2V.nl.

[8] Peter Bienstman. *Rigorous and efficient modelling of wavelength scale photonic components*. PhD thesis, Ghent University, Belgium, 2001.

[9] Ladislav Prkna. *Rotationally symmetric resonant devices in integrated optics*. PhD thesis, Faculty of Mathematics and Physics, Charles University, Prague, July 2004.

[10] Dietrich Marcuse. *Light Transmission Optics*. Bell Laboratories Series, 1972.

[11] C. Vassallo. *Optical Waveguide Concepts*. Elsevier, 1991.

[12] Remco Stoffer et al. Comparison of coupled mode theory and FDTD simulations of coupling between bent and straight optical waveguides. In Francesco Michelotti, Alfred Driessen, and Mario Bertolotti, editors, *Microresonators as building blocks for VLSI photonics*, pages 366–377. American institute of Physics, October 2003. (International school of quantum electronics, 39th course).

[13] Remco Stoffer et al. Simulations of vertically-coupled microdisk resonators by 3-D vectorial coupled mode theory. In *ECIO 2005*, April 2005.

[14] D.R. Rowland and J.D. Love. Evanescent wave coupling of whispering gallery modes of a dielectric cylinder. *IEE Proceedings - J*, 14(3):177–188, June 1993.

[15] M. Matsuhara and A. Watanabe. Coupling of curved transmission lines, and application to optical directional couplers. *Journal of the Optical Society of America*, 65(2):163–168, Febuary 1975.

[16] Kostadin Dimitrov Djordjev. *Active microdisk resonant devices and semiconductor optical equalizers as building blocks for future photonic circuitry*. PhD thesis, University of Southern California, U.S., December 2002.

[17] K. R. Hiremath et al. Multimode circular integrated optical microresonators: coupled mode theory modelling. In *9th IEEE Leos Benelux symposium*, 2004. Ghent.

[18] Kostadin Djordjev et al. High-Q vertically coupled InP microdisk resonators. *IEEE Photonics Technology Letters*, 14(3):331–333, March 2002.

[19] M. Hammer et al. *Microresonators as building blocks for VLSI photonics*, chapter Microresonator devices, pages 48–72. October 2004. (International school of quantum electronics, 39th course).

[20] A. Melloni et al. Circuit-oriented modelling of ring-resonators. In *Optical waveguide Theory and Numerical Modelling (OWTNM)*, 2004.

[21] Hyun Shik Lee et al. A nonunitary transfer matrix method for practical analysis of racetrack microresonator waveguide. *IEEE Photonics Technology Letters*, 16(4):1086–1088, April 2004.

[22] W. R. Headley et al. Polarization-independent optical racetrack resonators using rib waveguides on silicon-on-insulator. *Applied Physics Letters*, 85(23):5523–5525, December 2004.

[23] B.E. Little et al. Very high-order microring resonator filters for WDM applications. *IEEE Photonics Technology Letters*, 16(10):2263–2265, October 2004.

[24] B.E. Little. Advances in microring resonators. In *Integrated Photonics Research 2003*, 2003.

[25] Y. Kokubun et al. Polarisation-independent vertically coupled microring resonator filter. *IEE Electronics Letters*, 37(2):90–92, January 2001.

[26] Dion J.W. Klunder et al. A novel polarization-independent wavelength division-multiplexing filter based on cylindrical microresonators. *IEEE Journal of Selected Topics in Quantum Electronics*, 8(6):1294–1299, November/December 2002.

[27] Dietrich Marcuse. *Theory of dielectric optical waveguides*. Bell Laboratories Series, 1974.

[28] Brent E. Little and Sai T. Chu. Theory of polarization rotation and conversion in vertically coupled microresonators. *IEEE Photonics Technology Letters*, 12(4):401–403, April 2000.

[29] A. Melloni. Polarization conversion in ring-resonator phase shifters. *Optics Letters*, 29(23):2785–2787, December 2004.

[30] Manoulatou et al. Coupling of modes analysis of resonant channel add-drop filters. *IEEE Journal of Quantum Electronics*, 35:1322–1331, 1999.

[31] Brent E. Little and Juha-Pekka Laine. Surface-roughness-induced contradirectional coupling in rings and disk resonators. *Optics Letters*, 22(1):4–6, January 1997.

[32] V. Van et al. Propagation loss in single-mode GaAs-AlGaAs microring resonators: measurement and model. *Journal of Lightwave Technology*, 19(11):1734–1739, November 2001.

[33] P. K. Tien. Light waves in thin films and integrated optics. *Applied Optics*, 10:2395–2419, November 1971.

Chapter 6

Fabrication and measurement of devices

In this chapter the fabrication of devices and simulations on these structures will be discussed. We will start off with a brief summary of the processing, which comprises several elements introduced in the preceding chapters.

6.1 Fabrication

6.1.1 Entire processing

The entire processing sequence used here is illustrated in Fig. 6.1. It starts off with the epitaxial layer structure, comprises of two waveguide core layers and a waveguide etch stop layer just above the substrate, Fig. 6.1(a). The layer thicknesses used for most of the passive microrings fabricated here can be found in Table 6.1. Next, the bus waveguides are etched to a depth of 1 μm, so they are etched completely through the core layer, Fig. 6.1(b). A SiO_2 hard mask is used for the etching, which is done with a methane and hydrogen RIE process. The bus waveguides have a width of 800 nm, 1 μm or 1.4 μm. They widen to 3 μm to facilitate in- and output coupling. In a next lithography and etch step, alignment markers are defined, which are etched more deeply to allow aligning the microring with the bus waveguides from the backside. Because the waveguides have already been etched quite deeply, a thick layer of photoresist or even two layers of photoresist have to be used to cover the structures well and provide a sufficiently thick layer on top of the ridges to act as a mask for the etching. Next the wafer is bonded upside down onto a transfer substrate (which is GaAs) with BCB. The procedure for this is described in Chapter 4. The original InP substrate is then removed

	Composition	Layer thickness	Refractive index
Cladding layer	InP	300 nm	3.16
Bus waveguide core layer	Q(1.3μm)	500 nm	3.36
Separation layer	InP	500 nm	3.16
Ring waveguide core layer	Q(1.3μm)	500 nm	3.36
Cladding layer	InP	300 nm	3.16
Etch stop layer	Q(1.3μm)	200 nm	3.36
Substrate	InP		3.16

Table 6.1: Layer structure 1

making the alignment markers visible, Fig. 6.1(c). The microring is now lithographically defined and etched to a depth of 1 μm. In this way a thin layer (with thickness t usually around 200 nm) of InP is not etched as depicted in Fig. 6.1(d). The purpose of this layer is to alleviate alignment tolerances. This is discussed in more detail in the following paragraph.

Afterwards the device is cleaved and AR-coated to remove Fabry-Perot fringes from reflections at the cavities. The quality of this coating varied somewhat from sample to sample so Fabry-Perot fringes were not always removed that well.

6.1.2 Unetched InP middle layer

The coupling coefficients are sensitive to misalignment of the microring with respect to the bus waveguides. To make the design more tolerant, a middle layer of InP with thickness t is left unetched. The field profile of the bent waveguide spreads out laterally due to this layer and causes the field overlap to be less influenced by misalignment in the lateral direction. This layer should however not be too thick to avoid high radiation losses for sharp bends. Figure 6.2 shows a simulation (done with Fimmwave) of the radiation loss of a bent waveguide with the structure as described above, with a radius of 20 μm and a width of 1 μm, as a function of the thickness of the middle layer of InP. This is a simulation for only a moderately bent waveguide, radiation losses should stay negligible down to radii of 10 μm or even less. To limit the radiation loss, the unetched middle layer was always thinner than 300 nm. For thicknesses t below 500 nm the modes are clearly polarized. However in the region between 500 nm and 1 μm they become hybrid.

Simulations indicate that the effect of this layer on the alignment tolerance is small though. Fig. 6.3 shows a simulation of the influence of the alignment

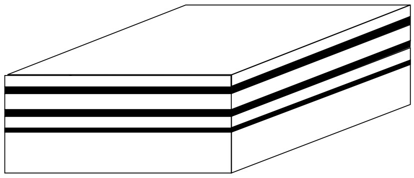

(a) The epitaxial layer structure

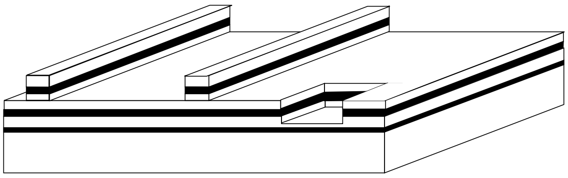

(b) The etching of the bus waveguides

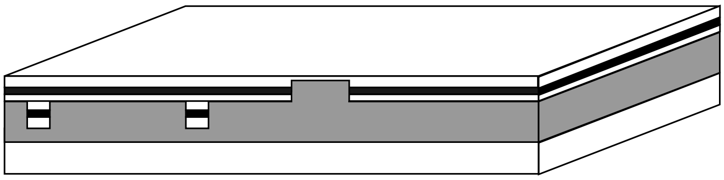

(c) The wafer bonding and substrate removal

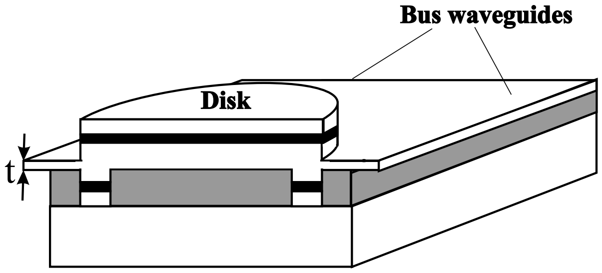

(d) The vertically coupled microdisk resonator

Figure 6.1: The processing sequence for vertically coupled microring resonators fabricated with wafer bonding

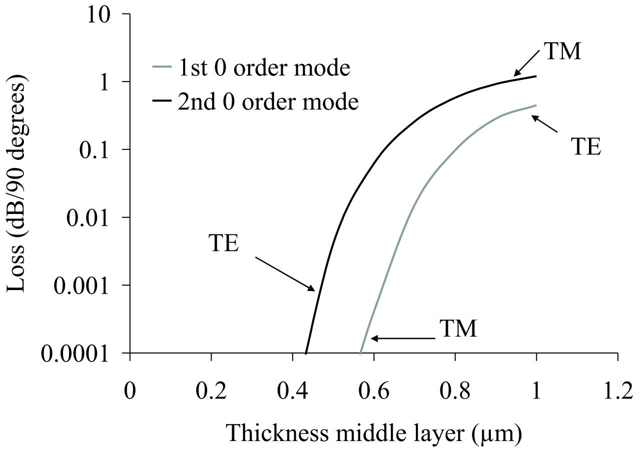

Figure 6.2: Radiation loss as a function of the thickness of the middle layer for a 20 μm radius bend 1 μm wide

on the coupling of a 10 μm radius disk to a 0.8 μm wide bus waveguide in the case where no middle layer is left and the case where a 300 nm middle layer is left. The coupling coefficients were scaled so that they both have a maximum of one, to make comparison easier. The shift of the bus waveguide with respect to the ring is defined in Fig. 6.5 and is negative when the bus waveguides shift inwards. The middle layer has a positive influence on the alignment tolerance. Especially around the maximum a fairly flat top can be seen but the effect of misalignment on the coupling coefficient is still large considering the fact that an alignment tolerance of ± 300 nm had to be taken into account.

Because this middle layer did not make the device tolerant enough to misalignment, the mask was designed containing multiple identical microrings that only differed in their alignment with the bus waveguides. One microring was on mask perfectly symmetrically aligned with the bus waveguides and two other microrings had an offset of ±160 nm compared to the bus waveguides. This allowed for at least one fairly symmetrically aligned microring after fabrication. To increase alignment accuracy, Vernier structures were added to the traditional alignment structures. These can be seen in Fig. 6.4 where good alignment can be seen in the vertical direction but not in the horizontal direction.

The alignment tolerances were supposed to be in the range of 300 nm on either side but sometimes errors greater than this were observed. This was probably partly due to the presence of the ramps (see Chapter 4) that

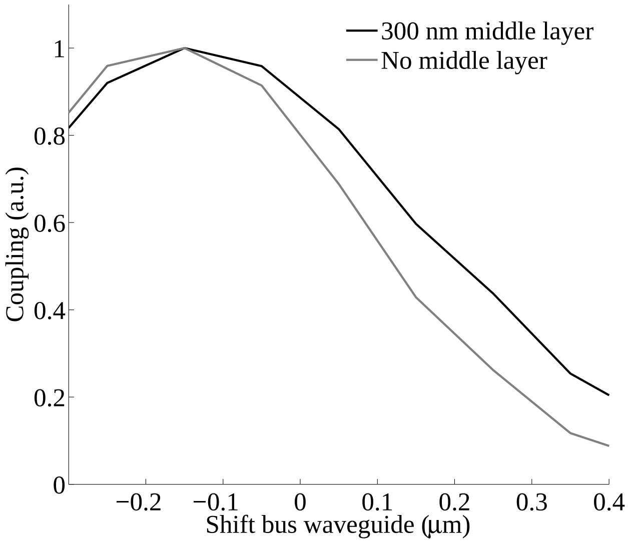

Figure 6.3: The influence of the thickness of the middle layer on the alignment tolerance for a 10μm disk coupled to a 0.8 μm wide bus waveguide

appeared on the edge of the membrane after substrate removal. Because we use contact alignment for the lithography this made alignment of the mask to the sample more difficult.

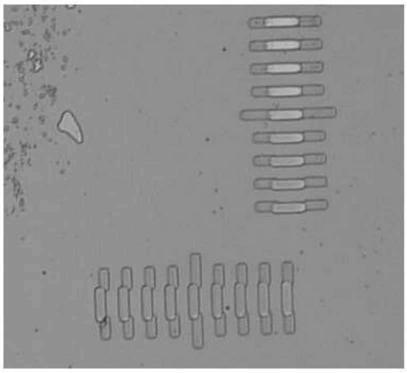

Figure 6.4: Vernier structures for alignment between the different lithography steps

The epitaxial wafers used were ordered from outside vendors and several times a large deviation (around 10%) of the desired layer thicknesses was observed. This sometimes resulted in the complete removal of the middle layer. The initial design was to use an unetched middle layer of 200 to 300 nm thickness.

6.1.3 Coupling simulations

First of all it is important to mention that these devices are in fact all membrane devices, thin layers of InP surrounded by low index contrast material. This makes for a very different situation compared to traditional InP based devices: even a straight waveguide of only 0.8 μm wide is highly multimodal. Apart from the zero order TE and TM modes, and the first order TE and TM modes in the lateral direction, higher order modes in the vertical direction also appear. However, simulations and measurements indicate that these higher order modes do not couple easily to the disk, due to 'phase mismatch' and limited field overlap. By positioning the lensed fiber for incoupling carefully, the higher order modes in the bus waveguide should also not be excited. When aligning the lensed fiber, the spot exiting the waveguide can be seen using an IR-camera. This spot does not have the shape of a higher order mode. On top of that the alignment is also optimized by using a power detector and optimizing the power output out of the waveguide. It is logical that the highest power would result from exciting the zero order mode.

Several 3D full-vectorial simulations were done on this structure. For the coupled-mode calculations the entire structure (Fig. 6.5) was split up into two pieces, illustrated in Figs. 6.6(a) and 6.6(b), that were used to calculate the individual modes of the straight and the bent waveguide.

The modes of a disk resonator were simulated and results show that there is a region of hybridness (as was explained in Section 5.2.2) where the modes do not have clear TE or TM polarizations. The region of hybridness is situated around a radius of 15 μm and can be seen in Fig. 6.7. Because the two modes are very similar in this region, they can both be excited by a single mode in the bus waveguide and this can result in polarization rotation.

6.2 Measurement set-up

The basic measurement set-up used is schematically depicted in Fig. 6.8. The set-up is changed depending on the measurement. It consists of a laser, tunable from 1.5 to 1.64 μm, coupled to fiber, which is led through a polarizer and spliced to a lensed fiber. The lensed fiber is used to launch the signal into the component. For most measurements the signal is then collected at the output by an objective and focused onto a detector. Alignment is done

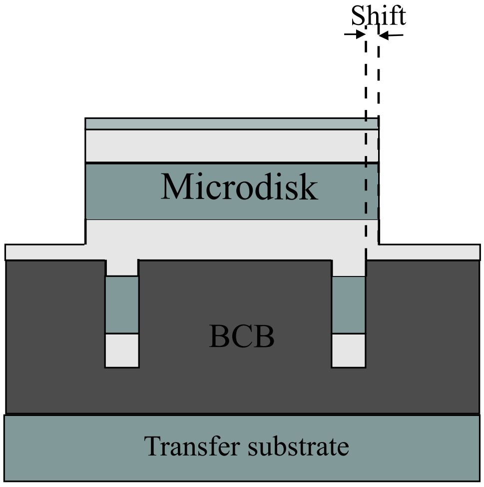

Figure 6.5: The complete structure for coupled mode simulations

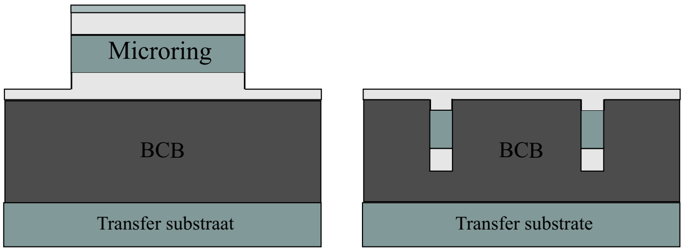

(a) The structure used for calculating the modes of the microdisk

(b) The structure used for calculating the modes of the straight waveguide

Figure 6.6: The two structures used as basis for the coupled mode calculation

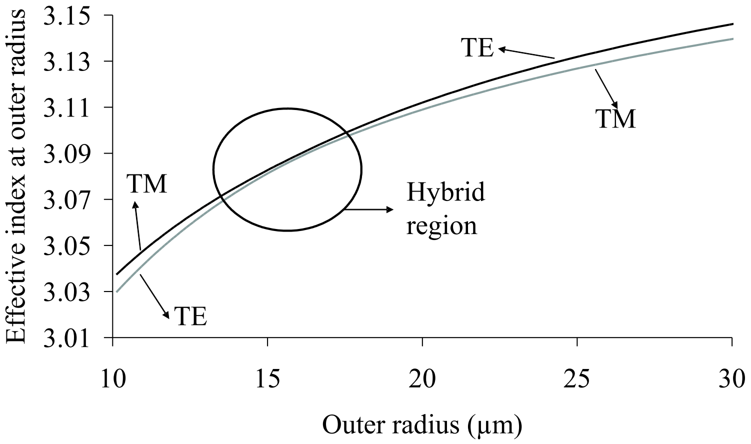

Figure 6.7: Calculation of the effective index of the two zero order bend modes to determine the region of radius where the modes are hybrid

by first visualizing the output signal onto an IR camera before inserting the detector. After incoupling had been optimized using the IR camera, the objective could easily be replaced by a lensed fiber allowing to lead the signal to an EDFA and an oscilloscope for visualization. An EDFA and attenuator can be added before the component to measure non-linear effects.

6.3 Fitting measurements

Extracting parameters such as coupling coefficients and loss from a measurement by means of fitting proved to be difficult in several cases. There are a number of reasons for this. As it is always possible that the coupling of the microring is asymmetric at least three parameters have to be fitted: the incoupling coefficient, the outcoupling coefficient and the roundtrip loss. To do this three quantities are measured: the finesse, the minimum reflection and the maximum transmission. From these three quantities the three parameters can be extracted. However the three measured quantities tend to differ from resonance to resonance. There is an error on the value of the maximum transmission, since to measure this the power has to pass a bend to be coupled to the output side for measurement as can be seen on Fig. 6.9. The straight waveguides in this figure were drawn next to the ring and not under the ring for clarity. The loss in this bend is not accurately known because

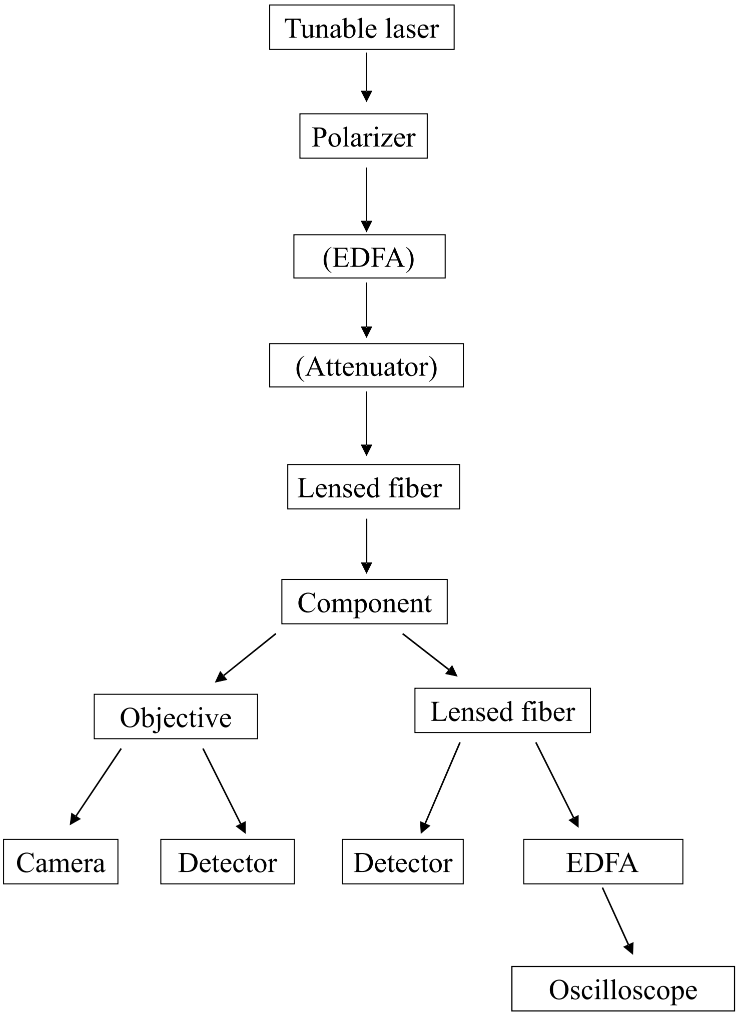

Figure 6.8: Measurement setup

the etching process was not good enough and showed a large spread in loss figures. The AR-coatings were not always perfect resulting in uncertainty on the minimum reflection.

The coupling coefficient can be estimated by simulation and then used to fit to the measurement. The problem is that it requires a destructive SEM measurement to determine the alignment accuracy, which influences the coupling coefficient to a large extent. The deviations in the thicknesses of the epitaxial layers from what was ordered, especially the thickness of the middle InP separation layer, influenced the coupling coefficient significantly. Figure 6.10 shows the influence of the thickness of this middle InP cladding layer on the coupling coefficient for the coupling of the zero order mode of the straight waveguide to the zero order TE mode of the bent waveguide, for a 30 μm radius disk. It was assumed that for all thicknesses the InP layer was etched 150 nm from the side of the bus waveguides and 150 nm from the side of the ring. This results in changes of the thickness of the middle layer left unetched but this is most representative of the case where a certain layer thickness is expected but not provided. Obviously the influence of this thickness on the coupling coefficient is large.

For microrings with higher order mode effects the problem becomes even more difficult due to the increased number of parameters to be fitted. However in cases of reasonably 'clean' measurements, fits were done.

There is one other parameter that needs to be fitted, which is the group index. This can be done easily by looking at the change of the FSR with the wavelength. Values obtained in this way correspond well with values calculated with Fimmwave, taking into account both the waveguide dispersion and the material dispersion and result in a group index around 3.85 for a 30 μm radius disk.

6.4 Measurements of passive devices

6.4.1 Radii outside the hybrid region

For the radii below and above the hybrid region (see Fig. 6.7) the following graphs show some simulations of coupling to waveguides with different widths and the influence of the shift of the bus waveguide.

- One mode in the bend excited

  In Fig. 6.11 the simulated coupling versus the alignment can be seen for a 0.8 μm, 1 μm and a 1.4 μm wide straight bus waveguide coupled to the zero order mode of a 20 μm radius disk. It is clear that for this radius,

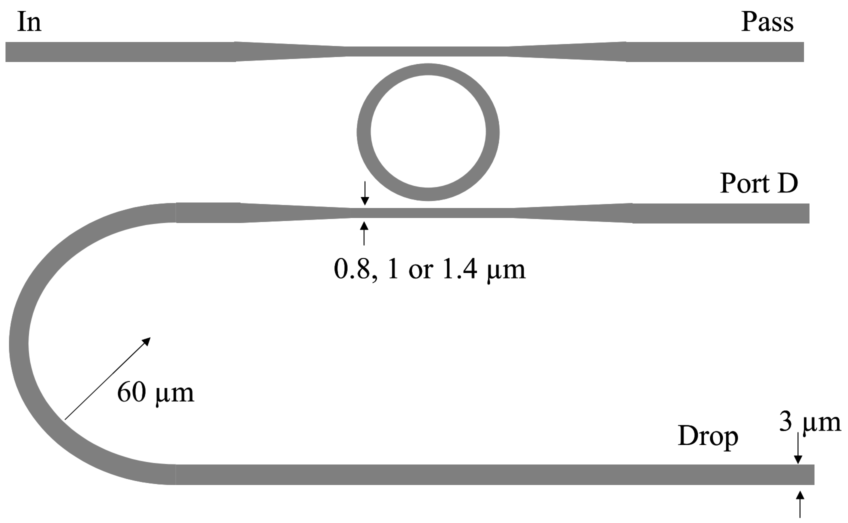

Figure 6.9: The layout of the microring on the mask, the pass port is coupled back to the righthand side for measurement

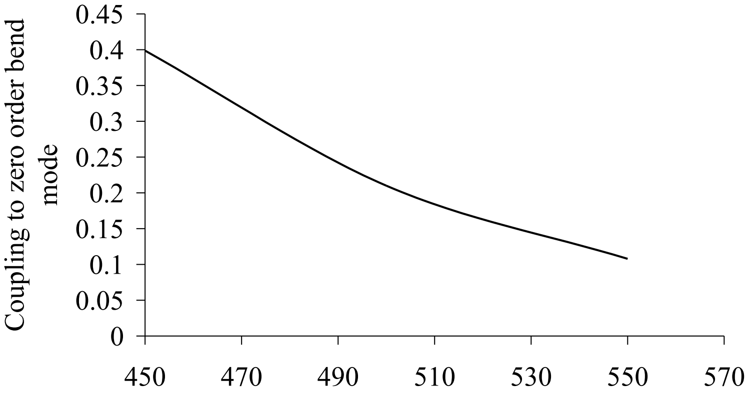

Figure 6.10: Influence of the thickness of the middle InP cladding layer on the coupling coefficient

the straight waveguide does not have to be smaller than 1 μm to achieve sufficient coupling, a narrower bus waveguide may even be too narrow for good coupling. With smaller waveguides one can try to achieve single mode waveguides. In the current layer structures this requires a waveguide width of 500 nm and this does not eliminate the vertical higher order modes. In a first design only bus waveguide widths of 1 μm and 1.4 μm were used because smaller waveguides could not be well defined with our lithography system.

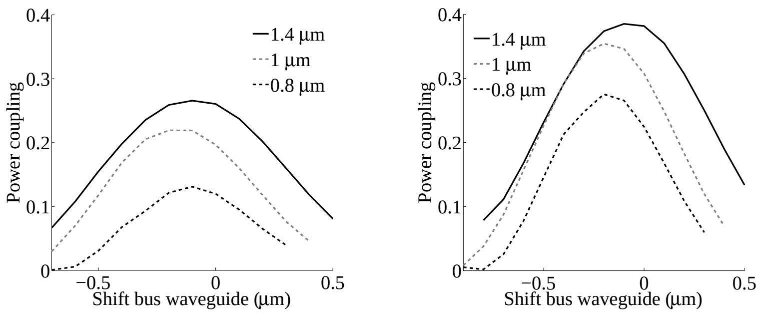

(a) TE

(b) TM

Figure 6.11: Coupling to zero order TE and TM bend mode for a 20 μm radius disk versus the alignment for different straight waveguides

Figure 6.12 shows a TE measurement of a 20 μm radius disk coupled to a 1.4 μm wide straight waveguide. The minimum reflection fluctuates with the wavelength, behaviour that can be observed in most microrings we fabricated. The explanation for this is probably a combination of several factors. First of all, the coupling coefficient is known to be wavelength dependent. In several microrings, counter-directional coupling appears because light can be observed at port D (see Fig. 6.9) which is probably also a wavelength dependent effect. Some slight fluctutation can still result from the AR-coatings not being perfect. Waveguide losses certainly also contain some wavelength dependence.

Figure 6.13 shows the coupling to the zero order mode of a 10 μm radius disk. Coupling is now better for a 1 μm wide waveguide but the difference is not that big. In a second design, waveguides widths down to 0.8 μm were included on the mask. This was possible only then because a new mask aligner had been purchased allowing to accurately define these smaller waveguides. Figure 6.14 shows a TE measurement

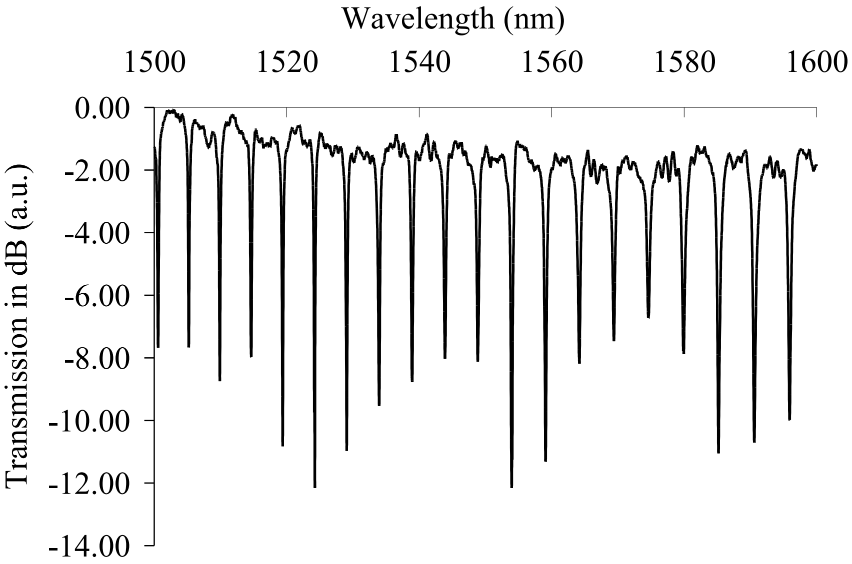

Figure 6.12: TE measurement of a 20 μm radius disk coupled to a 1.4 μm wide waveguide

of a 10 μm disk coupled to a 0.8 μm straight waveguide. This device had no AR-coatings on the facets and therefore there are Fabry-Perot fringes resulting from reflections on the facets. The FSR of this device is around 10 nm.

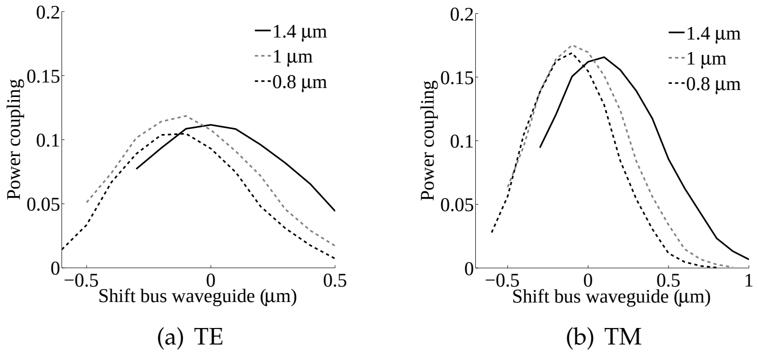

(a) TE

(b) TM

Figure 6.13: Coupling to zero order TE and TM bend mode for a 10 μm radius disk versus the alignment for different straight waveguides

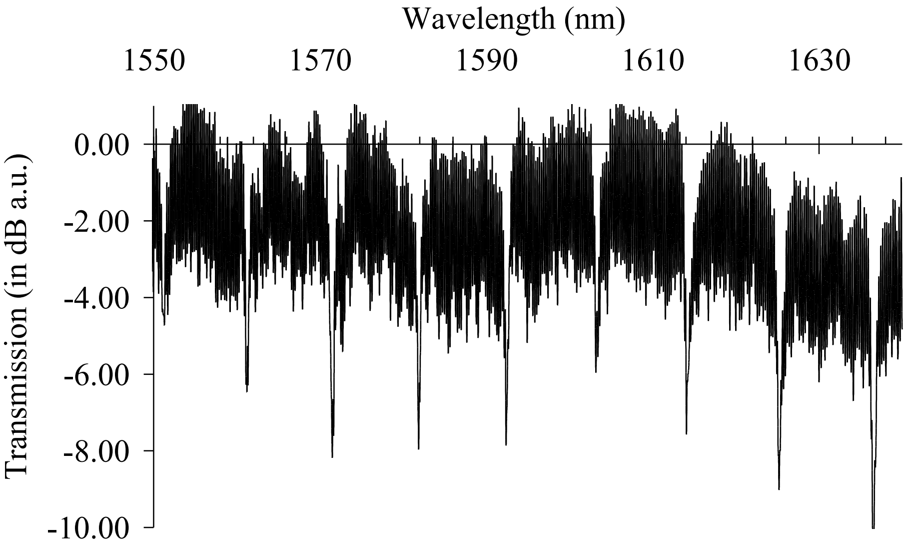

Figure 6.14: Measurement of the pass port of a 10 μm radius disk in TE

The masks contained both disks and rings but the best functionality always came from the disks, probably due to their lower scatter loss. This could be at the expense though of excitation of higher order modes in the disk if the design was not carefully made.

- Polarization influence

  If the microring has been designed properly one can stay clear from hybrid modes. It is then possible that the TE/TM-mode from the input bus waveguide couples well with the TE/TM mode of the microring respectively. Both polarisations are then clearly distinct as is illustrated in Fig. 6.15, which shows a measurement of a 30 μm radius disk, which has well defined polarizations.

- Excitation of higher order bend modes

  In Fig. 6.16 the calculation of the coupling from the zero order TE mode in the straight waveguide (1 μm wide) to the zero order, first order and second order TE mode in the disk can be seen for a radius of 30 μm as a function of z (propagation along the straight waveguide). This radius is out of the region of hybridness for the bent waveguide modes. The secondary peaks that were measured (which can be seen in Fig. 6.17) cannot be due to polarization rotation and result from excitation of the

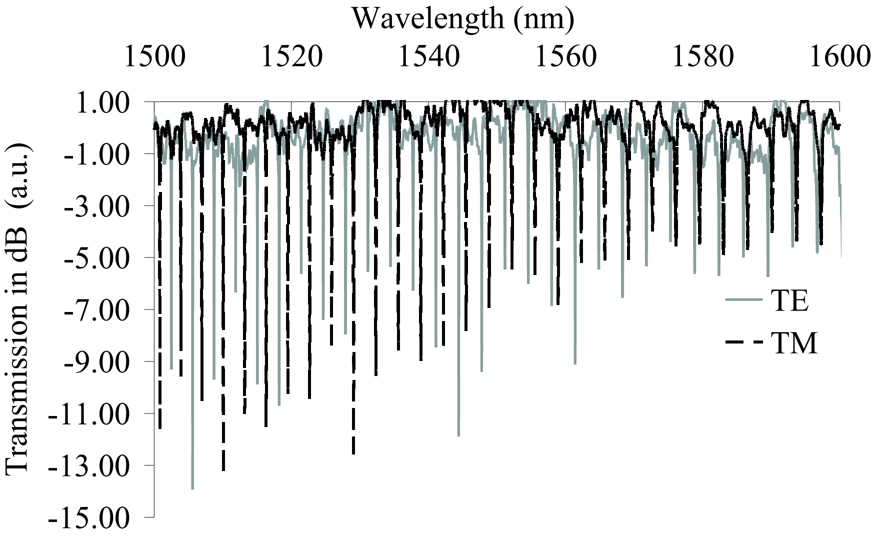

Figure 6.15: Response for the two different polarizations

higher order mode, which is clearly visible in Fig. 6.16. In the pass port some dips due to the second order bend mode are also visible but the excitation of this mode was quite weak. The same behaviour can be observed for TM in Fig. 6.18 where the effect of a second order mode in the microdisk is more clearly visible.

Figure 6.19 shows a complete simulation of the pass and drop port responses of a 30 μm radius disk. The simulation comprised coupling from the zero order TE mode of the straight waveguide to the zero order and first order TE mode of the bent waveguide. The procedure for this simulation was explained in Section 5.4. The simulation clearly displays the same behaviour as seen in Fig. 6.17 but the correspondence is not perfect. The measured peaks are around 0.15 nm wide, while the simulated ones are around 0.4 nm. Fitting indicates that the coupling coefficients are around 10%, this is lower than was expected and is a behaviour observed for all the microrings fabricated with this layer structure, which leads us to believe that it was grown somewhat too thick. Unfortunately no material remained to check this claim. From fitting, the losses for the bent waveguides in the microring were estimated to be around α = 7/cm. However, again, significant spread could be observed around this number, with losses up to 13/cm. This device had

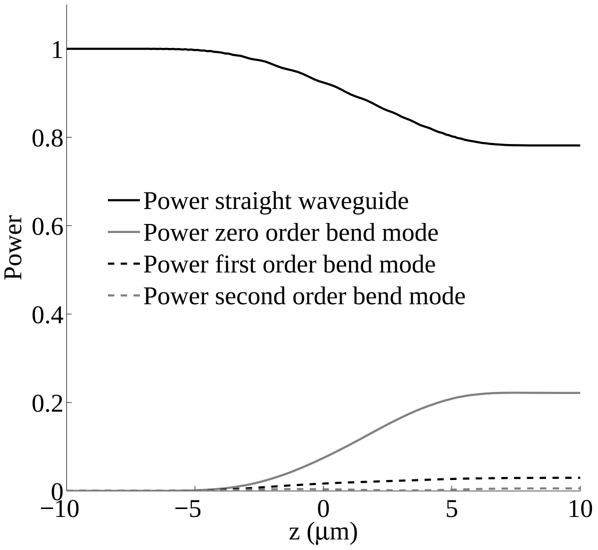

Figure 6.16: Simulation of the coupling of the zero order TE mode in the straight waveguide to the different TE modes in a 30 μm disk

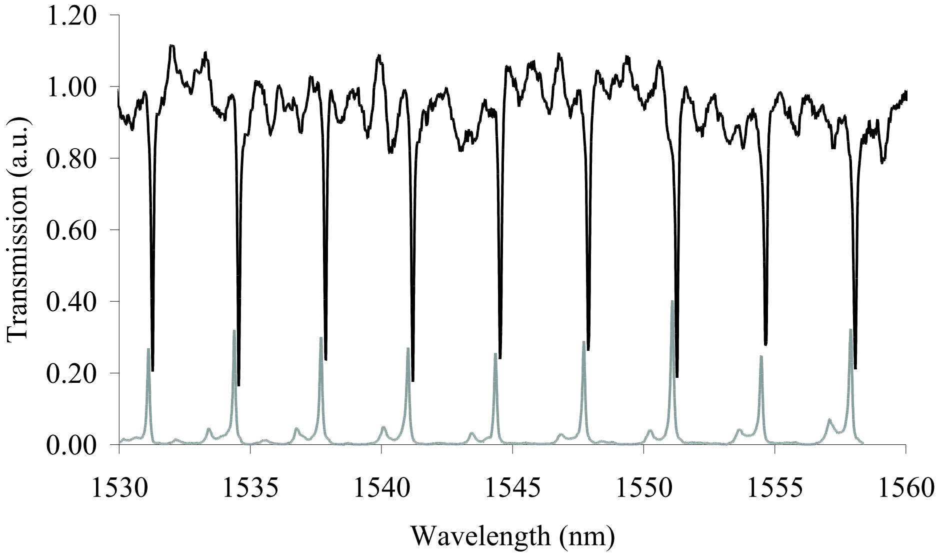

Figure 6.17: Measurement of the TE characteristic of a 30 μm disk coupled to a 1 μm wide straight waveguide

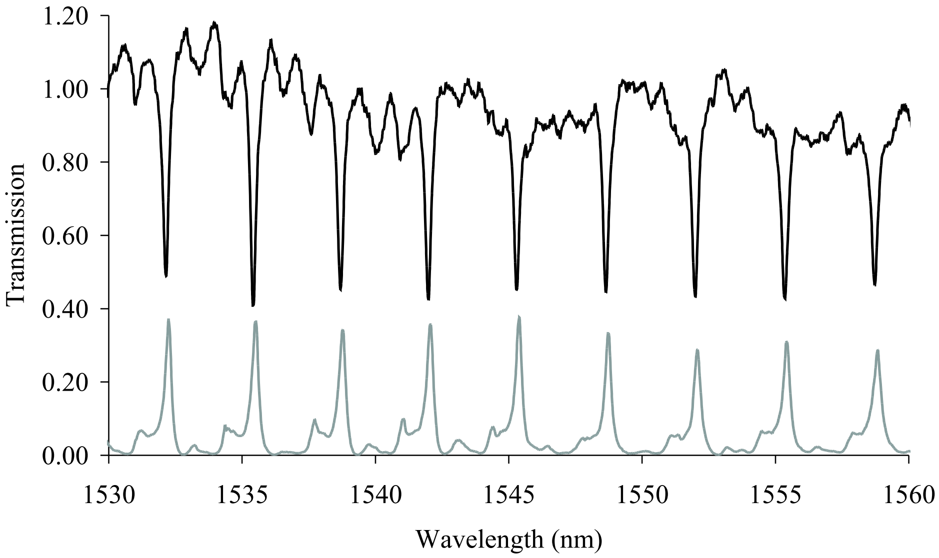

Figure 6.18: Measurement of the TM characteristic of a 30 μm disk coupled to a 1 μm wide straight waveguide

a Q-value around 1100 in TE, an FSR around 3.5 nm and a Finesse of about 25.

6.4.2 Radii inside hybrid region: polarization rotation

Simulations were also done for radii in the hybrid region, where polarization rotation can be expected. If one is working in the region of hybrid modes, the chance of exciting the two hybrid modes at the same time and causing polarization rotation is very likely. Figure 6.20 shows a simulation of a 0.8 μm wide waveguide coupled to the two hybrid zero order modes of a 15 μm radius disk. The straight waveguide mode was purely TE. The coupling to both the hybrid modes is very clear.

Figure 6.21 shows a measurement of a 15 μm radius disk coupled to a 0.8 μm wide straight waveguide. The measurement of the pass port is a measurement where a TE mode is injected in the straight waveguide and the power at the pass port is measured after a TE polarizer. This pass port clearly shows more than one resonance. The graph also shows two measurements of the drop port, one where TE light was injected in the microring and the measurement at the drop port was done with a TE polarizer and another one with TE

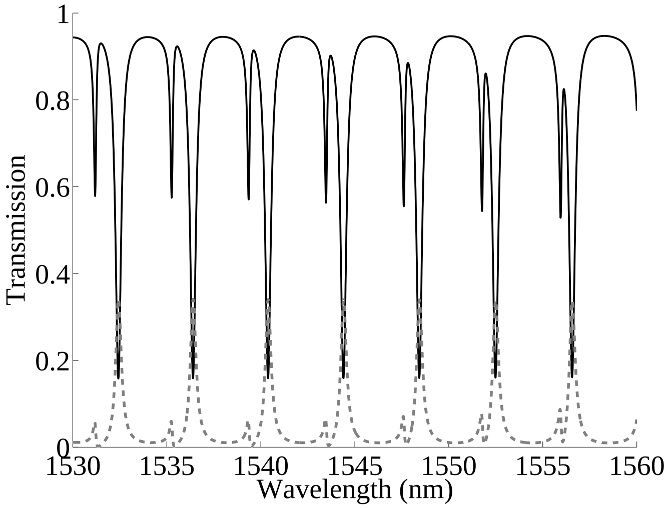

Figure 6.19: Simulation of the characteristic of a 30 μm radius disk where 2 bent waveguide modes are excited

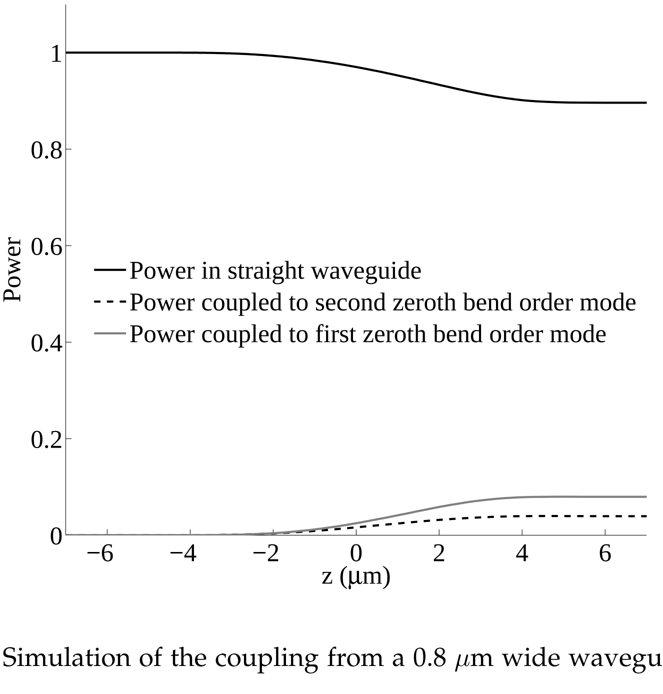

Figure 6.20: Simulation of the coupling from a 0.8 μm wide waveguide to a 15 μm radius disk

light injected and measured with a TM polarizer. From the drop port measurement it is clear that at certain resonances quite some power is converted into the TM polarization, a clear indication of polarization rotation. This is for instance very clear for the resonance around 1560 nm. In the pass port the power of resonance drops at higher wavelengths, this is due to some drift of the lensed fiber used to couple the power into the waveguide. The resonances in the drop port and the resonances in the pass port seem to be slightly shifted in wavelength. This is probably due to temperature effects as the device is quite temperature sensitive which will be exploited in the thermo-optic tuning of the device. Temperature-controlled measurements were not possible at that time.

Similar graphs could be observed when TM light was injected into the straight waveguide.

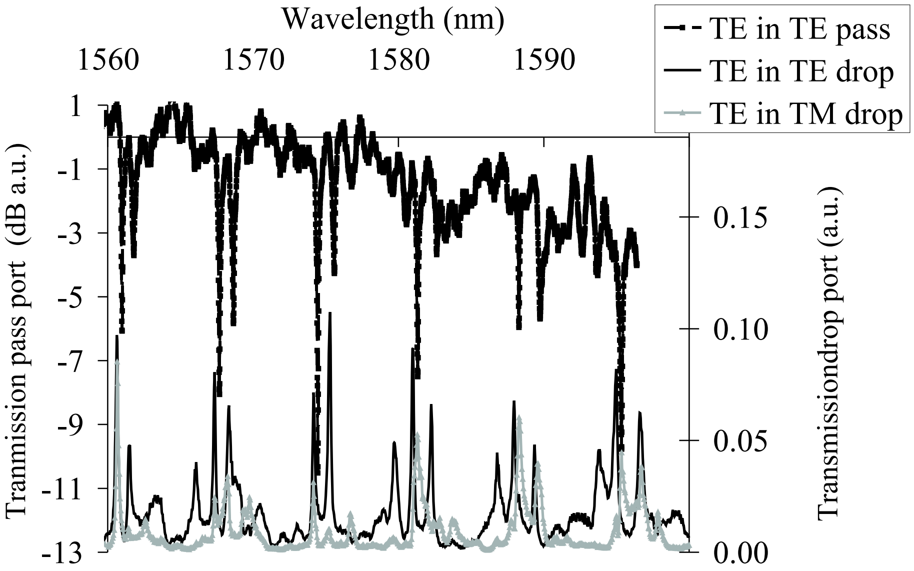

Figure 6.21: Polarization rotation due to hybrid modes

6.4.3 Shifting of the bus waveguides

To illustrate that the effects of misalignment can be large, Fig. 6.22 shows the measurement of a 30 μm radius disk with bus waveguides that had no shift with respect to the microring and bus waveguides that are shifted over 100 nm inwards, increasing the coupling coefficient. The influence of this 100 nm shift is very clear. The symmetrical alignment of the microring with respect to the bus waveguides was checked with SEM. The middle layer was however also thinner than designed.

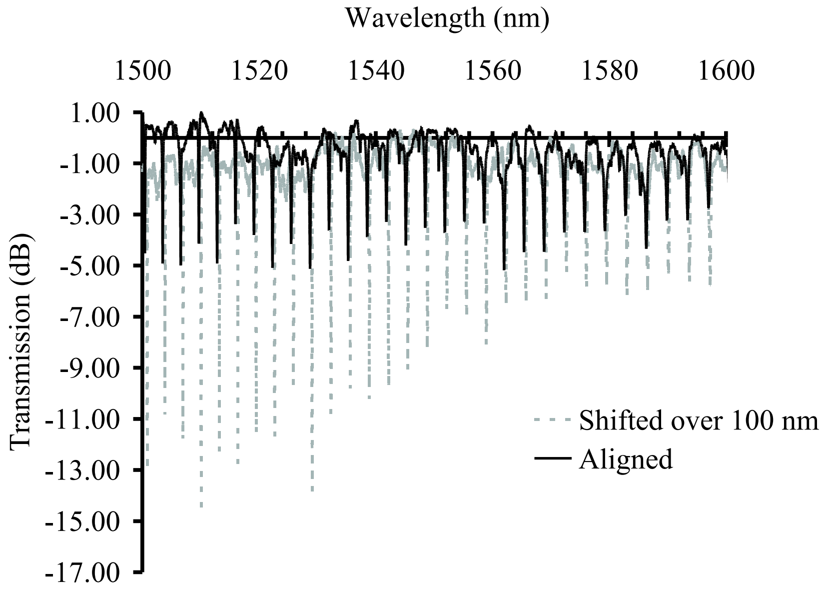

Figure 6.22: Pass port of a 30 μm disk coupled to a bus waveguide with zero shift and a bus waveguide shifted over 100 nm inwards

These shifts in the position of the bus waveguides can make the microring resonator asymmetric and closer to critical coupling. Critical coupling is the situation where all the power is extracted from the input waveguide (see Section 2.4.3). Figure 6.23 shows the measurement of the pass port of a 10 μm radius device coupled to bus waveguides with zero shift and bus waveguides with 160 nm shift in the same direction. In the latter case the microring resonator has become asymmetric. There is some increase in the extinction ratio because the device has become asymmetric but it is still far from the criterion for critical coupling.

6.5 Thermo-optic tuning

To provide tunability to the microring, Cr-contacts were added for thermo-optic tuning, which was expected to be efficient due to the low thermal conductivity of the BCB. After the initial processing, as shown in Fig. 6.1, poly-

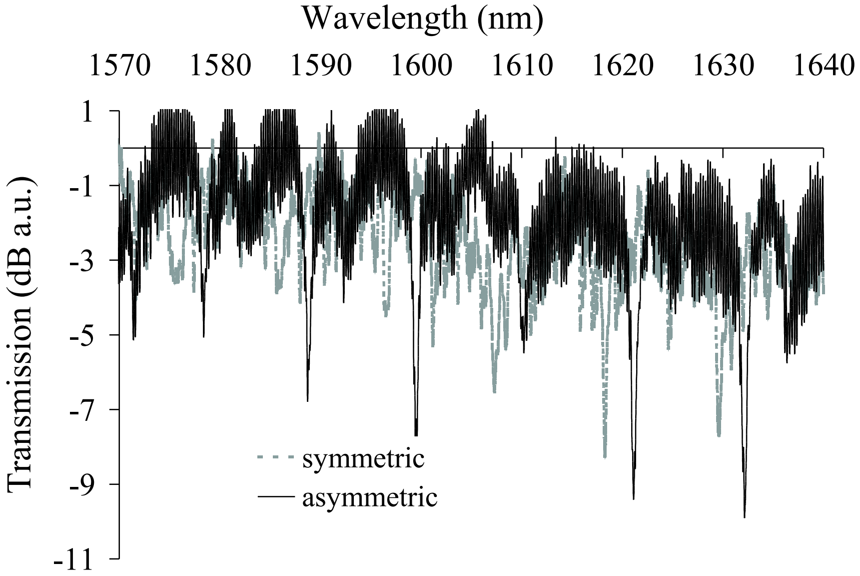

Figure 6.23: Pass port of a 10 μm disk symmetrically and asymmetrically coupled

imide was spun on top of the sample and slightly thinned. A very thin layer of Ti was then deposited to improve adhesion followed by lift-off of the Cr-contacts. A picture of a microring with Cr-contacts on top can be seen in Fig. 6.24. Most of the heat is created at the edge of the microring where the Cr-paths are smaller.

The subsequent shift of the pass port of the microring is demonstrated in Fig. 6.25 for a microring with a radius of 20 μm and a Q of 2500. The total wavelength shift versus input power can be seen in Fig. 6.26. This is a TE measurement of a disk resonator with a radius of 20 μm.

It is clear that a very high tuning range can be achieved with only limited input power: with only 50 mW of input power a tuning range of 15 nm can be achieved, or 0.3 nm/mW. From literature it is known that the dependence of the refractive index n of InP on the temperature T is the following:

$$\frac{dn}{dT} = \frac{2\,10^{-4}}{K}$$

This leads to a temperature change of 165 °C for 15 nm tuning range. This number is in the same range as what is calculated from an approximate model of the expected temperature rises based on the thermal resistances of the different layers.

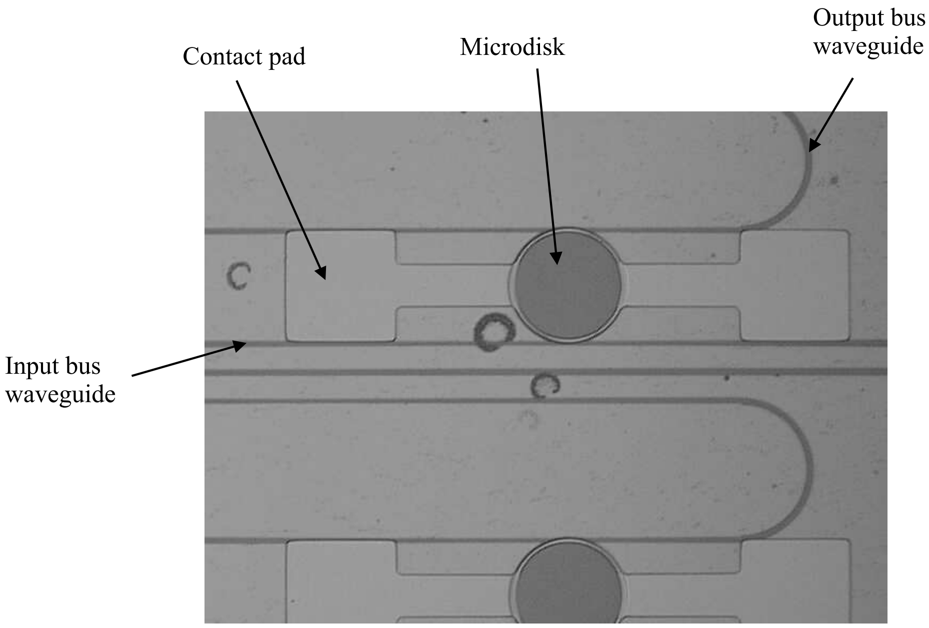

Figure 6.24: Picture of thermo-optically tunable microring

The layout of the contacts allow for a relatively localized thermo-optic effect: while tuning one ring resonator, the wavelength characteristics of another ring resonator at 250 μm distance (center to center) was measured. Up till 25 mW input, there was no effect of the heating on the neighbouring ring.

6.6 Optical bistability

The previous section demonstrated the efficient thermo-optic tuning of the device. This was then also used to show thermal bistable behaviour in the device. The heating of the device influences the refractive index contrast and can be used to make the microring resonator optically bistable. Similar work was published by Ibrahim, references can be found in Chapter 3.

A system is optically bistable if two output states are possible for the same input values. In our case this means that different transmissions are possible for the same wavelength. Figure 6.27 shows the drop characteristic of a normal microring resonator. However when sufficient power is injected into the microring this peak will change shape and the characteristic measured will depend on the direction in which the wavelength is swept. If we assume first

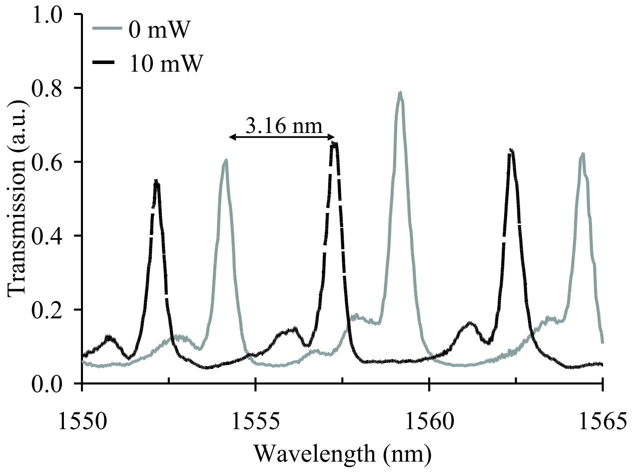

Figure 6.25: Example of the thermo-optic tuning of a 20 μm radius microdisk resonator

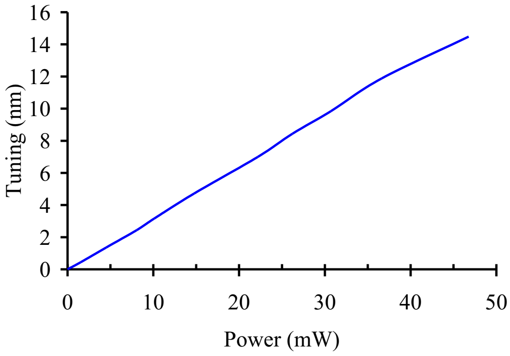

Figure 6.26: Tuning range versus input power

that the wavelength is swept from low to high wavelengths, then the following happens. As the wavelength approaches the resonance, more and more power is stored in the microring, this power causes heating and causes the refractive index to shift, which causes the peak to shift to higher wavelengths (as was demonstrated in the previous section). At a certain point however the shift is at its maximum and the power drops as is indicated in Fig. 6.27 by the arrow for the forward direction. If the wavelength is swept in the other direction a different behaviour is observed. As the wavelength approaches the resonance, the power coupled into the microring causes the peak to change shape again, but now the jump in power will take place at a different point.

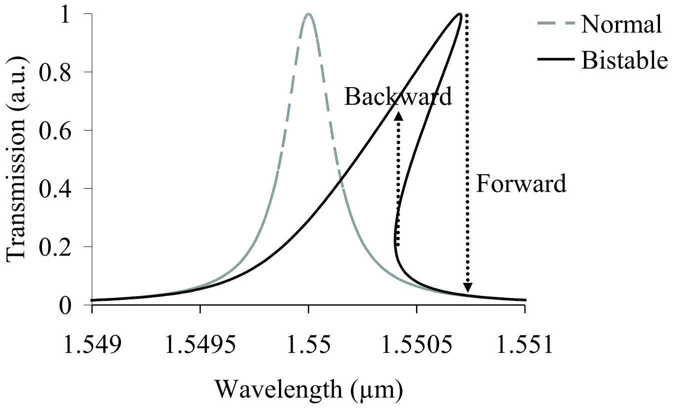

Figure 6.27: Shape of the transmission peak for optical bistable behaviour

This was demonstrated experimentally by placing an EDFA and an attenuator after the tunable laser so the amount of power in the microring could slowly be increased. This is shown in Fig. 6.28 where the different graphs for different amounts of attenuation clearly shows how the device is moving towards bistable behaviour. The last graphs (with 0.5 dB and 1 dB attenuation) were measured once by sweeping the wavelength incrementally and once decrementally. The jump appeared at different wavelengths indicating bistability had been reached. Further non-linear experiments were not possible due to lack of equipment.

6.7 MMI coupled microdisk resonators

Another device was designed and fabricated consisting of two microrings - with different radii - coupled with an MMI as can be seen in Fig. 6.29. Light

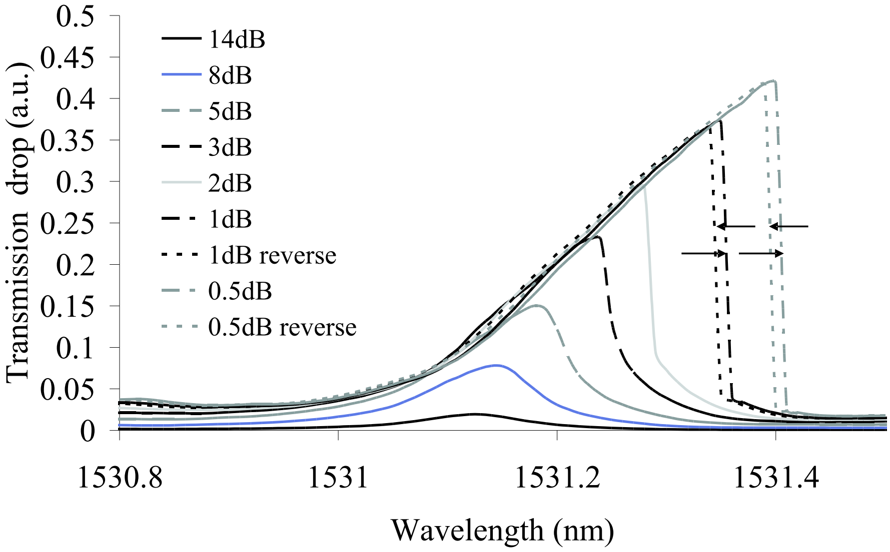

Figure 6.28: Evolution of the pass port towards bistability

injected from the right hand side is split into two signals by the MMI and only wavelengths that are in resonance in both the disks will return to the MMI where the output signal is again available at the right hand side. Both disks can be tuned thermo-optically to overlap their resonances. The two microdisks had slightly different radii, resulting in different FSR's and use could be made of the Vernier-effect to fabricate a widely tunable filter. The device could for instance be useful in a tunable laser. Figure 6.30 shows a simulation results of the expected performance of the device. This devices contained microrings with a radius of 20 μm and 15 μm. The Vernier-effect is clearly visible: where the peaks of the two rings overlap a peak appears for the entire device. The FSR of the entire device is significantly bigger than that of the single rings.

A new layer structure - described in Table 6.2 - was used to fabricate this device. Layer structure 2 was originally intended for a metallic bonding, hence the thick cladding. The composition of the core layer of the bus waveguides is also different compared to the previous structure. The lower bandgap wavelength was used to improve the coupling efficiency but the effect of this is actually quite small. At the same time the devices would also be fabricated on the previous layer structure. However early on in the process-

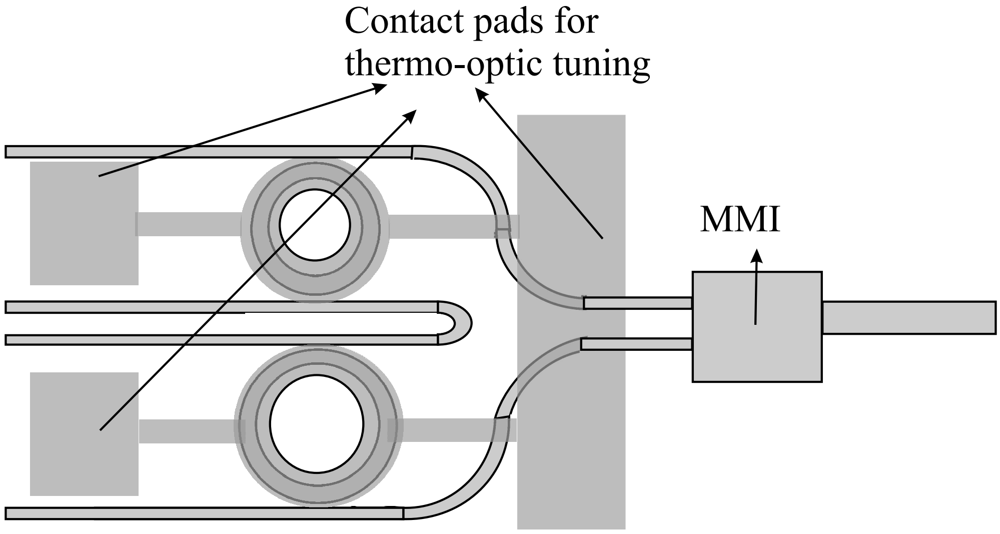

Figure 6.29: Layout of the device

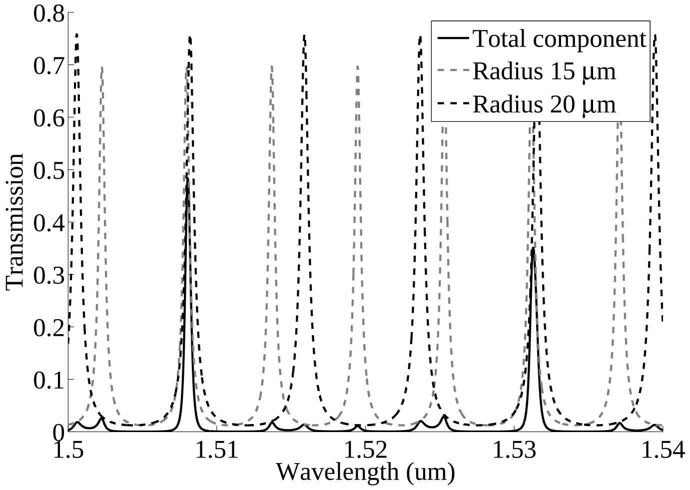

Figure 6.30: Simulation of the output of the component

ing an error occurred and the last piece of layer structure 1 could no longer be used.

Simulations on this new layer structure indicated the presence of more higher order modes in the straight waveguide. These extend however quite far into the thick lower cladding layer and the field overlap with the disk

	Composition	Layer thickness
Cladding layer	InP	1500 nm
Bus waveguide core layer	Q(1.2μm)	500 nm
Separation layer	InP	500 nm
Ring waveguide core layer	Q(1.3μm)	500 nm
Cladding layer	InP	500 nm
Etch stop layer	Q(1.3μm)	100 nm
Substrate	InP	

Table 6.2: Layer structure 2

modes is very limited, hence no significant coupling is to be expected. The coupling efficiency of the zero order straight waveguide mode and the zero order disk mode is also smaller than in the previous layer structure.

The device was fabricated, as shown in Fig. 6.31, but no satisfactory behaviour was observed. Separate MMI's were put on the mask and functioned well. Four different ports (on the left of Fig. 6.29) are available for measurement. Measurements of the outer ports should result in tranmissions similar to the regular pass port of a microring. However no clear resonances could be observed. The power at the drop ports (the inner ports) was very low and no clear resonance peaks could be seen.

A few problems could be the cause of this. First of all it was noticed that at least the thick cladding layer was significantly thinner than designed, about 10 % and probably this is the case for the other layers also. This resulted in no middle layer being left and alignment tolerances being bad. Second, after the move to the new cleanroom significant effort was put into recalibrating and optimizing the etching process. This delayed processing for several months and in the end a reasonable process seemed to have been established. However together with the MMI coupled rings an old mask containing single rings was processsed on this new layer structure. Very few of these functioned and the ones that did exhibited a very high loss (α was around 30/cm) leading to believe that despite significant efforts the etching process was not yet optimal after the move to the new cleanroom.

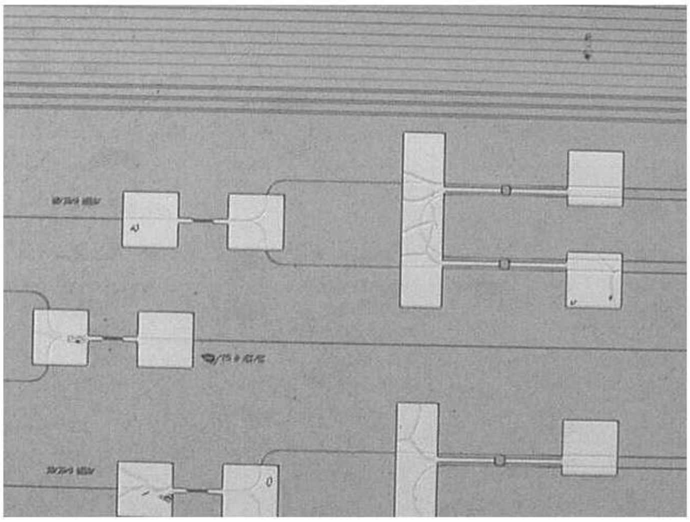

Figure 6.31: Picture of a fabricated device with MMI coupled rings

6.8 Dispersion

To have an idea of the effect of dispersion the eye diagram was measured using a 10 Gbit/s modulated signal that was injected into the microring after amplification with an EDFA. The output was collected with a lensed fiber and visualised on an oscilloscope. The resulting eyediagram for a microring with 20 μm radius and with a Q-factor of 3500 can be seen in Fig. 6.32. A simulation of the response of a 10 Gbit/s signal for a microring with a Q of 3500 was shown in Section 2.2.9. The flanks of the eye are clear and steep, the zero and one level are quite noisy, probably due to the low power output. Use of this ring up to at least 20 Gbit/s should not be a problem, the equipment to test this was not available though.

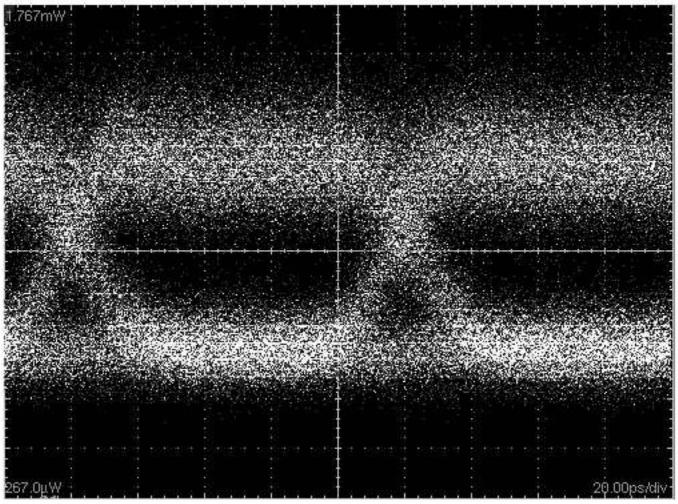

Figure 6.32: Eye-diagram of a 10 Gbit/s signal after passing through a microring with a Q-value of 3500

6.9 Conclusions

A variety of microring resonators have been fabricated, with different radii coupled to different waveguide widths. Different phenomena could be observed in the measurements such as polarization rotation and coupling to higher order modes. These could be explained by simulations. This indicates that the simulation tool can be used to design proper microrings and avoid deleterious effects such as excitation of hybrid or higher order modes.

Very efficient thermo-optic tuning was demonstrated due to the low thermal conductivity of BCB. This also allowed the demonstration of thermal bistability. A widely tunable filter was proposed and fabricated but no good results were obtained probably due to the lack of quality of the etching process.

Chapter 7

Conclusions

7.1 Conclusions

The two keywords for this work have been microring resonators and wafer bonding. The wafer bonding process using BCB that the author has developed in the university cleanroom, has proven to be fairly easy to use once all the process parameters are known and does not require anything other than standard cleanroom equipment. It allows the integration of very different materials, an important step on the road to combining different material systems in heterogeneous integration and exploiting the strengths of each material. The development of various different membrane type devices has been demonstrated by the fabrication of LED's and lasers, the first active devices fabricated with this technique. The reliability tests have proven the quality of the process.

Microdisk resonators, versatile and compact components, have been fabricated using this BCB wafer bonding. Fabricating micoring resonators is but one thing, the other is designing them. This has long proved to be quite difficult due to the absence of 3D bend mode solvers and ways to efficiently calculate the coupling between the bent waveguide and the straight waveguide. These difficulties have been overcome, a small survey of the different commercial mode solvers has been given, showing that they are very useful instruments. However, not all structures can be simulated yet, especially bent waveguides with small radii and high refractive index contrasts. The coupled mode theory implemented by the author and using the modal fields provided by commercial mode solvers, is an efficient way of calculating the coupling coefficients even in three dimensions, fully vectorial and for multimodal waveguides.

This modelling has allowed us to explain the behaviour exhibited in the wide range of devices fabricated, behaviour such as coupling to higher order modes and polarization rotation. To our knowledge, these are the first comparisons of microring simulations using this technique with actual measured devices.

The low thermal conductivity of BCB was exploited to make the microring resonators thermo-optically tunable which proved to be a very efficient process. The next step was to combine two microrings to create an even more widely tunable filter by using the Vernier effect. Processing issues have unfortunately prevented this.

7.2 Future work

The possible roads for future work are plenty, both for microring resonators and for wafer bonding.

First of all, let us have a look at a few things that could help improve the functionality and fabrication of single microring devices. Now that the tools are available to simulate the microring resonator, its design can be made much more carefully. This includes avoiding polarization rotation and excitation of higher order modes and accurately designing the amount of coupling wanted. However, more accurately grown epitaxial layer structures should be available then, as the thickness of these layers influences the coupling coefficient significantly. Also, to accurately design a good microring, the waveguide losses should be well known beforehand. This lack of a reproducible etching process has hampered work significantly. Alignment tolerances have proven to be important also and should always be taken into account. To assess the alignment tolerance without destroying the device, extra markers on the side of the samples could be useful. These pieces will be cleaved off anyway and can be taken to the SEM.

The first thing to do after etching has been optimized, is to re-process the MMI coupled rings. A next step could be to integrate the microring resonator or the MMI coupled rings with a laser, in the latter case creating a widely tunable laser. Other active devices with microrings are also possible. For these devices the high thermal resistance created by the BCB wafer bonding can be a problem but this could be minimised by further developing the thin bonding layers mentioned in this work.

On the wafer bonding side, the route to heterogeneous integration is now open. Possible ways of coupling light from, for instance an InP active membrane to an SOI waveguide, are already being studied and a new interesting research area has opened up. This is the topic of several projects and PhD's that have already started.